12-14-2015

Optimization of Shell Growth and Influence of Surface Ligands for Colloidal CDSE/CDS Core/Shell Quantum Dots

Rui Tan
University of South Carolina - Columbia

OPTIMIZATION OF SHELL GROWTH AND INFLUENCE OF SURFACE LIGANDS FOR COLLOIDAL CDSE/CDS CORE/SHELL QUANTUM DOTS

by

Rui Tan

Bachelor of Science
University of Science and Technology of China, 2006

Submitted in Partial Fulfillment of the Requirements

For the Degree of Doctor of Philosophy in

Chemistry

College of Arts and Sciences

University of South Carolina

2015

Accepted by:

Andrew B. Greytak, Major Professor

Mark A. Berg, Committee Member

Dmitry V. Peryshkov, Committee Member

Scott R. Crittenden, Committee Member

Lacy Ford, Senior Vice Provost and Dean of Graduate Studies

DEDICATION

This dissertation is gratefully dedicated to my dear wife Lanlan Meng, who is always there to encourage and support me throughout the entirety of my PhD. To my loving parents Jun Jiang and Zhenju Tan, I extend a special feeling of gratitude for their endless love, constant support and encouragement to me throughout the years. It is their patience and guidance at an early age that built a solid foundation of my values and passions for life and science.

I also dedicate the dissertation to my church family and many friends who have supported and loved me throughout my endeavors. I want to give my sincere thanks and appreciation for all they have done, especially to Ron and Marianne Parker, Ray and Gail Moore who loved and encouraged me with kindness and thoughtfulness and treated me as family.

ACKNOWLEDGEMENTS

It has been a fruitful and thankful five years in my life. I have learned and experienced a lot during the time I have pursued my PhD. I could not have gotten where I am today without the support, patience and partnership of a great number of people.

I want to express my deepest thanks and appreciation to my advisor Dr. Andrew B. Greytak, for his continuous guidance and support of my Ph.D study and research, as well as his patience, motivation, enthusiasm and immense knowledge. His help has been greatly appreciated during my five years of research and writing of this thesis.

Besides my advisor, I want to acknowledge with gratitude my committee chairman, Dr. Mark A. Berg, who mentored me with great patience, not only with instructions of knowledge and science but also in helping me to find my way of life and passions of my career. I also want to give thanks to my committee members Dr. Linda Shimizu and Dr Dmitry V. Peryshkov for their generosity in allowing me to use experimental instruments and Dr. Scott R. Crittenden for his patience. And thanks to all the above professors for agreeing to serve on my committee. And I want to thank Dr. Natalia B. Shustova for her enthusiasm in collaboration on projects and sharing of instruments.

I would like give thanks to all the lab mates, Yi Shen, Pravin Paudel, Megan Y. Gee, Stephen K. Roberts, Bobby Barker, Preecha Kittikhunnatham, and Adam Roberge, who have collaborated and helped with the projects in this dissertation.

I also want to give thanks and my great gratitude to my friends during my time at

the University of South Carolina for all their company and friendship. To Ping Li, Haorui Wu, Weiwei Xu, Xueyang Li, Li Wang, Ying Zheng, because of you all, my life is full of joy and happiness during my years in Columbia. I want to address my very special thanks and appreciations to my church family in Columbia. It is a great blessing for me to be part of this family. Thanks to Ron and Marianne Parker and Ray and Gail Moore for your continuous love, encouragement and support for me and my wife. I am especially thankful for your preparation of my wedding, which was my most cherished memory. Thanks to all family members: Joshua and Selina Guo, Eun Son Lim, Al and Linda Ringwald, Ye Lin and Jinwen Chen, Oliver Wang, Meixuan Lin, Jing Li. Thank you all for your love and care that raised my spirits when I was weary.

My deepest thanks are to my dear Mom and Dad, Jun Jiang and Zhenju Tan, for your unconditional love, endless encouragement and patience that raised and supported me throughout my life. Also, I want to express my gratitude to my cousins Huihua Huang and Huifen Huang, who are taking care of my parents for me while I study abroad

At last, my dear wife, Lanlan Meng is the greatest blessing that has ever happened to me. She has continuously helped, encouraged and supported me with love and patience throughout this difficult period in the most positive way.

ABSTRACT

Progress in the colloidal synthesis of semiconductor quantum dots (QDs) has triggered a burst of research toward applications in QD based light emitting diodes, biological imaging as fluorescent tags, and advanced solar cell designs. In order to adjust and optimize the photo physical properties of QDs, QD heterostructures have been introduced and widely explored. This dissertation is focused on studies of growth of semiconductor colloidal CdSe/CdS core/shell quantum dots and the influences of neutral surface ligands to their photo-physical properties.

Chapter 1 provides an introduction of the concept of semiconductor colloidal nanoparticles, core/shell heterostructures and the synthesis methods as well as the importance and applications.

In chapter 2, we monitor effective bandgap energy shifts and free reagent concentration during the formation of CdS shells on CdSe nanocrystals to test the hypothesis that alternating addition of stoichiometric doses of precursors can effectively saturate surface sites and thereby enforce conformal shell growth. The selective ionic layer addition and reaction (SILAR) mechanism has been proposed to describe growth under such conditions and the method is attractive because of the opportunity to (1) avoid cross-reaction of precursors in growing binary films in solution and (2) enforce conformal growth, rather than regioselective growth, by saturating all available surface sites in a self-limiting manner in each half-cycle. The strong redshift that takes place when CdS shells are grown on CdSe cores provides a convenient process monitoring tool

that complements Scanning Transmission Electron Microscopy (STEM) imaging and analytical measurements of free reagent concentration. We find that under commonly-used conditions, a cadmium oleate precursor reacts incompletely at chalcogenide-saturated nanocrystal surfaces. Although approximately spherical particles are obtained, the growth does not proceed via saturating cycles as described in the SILAR mechanism. This has implications for the rational control of conformal and regioselective growth of epilayers on nanocrystal quantum dots and higher-dimensional chalcogenide semiconductor nanostructures via solution processes.

In chapter 3, we describe an experiment designed to identify the role of specific molecular ligands in maintaining the high photoluminescence (PL) quantum yield (QY) observed in as-synthesized CdSe/CdZnS and CdSe/CdS quantum dots (QDs). Although it has been possible for many years to prepare core/shell quantum dots with near-unity quantum yield through high-temperature colloidal synthesis, purification of such colloidal particles is frequently accompanied by a reduction in quantum yield. Here, a recently established gel permeation chromatography (GPC) technique is used to remove weakly associated ligands without a change in solvent: a decrease in ensemble QY and average PL lifetime is observed. Minor components of the initial mixture that were removed by GPC are then added separately to purified QD samples to determine whether reintroduction of these components can restore the photophysical properties of the initial sample. We show that among these putative ligands trioctylphosphine and cadmium oleate can regenerate the initial high QY of all samples, but only the “L-type” ligands (trioctyphosphine and oleylamine) can restore the QY without changing the shapes of the optical spectra. On the basis of the PL decay analysis, we confirm that quenching in

GPC-purified samples and regeneration in ligand-introduced samples are associated chiefly with changes in the relative population fraction of QDs with different decay rates. The reversibility of the QY regeneration process has also been studied; the introduction and removal of trioctylphosphine and oleylamine tend to be reversible, while cadmium oleate is not. Finally, isothermal titration calorimetry (ITC) has been used to study the relationship between the binding strength of the neutral ligands to the surface and photophysical property changes in QD samples to which they are added.

In chapter 4, the influence of different mixtures of solvents (such as amines), are studied as to increase the synthetic yield of the shell for core/shell nanoparticles when using SILAR based techniques for shell growth. Conversion of shell precursors to surface-adsorbed equivalents should be maximized for effective control of shell growth. Here, UV-vis absorption and photoluminescence spectroscopy are applied to monitor shell growth. Additionally, during the shell growth, the free precursor concentration is measured by Inductively Coupled Plasma Mass Spectrometry (ICP-MS), and fitted with Langmuir isotherm model which reveals the influence of different solvents on the fractional occupation of shell precursor equivalents on the QD surface. The binding affinities of the solvent molecules to the QD surface are also studied to understand the influence of such interactions on shell growth. This study is important for understanding the mechanism of growing the core-shell nanoparticles via SILAR technique and provides conditions under which precursor binding and synthetic yield can be increased, which could be applicable to synthesis of isotropic and anisotropic core/shell nanoparticles in an advanced and controllable manner.

PREFACE

The dissertation is based on original work by the author, Rui Tan, with the advice and collaboration of Dr. Andrew Greytak and members of his research group.

A version of chapter 2 has been published in *Chemistry of Materials.* Reprinted with permission from Tan, R.; Blom, D. A.; Ma, S.; Greytak, A. B. *Chem. Mater.* **2013***, 25* (18), 3724–3736. http://pubs.acs.org/doi/abs/10.1021/cm402148s. Copyright 2013 American Chemical Society. I was the lead investigator, responsible for all major areas of concept formation, data collection and analysis, as well as the majority of manuscript composition. Doug Blom was in charge of STEM measurements and Shuguo Ma was in charge of XPS measurements. Andrew Greytak was the supervisory author on this project and was involved throughout the project in concept formation and manuscript edits.

A portion of chapter 3 has been published in the Journal of *ACS Nano.* Reprinted with permission from Shen, Y.; Tan, R.; Gee, M. Y.; Greytak, A. B. *ACS Nano* **2015**, *9* (3), 3345–3359. http://pubs.acs.org/doi/abs/10.1021/acsnano.5b00671. Copyright 2015 American Chemical Society. All authors contributed to the writing of the manuscript. The major experimental design and execution were done by Yi Shen and myself. Yi Shen was responsible for purification, quantum yield measurement and NMR; I am responsible for photo-luminescence lifetime measurements and fitting of decay curves. Isothermal titration calorimetry (ITC) and data analysis was performed by Megan Gee. Andrew Greytak was the supervisory author on this project and was involved throughout the project in concept formation and manuscript edits. .

I was the lead investigator for the original, unpublished work/projects located in chapter 4, where I was responsible for all major areas of concept formation, data collection and analysis, as well as the majority of manuscript composition. Andrew Greytak was the supervisory author on this project and was involved throughout the project in concept formation and manuscript edits. Stephen K. Roberts had greatly assisted with data collection and manuscript edits. Doug Blom was responsible to all the STEM measurements and image collection.

TABLE OF CONTENTS

LIST OF TABLES

LIST OF FIGURES

LIST OF ABBREVIATIONS

CdOA ..... Cadmium oleate

CdTDPA ..... Cadmium-tetradecylphosphonate

DOM ..... Di-n-octylamine

GPC ..... Gel Permeation Chromatography

ML ..... Monolayer

ML eq. ..... Monolayer Equivalent

OAM (OAm) ..... oleylamine

ODE 1-octadecene

PL. ..... Photoluminescence

PLQY ..... Photoluminescence Quantum Yield

QD ..... Quantum Dot

QY ..... Quantum Yield

SILAR ..... Successive Ionic Layer Adsorption and Reaction

STEM ..... Scanning Transmission Electron Microscopy

TCSPC ..... Time-correlated single photon counting

TDPA ..... Tetradecylphosphonic acid

THM ..... Tri-n-hexylamine

TOP ..... Tri-n-octylphosphine

TOPO ..... Tri-n-octylphosphine oxide

XPS ..... X-ray photoelectron spectroscopy

CHAPTER 1

INTRODUCTION TO SEMICONDUCTOR QUANTUM DOTS

1.1. Introduction

Semiconductor nanocrystals known as quantum dots (QDs) are roughly spherical pieces of direct bandgap semiconductors with diameters on the order of 1-10 nm. The most well-known examples are II-VI material such as CdS, CdSe, ZnSe. A typical QD consists of a spherical semiconductor core surrounded by a layer of organic surfactant molecules that provide chemical and electrical insulation. Sometimes a higher-band-gap semiconductor shell is put between the core and the organic "caps" to provide further isolation of the core, and form a core/shell heterostructure. Since the size of quantum dot is of the same magnitude as the de Broglie wavelength of the electron wave function, the electronic states are confined in all three spatial dimensions; this will result in quantum confinement and give rise to electronic and optical properties that differs from those of bulk materials.

For semiconductors, in which the electronic states are delocalized throughout the material, the filled and empty electronic states are separated by an energy bandgap; this is intrinsic to the type of material. The continuous nature of these states in bulk semiconductor results in a band structure-conduction band for continuous electronic states and valence band for continuous hole states. In bulk semiconductors, the electrons are unconfined and experiencing the boundless periodic electric potential of the crystal lattice. When electrons are excited from the valence band to the conduction band they will relax to

near the band edge before recombining radiatively or non- radiatively with holes in the valence band to return to the ground state. Radiative recombination results in emission of photons with energies near the bandgap (E_g). Since the bandgap is constant in bulk materials, the energy of emitted photons is independent of the material size. Compared to bulk semiconductors, which has continuous electronic density of states within valence band and conduction band, as the three effective spatial dimensions that constrain the electron's wave function are reduced one by one to the length scales that are comparable to the characteristic lengths of electron-hole pairs-exciton Bohr radius (usually within 10 nm), the material changes from 3-D bulk to 2-D quantum well to 1-D quantum wire (nanowire)

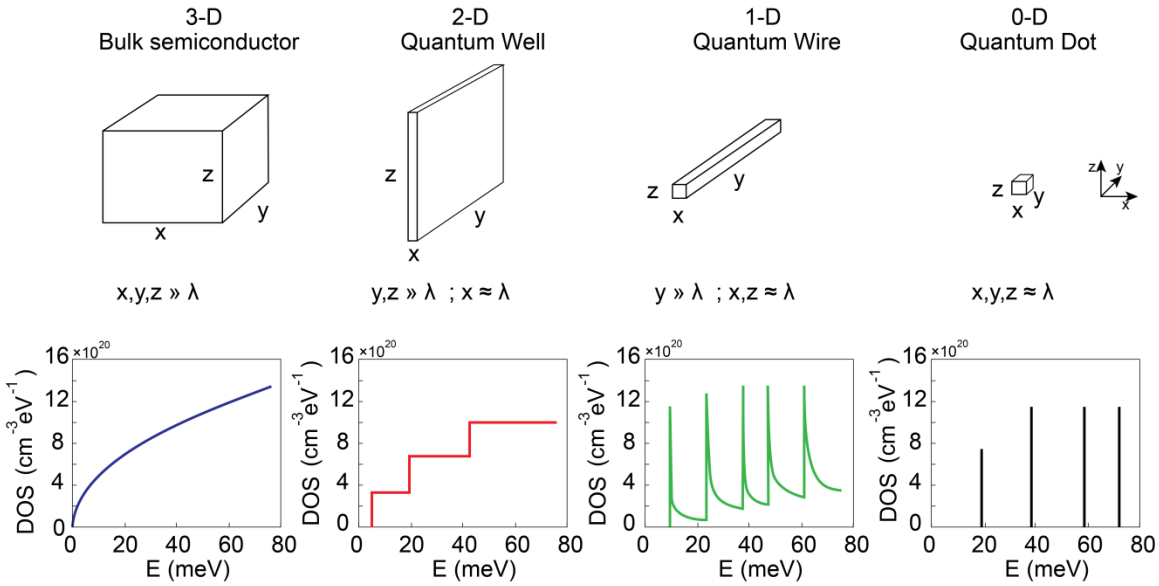

Figure 1.1 The electronic density of state as a function of energy varies from 3-D bulk semiconductor to 0-D quantum dot.

to 0-D quantum dot and the density of states changes from continuous states to discrete states. (**Figure 1.1**) The position of such discrete electronic states varies as the size of the quantum dots changes. As a result, the smaller the quantum dots, the electrons are more

strongly confined inside, which leads to larger effective bandgap. In contrast, bigger quantum dots have the electrons that are distributed and relaxed in a larger space and cause the effective bandgap to decrease and approach the bandgap of the bulk materials. This unique physical character of quantum dots leads to their most striking and distinguishing property - the size dependence of bandgap absorption and emission. For example, the photoluminescence and electroluminescence emission for CdSe quantum dots can be tuned within the visible spectrum from wavelength of 473 nm to 655 nm by tuning the nanocrystal size (diameter) from 2.1 nm to 7.5 nm,[1,2] and for InP quantum dots from 520 nm to 760 nm by changing the size from 2nm to 6nm.[3] Within the region of 1 nm and 10 nm, where the size (radius) of quantum dots is smaller than the bulk-exciton Bohr radius, the electron-hole pairs within, as well as their wave functions, are confined by the crystal boundary. Even a little variation of such boundary will lead to significant changes of the positions of the discrete electron and hole states, hence the effective bandgap. The result is a smoothly varying function of emitted photons with energy dependent on the quantum dot size. Theoretically, such size-dependent optical properties can be modeled by the effective mass approximation based on quantum confinement, which predicts energy bandgap is proportional to $1/R^2$.[4,5]

As a result of such distinctive advantages, colloidal semiconductor quantum dots has triggered a burst of research toward applications in biological imaging as fluorescent tags,[6–14] QD-based light emitting diodes (LED)[15–25] for displays, as well as pH sensors[26,27] and thermal sensors.[28,29] Besides emitting fluorescence photons by the radiative recombination of electron-hole pairs generated by incident light, the carriers can potentially be separated and drive a current through an external circuit, which makes

quantum dots an extraordinary candidate as the light absorber in solar cells[30–35] and focal plane arrays.[30]

1.2. Synthesis of quantum dots

In order to produce quantum dots with well-defined shapes (typically spherical) with narrow size distribution, the reaction is kinetically controlled by running the system far from the global equilibrium. In particular, the reaction is frequently designed to have a brief nucleation phase and longer growth phase. In a typical synthesis, firstly metal precursors are activated in a high boiling point solvent at a high temperature. Secondly, after a fast injection of chalcogenide precursors (**Figure 1.2**, **1.**) at high temperature nuclei are formed during an initial rapid nucleation phase where the nucleation rate ($R_{nucleation}$) is much higher than the surface growth rate (R_{growth}). Thirdly, following nucleation, when the precursor concentration has decreased lower than the nucleation threshold where $R_{nucleation}<R_{growth}$, homogeneous growth of particles is enforced by precursors **(Figure 1.2**, **2.**). The reaction is then quenched (**Figure 1.2**, **3.**) by lowering the temperature or introducing a stabilizing agent that stops further reaction at the nanocrystal surfaces. Finally, after the temperature is reduced and Ostwald ripening (**Figure 1.2**, **4.**) has stopped, nanocrystals stop growing and typical quantum dots are formed.[31–33]

A vast number of studies have been focused on the synthesis of colloidal semiconductor quantum dots over the past decades, particularly for CdSe quantum dots, after the discovery by Michael Steigerwald using organometallic reagents at low temperature, yet achieving moderate size distributions.[34] Later on, high boiling point coordinating solvent mixtures such as mixtures of tributylphosphine (TBP) and tributylphosphine oxide (TBPO),[35] as well as mixtures of trioctylphosphine (TOP) and

trioctylphosphine oxide (TOPO),[6] was introduced by Moungi Bawendi, and allowed synthesis at high temperature along with utilization of phosphine chalcogenide TOPSe as selenium source and successfully achieving CdSe quantum dots from 2-10 nm in diameter with narrow size distributions.[6]

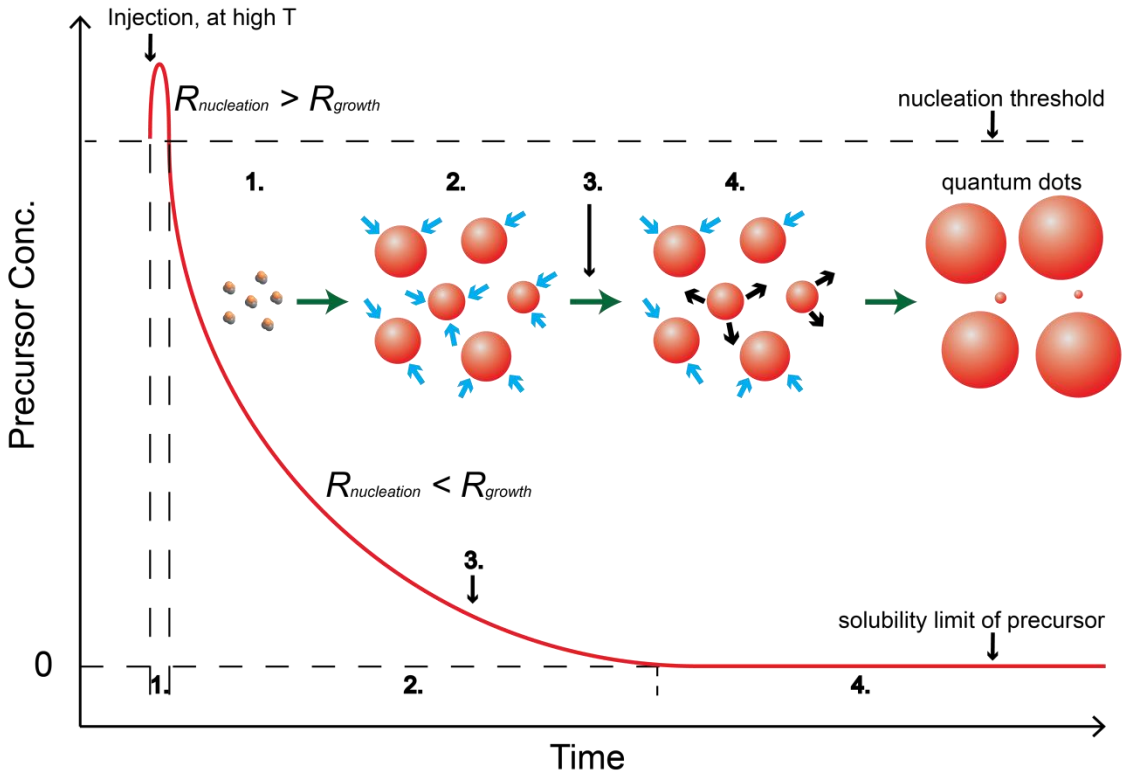

Figure 1.2 Typical reaction coordinates of synthesis of monodispersed colloidal QDs. **1.** Nucleation at high temperature (far from equilibrium) **2.** Nanocrystal growth. **3.** Reaction quenching. **4.** Ostwald ripening.

This "hot-injection" synthetic method in high temperature with low cost solvents leads to kinetic nucleation far from thermodynamic equilibrium and has been widely studied, extended and modified for quantum dots synthesis of other types[36–39] and structures[40–44] (including ref 13a,d,e,p in ref40) as well as other nanoparticles.[45–48] However, since the nucleation rate is fast, quenching the reaction in a consistent manner to get consistent sizes of particles from batch to batch is challenging and limited in

control. Recently, more moderate methods have been developed by Ou Chen *et. al* [49] using low cost SeO_2 as the selenium precursor for a non-injecting synthesis conducted in air without the need for any oxygen-free manipulation, producing high quality CdSe QDs, as well as other typical metal selenide QDs such as PbSe and $Pd_{4.5}Se$ with high crystallinity and narrow size distribution. Very recently, Jonathan Owen[50] developed a library of thioureas whose substitution pattern tunes their conversion reactivity. The tunable and faster thiourea conversion kinetics increase the extent of crystal nucleation allowing the nanocrystal concentration to be adjusted and reaching a desired crystal size at full conversion.[50] High quality QDs with narrow size distributions were achieved utilizing these new methods which opens the door for further modification, adjustment and optimization for semiconductor quantum dot synthesis.

1.3. Quantum dot core/shell heterostructures

In order to optimize and adjust the photo-physical properties of quantum dots, core/shell heterostructures have been introduced and widely explored.[51–66] Representative examples for core and shell composed of type II–VI, IV–VI, and III–V semiconductors include CdSe/CdS[51,54,62,63], CdTe/CdSe[56] ,CdSe/ZnS,[52,53] and InAs/InP.[67]

Design considerations in choosing core and shell materials include lattice mismatch and bandgap offsets/alignments, in order to create stable Type I, Type II, reverse Type I, quasi-Type II heterostructures (**Figure 1.3**) Reduction of lattice mismatch between core and shell materials minimizes strain and provides robust quantum dots amenable to surface modifications.[68] Choosing materials with different bandgap offsets/alignments will allow control of degree of confinement in order to tune radiative wavelengths[56], lifetimes[55,69] and charge separations.[70,71] For CdSe QDs, shell materials such as CdS (with small lattice mismatch), ZnS (with high bandgap offsets) and CdZnS

alloys are frequently composed of sulfide based materials to enable stability under ambient conditions.[51,52,72] Sometimes alloy shells or gradient shells are engineered to achieve both lattice mismatch minimization, core/shell interface states elimination and bandgap offsets/alignments design.

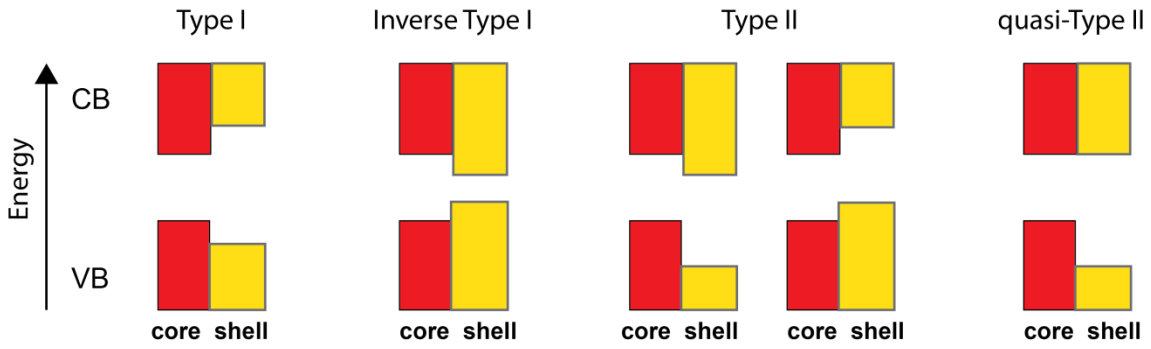

Figure 1.3 Types of conduction and valence band alignment for semiconductor core/shell nanoparticles.

There are several advantages of quantum dot core/shell structures versus core-only quantum dots. Firstly, an enclosing shell will introduce chemical passivation by eliminating dangling bonds and suppressing oxidation at the surface of the core. Secondly, a high density of states above shell bandgap is built which can further increase the excitation rate (absorption cross-section) and enhance light harvesting. Thirdly, typically for Type-I alignment (**Figure 1.3**,Type I), the shell with larger bandgap can increase the electronic isolation from the core by introducing barriers between band-edge electron and hole states and surface-associated trap states so that radiative recombination rate as well as photoluminescence quantum yield is increased. For Type-II alignment (**Figure 1.3**,Type II) with staggered bandgap, the charge carriers separation are enhanced as a result of the conjunction of shell with lower conduction band and lower valence band (or higher conduction band and higher valence band), because the electrons (or holes) favor

lower conduction band-edge (higher valence band-edge) in the shell while the holes (electrons) are confined in the core by lower valence band (higher conduction band) of the shell. Type-II core/shell quantum dots are useful as they can possess longer emission lifetimes (e.g., CdTe/CdSe[56,73,74] and ZnSe/CdSe[75]) and as more suitable lasing materials than homogeneous quantum dots.[76,77]

Both isotropic and anisotropic core/shell structures have properties that can lead to different advantages. In certain applications, (**Figure 1.4**) taking CdSe/CdS nanoparticle for example, in bare CdSe cores excited electrons are easily trapped by the surface states and cause a high non-radiative decay rate (k_{nr}) (**Figure 1.4**, left).

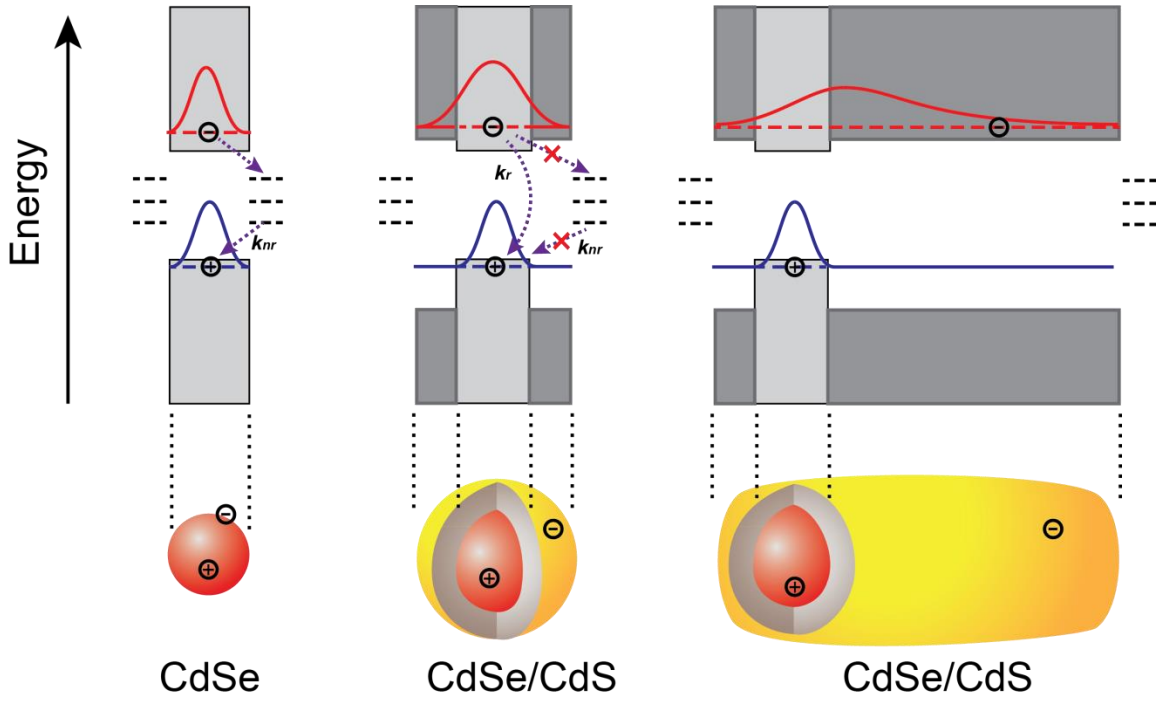

Figure 1.4 Scheme of energy alignments for CdSe QD, isotropic CdSe/CdS core/shell QD and anisotropic CdSe/CdS dot-in-rod nanorod.

Introducing materials with higher bandgap than the CdSe core like CdS or ZnS to form an isotropic (spherical) shell could enhance the photoluminescence quantum yield (PLQY), brightness and photo-stability as a result of isolation from the surface trapping

states and recombination pathways (**Figure 1.4**, center). Anisotropic dot-in-rod heterostructures can enhance charge separation in photovoltaic applications, because electrons with small effective mass can delocalize over the entire particle since the wave function of electrons could extend to the entire particle, while holes with large effective mass and confined by the lower valence band of the shell will localize in the core region (**Figure 1.4**, right).

Core/shell heterostructures composed of other materials with different bandgap and band alignments as well as with shells in different shapes will result in different population, density and delocalization/localization of carriers in the core and shell region. Anisotropic shells with shapes other than spherical and elongated can also lead to unique photophysical and electronic properties. For example, the tetrapod-shaped CdSe/CdS nanoparticles[55] are reported to have holes localized in one of the four CdS arms and drag the electron toward the arm where they both localize and recombine resulting in emission from CdS because of coulomb potential[78], and displayed anisotropic optical emission[79], and even multiexcitonic dual emission.[80] Structures such as $CdS_{1-x}Se_x$ nanorods with axial anisotropy (a CdSe-rich head and a CdS-rich tail) also been studied and show effective electronic communication between the nanorod head and tail segments.[81]

1.4. Synthesis of isotropic core/shell quantum dots

Two synthetic routes are commonly used to achieve enforcement of isotropic growth of a semiconductor shell material over a quantum dot core.

The first method requires simultaneous addition of highly reactive precursors. The introduction of diethyl zinc, dimethyl cadmium, and bis(trimethylsilyl) sulfide to the CdSe core solution to grow CdSe/CdS core/shell particles was developed in the mid 1990s.[51,52,72] These syntheses are usually conducted at lower temperatures than quantum

dot core synthesis and kept low precursor concentration, to prevent the nucleation of shell material to form new clusters or even quantum dots. However, this method still has limited control of the particle morphology and the resulting particles can have a broad size distribution. Meanwhile, the requirement of highly reactive and expensive organic-metallic precursors increases the experimental execution difficulty and limits extension of such methods for massive production.

The second method utilizes Successive Ionic Layer Adsorption and Reaction (SILAR)[64,65] which is inspired by atomic layer deposition techniques. The SILAR method has been applied in order to enforce formation of isotropic core/shell quantum dots. It is designed to (1) enforce conformal growth by saturating all available surface sites in a self-limiting manner in each half-cycle; (2) avoid the simultaneous presence of both metal and chalcogenide precursors in solution so as to minimize the rate of homogenous nucleation of new nanoparticles of the shell material. As excess reagent is typically not removed following each half-cycle, reagent doses must be calculated to provide exactly one monolayer per QD in order to satisfy the requirements above simultaneously.

Although approximately spherical core/shell quantum dots can be obtained, it was unclear whether the reaction mechanism can achieve the above goals simultaneously. There was no solid evidence that the quantum dot surfaces are completely saturated and stabilized before the next addition. Even if the dose equivalent to one monolayer can be accurately calculated and precisely introduced, a limitation in the reactivity of the chosen shell precursors with the nanoparticle surface could result in cross-reactions in solution and undesired nucleation of nanoparticles. Studies about the mechanism of the SILAR approach and further improvements of the core/shell growth are still necessary.

1.5. Thesis overview

In order to achieve core/shell quantum dots with optimized/enhanced PLQY and photo-stability, several requirements must be met during and after synthesis. 1. A fine/compact crystal structure with minimum/no defects in the core as well as in the shell. 2. Minimum lattice mismatch and strain between the core and shell interface to avoid electron trapping and non-radiative decay. 3. Elimination of impurities in the colloidal solution from particle nucleation as a result of cross-reaction by the shell precursors. 4. Passivation of the nanocrystal surfaces by ligands eliminate surface trapping states and balance surface charges, as well as protection from oxidation.

In this thesis, the studies are focused on enhancing core/shell quantum dot properties-morphologies, synthetic yields, PLQY and overall brightness-by optimizing the synthetic methods and solvent conditions as well as the efforts to purify and modify the surface passivation. Although the prototypical CdSe/CdS core/shell quantum dot is used as the study system, all these studies can potentially be applied and extended to other core/shell quantum dots.

The first study in Chapter 2 is focused on probing the surface saturation condition during the core/shell growth via SILAR method, in which it is revealed the limited saturation of quantum dot surfaces by the shell precursors is the factor that leads to poor morphology, broad size distribution and the formation of nanoparticles of shell precursors as impurities when full monolayer equivalents are applied. A modified SILAR method is proposed and successfully enhanced the properties of the final core/shell quantum dots. Quantum dots produced by this method have been applied in several sub-sequential studies in our lab.

Chapter 3 is a study of the influence of surface ligands on the quantum yields and photoluminescence lifetime of the core/shell quantum dot. We found that the surface ligands play a critical role in terms of maintaining and enhancing the photophysical properties. Without the protection and passivation of the appropriate neutral ligands, quantum yields as well as photoluminescence lifetimes of core/shell quantum dots will decrease dramatically and both can be regenerated by reintroduction of such ligands because of their good passivation properties. The photoluminescence lifetime analyzed by applying a method which reconvoluted multiple-exponential components with the instrument response function companied with support plane analysis to determine confident limit reveals that the reduction and regeneration in QY are associated with the changes in the relative population between a subset with lifetime comparable to the radiative lifetime and a subset with significantly shorter lifetimes. Isothermal titration calorimetry (ITC) also applied to study the interactions between the neutral ligands to the quantum dot surfaces and determined the bonding constant, which proved such interactions are responsible to the changes of QY. This study provides a good understanding of the relationship between quantum dot surface and its photophysical properties as well as a way for properties enhancement.

The studies in Chapter 4 are focused on understanding the effect of solvent mixture on the growth of core/shell quantum dots by SILAR technique. Three types of amines-primary, secondary, tertiary amines - were utilized as the growth solvent and we found that the competition between the surface passivation by primary amine and the surface adsorption of shell precursors is a limiting factor towards achieving high quality core/shell quantum dots-in terms of size distribution, particle morphologies, elimination

of impurities and particle solubility. Switching the solvent mixture to tertiary amines will dramatically increases the shell synthetic yield, eliminates nucleation by cross-reactions, and achieves core/shell quantum dots with narrower size distribution and more uniform morphologies. The reaction between metal precursor and the core surface can be fit to a Langmuir-isotherm model which allowed us to characterize the enhancement in binding constant achieved in the tertiary amines. This study emphasized the influence of the solvent on surface reactivity in nanocrystal growth, and revealed a better solvent condition to optimize and enhance growth of isotropic CdSe-based core/shell quantum dots.

CHAPTER 2

PROBING SURFACE SATURATION CONDITIONS IN ALTERNATING LAYER GROWTH OF CDSE/CDS CORE/SHELL QUANTUM DOTS*

2.1. Introduction

The surfaces of a roughly spherical nanocrystal necessarily include regions that do not share the same symmetry with respect to the crystal lattice and are therefore structurally distinct.[82–85] These structurally distinct regions may naturally possess different reaction rates towards ligand exchange reactions or further crystal growth.[86] In some cases, regioselective crystal growth, such as the formation of CdSe/CdS rod/tetrapod core/shell structures,[54,55,87–89] $CdS_{1-x}Se_x$ nanorods with axial anisotropy,[81,90,91] multi-component nanobarbells,[92] or CdSe/CdS core/shell nanoplatelets,[93] can be desirable as it leads to properties such as a highly polarized excited state,[70,71,79] high sensitivity to non-isotropic external stresses,[89] multiexcitonic dual emission,[80] and the capability to engineer charge and energy flows that are valuable in applications.[55,94,95] In other cases, enforcing conformal/isotropic growth, such as formation of spherical CdSe/CdS or CdSe/ZnS core/shell quantum dots, is desirable as it will lead to increased photoluminescence quantum yield (QY),[24,57,61,62,96] excitation rate (absorption cross-section),[97] and photo- and chemical stability.[10,98] Both the synthetic methods and the optical/electrical properties of such core-shell heterostructures have been widely studied.[63,72,99–102] While presenting important opportunities, the strong influence of the shell morphology on the

*Reprinted with permission from Tan, R.; Blom, D. A.; Ma, S.; Greytak, A. B. *Chem. Mater.* **2013**, *25* (18), 3724–3736. http://pubs.acs.org/doi/abs/10.1021/cm402148s. Copyright 2013 American Chemical Society.

properties of weakly-confining core/shell systems imposes a strong requirement of structural homogeneity among particles during shell synthesis if homogeneous electronic properties are to be achieved. In the si0mplest case, this is a requirement for conformal shell growth on all surfaces and suppression of homogeneous nucleation of the shell material.[61] The development of a controllable method for growing shells with different morphology is necessary and an understanding of the shell growth mechanism at play in existing procedures should aid in the synthesis of a new generation of core-shell heterostructures.

Alternating layer deposition techniques use a sequence of self-limiting surface reactions to build up conformal thin films on surfaces that may be structurally heterogeneous. Atomic layer deposition (ALD) is an example of such a process using vapor-phase reagents.[103–106] Selective Ionic Layer Adhesion and Reaction (SILAR) is an analogous technique for growing binary films from solution,[107,108] in which addition of each ion type is nominally self-limiting. The goals of such an approach are to: (1) saturate available surface binding sites in each half-cycle in order to enforce conformal growth; and (2) avoid the simultaneous presence of both precursors in the solution or vapor so as to prevent uncontrolled surface growth or homogeneous nucleation of film material. While SILAR was originally developed for use on planar substrates,[107,109] over the last decade alternating-layer methods have been extensively applied to growth of shells on colloidal nanocrystals.[62,64–66,97,110,111]

In typical thin film growth by SILAR (or ALD), an excess of reagent is used in each half-cycle step to drive the surface reaction to completion at all available sites. The excess is easily removed before the next step. However, it is tedious to separate colloidal

particles from excess rea-gent in each half-cycle. Ithurria and co-workers recently described a SILAR procedure (termed colloidal ALD)[112] that couples QD surface reactions to solubility changes in order to achieve such separation in a biphasic solvent environment, and SILAR has also been applied to sup-ported nanocrystal QDs.[113,114] However, more typically, reagents are added in doses that are calculated to provide exactly 1 monolayer (ML) of coverage per nanocrystal in the sample, and they are not removed between steps.[64,110] If the dose is too small, some surface sites will remain vacant, while if the dose is too large, reagent will remain at the end of the step and could lead to nucleation or non-self-limited growth when the complementary reagent is introduced in the subsequent half-step. Importantly, even if 1 ML equivalent is added precisely, the surface reaction may not run to completion in the absence of excess reagent, instead reaching an equilibrium state with dissolved species.

Despite these concerns, a great deal of success has been achieved in terms of forming isotropic shells by SILAR-based methods, notably in the case of CdSe/CdS core/shell quantum dots.[62,64–66,97,110] These achievements have spawned increasing interest in the mechanisms of growth and intermediates that are formed in these alternating layer addition procedures. Mulvaney et al. have examined changes in surface enrichment and effective bandgap under single reagent addition to CdSe QDs.[115] Krauss et al. have reported significant changes in surface enrichment and photoluminescence associated with alternating layer addition to CdS QDs.[116] Vela and coworkers have recently examined limitations of the SILAR procedure in controlling the growth of very thick CdS shells on CdSe QDs.[110] These studies provide significant guidance in the preparation of high-quality core/shell nanocrystals, but did not specifically address the

conditions under which effective saturation of the surface with respect to single reagent addition is achieved, or whether the dose per cycle plays a significant role in controlling core/shell growth. A more complete understanding of crystal growth under alternating layer addition conditions should be applicable to development of rational strategies for isotropic and regioselective shell growth on various nanoscale and thin film substrates.

In the work described below, we revisit the SILAR approach to grow CdSe/CdS core/shell NCs. We use three independent methods to monitor the extent of reaction when precursors for a CdS shell are added separately to CdSe nanocrystal cores. As a qualitative measure of reaction progress, we note that the formation of CdS shells leads to a strong redshift of the lowest-energy absorption feature of the small CdSe nanocrystal QDs used here due to relaxed confinement potentials for the electron and hole.[62,66] The position of the lowest-energy absorption feature can therefore be used to detect reaction progress. Independently, we use inductively coupled mass spectrometry (ICP-MS) to monitor the concentration of free Cd species in the reaction. We also characterized the size and shape distribution of core/shell products through the use of Scanning Transmission Electron Microscopy (STEM). With these tools in hand, we vary the order and amounts of the Cd and S precursor doses. $Cd(oleate)_2$ is used as the Cd precursor and bis(trimethylsilyl) sulfide ($(TMS)_2S$) is used as the S precursor for the formation of the CdS shell.

Firstly, we are able to identify the native surface condition (reactivity) of the CdSe cores by varying the order of Cd and S addition. Despite XPS and ^{31}P NMR data indicating a Cd/Se elemental ratio slightly greater than unity, the initial surface shows reactivity toward addition of Cd but not toward the addition of S. Secondly, we perform

titration experiments in which we identify two regimes of response to Cd addition and find that addition of the Cd precursor beyond 1 ML equivalent continues to cause red shifting, consistent with an incomplete surface reaction subject to equilibrium with dissolved species. The presence of unbound Cd is confirmed by ICP-MS. We also show that the reactivity of the nanocrystals toward S addition is entirely determined by the total amount of Cd added. Thirdly, we conduct a series of alternating-addition shell growths using sub-ML equivalent doses and find that lower doses favor greater redshifts, consistent with an overall higher synthetic yield for shell growth at small doses due to loss of precursors to cross-reaction when larger doses are used. Analysis of STEM images supports the finding of higher synthetic yield for sub-monolayer doses without loss of structural control.

2.2. Calculation of monolayer equivalency.

In what follows, the value of 0.337 nm, or half of the wurtzite *c*-axis unit cell dimension for CdS, is considered to be the marginal increase in radius associated with 1 monolayer (ML) of surface coverage,[52] in keeping with previous SILAR literature.[62,65,117] A quantity of shell precursors can then be expressed as a number of ML equivalents by considering the marginal increase in radius that would result if these reagents reacted quantitatively to form a shell of uniform thickness on all particles in the sample.

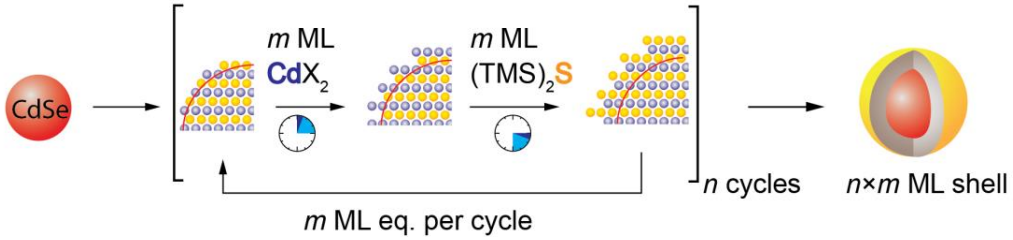

Figure 2.1 Scheme of growth of CdSe/CdS core/shell quantum dot via SILAR. Copyright 2013 American Chemical Society

For the case of isotropic shells on approximately spherical particles, the dose *d* (number of moles of shell precursor per mole of particles) equivalent to *m* ML of shell growth can be calculated by dividing the incremental volume associated with such an increase in radius by the molar volume (V_m) of the shell compound.

In the SILAR process, reagents are added stepwise in an alternating fashion; in a process that is designed to provide 1 ML per cycle, reagents equivalent to *n* ML total shell thickness would be provided in *n* SILAR cycles. In the present work, we generalize this description to include a variable number *m* of ML equivalents per SILAR cycle (**Figure 2.1**), such that the total number of ML equivalents added in the process is given by $n \times m$.

For a shell of total thickness $t = n \times m \times (c/2)$ applied to cores of radius r_0, where *c* is the wurtzite *c*-axis unit cell dimension for CdS, the total equivalent dose *d* is given by (Equation1) and the incremental dose d_i for each cycle *i* can be calculated by considering the radius increase required in each cycle (Equation2):

$$d = \frac{\frac{4\pi}{3}\left[(r_0 + t)^3 - r_0^3\right]}{V_m} = \frac{\frac{4\pi}{3}\left[\left(r_0 + n \times m \times \frac{c}{2}\right)^3 - r_0^3\right]}{V_m} \quad \cdots\cdots \text{eq. 1}$$

$$d_i = \frac{\frac{4\pi}{3}\left(r_i^3 - r_{i-1}^3\right)}{V_m} \quad \cdots\cdots \text{eq. 2}$$

where *i* runs from 1 to *n* and r_i represents the nominal radius after *i* cycles with $r_i = r_0 + i \times m \times (c/2)$. In this description the number of ML equivalents in each cycle *m* is considered to be held constant, but the corresponding dose for each cycle will increase as the radius (and surface area) increases. A sample calculation is provided in the following

section. The CdSe core radius (r_0) was determined from a calibration curve used previously[62,118] on the basis of the wavelength of the lowest-energy absorption feature, and the quantity (number of moles) of cores in a given sample was determined by estimating the molar extinction coefficient based on this radius in the manner of Leatherdale et al.,[119] which is supported by more recent work from Jasieniak et al.[120]

2.3. Sample calculation of monolayer equivalency

After synthesis, a portion of the CdSe cores were washed via 2 cycles of precipitation/redissolution in a manner described previously,[62] and then brought into a measured volume (2.0 mL) of hexane, 10 μL of which was diluted in 2.5 mL of hexane in a quartz cuvette to obtain a spectrum for determination of effective radius and extinction coefficient via a calibration curve (**Figure 2.2**). For the example shown, the radius of the CdSe cores (r) was determined to be 1.72 nm, and the quantity of QDs in the 2.0 mL stock solution was determined to be 1.67×10^{-7} mol by the Beer-Lambert law assuming the extinction coefficient at 350 nm is proportional to r^3.[119] The calculation of monolayer equivalency is sensitive to the method by which the size and extinction coefficient of the CdSe core sample are assigned; for example, the use of an alternative sizing curve from Yu et al.[121] causes the doses we report here to correspond to slightly smaller ML equivalent thickness.

The remainder of the stock solution is transferred in entirety into the shell growth flask. The necessary dose di for each SILAR cycle can then be calculated as described in the narrative. Two examples are shown in **Table 2.1** and **Table 2.2** for the application of 2.0 monolayer equivalents (2.0 ML) to the sample described in **Figure 2.2**, with m = 1.0 or m = 0.4 ML/cycle, with reagent volumes indicated for a concentration of 0.1 M.

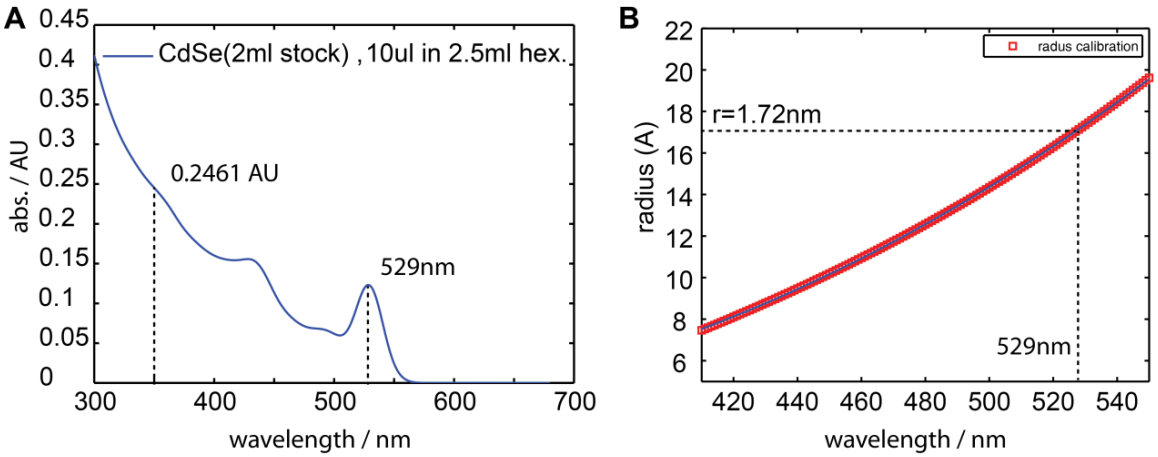

Figure 2.2 (A) Absorption spectrum for CdSe cores with a lowest energy absorption feature peaking at 529 nm, and showing the absorbance at 350 nm of 0.2461 A.U. (B) Size calibration curve used to assign the nominal radius of CdSe cores with absorbance peaks 410-550 nm.[62,118] Copyright 2013 American Chemical Society

Table 2.1 Sample calculation for 167 nmol of QDs with r_0 = 1.72 nm, m = 1.0, n = 2, $n \times m$ = 2.0.

ML eq.	Eq. thickness t (nm)	d (mol / mol QD)	d_i (mol / mol QD)	Reagent vol. (mL)	Predicted r_i (nm)
1.0	0.337 nm	301	301	0.503	2.06
2.0	0.674 nm	719	418	0.697	2.40

Table 2.2 Sample calculation for 167 nmol of QDs with r_0 = 1.72 nm, m = 0.4, n = 5, $n \times m$ = 2.0.

ML eq.	Eq. thickness t (nm)	d (mol / mol QD)	d_i (mol / mol QD)	Reagent vol. (mL)	Predicted r_i (nm)
0.4	0.135 nm	108	108	0.180	1.86
0.8	0.270 nm	232	124	0.208	1.99
1.2	0.404 nm	375	143	0.238	2.13
1.6	0.539 nm	537	162	0.270	2.26
2.0	0.674 nm	719	182	0.304	2.40

2.4. Redshift of exciton as an indication of reaction progress.

The formation of CdS shells on CdSe QDs is associated with a large redshift of the effective bandgap due to delocalization of the lowest excited state into the shell.[62,66] Because of the sensitivity of the excited state to such shell growth, the shift in the

position of the lowest-energy absorption maximum can be used as an indicator of shell growth reaction progress. **Figure 2.3** displays the change in the absorption and emission line shape of a CdSe nanocrystal sample following successive half-cycles of CdS growth by SILAR. In each half-cycle, a dose of a single precursor (containing Cd or S; here, Cd is added first) is injected over a period of 3 minutes, and then 12 minutes is allowed for the reaction to take place before the next half-cycle. The spectra are monitored at the completion of each half-cycle by drawing a small aliquot for analysis just prior to the subsequent step. In this process, redshifts are observed for each introduction of Cd and S. The addition of precursors corresponding to 1 monolayer (ML) equivalent shell thickness is associated with a total redshift of 18 nm.

The shell growth process examined in **Figure 2.3** and the studies described below are modifications of one reported re-cently[62] and is similar to much of the QD SILAR literature that has emerged since the original report by Li et al.[64] One difference is the use of $(TMS)_2S$ as the sulfur precursor, in contrast to many studies[64,65,110,117] that use elemental sulfur in combination with octadecene[122] and alkylamine[123] reductants as the sulfur source.

Several features are apparent in the energy shift results shown in **Figure 2.3**. Firstly, in the method shown, where the Cd precursor is added first, both the addition of Cd and the addition of S lead to redshifts in the absorption and emission spectra. Secondly, the shifts associated with Cd and with S are unequal, with a greater shift observed for S addition; this pattern is maintained through several monolayers of growth. Thirdly, comparison of the absorption spectrum of the CdSe nanocrystal sample prior to injection into the shell growth mixture ("initial" CdSe sample), and after being degassed

and brought to temperature in the shell growth solvent (but prior to introduction of any shell precursors: "heated" CdSe sample) reveals a small blue shift.

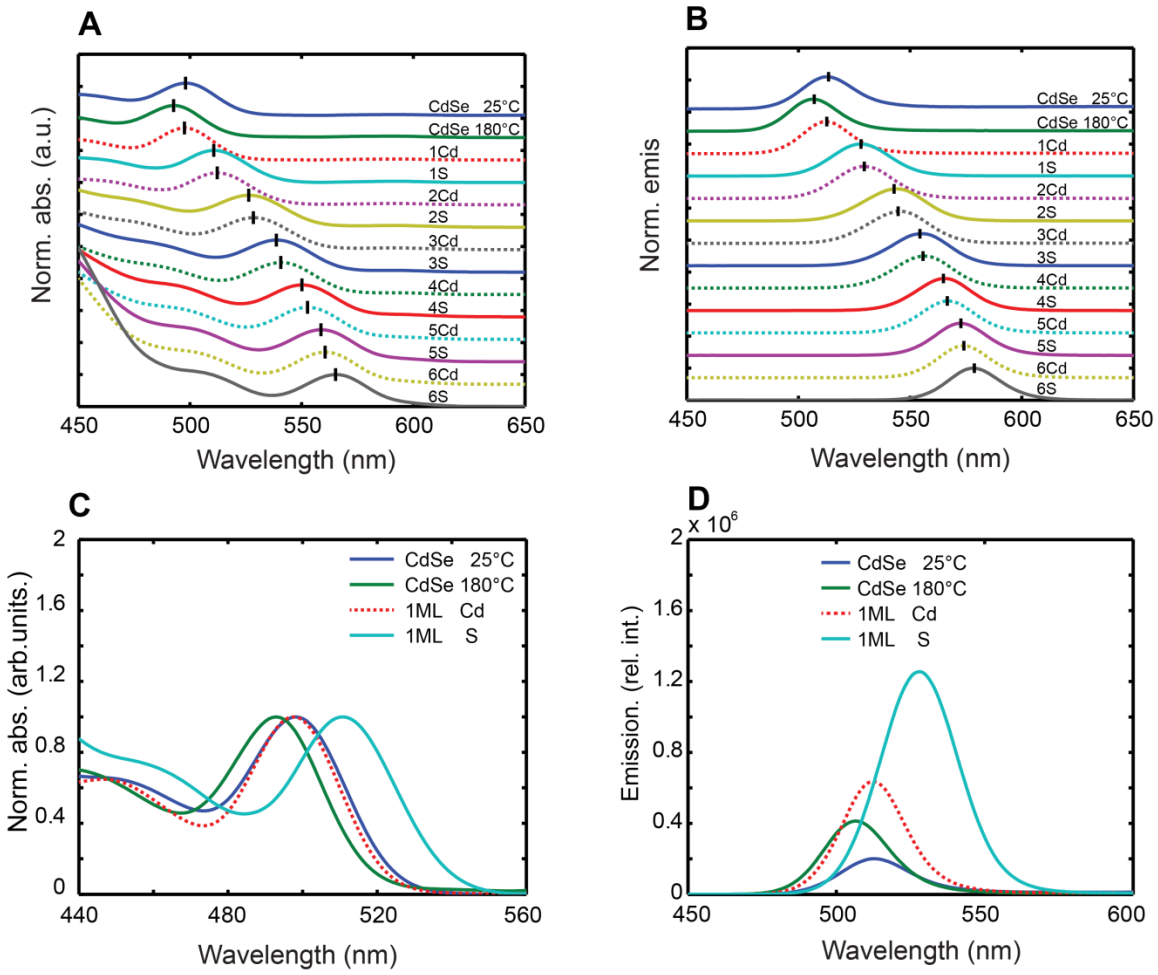

Figure 2.3 Evolution of the normalized absorption spectrum (**A**) and emission spectrum (**B**, 365 nm excitation) during CdS shell growth on CdSe QD cores. (**C**) Detail of absorption spectrum changes upon addition of the first ML eq. of CdS precursors. (**D**) Detail of emission spectra for the first ML eq., normalized by the absorption of each sample at the excitation wavelength so that relative brightness may be compared. Copyright 2013 American Chemical Society

We interpret the presence of a redshift upon addition of Cd, and subsequent addition of S, as evidence of shell-growth reaction progress in each case: at least a portion of the precursor is able to react with the nanocrystal surface in each of these half-

cycles. The difference in the extent of the redshifts between Cd and S cycles is unsurprising and cannot alone be interpreted as a difference in reactivity, because incorporation of these two elements at the surface of the nanocrystal lattice cannot be expected to lead to an equal perturbation of the electronic states. However, we will argue below that the extent of shifting upon the introduction of the same precursor under different reaction conditions can be used as a means to compare reactivity in those differing conditions. The small blue-shift upon initial heating may be associated with a small amount of etching of the CdSe surface[110] and will be discussed further below.

The relative PL intensity of the particles through the first cycle of shell growth is presented in **Figure 2.3 D**. The brightness of the cores increases after heating to the shell growth temperature in ODE/oleylamine solvent. Further increases are seen after introduction of $Cd(oleate)_2$ and of $(TMS)_2S$. A larger increase happens after the S addition than after the previous Cd addition, and this pattern of brighter PL after addition of S than of Cd continues through several addition cycles. The relative QY is maximized for 5-6 ML of CdS shell and starts decreasing for thicker shells, consistently with previous observations.[24,97]

2.5. Initial reactivity of CdSe NCs towards shell precursors: Order of addition.

The SILAR mechanism nominally proceeds via intermediates for which the surfaces are saturated with respect to the addition of one reagent. Accordingly, it is important to establish the reactivity of the initial core surface: in other words, which element of the shell compound (Cd or S) should be introduced first? We have investigated this by performing otherwise equivalent CdS shell growth procedures on CdSe core samples taken from the same batch, in which the order of addition of Cd and S

precursors is reversed. **Figure 2.4A** and **2.4B** showed the progression of absorption and emission spectra during the application of 2 monolayer equivalent (ML eq.) of CdS to CdSe QDs cores with an effective radius of 1.63 nm. Reagents were added at doses of 1 ML per cycle, with Cd first (**Figure 2.4A**) or S first (**Figure 2.4B**). In each addition step, the required reagent volume was pumped in over a period of 3 minutes, with a total of 15 minutes elapsing between the start of each half-cycle. Aliquots (typically 50 μL) were withdrawn every 1 minute during the injection time and every 2 minutes during the waiting time and diluted in hexanes at room temperature; absorption/emission spectra of these aliquots were recorded by Thermo Scientific Evolution Array UV-Visible Spectrophotometer and Ocean Optics USB 4000 spectrometer under 365 nm LED excitation. The positions of the lowest-energy absorption and emission peaks are plotted as a function of time in **Figure 2.4C** (Cd first) and 2.4D (S first). Both CdSe core samples experienced a blue shift upon heating to the shell growth temperature (180 ℃), versus the spectrum recorded following purification.

The Cd precursor was prepared by introducing $Cd(oleate)_2$ stock solution in a solvent of 50:50 ODE and TOP with two equivalents of 1-decylamine (vs. Cd) added to yield a Cd concentration of 0.1 M. The sulfur precursor was 0.1 M solution of $(TMS)_2S$ dissolved in TOP. A computer-controlled syringe pump (J-KEM Scientific Dual Syringe Pump, Model 2250) was used to introduce reagents accordingly and to assure the accuracy of the dose and timing regimes described. Multiply rinsing cycles with the Cd and sulfur precursors were applied before adding to the reaction flask to avoid any dilution by the solvent in the addition inlet and to ensure the correct precursor concentrations at the very first addition.

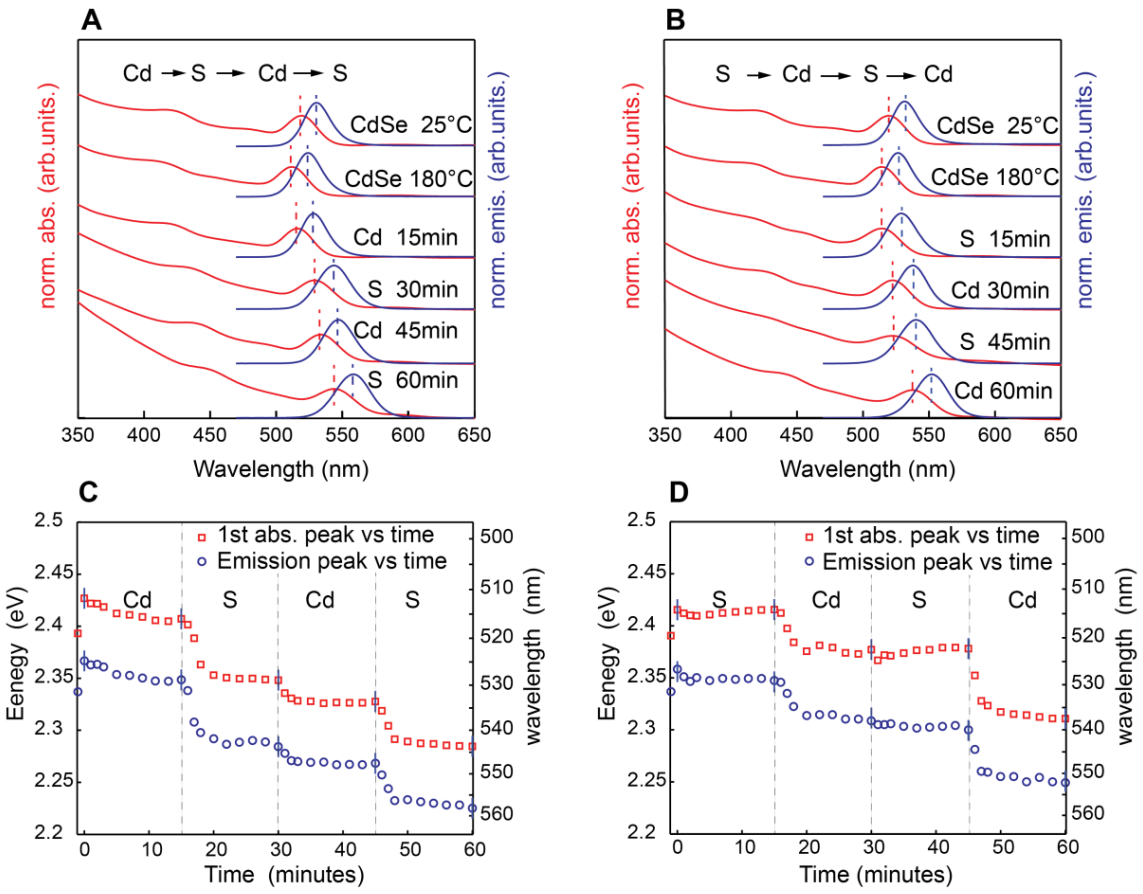

Figure 2.4 Effect of reagent addition order on the evolution of absorption and emission spectra during CdS shell growth. (A,B) Absorption spectra (red) and emission spectra (blue) of aliquots taken during the CdS shell growth process up to 2 ML eq. thickness. (A) $Cd(oleate)_2$ added first. (B) $(TMS)_2S$ added first. The quantity of cores is 93 nmol, r_0=1.63 nm. (C,D) Shift of effective band gap (red) and peak emission energy (blue) of QDs as a function of time for 2 ML of CdS shell growth. (C) $Cd(oleate)_2$ added first. (D) $(TMS)_2S$ added first. 106 nmol QDs, r_0=1.63 nm. The data point to the left of time zero describes an aliquot from the initial cores at 25 ℃, and the point at time zero describes an aliquot drawn after the QDs have been added to the reaction solvent and heated to 180 ℃, just prior to the introduction of the shell growth reagent. Copyright 2013 American Chemical Society.

A strong red-shift (decrease of effective band gap and emission energy) was observed after 2 ML equivalent of CdS reagent addition in both cases. When starting with $Cd(oleate)_2$ (**Figure 2.4C**), a red-shift was observed during the first 3 minutes (addition

time) for both $Cd(oleate)_2$ and $(TMS)_2S$, while a nearly constant value was observed during the final minutes of each waiting time. The redshift associated with addition of $(TMS)_2S$ was larger than that associated with addition of $Cd(oleate)_2$. A notably different result was observed when starting with $(TMS)_2S$ (**Figure 2.4D**): no significant red-shift was observed until the next addition of $Cd(oleate)_2$, which resulted in a large red-shift. The second addition cycle displayed the same trend, with no shift upon $(TMS)_2S$ addition followed by a red-shift on introduction of $Cd(oleate)_2$. The shifts associated with Cd addition in the sulfur-first sample are larger than those observed in the Cd-first sample; however, because of the minimal shift on S addition, the overall redshift after 1 ML and 2 ML equivalent was smaller for the S-first than the Cd-first sample. The results shown in **Figure 2.4** are representative of those observed in numerous similarly-prepared samples.

Based on the redshift observed upon Cd addition when Cd is added first, we can conclude that $Cd(oleate)_2$ displays reactivity toward the CdSe QD surface. In contrast, the absence of a redshift when S is added first suggests that either $(TMS)_2S$ does not result in addition of S to the CdSe QD surface, or that addition of S to the surface does not cause a redshift of the lowest excited state. We can exclude the second possibility because of the very large redshift that is observed when $(TMS)_2S$ is added following $Cd(oleate)_2$. The difference in behavior upon S addition before and after Cd addition can be explained within the SILAR model by an initial CdSe QD surface that is saturated with respect to addition of chalcogenide, but can be elaborated via the addition of Cd. Moreover, the larger overall red-shift after 2 ML eq. for growth starting with $Cd(oleate)_2$ suggests a higher synthetic yield (fraction of CdS precursor dose that yields CdS shell material) for the shell growth process in this case.

The observation of greater reactivity of the initially-prepared surface toward Cd than toward S is somewhat surprising in view of published work[124,125] that identifies CdSe QDs prepared with alkyl carboxylate or phosphonate precursors as being metal-rich and chiefly capped with anionic ("X-type") ligands following purification by multiple precipitations: a "metal-rich" surface might be expected to display greater reactivity towards S. Most SILAR literature for growth of CdS on CdSe cores does indeed describe the addition of the Cd precursor prior to the S precursor,[64,65,110] though Mulvaney's group has described the addition of sub-monolayer quantities of Cd to bring about a metal-rich surface prior to starting complete cycles with addition of S.[66]

2.6. Titration experiments: Single reagent addition.

In order to better understand how the addition of reagents influences the subsequent reactivity of the QDs towards shell growth, we devised a series of "titration" experiments in which each reagent addition is divided into a series of discrete sub-monolayer steps, and the sample is monitored over the course of the addition by withdrawing aliquots. The rate of addition is designed to be slow enough that the sample is close to equilibrium throughout; in this way, sample parameters such as absorption and emission energies can be plotted as a function of the monolayer-equivalent dose that has been added. This should in principle allow us to identify, for example, turning points associated with saturation of the QD surface with respect to a single reagent.[115] In the first titration experiment, matched CdSe core samples are treated with an excess of either $Cd(oleate)_2$ or $(TMS)_2S$. A detailed description of the dosing scheme is provided in **Table 2.3**. The titration experiments were conducted at an elevated temperature of 200 ℃ to speed equilibration. In each case, the reagent was added in a series of 20 steps. In each

10-minute step, an equal volume corresponding to 1/10 of 1 ML eq. of shell precursor was pumped into the reaction pot over 3 minutes; after a 7 minute waiting time, an aliquot was drawn for analysis before continuing to the next step. The Cd and sulfur precursors were prepared to yield a concentration of 0.1 M, respectively (see experimental section for details). Absorption and emission spectra of all aliquots of 20 titration steps were recorded and shown in **Figure 2.5**. The change in absorption effective bandgap that is observed when CdSe QDs with an effective radius of 1.88 nm are treated with 2 ML eq. of $Cd(oleate)_2$ or $(TMS)_2S$ are shown in **Figure 2.6**.

Table 2.3 Detailed description of dosing in titration experiments

Experiment	**QD cores**		**Addition**				
	QDs (nmol)	r_0 (nm)	1	2	3	4	5
Single reagent: Cd (Fig. 3)	91.6	1.88	**Cd, 1st ML** 32.3 µmol (10 steps)[a]	--	**Cd, 2nd ML** 43.8 µmol (10 steps)		
Single reagent: S (Fig. 3)	68.9	1.86	--	**S, 1st ML** 23.8 µmol (10 steps)	--	**S, 2nd ML** 32.3 µmol (10 steps)	
Complete monolayer (Fig. 4)	167	1.72	**Cd, 1st ML** 50.3 µmol (10 steps)	**S, 1st ML** 50.3 µmol (10 steps)	**S, (ex.)**[b] 69.7 µmol (10 steps)		
Multiple cycles (Fig. 5, **Exp. 1**)	81.1	1.80	**Cd, 0.4 ML** 10.6 µmol (4 steps)	**S, 1 ML**[c] 26.4 µmol (10 steps)	**S, (ex.)** 36.2 µmol (10 steps)		
Multiple cycles (Fig. 5, **Exp. 2**)	50.6	1.82	**Cd, 1st ML** 16.9 µmol (10 steps)	**S, 1st ML** 16.9 µmol (10 steps)	**S, (ex.)** 23.1 µmol (10 steps)		
Multiple cycles (Fig. 5, **Exp. 3**)	86.4	1.80	**Cd, 1st ML** 28.2 µmol (10 steps)	**S, 1st ML** 28.2 µmol (10 steps)	**Cd, 2nd ML** 38.6 µmol (10 steps)	**S, 2nd ML** 38.6 µmol (10 steps)	**S, (ex.)** 50.7 µmol (10 steps)

[a]The total reagent quantity shown was added in a series of equal steps as described. [b]Reagent dose for "excess" S is calculated on the basis of the amount that would be contained in an additional complete ML. [c]In this experiment, 1 ML S represents an excess versus the amount of Cd that has been added in the first addition.

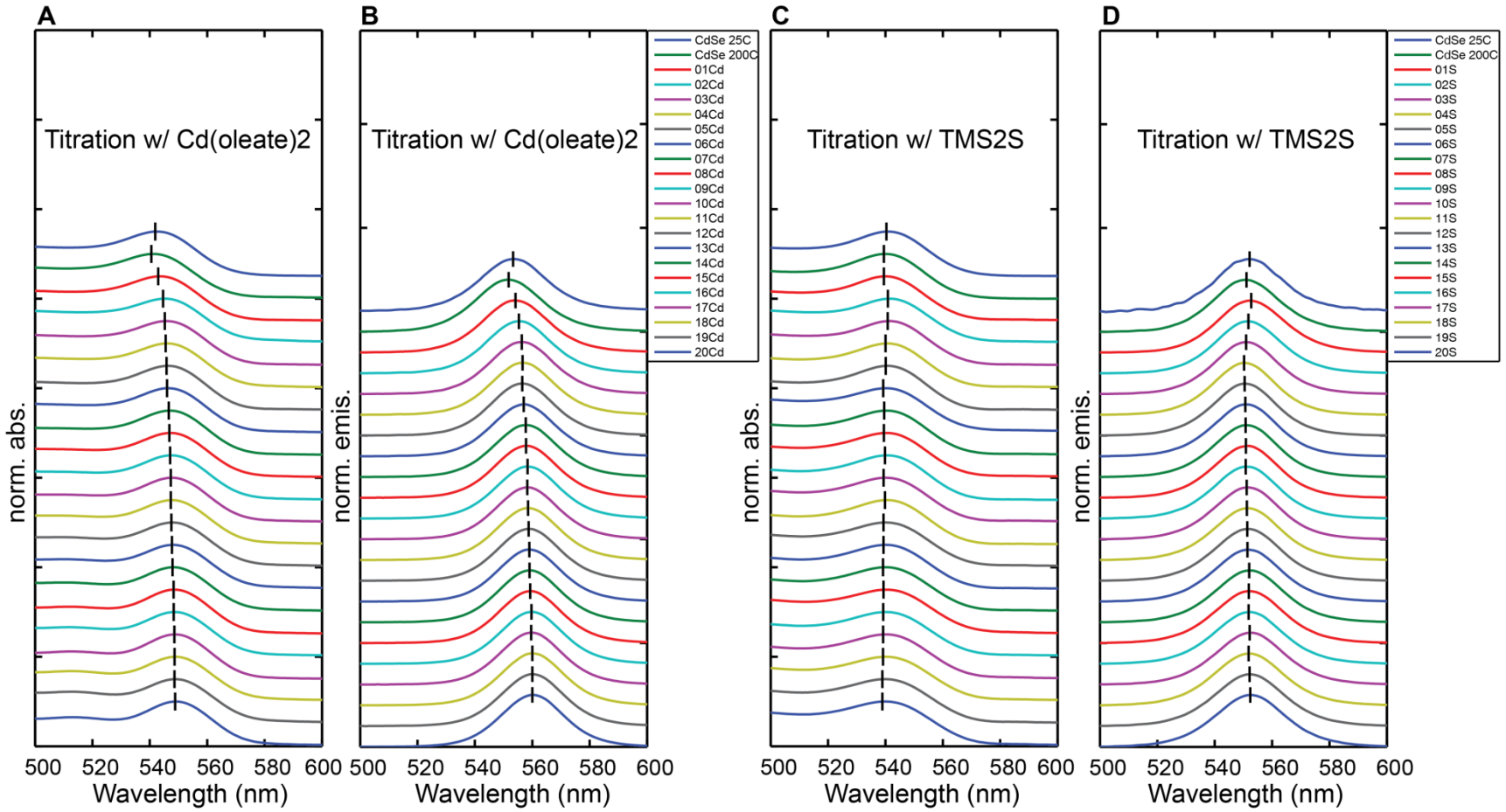

Figure 2.5. (A) Absorption and (B) emission spectra for titration with $Cd(oleate)_2$; (C) absorption and (D) emission spectra for titration with $(TMS)_2S$, both titration added step wise until 2 ML eq. Copyright 2013 American Chemical Society

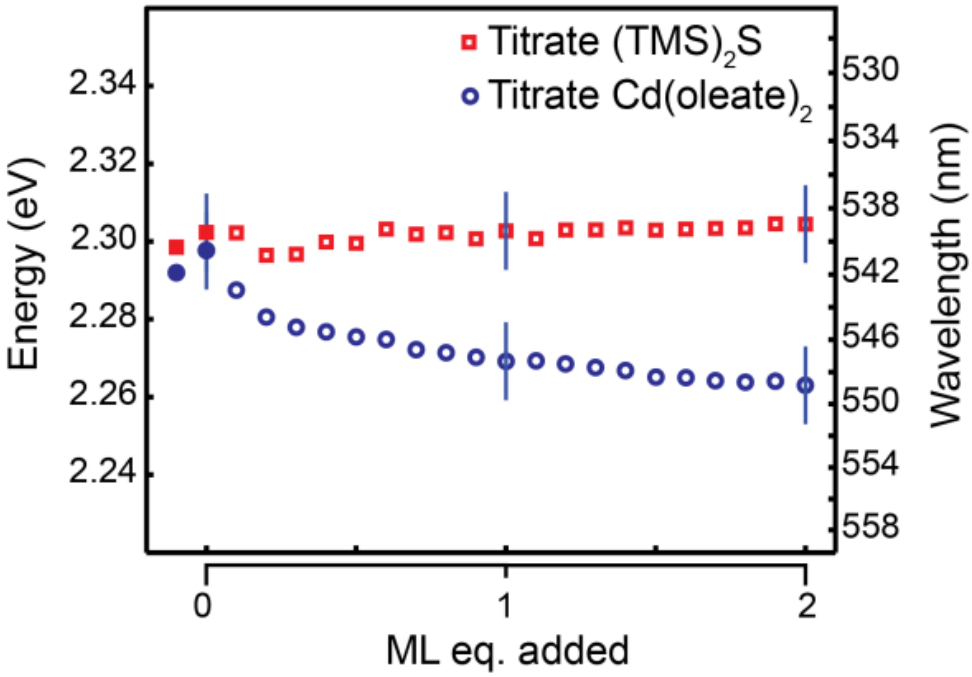

Figure 2.6 Shift of effective band gap (lowest energy absorption peak energy) vs. equivalent dose for stepwise addition of a single reagent up to 2 ML equivalent: $Cd(oleate)_2$ (circles) or $(TMS)_2S$ (squares). In each case the data points before time zero indicate the initial CdSe core sample. (See **Table 2.3** for experimental details) Copyright 2013 American Chemical Society.

In **Figure 2.6**, for titration of $Cd(oleate)_2$, a large red-shift occurs over the first ~0.3 ML eq.; a more gentle red-shift is observed out to 1.0 ML, and continues all the way out to 2.0 ML. The energy level shifts that we observed under Cd addition were largely stable for longer waiting times. For titration of $(TMS)_2S$, no consistent trend was observed in the absorption peak position from 0 to 1.0 ML, in agreement with the results in **Figure 2.6**, and indeed no shift was seen as far as 2.0 ML eq; The shifts of emission peaks and full width at half maximum (FWHM) of the aliquots are presented in **Figure 2.7**. The relative QY under $Cd(oleate)_2$ addition (**Figure2.7D**) continues to increase

between 1.0 and 2.0 ML eq. added; under $(TMS)_2S$ addition there is an initial increase at low equivalencies but little change thereafter.

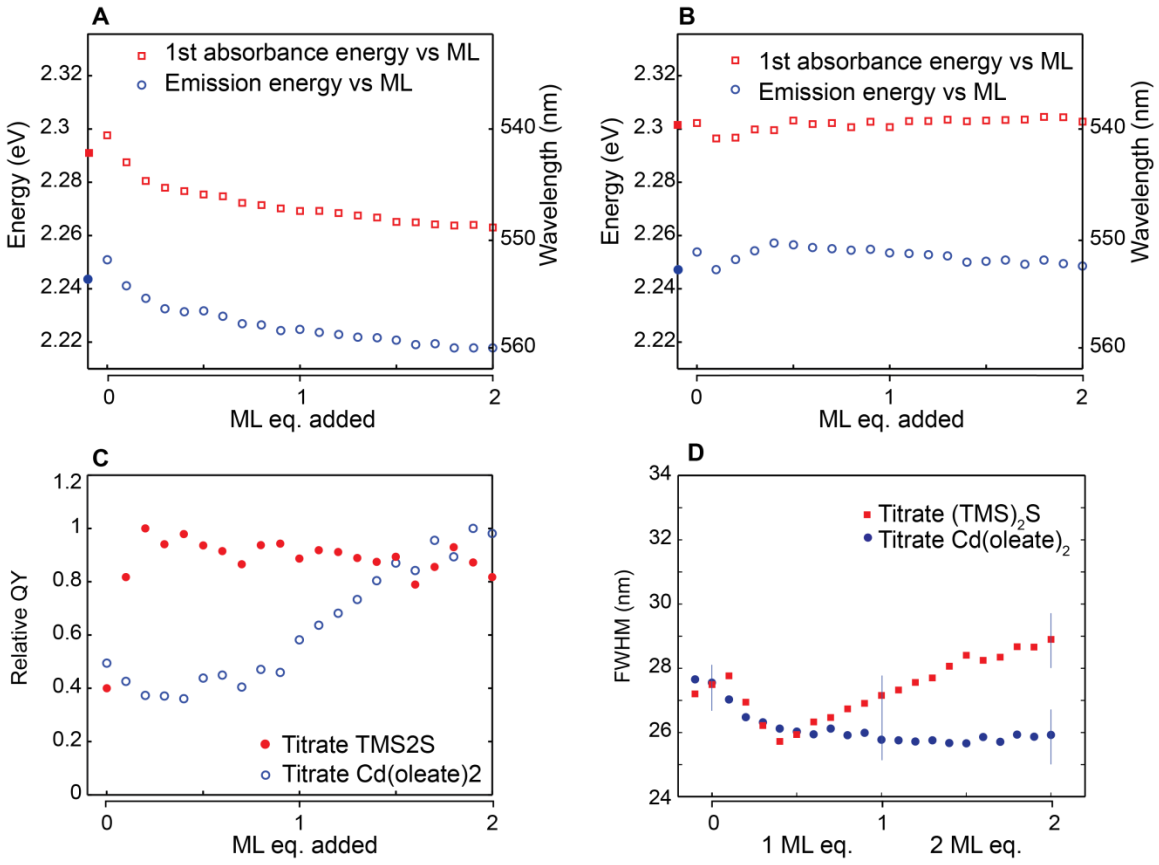

Figure 2.7. (A,B) Band gap energy shift and emission energy shift for titration of: (A), $Cd(oleate)_2$; (B), $(TMS)_2S$. (C) Relative QY during titration of $Cd(oleate)_2$ and $(TMS)_2S$. The highest QY in each series is normalized to 1. (D) FWHM of emission peak for QDs during titration with $Cd(oleate)_2$ and $(TMS)_2S$. Copyright 2013 American Chemical Society.

The $Cd(oleate)_2$ titration result is significant because it shows (1) a change in the rate of energy level shift with respect to reagent addition at less than 1 ML eq.; (2) continuing reactivity past 1 ML eq. The first of these observations could be an indication of (at least) two different types of binding site for Cd, but is difficult to interpret based on energy-level shifts alone. The second observation is a clear indication that the extent of

reaction continues to increase at > 1 ML eq. The ML equivalencies are an estimate based on the core size calibration curve and the increase in radius that is taken to represent 1 ML; however, given the agreement between this estimate and TEM measurements of shell thickness in previous studies,[62,66] we believe it to be sufficiently accurate to conclude that the addition of a stoichiometric quantity of $Cd(oleate)_2$ is insufficient to saturate all Cd binding sites under these reaction conditions. Instead, we surmise that the CdSe core surface includes sites for which high fractional occupation by Cd can only be achieved in equilibrium with experimentally significant solution concentrations of $Cd(oleate)_2$, which can be achieved by the addition of excess Cd. This conclusion, which is problematic for the SILAR mechanism, is supported by measurements of dissolved Cd during additional titration experiments described below.

2.7. Titration experiments: Complete monolayer.

The indication of free Cd present after 1.0 ML equivalent dose, together with evidence for high-yielding shell growth from $Cd(oleate)_2$ and $(TMS)_2S$ when Cd is added first, prompted us to examine how the effective bandgap, as well as the solution Cd concentration, varies over the course of a complete SILAR cycle. **Figure 2.8** presents a titration experiment in which CdSe cores were treated first with the of 1 ML of $Cd(oleate)_2$, followed by the addition of excess $(TMS)_2S$, at a constant temperature of 200 ℃ (details are in **Table 2.3**). The absorption and emission spectra that recorded for each aliquot as well as the effective bandgap shifts and emission energy shifts were shown in **Figure 2.9**. Each aliquot was drawn at the end of each 0.1 ML eq. dose addition step. For a subset of these aliquots, the solution Cd concentration was determined by precipitating the QDs with acetone and analyzing the supernatant for Cd via ICP-MS.

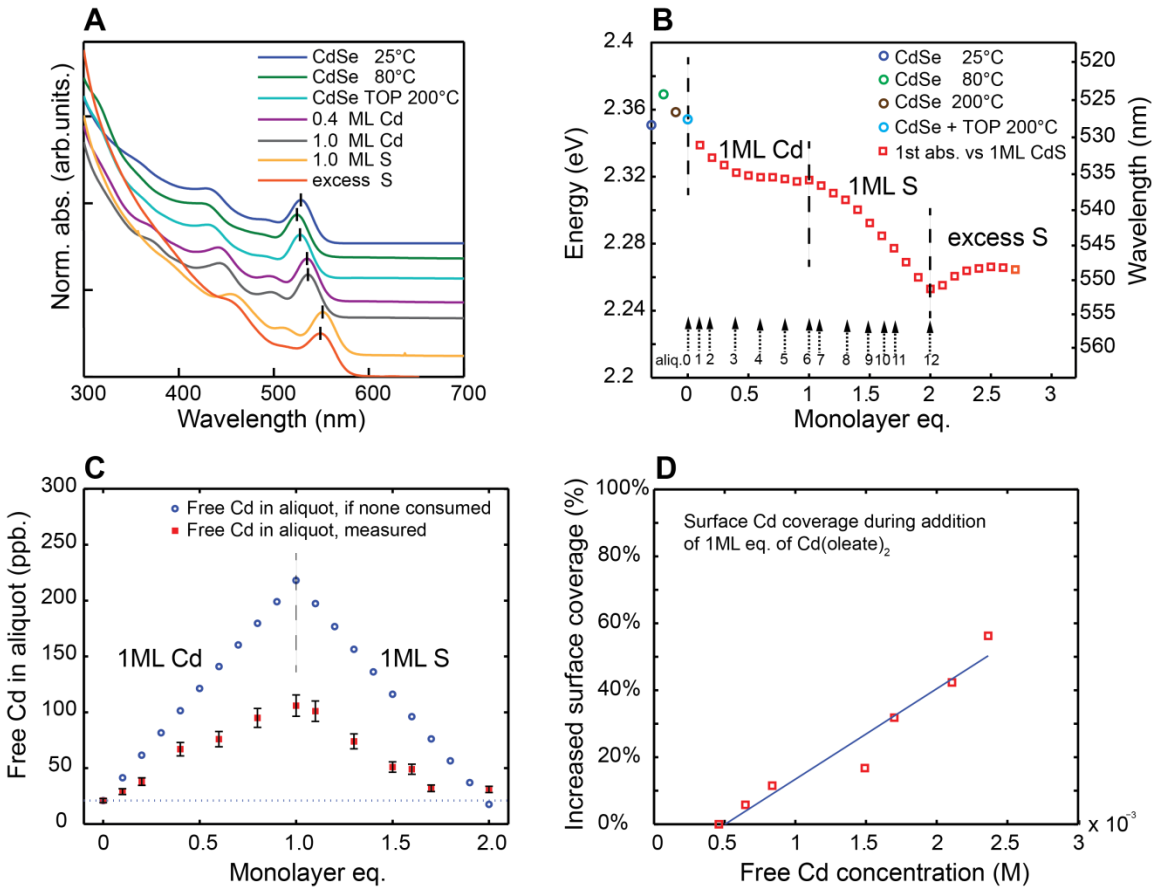

Figure 2.8 Titration of one complete ML eq. of CdS shell growth. (A) Selected absorption spectra, normalized by the height of the lowest energy exciton peak and vertically offset for clarity. (B) Shift of effective band gap during first ML of CdS shell growth. A selection of 12 aliquots was analyzed further with ICP-MS; these are indicated by the numbers and arrows at the bottom of the plot. (C) Free Cd concentration ([Cd]) measured by ICP-MS. The red squares indicate the measured [Cd] in the aqueous digest of the supernatant of the selected aliquots after QDs have been removed by precipitation; blue circles indicate the values that would be expected if all of the added Cd remained in free solution (i.e. none consumed). Free Cd concentration continuously increasing over the addition of $Cd(oleate)_2$ and decreasing followed the addition of $(TMS)_2S$, finally completely consumed after the addition of 1 ML eq. dose of $(TMS)_2S$ (D) Increase in surface coverage of Cd as a function of [Cd] during the $Cd(oleate)_2$ addition cycle shown in (A-C). Surface coverage is expressed as a percentage of 1 ML eq. dose and is calculated from the difference between total added Cd and the amount remaining in free solution. The surface coverage only reaches ~60% even after 1 ML eq. dose of $Cd(oleate)_2$ were added. Experimental details are provided in **Table 2.3**. Copyright 2013 American Chemical Society.

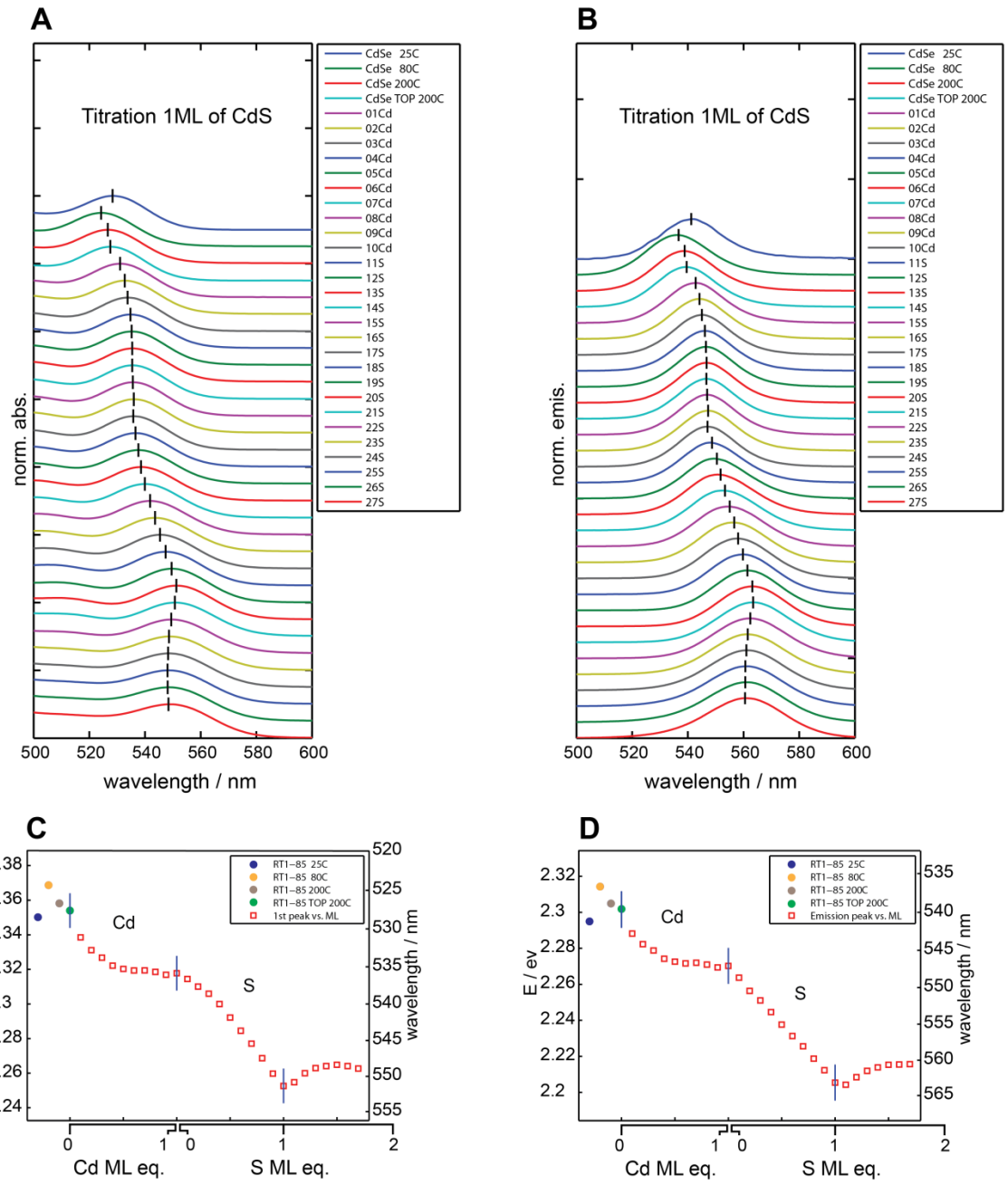

Figure 2.9 (A), Absorption and (B), emission spectra for titration with **complete monolayer** of CdS shell. (C), Band gap energy shift and (D), emission energy shift for titration with **complete monolayer** of CdS shell. Copyright 2013 American Chemical Society.

The resulting changes in spectrum and effective bandgap are shown in **Figure 2.8A, B**. As before, two different red-shifting rates steps were observed over the course

of the 1 ML $Cd(oleate)_2$ half-cycle, followed by a strong and continuous red-shift when $(TMS)_2S$ was added. The addition of $(TMS)_2S$ was continued to excess (past 1 ML) in order to investigate saturation effects. Indeed, the redshift of the effective bandgap abruptly stops, and in fact reverses direction, at 1 ML – the point at which precisely equal amounts of Cd and S precursor have been introduced. The reason for the blue-shift at excess (TMS)2S is not presently clear, but the fact that it happened right after a full 1 ML dose of Cd and S precursors suggests that the change in behavior is associated with depletion of the reactivity provided by the added Cd.

Figure 2.8C shows the total Cd concentration ([Cd]) detected by ICP-MS in aliquots sampled throughout the complete 1 ML SILAR cycle (red squares). A small but measureable [Cd] was found after bringing the CdSe core sample to temperature in the shell growth solvent; a much larger concentration builds in as $Cd(oleate)_2$ is added. It is clear that while [Cd] continuously increased during titration of $Cd(oleate)_2$, [Cd] was lower than would be expected if all of the added Cd remained in solution (i.e. if none were consumed by reaction with the QD surface: blue circles).

This indicates that some, but not all, of the added Cd reacts with the initial CdSe surface, in agreement with our interpretation of the results shown in **Figure 2.6**. With our knowledge of the total amount of Cd added, the amount that remains in solution, and the estimated dose corresponding to 1 ML, it is possible to construct a plot of the fractional occupancy of surface sites by Cd as a function of the solution concentration (**Figure 2.8D**). Interestingly the amount of bound Cd is seen to increase late in the Cd cycle, even though the effective bandgap experiences only a small redshift in this region. And the surface coverage only reaches ~60% even after 1 ML eq. dose of $Cd(oleate)_2$.

In the subsequent half-cycle in which $(TMS)_2S$ is titrated in, the free Cd is continuously consumed, consistent with the formation of a CdS, and after 1 ML eq. of $(TMS)_2S$, [Cd] has nearly returned to its starting value. Exhaustion of the free Cd coincides with the endpoint observed in the redshift data shown in **Figure 2.8B**.

The high concentration of free Cd at the conclusion of the Cd addition cycle indicates incomplete saturation of the QD surface and would appear to increase the risk of nucleation of CdS particles by cross-reaction between $Cd(oleate)_2$ and $(TMS)_2S$. These conditions are contrary to the SILAR mechanism and potentially detrimental to the conformal and high-yielding shell growth process that the SILAR procedure is designed to provide. At the same time, these observations imply that a benefit may be obtained by reducing the dose per cycle from a full monolayer to a sub-monolayer dose in order to suppress nucleation[32,126] and increase synthetic yield, while retaining a largely spherical shell.

2.8. Titration experiments: Multiple cycles.

In additional titration experiments we investigated (1) a sub-monolayer SILAR cycle applied to CdSe QDs and (2) application of two sequential, complete monolayer cycles of CdS shell growth. The absorption spectra (normalized to the bandgap absorption peak) of the progression for the above 3 multiple-cycle titration experiments are shown in **Figure 2.10**. Each aliquot was withdrawn at the end of each 0.1 ML eq. dose addition step and diluted in ~2 mL of hexane at room temperature for absorption and emission (red-shifts of the peaks are similar to red-shifts of bandgap absorption) measurements. The curves of the effective bandgap versus effective dose are displayed in **Figure 2.11**.

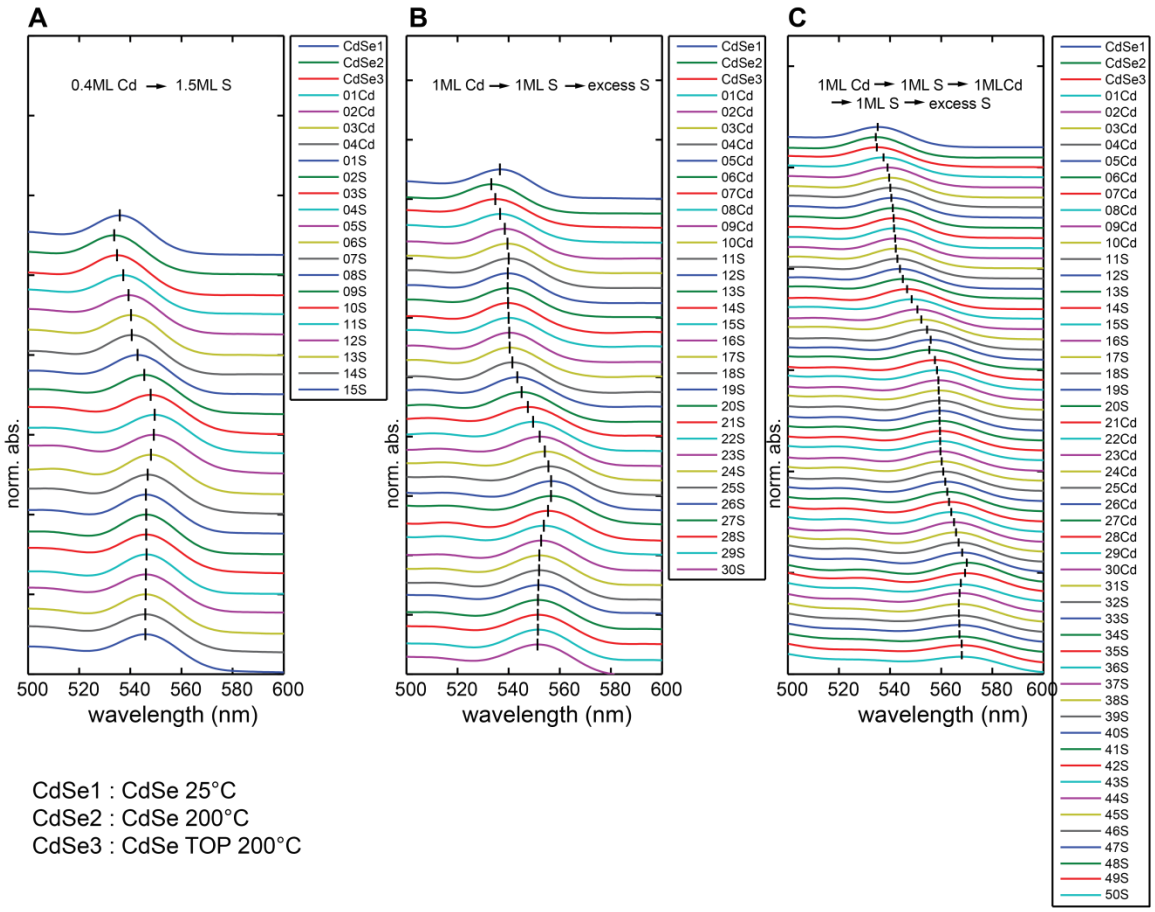

Figure 2.10. Absorption spectra for multi-cycle titration experiments. (A) Sub-monolayer titration; (B) one complete monolayer titration; (C) two complete monolayer titration. Copyright 2013 American Chemical Society.

In **Figure 2.11**, in the sub-monolayer experiment, $Cd(oleate)_2$ was titrated until 0.4 ML eq. dose; we then switched to $(TMS)_2S$ and continued to excess. Whereas $(TMS)_2S$ added to the native CdSe cores produced no redshift, after 0.4 ML eq. $Cd(oleate)_2$, a strong redshift was observed on introduction of $(TMS)_2S$ and continued until 0.4 ML eq. $(TMS)_2S$. Just as in the case where 1.0 ML of $Cd(oleate)_2$ was added, an apparent end-point is observed exactly at the point where the amount of added $(TMS)_2S$ matches the amount of added $Cd(oleate)_2$. The amount of $(TMS)_2S$ that can contribute to

shell growth appears to be determined by the amount of added Cd(oleate)$_2$; the initial core surface is thus evidently saturated with respect to addition of S and the system is unstable towards the addition of excess (TMS)$_2$S.

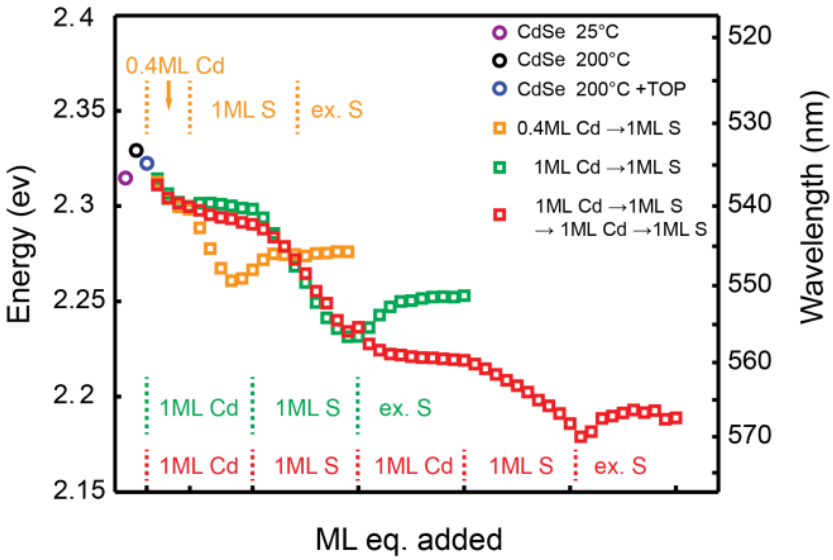

Figure 2.11 Comparison of effective band gap shift versus equivalent dose for three titration experiments. Brown: sub-monolayer titration; Green: titration of 1 ML CdS shell; Red: titration of 2 ML CdS shell. Experimental details are provided in **Table 2.3**. Copyright 2013 American Chemical Society.

When we followed the effective bandgap shift throughout two complete SILAR cycles at 1 ML per cycle (starting with Cd, and continuing to excess (TMS)$_2$S with the second S cycle), the behavior through the second ML eq. was very similar to the first. In particular, in the second Cd cycle, a rapid redshift at low dose was followed by a slower shift at higher equivalency; addition of (TMS)$_2$S produced a strong and continuous redshift until an amount equal to the amount of Cd had been reached, at which time an apparent end-point is reached and a blue shift is seen on addition of excess (TMS)$_2$S. These observations are notable because whereas the first SILAR cycle is applied to the

CdSe QD surface, the second cycle is added to QDs that nominally bear a CdS shell of 1 ML thickness, suggesting that observations made for precursor reactivity are not intrinsic to the first monolayer or the material interface.

2.9. Sub-monolayer dose experiments:

a. Redshift of the band-gap absorption peak.

We next investigated the dependence of shell growth on the dose (number of ML equivalents m) per cycle, using redshift as well as scanning transmission electron microscopy (STEM) as analytical tools. The experiments above revealed that a significant fraction of the added Cd remains in solution at the conclusion of the Cd addition cycle, raising the possibility that undesirable homogeneous nucleation of CdS particles might occur upon introduction of $(TMS)_2S$. If so, such nucleation might be minimized by moving to smaller doses that leave a lower solution concentration of Cd.

The progression of the redshift of the absorption is shown in **Figure 2.12**. and **Figure 2.13** displays the redshift versus ML equivalent thickness observed when CdSe cores from the same batch were treated with precursors sufficient to form a CdS shell of 4 ML total thickness using full-monolayer (m = 1.0) or sub-monolayer (m = 0.6, m = 0.2) SILAR processes. In each case, the number of cycles n was chosen so that $n \times m = 4.0$, and the data points mark the effective bandgap of aliquots drawn at the conclusion of each complete (Cd + S) cycle. The overall red-shift for both sub-monolayer growth experiments is larger than that seen for full-monolayer growth, which is consistent with a greater shell thickness corresponding to a higher synthetic yield, assuming similar shapes and size distributions in the resulting samples. In the case shown, the effective bandgap versus thickness traces for 0.6 ML dose and 0.2 ML dose are overlapped with each other,

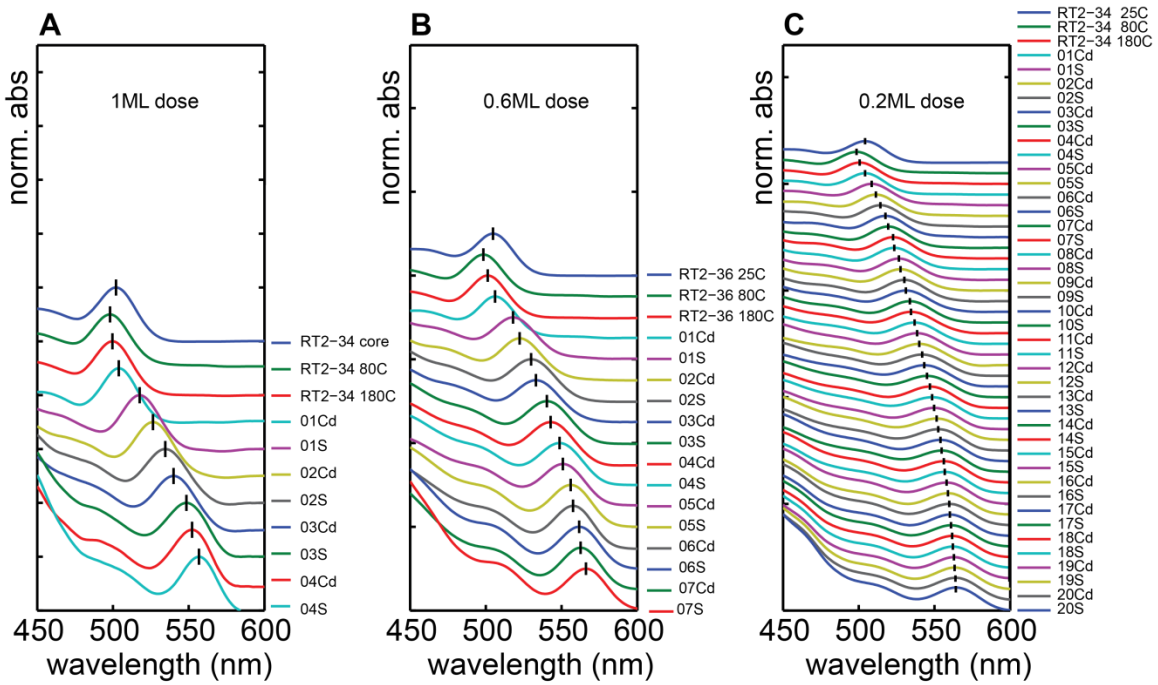

Figure 2.12 Absorption spectra for the sub-monolayer dose experiment for the growth of CdS shells with dose per cycle *m* = 1 ML, 0.6 ML, and 0.2 ML. (A), 1 ML dose; (B), 0.6 ML dose; (C), 0.2 ML dose. Copyright 2013 American Chemical Society.

suggesting that reduction of the dose below 0.6 ML did not cause a measurable increase of synthetic yield. In a series of similar experiments, we have consistently observed larger redshifts at lower doses per cycle m, however, in some cases we do observe an increase in redshift at doses below 0.6 ML, see for example in **Figure 2.14**. These observations strongly suggesting reducing dose to sub-monolayer equivalency is an effective strategy for increasing shell synthetic yield and result in larger spherical core/shell nanoparticles via SILAR technique. Our following Scanning transmission electron microscopy and X-ray photoelectron spectroscopy also strongly supported these conclusions.

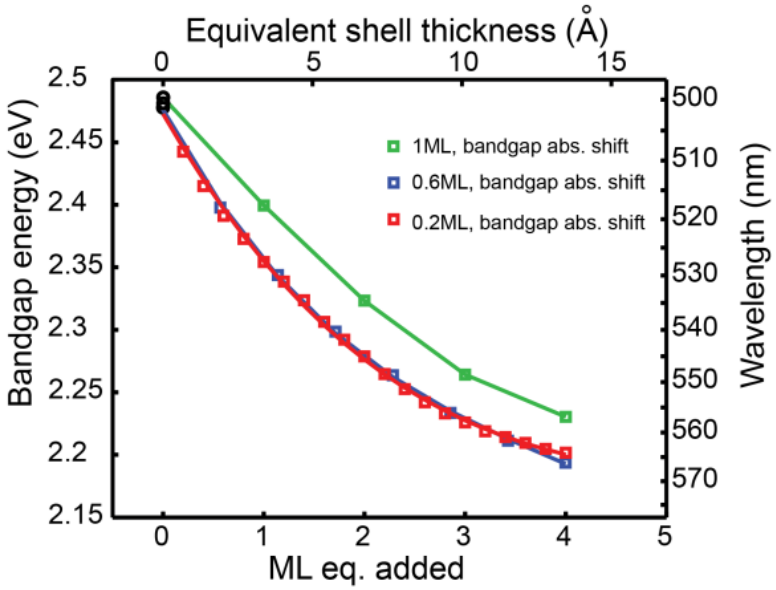

Figure 2.13 Comparison of effective band gap versus equivalent thickness for the growth of CdS shells with dose per cycle m = 1 ML, 0.6 ML, and 0.2 ML. Data points are shown at the conclusion of each complete cycle of $Cd(oleate)_2$ and $(TMS)_2S$ addition. CdSe core radius r_0 = 1.47 nm. Copyright 2013 American Chemical Society.

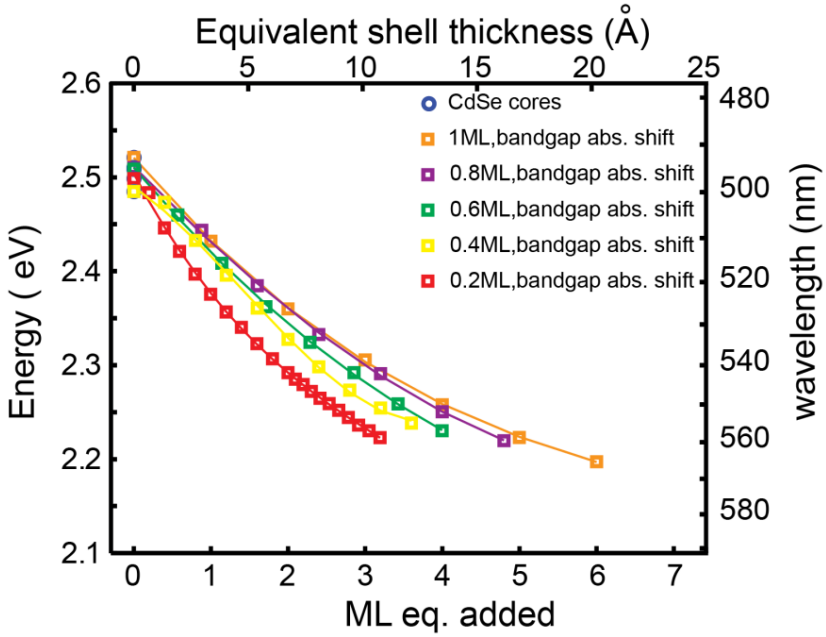

Figure 2.14 Result of sub-monolayer shell growth experiments similar to **Figure 2.13** of the narrative, with a different core batch. The red-shifts at the same ML equivalent became progressively larger when the sub-monolayer dose decreased from 1ML eq. to 0.2 ML eq Copyright 2013 American Chemical Society.

b. STEM images of samples grown with complete-ML & sub-ML reagent doses.

Scanning transmission electron microscopy (STEM) was used to examine the morphological characteristics of core/shell samples grown with different dose per cycle *m*. **Figure 2.15** shows representative dark-field images of the core/shell samples studied in **Figure 2.12**, as well as the underlying CdSe QD cores, at two different magnifications. The CdSe cores used in this experiment displayed a lowest-energy absorption peak at 508 nm; on this basis we assigned effective radius of 1.48 nm and determined the shell precursor doses necessary for the stepwise growth a CdS shell with a total thickness of 4 ML (1.35 nm), leading to a predicted total radius of approximately 2.8 nm for spherical particles at 100% synthetic yield.

Analysis of representative STEM images of the CdSe cores (**Figure 2.15A-B**) revealed particles approximately circular in cross section with an average radius of 1.49 nm (**Figure 2.16A-B**). A thresholding algorithm was applied to delineate particles from back-ground and a watershed analysis was applied to resolve juxtaposed particles.

After 4 ML eq. of shell growth via full monolayer SILAR steps (m = 1.0, **Figure 2.15C-D**), the sample contains larger particles consistent with the formation of CdS shells; no significant contrast is obtained between CdSe and CdS in this imaging mode. However, the larger particles are accompanied by a number of smaller particles with a wide size distribution. In the cases with sub-monolayer shell growth (m = 0.6, **Figure 2.15E-F**; m = 0.2, **Figure 2.15G-H**), larger and nearly spherical particles are present but the small particles are nearly absent.

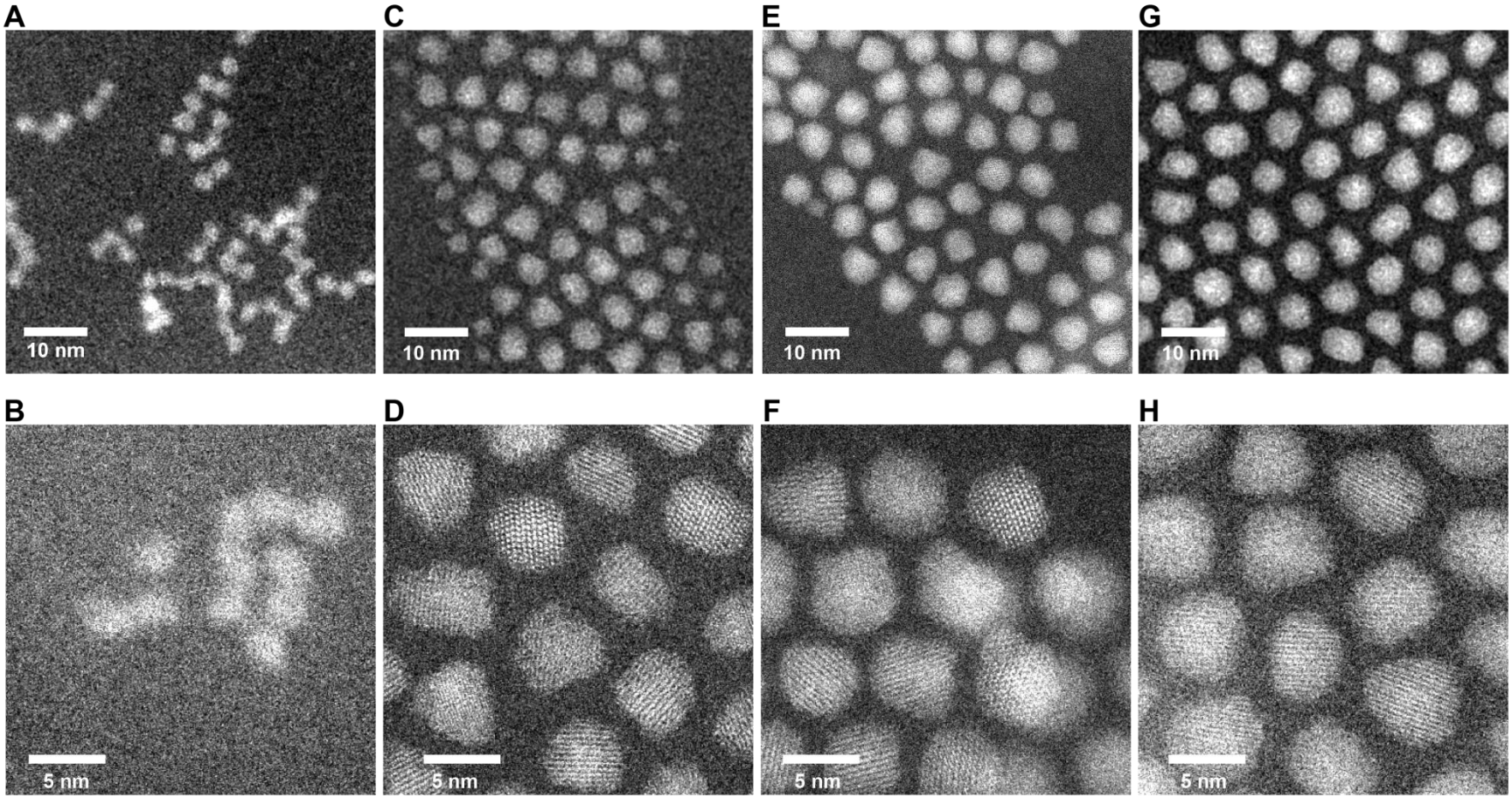

Figure 2.15 STEM images of CdSe cores and CdSe/CdS core/shell QDs. (A,B) CdSe cores shown at two different magnifications. (C,D) CdSe/CdS core/shell QDs, *m* = 1.0 ML dose per cycle. (E-F) CdSe/CdS core/shell QDs, *m* = 0.6 ML dose per cycle. (G-H) CdSe/CdS core/shell QDs, *m* = 0.2 ML dose per cycle. Powder X-ray diffraction data for the sample shown in (G-H) is included in **Figure 2.21**. Copyright 2013 American Chemical Society.

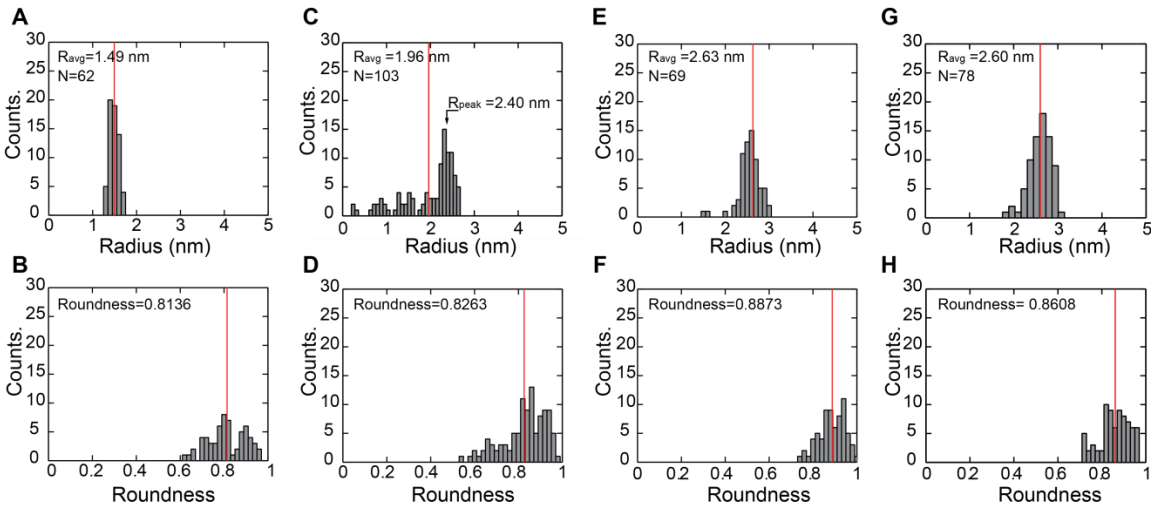

Figure 2.16 Histogram of radius and roundness values for CdSe cores (A, B) and CdSe/CdS core/shell QDs, m = 1.0 ML dose per cycle (C, D); CdSe/CdS core/shell QDs, m = 0.6 ML dose per cycle (E, F); CdSe/CdS core/shell QDs, m = 0.2 ML dose per cycle (G-H). Average values are indicated by red vertical lines. Copyright 2013 American Chemical Society.

$$Roundness = 4 \times \frac{[Area]}{\pi \times [Major\_axis]^2} \quad \text{.....eq. 3}$$

To characterize particle size and shape, we plotted the distributions of particle radius (based on observed cross-sectional area) and of particle roundness, **Figure 2.16**. Roundness is defined as (equation3) and is equal to 1 for a perfectly circular cross section and < 1 for oblate shapes. In **Figure 2.16 C-D**, compared to the results for m = 1.0, the sub-monolayer samples displayed tighter size distributions, a larger radius among the large particles, and higher roundness values. The larger radius for sub-monolayer doses is consistent with formation of a thicker shell, which explains the larger redshift observed for these samples compared to the m = 1.0 sample in **Figure 2.13**. Only small differences in histogram of radius and roundness were seen between m = 0.6 (**Figure 2.16E-F**) and

m = 0.2 (**Figure 2.16G-H**), in keeping with the negligible differences in red shift values between these samples.

We attribute the small particles seen in the sample made using full monolayer SILAR doses to the nucleation of CdS particles by cross-reaction of the shell precursors in solution. In particular, the high solution concentration of Cd at the conclusion of $Cd(oleate)_2$ addition steps provides the opportunity for nucleation reactions to take place. This diverts material from the shell growth process, resulting in a smaller increase in radius due to a thinner shell. Switching to a lower dose per cycle (m = 0.6) was sufficient to suppress such nucleation in this case; suppression is achieved even though, based on our earlier results, a significant fraction of the added Cd remains in solution even in this case. Studies of nucleation and growth of colloidal CdSe nanocrystals[32,126] suggest that the nucleation rate may be more sensitive to the free Cd concentration than is the surface growth rate, since nucleation reactions are frequently of high order.[31,33]

A concern in moving to lower dose per cycle is that it is not possible to enforce isotropic growth by saturating all surface sites; it would be possible in principle to, instead, selectively elaborate certain facets. In fact, we do not see evidence of strongly anisotropic growth even at m = 0.2 ML under these reaction conditions. The roundness values for the sub-monolayer samples are actually higher than those seen at m = 1.0 ML, and this trend is supported by the visual appearance of the particles in the images. We note that high roundness has also been achieved under high dose per cycle in the biphasic method reported by Ithurria et al., suggesting that SILAR growth can be self-limiting if excess reagents are removed in each step.[112] The loss of material to nucleation complicates the rational design of specific core/shell structures, and can also be

detrimental to the ensemble QY if the particles of the shell material are not removed from the sample.[61] Based on the results shown here, under commonly-used SILAR conditions in homogeneous solution, sub-monolayer growth is preferable to the introduction of full monolayer equivalents because it is able to suppress nucleation, while maintaining isotropic growth.

c. XPS analysis for samples grown with complete-ML and sub-ML dose

It is also useful to use X-ray photoelectron spectroscopy (XPS) to characterize the elemental ratio of Cd, Se and S for the above CdSe/CdS core/shell samples grown with m = 1.0 ML, m = 0.6 ML and m = 0.2 ML. The XPS results are shown in **Figure 2.17.**

The method to determine the elemental ratio is based on previous work.[115,116,127–129] Briefly, the intensity of a given photoelectron signal (Cd $3d_{5/2}$ and Cd $3d_{3/2}$ for cadmium; Se $3d_{5/2}$ and Se $3d_{3/2}$ for selenium; S $2p_{1/2}$ and S $2p_{3/2}$ for sulfur) has to be corrected by the relative atomic sensitivity factor, $S = f\sigma\theta y\lambda AT$. Here, f is the X-ray flux, σ is the cross section for the photoelectric process, θ is the equipment angular factor, y is the efficiency for formation of photoelectron with the full kinetic energy, λ is the escape depth of photoelectrons of that kinetic energy, A is the area of the sample being probed, and T is a factor for the efficiency of detecting electrons of a given kinetic energy. In a homogeneous bulk material, the escape depth equals to λ which is a constant value named the electron mean free path; for nanocrystals with the size around several nanometers, the appropriate way to account for the escape depth is to integrate over the entire region of interest, modifying the intensity from each point by an exponential factor that decreases with depth away from the surface, $\int_0^d e^{-z/\lambda} dz$, d is the depth of the sample, z is the distance from an arbitrary point within the nanocrystal to the surface in the

direction of the analyzer. In spherical polar co-ordinates for spherical QDs, $z = \sqrt{R^2 - r^2 \sin^2\theta} - r\cos\theta$, the expression becomes:

$$J = 2\pi \int_0^R \int_0^\pi e^{-\frac{\sqrt{R^2 - r^2\sin^2\theta} - r\cos\theta}{\lambda}} \cdot r^2 \sin\theta dr d\theta \quad \cdots\cdots \text{eq. 4}$$

And the electron mean free path λ, is obtained from the universal equations.[130] The values used for CdSe were: molecular weight 191.37 g/mol, density 5.66 g/cc, bandgap was correlated to the first absorption peak and the number of valence electrons was assumed to be 18, the calculated λ_{cd3d} = 2.08 nm, λ_{se3d} = 2.58 nm, λ_{s2p} =2.49 nm so Cd/Se elemental ratio could be determined as:

$$ratio_{Cd/Se} = \left(\frac{I_{cd} \cdot \lambda_{Cd}}{S_{Cd} \cdot J_{Cd}}\right) / \left(\frac{I_{Se} \cdot \lambda_{Se}}{S_{Se} \cdot J_{Se}}\right) \quad \cdots\cdots \text{eq. 5}$$

$$ratio_{S/Se} = \left(\frac{I_S \cdot \lambda_S}{S_S \cdot J_S}\right) / \left(\frac{I_{Se} \cdot \lambda_{Se}}{S_{Se} \cdot J_{Se}}\right) \quad \cdots\cdots \text{eq. 6}$$

The ratio given by the above equations is based on the fact that the two elements are occupied with the same volume. For CdSe core, the volume difference between two elements is negligible; for CdSe/CdS core/shell nanoparticles Cd, Se and S all occupied different volumes, for example Se only appeared in the core region and S only in the shell, however for Cd it occupied the volume of the whole core/shell nanoparticles. So the true elemental ratio of Cd/Se as well as S/Se should be scaled with the different of volumes. (V_{Cd}= $(4/3)\pi r^3$ nm^3 ;V_{Se}= $(4/3)\pi r_0^3$ nm^3 ;V_S=$(4/3)\pi(r^3-r_0^3)$ nm^3, where r is radius of the CdSe/CdS core/shell particle and r_0 is radius of the CdSe core) Samples were drop-cast from hexane solution onto gold-coated Si wafers. The sample taken from the shell growth solution was purified by precipitating once with acetone.

The XPS results are shown in **Figure 2.17** and **Table 2.4**.

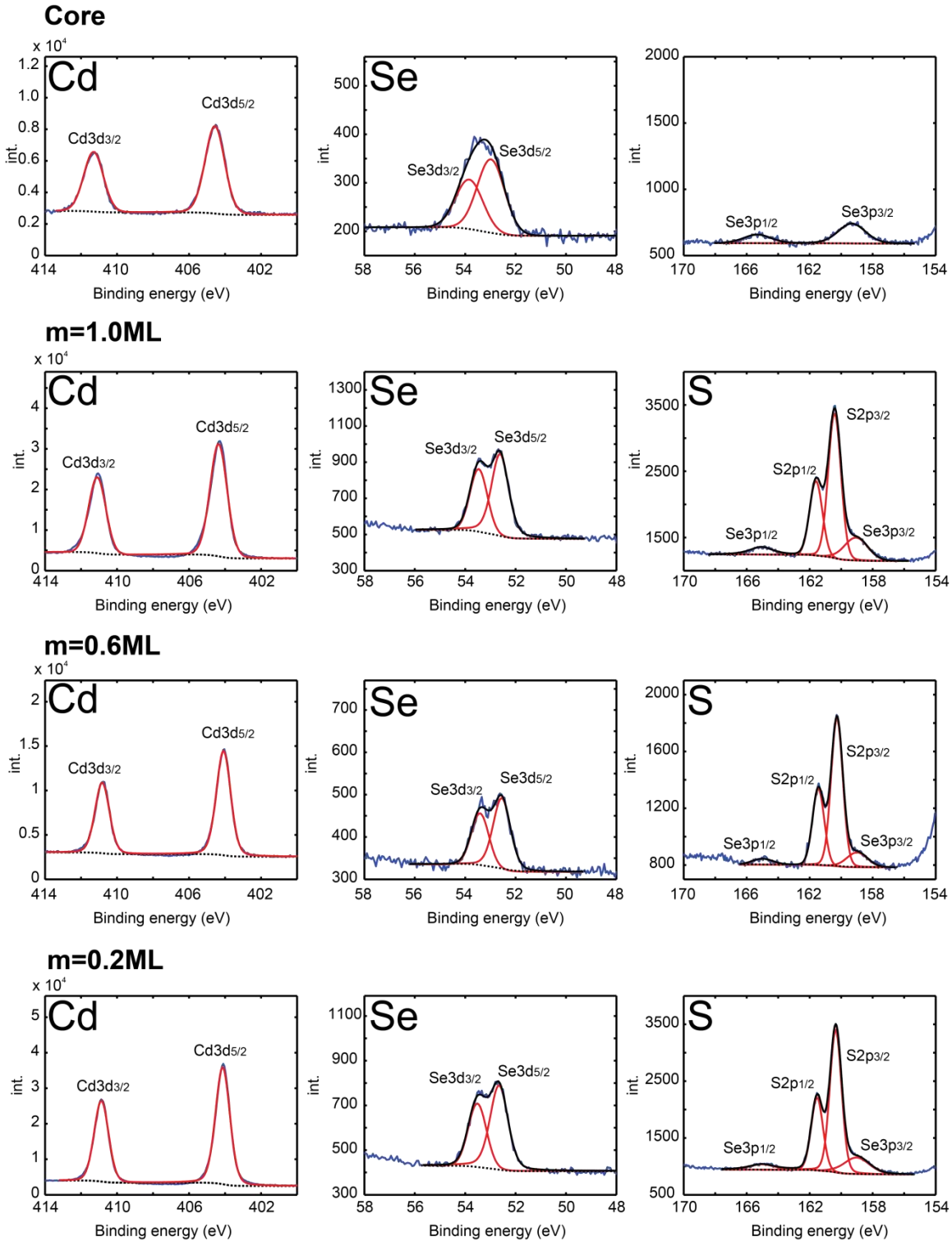

Figure 2.17 XPS results of Cd, Se and S for CdSe cores and CdSe/CdS core/shell QDs with m = 1.0 ML, m = 0.6 ML and m = 0.2 ML dose per cycle.

Table 2.4 XPS results for samples shown in **Figure 2.17**

	Peak	Binding Energy (eV)	Area[a]	FWHM (eV)
CdSe core	Cd $3d_{3/2}$	411.31	5292.33	1.29
	Cd $3d_{5/2}$	404.57	7938.49	1.29
	Se $3d_{3/2}$	53.84	138.32	1.28
	Se $3d_{5/2}$	52.98	207.48	1.28
	Se $3p_{1/2}$	165.32	148.81	2.04
	Se $3p_{3/2}$	159.32	347.17	2.04
CdSe/CdS m=1.0ML	Cd $3d_{3/2}$	411.10	22328.77	1.12
	Cd $3d_{5/2}$	404.36	34470.49	1.12
	Se $3d_{3/2}$	53.46	299.22	0.81
	Se $3d_{5/2}$	52.62	448.84	0.81
	S $2p_{1/2}$	161.60	1130.84	0.95
	S $2p_{3/2}$	160.42	2261.69	0.95
	Se $3p_{1/2}$	165.06	274.95	1.76
	Se $3p_{3/2}$	159.06	641.46	1.76
CdSe/CdS m=0.6ML	Cd $3d_{3/2}$	410.82	8577.37	0.94
	Cd $3d_{5/2}$	404.08	12866.06	0.94
	Se $3d_{3/2}$	53.41	109.00	0.82
	Se $3d_{5/2}$	52.55	163.50	0.82
	S $2p_{1/2}$	161.45	499.05	0.87
	S $2p_{3/2}$	160.27	998.10	0.87
	Se $3p_{1/2}$	165.00	72.83	1.54
	Se $3p_{3/2}$	159.00	169.91	1.54
CdSe/CdS m=0.2ML	Cd $3d_{3/2}$	410.93	22377.43	0.95
	Cd $3d_{5/2}$	404.19	33566.15	0.95
	Se $3d_{3/2}$	53.55	254.88	0.82
	Se $3d_{5/2}$	52.69	382.32	0.82
	S $2p_{1/2}$	161.58	1198.51	0.86
	S $2p_{3/2}$	160.40	2397.02	0.86
	Se $3p_{1/2}$	165.13	220.97	1.69
	Se $3p_{3/2}$	159.13	515.52	1.69

[a] Peaks for Cd, Se and S were fit with XPSpeak program; the resulting fitting curves are shown as red lines in **Figure.2.17**

Figure 2.17 showed the XPS results of Cd, Se and S for CdSe cores and CdSe/CdS core/shell QDs with *m* = 1.0 ML, *m* = 0.6 ML and *m* = 0.2 ML dose per cycle. In order to determine the elemental ratio, the intensities of peaks for each element were split and fit by XPSpeak program (in **Figure 2.17**, blue peaks were raw intensities, red peaks were fitted peaks); for sulfur, the binding energy of electrons for S 2p orbital are very close to the binding energy of electrons for Se 3p orbital, as a result the S $2p_{1/2}$ and S $2p_{3/2}$ peaks are overlapped with Se $3p_{1/2}$ and Se $3p_{3/2}$ peaks, so the right XPS intensity for sulfur should corrected by subtracting the intensities form Se $3p_{1/2}$ and Se $3p_{3/2}$ (**Figure 2.17**) The elemental ratios are determined and displayed in **Table 2.5**. For CdSe cores, the high Cd/Se ratio suggesting a Cd rich surface and it is clearly shown that the *m*=0.6 ML core/shell particles and *m*=0.2 ML core/shell particles have higher Cd/Se and S/Se ratios that *m*=1.0 ML core/shell particles. Because the same monolayer equivalent of Cd and S precursors were introduced for shell growth, this strongly supported our conclusion that a higher shell synthetic yield can be achieved by reducing the dose to sub-monolayer equivalent.

Table 2.5 Elemental ratios for the above samples.

	ratio_Cd/Se	ratio_S/Se
CdSe core	4.33[a]	-
CdSe/CdS core/shell, *m*=**1.0** ML	8.57	5.30
CdSe/CdS core/shell, *m*=**0.6** ML	11.85	8.46
CdSe/CdS core/shell, *m*=**0.2** ML	10.18	6.73

[a] the high Cd/Se ratio indicating a Cd-rich surface for this core.

2.10. Study of the CdSe core surface by XPS and ^{31}P NMR.

We conducted X-ray photoelectron spectroscopy (XPS) and NMR analyses to characterize the surface of the CdSe QDs prior to shell growth. In particular, we studied CdSe cores as purified (precipitated twice with acetone from hexane) at 25 ℃, and the same cores retrieved from the shell growth solvent (ODE and oleylamine) after heating for 2 hours at 80 ℃ and prior to introduction of shell precursors.

For XPS analysis, samples were drop-cast from hexane solution onto gold-coated Si wafers. The sample taken from the shell growth solution was purified by precipitating once with acetone. The results are shown in **Figure 2.18.** The binding energies indicated by the Cd 3d and Se 3d peak positions are very similar between the two samples; however, the relative intensities of the two elements are different. By comparing the integrated Cd 3d and Se 3d intensities, we obtained an estimate of the Cd/Se elemental ratio based on the method in section 2.9 c. After correcting for the difference in the relative sensitivity factors ($S = f\sigma\theta y\lambda AT$) of the two elements (**Table 2.6**), see section 2.9 c for details of analysis method, the elemental ratio was determined to be Cd/Se=1.23 for the initial cores, and Cd/Se=1.02 for the heated cores. The decrease in Cd/Se ratio, together with the blue shift of the lowest-energy excited state as seen in the UV-VIS absorbance data, are consistent with the desorption of excess Cd into solution on heating in the shell growth solvent; a small amount of dissolved Cd was likewise observed in solution by ICP-MS prior to introduction of the Cd oleate shell precursor. (see **Figure 2.8D**)

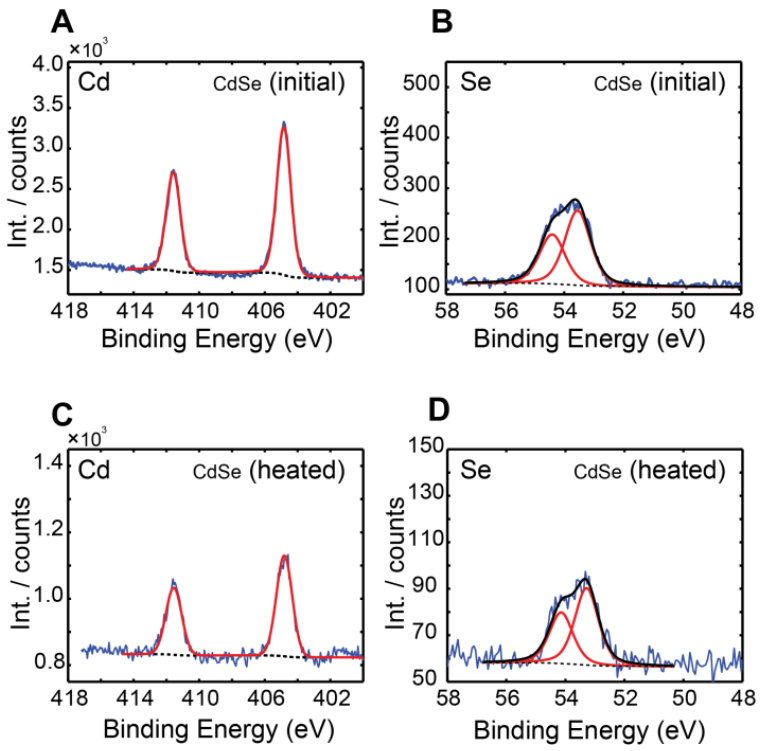

Figure 2.18 XPS scans of the Cd 3d and Se 3d regions for initial CdSe cores after purification, and CdSe cores recovered after heating in the shell growth solvent. Copyright 2013 American Chemical Society.

Table 2.6 XPS raw data for initial and heated CdSe NCs in **Figure 2.18**

	Peak	Binding Energy (eV)	Area[a]	FWHM (eV)
CdSe initial	Cd $3d_{3/2}$	411.58	1388.90	1.01
	Cd $3d_{5/2}$	404.84	2083.35	1.01
	Se $3d_{3/2}$	54.40	130.51	1.04
	Se $3d_{5/2}$	53.54	195.77	1.04
CdSe heated	Cd $3d_{3/2}$	411.55	246.66	1.14
	Cd $3d_{5/2}$	404.81	369.98	1.14
	Se $3d_{3/2}$	54.14	27.19	0.95
	Se $3d_{5/2}$	53.28	40.79	0.95

The initially-purified QDs are capped by phosphorus-containing ligands; so we employed ^{31}P NMR to investigate the population of the ligands on CdSe core surface initially, and just prior to shell growth. The NMR samples were prepared by dissolving the purified and dry CdSe QDs in solvent toluene-d_8.

As shown in **Figure 2.19A**, after 2 cycles of precipitation, three sharp peaks are observed that we assign to TOP (–32.20 ppm), TDPA (35.31 ppm), and TOPO (46.26 ppm). A broader peak is observed at 25.85 ppm and we associate this with TDPA bound to the QD surface.[124,131] Following heating in the shell growth solvent, the QDs were isolated by precipitation, and the re-dissolved QD sample (**Figure 2.19B**) and the supernatant (after removal of light solvents, **Figure 2.19C**) were analyzed separately. By comparing these spectra, it can be seen that after the initial purified CdSe cores are introduced to the shell growth solvent and heated to 200 ℃, TOP, TOPO and TDPA are all found in the shell growth solvent. In addition, a new peak at 18.5 ppm in the supernatant spectrum indicates the formation of dialkylpyrophosphonate (DP) species[131,132] by condensation. We also see in **Figure 2.19B** that a broad phosphorus signal remains, which could be associated to the TDPA/DP that strongly bonded to the CdSe core surfaces, and results in broad variation of ^{31}phosphorus relaxation. Assigning this as ionically-bound phosphonate (or DP) ligands would indicate that the surface remains slightly Cd-rich, because of the requirement of charge balance by these ligands, in agreement with the XPS measurement.

The agreement of our XPS and ^{31}P NMR results proved that after degasing and prior to the shell growth, the CdSe cores have reached to a surface with only slightly Cd-rich and almost stoichiometrically equivalent with Cd and Se.

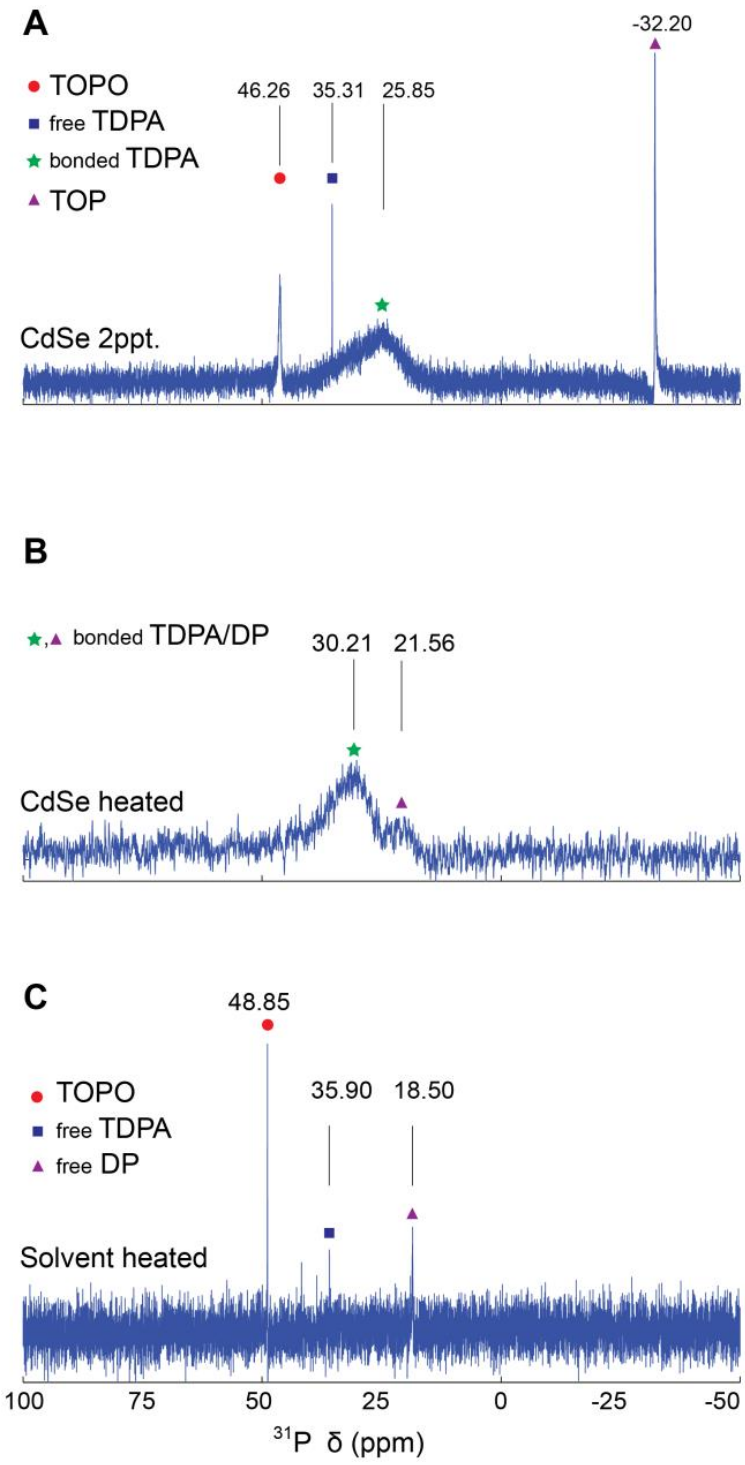

Figure 2.19 ^{31}P NMR analysis of CdSe QD samples used in core/shell growth. (A) Initial CdSe cores after 2 times precipitation. (B, C) Analysis after heating in shell growth solvent (oleylamine and ODE): (B) CdSe cores recovered by precipitation; (C) supernatant after precipitation of QDs. Copyright 2013 American Chemical Society.

2.11. Discussion

Based on our observations when monitoring the shell growth process as described above, we propose the following model. The as-prepared CdSe QD cores are terminated by a ligand shell that includes anionic alkylphosphonate ligands.[131] After purification by two cycles of precipitation/redissolution, most ligand species are removed except for strongly-bound alkylphosphonates (or pyrophosphonates) whose charge is balanced by an excess of Cd^{2+} ions at the nanocrystal surface.[124] Following heating in the overcoating solvent, a portion of previously surface-bound Cd departs as soluble Cd alkylphosphonate, resulting in a decrease of the QD effective radius and small blue shift of the first absorption peak, forming a more nearly neutral surface; this surface is likely stabilized by the oleylamine solvent acting as a dative (L-type) ligand to Cd sites at the surface[133] and/or to dissolved Cd alkylphosphonate species.[134]

Potential sites for binding of excess Cd-compensated by X-type ligands-are occupied subject to an equilibrium with dissolved species. Based on our ICP-MS results, the solution concentration of Cd remains small prior to the introduction of the $Cd(oleate)_2$ shell precursor. When it is introduced, the solution Cd concentration increases and this drives increased occupation of the surface by super-stoichiometric Cd, leading to a redshift. On both the CdSe and CdS surface, we see possible evidence for two or more different binding modes for Cd based on the rate of red shift with dose. Most importantly, a significant excess of $Cd(oleate)_2$ must be added to approach surface coverage by Cd at a density comparable to that found in 1 ML of CdS.

When $(TMS)_2S$ is added, it leads to a redshift corresponding to shell growth only in the case that a stoichiometrically equivalent quantity of $Cd(oleate)_2$ has been

introduced prior. The endpoint is quite sharp, suggesting that the initial surface represents the most chalcogenide-rich composition that the system can support, and that the chemical reaction experienced by $(TMS)_2S$ proceeds with a large equilibrium constant. Based on previous reports,[131,135] it is likely that TMS_2S reacts quickly with the oxyacid anions to irreversibly form O-TMS byproducts, leaving the S^{2-} equivalent available to form CdS.

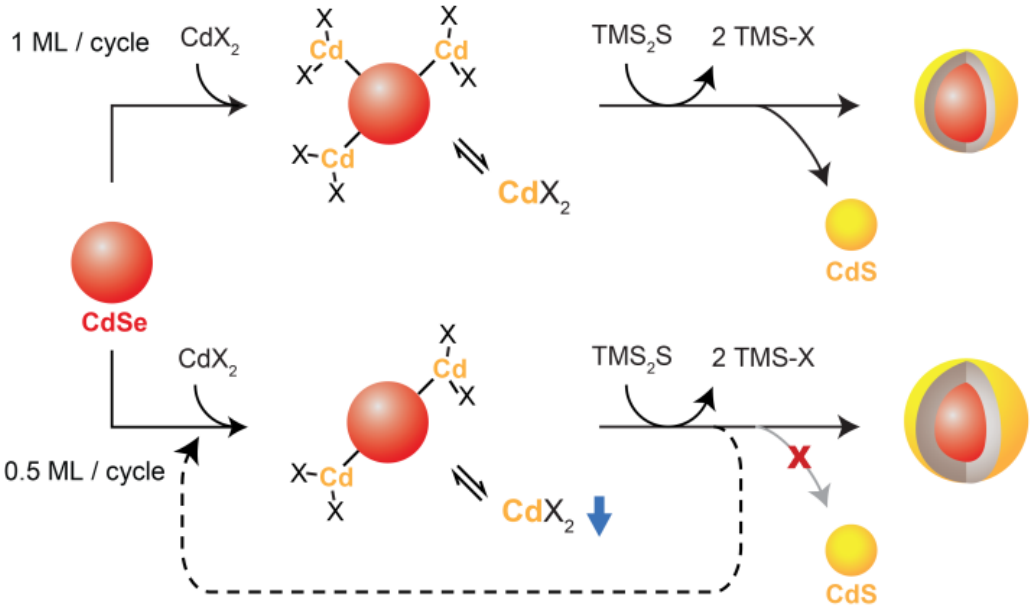

Figure 2.20 Scheme for full-monolayer vs. sub-monolayer shell growth. Copyright 2013 American Chemical Society.

When shell growth reagents are introduced in large (full monolayer) equivalents per cycle (**Figure 2.20**), a sufficient quantity of Cd remains in solution to permit nucleation of CdS particles upon introduction of $(TMS)_2S$ and to permit non-self-limited elaboration of the QD surface. It is our view that the significant solubility of $Cd(oleate)_2$ (and $Cd(phosphonate)_2$) above the CdSe/CdS surface under the reaction conditions is the

chief reason for this deviation from the SILAR model, this topic will be discussed in chapter 4. By reducing the dose per cycle, the Cd concentration at the conclusion of the addition cycle is sufficiently reduced that the nucleation rate can be greatly suppressed.

A great majority of the SILAR literature for the formation of Cd-based shells describes the use of the $Cd(oleate)_2$ precursor. Primary amines in the solvent mixture appear to play a role in stabilizing $Cd(oleate)_2$ in solution based on room temperature ligand exchange results.[134] In core/shell growth, replacing primary amines with a secondary amine (dioctylamine) is reported to improve control during the formation of thick shells via SILAR,[97,110] and addition of Cd carboxylate precursors in the absence of amines or olefins led to very high surface enrichment,[116] though the concentration of Cd in solution was not directly monitored in these cases. Here, we have found that a move to lower dose per cycle permits high-yielding shell growth and the formation of more spherical particles. Indeed, we have previously reported very high quantum yields for CdSe/CdS core/shell QDs formed using sub-monolayer (0.8 ML) equivalents under similar conditions.[62] Methods such as those employed here could confirm the changes in equilibrium between bound and soluble precursors that are associated with changes in reaction conditions, and more generally, aid the development of nanostructures with rationally controlled size, shape, and surface enrichment via surface reactions of controlled stoichiometry.

2.12. Experimental section

Materials The following chemicals were used as received. Cadmium oxide (CdO; 99.999%), Trioctylphosphine (TOP; 97%) and Trioctylphosphine oxide (TOPO; 99%) were purchased from Strem Chemicals. Oleic Acid (OA; 99%), 1-Octadecene (ODE; 90%

technical grade), 1-Tetradecylphosphonic Acid (TDPA; 98%) and Se (99.999%) were purchased from Alfa Aesar. Decylamine (95%) was purchased from Sigma Aldrich. Oleylamine (80-90%) and bis(trimethylsilyl) sulfide ($(TMS)_2S$; 95%) were purchased from Acros Organics. Toluene-d8 (D, 99.5%), were purchased from Cambridge Isotope Laboratories, Inc. 200 Proof Ethyl Alcohol (Ethanol) was obtained from Decon Laboratories, Inc. Acetone (99.9%) was purchased from VWR. Methanol (99.9%) was purchased from Fisher Scientific. TOPSe (2.2 M) was prepared by dissolving Se in TOP. A Stock solution of $Cd(oleate)_2$ in ODE was prepared by heating CdO in ODE with 2.2 eq. of oleic acid at 260 ℃ under nitrogen followed by degassing under vacuum at 100 ℃ for 20 minutes. Nanocrystal core and shell growth were carried out under nitrogen (N2) using Schlenk line techniques; air-sensitive reagents were prepared in a nitrogen filled glovebox.

Nanocrystal synthetic techniques for CdSe cores: A hot-injection technique was applied for synthesis of CdSe nanocrystals (NCs) cores.[62] For a representative synthetic route, CdO (0.12 g) was heated with TDPA (0.5500 g) at 330 ℃ in a solvent TOP (6 ml) and TOPO (6 g) under nitrogen flow until the solution became colorless. Following removal of evolved H2O under vacuum at 130 ℃, the solution was heated again to 360 ℃ under nitrogen. As-prepared TOPSe (1.3 mL) was injected rapidly into the reaction pot, which was immediately allowed to cool down to room temperature and stored as a yellow waxy solid. The Cd:TDPA:Se molar ratio is 1:2:3. The core radius was estimated by a calibration curve[62,118] describing the radius as a function of the position of the lowest-energy absorption peak. Powder X-ray diffraction data indicated a dominant wurtzite crystal structure (**Figure 2.21**). Each core batch provided sufficient material for

several core/shell growth experiments; all direct comparisons of nanocrystal reactivity were made between samples of CdSe QD cores taken from the same batch.

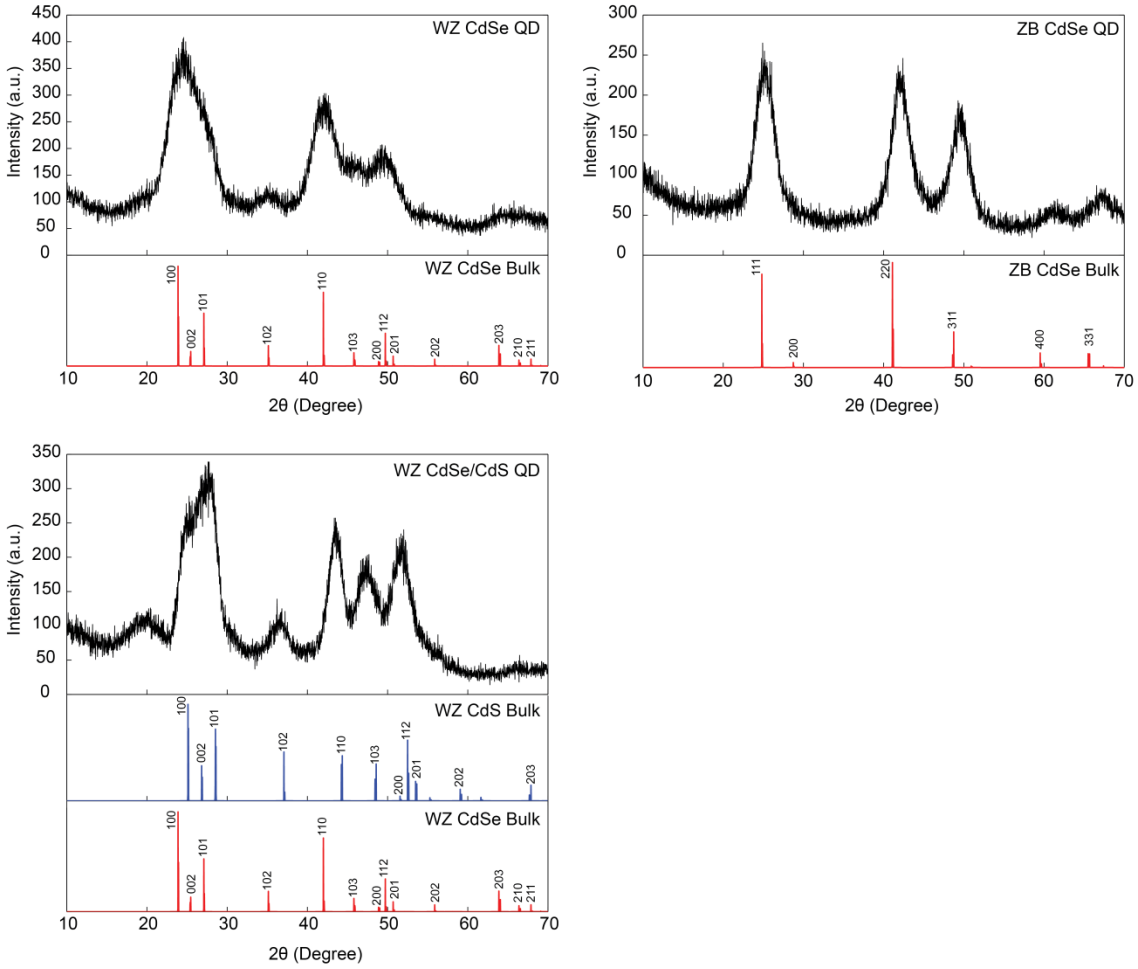

Figure 2.21 Powder X-ray diffraction patterns for CdSe cores and CdSe/CdS core/shell QDs. The left two panels show powder X-ray diffraction patterns for representative CdSe QD cores and CdSe/CdS core/shell QDs produced by the methods described in the narrative. The predominant structure is assigned as wurtzite in both cases. In the right panel a diffraction pattern for zincblende CdSe cores produced by a different method is shown for comparison. The radiation was Cu *Kα* with a wavelength of 1.5418 Å. The powder X-ray diffraction patterns for zincblende bulk CdSe (ICSD#180931), wurtzite bulk CdSe (ICSD#620420) and wurtzite bulk CdS (ICSD#154188) are obtained from ICSD (Inorganic Crystal Structure Database), FIZ Karlsruhe – Leibniz Institute for Information Infrastructure. Copyright 2013 American Chemical Society.

Synthesis of CdSe/CdS core-shell QDs: CdSe cores were washed via 2 cycles of precipitation/redissolution in a manner described previously,[62] and then brought into a measured volume of hexane for absorption measurements to determine the size and quantity of cores.[119] The cores were injected into the overcoating solvent (2:1 ODE:oleylamine (v/v, 9 ml total)) and degassed at 80 ℃ for 2 hours to remove hexane. The system was then placed under nitrogen and brought to the growth temperature before introducing shell precursors. The Cd precursor was prepared by introducing $Cd(oleate)_2$ stock solution in a solvent of 50:50 ODE and TOP with two equivalents of 1-decylamine (vs. Cd) added to yield a Cd concentration of 0.1 M. The sulfur precursor was 0.1 M solution of $(TMS)_2S$ dissolved in TOP. A computer-controlled syringe pump (J-KEM Scientific Dual Syringe Pump, Model 2250) was used to introduce reagents according to the dose and timing regimes described. For a routine shell growth process, a total waiting time of 15 min (or 10 min as described) was allowed to elapse between the start of each addition, and the precursors were added at a constant rate over a 3 min injection time. Reaction progress was monitored by periodically withdrawing a small aliquot of a measured volume (typically 50 μL) from the reaction flask and diluting it in hexanes at room temperature; these aliquots were analyzed for UV-vis absorption and fluorescence emission in hexanes solution, and in some cases were processed further to quantify dissolved Cd species by ICP-MS.

For the study of shell growth by changing the addition order of the precursors, the aliquots were taken every 1 min at the first 3 min and every 2 min until one addition cycle completed; for titration experiments and the sub-monolayer dose shell growth, the aliquots were taken 1 min before the end of each addition cycle. The absorption spectra

were recorded by a Thermo Scientific Evolution Array UV-Visible Spectrophotometer with hexane as the solvent as well as the blank in a 1 cm path quartz cuvette. The emission spectra were recorded by an Ocean Optics USB 4000 spectrometer under 365 nm LED excitation. At the end of the reaction, the temperature was reduced to room temperature, the product was retrieved quantitatively and the total volume was recorded for the calculation of the molar extinction coefficient.

Inductively Coupled Plasma-Mass Spectrometry Analysis: Inductively coupled plasma-mass spectrometer (ICP-MS) samples were prepared by the following method. Each aliquot of 20 μL was taken and dissolved in to 2.0 mL hexane. After recording absorption and emission spectra, 1 mL acetone and 3 mL methanol were added to precipitate QDs; samples were centrifuged at 5000 rpm (~3000 × g) for 5 min, then the supernatant was transferred into 20 mL sealed vials, and checked with UV light to make sure that it showed no absorption or fluorescence indicative of QDs left in solution. The samples were dried by removing the solvent in vacuum. 1 mL of aqua regia (3:1 hydrochloric acid: nitric acid, caution: highly corrosive; oxidizer) was introduced and was allowed to digest the sample for 2 hours. Then each of the samples was quantitatively transferred into a volumetric flask and brought to 50.0 mL with 2% HNO3, and the concentration of Cd^{2+} was measured by a Themo-Finnigan Element XR ICP-MS. A control experiment using $Cd(oleate)_2$ in ODE was designed to investigate the accuracy of this method in quantifying the amount of Cd^{2+}. The error was determined to be less than 6%.

X-ray Photoelectron Spectroscopy analysis: Samples of CdSe cores were prepared via drop-casting. As-synthesized or heated samples were washed via 2 cycles of

precipitation with acetone and methanol as anti-solvents. Portions of the cores (~30 nmol QDs) were diluted in hexane, then drop-casted on clean Au-coated Si chips (0.5 cm×0.5 cm) to form a thin film; the coated chip was pumped under vacuum for 10 hours before XPS measurement. XPS measurements were conducted using a Kratos AXIS Ultra DLD XPS system equipped with a monochromatic Al Kα source. The energy scale of the system is calibrated using an Au foil with Au 4f scanned for the Al radiation and a Cu foil with Cu 2p scanned for Mg radiation resulting in a difference of 1081.70 ± 0.025 eV between these two peaks. The binding energy is calibrated using an Ag foil with Ag 3d5/2 set at 368.21 ± 0.025 eV for the monochromatic Al X-ray source. The monochromatic Al *Kα* source was operated at 15 keV and 120 W. The pass energy was fixed at 40 eV for the detailed scans. A charge neutralizer was used to compensate for the surface charge. The base pressure of the system was $\sim 10^{-9}$ Torr. Elemental compositions were calculated from high-resolution spectra of C 1s, Cd 3d and Se 3d photoemission lines with pass energy of 40 eV. The binding energies were referenced to C 1s at 284.5 eV. XPS raw data were fit with the XPSpeak program using a Shirley background.

^{31}P NMR Analysis of QDs: The NMR samples were prepared by dissolving the purified CdSe QDs in solvent toluene-d_8. After synthesis/heating the CdSe QDs (90 mg) were crashed out via 1-time acetone-methanol precipitation. Then the sample was dissolved in toluene and pumped dry before re-dissolving in toluene-d_8 (0.6 mL) and transferred into a NMR tube. The ^{31}P NMR spectra of CdSe core samples were measured by a Bruker Avance III HD 400 with 512 scans.

Scanning Transmission Electron Microscopy imaging: After purification, the CdSe or CdSe/CdS core/shell QDs were brought into hexane to form a dilute solution

(1.1 μM), one drop of the solution was drop-casted on a clean TEM grid (400 mesh Cu grid with ultrathin carbon support film, Type-A, Ted Pella, Inc.) and pumped dry under vacuum for 2 hours. The STEM samples were imaged by JEOL 2100F 200 kV FEG-STEM/TEM equipped with a CEOS CS corrector on the illumination system. Prior to high magnification observation, a large specimen area was pre-irradiated with electrons for 10 minutes to polymerize surface hydrocarbons and therefore prevent their diffusion to the focused probe. The geometrical aberrations were measured and controlled to provide less than a $\pi/4$ phase shift of the incoming electron wave over the probe-defining aperture of 17.5 mrad. High angle annular dark-field (HAADF) STEM images were acquired on a Fischione Model 3000 HAADF detector with a camera length such that the inner cut-off angle of the detector was 75 mrad. A pixel dwell time of 16 μs was chosen.

CHAPTER 3

INFLUENCE ON QUANTUM YIELD AND FLUORESCENCE LIFE TIME OF COLLOIDAL CORE/SHELL QUANTUM DOTS BY NEUTRAL SURFACE LIGANDS*

3.1. Introduction

Because of their distinctive electronic structure, colloidal semiconductor quantum dots (QDs) exhibit size-tunable absorption and emission spectra,[84] large molar extinction coefficients,[119,120] two-photon excitation cross sections,[9,136] and high photostability[10,11] compared to most molecular fluorophores. These properties have led to great interest in QDs as light emitters in bioimaging[9,11–14] and display[15] applications and as light absorbers in solar cells[137–142] and focal plane arrays.[30] However, a limitation in many of these cases is the nonradiative decay rate, which competes with light emission or charge transfer.[143] Nonradiative decay is manifested in less-than-unity quantum yields in ensemble samples and in fluorescence intermittency (blinking) in single-particle measurements.[97,144–147] Whereas the radiative rate is largely controlled by the delocalized band-edge electronic states,[148–150] nonradiative decay rates can depend sensitively on the interfacial structure.[2,151] In particular, the surfaces are typically populated by exchangeable ligand layers, and numerous studies have examined the ability of ligand exchange to enhance or quench QD photoluminescence (PL).[2,62,97,134,152–155]

Core/shell nanostructures, in which a material with a larger bulk band gap encapsulates the core, are a highly effective way to create QDs with lower nonradiative

* Reprint with permission from Shen, Y.; Tan, R.; Gee, M. Y.; Greytak, A. B. *ACS Nano* **2015**, *9* (3), 3345–3359. http://pubs.acs.org/doi/abs/10.1021/acsnano.5b00671. Copyright 2015 American Chemical Society.

decay rates. As such a higher ensemble quantum yield (QY)[72] and higher on-time fractions among single dots can be achieved.[97,146] Indeed, it is possible to routinely achieve near-unity QY in the best-represented material systems such as CdSe/CdS.[62,156] One effect of a shell is to isolate the excited state from the surface by decreasing the wave function overlap with surface states. It is notable that even in samples with shells only a few monolayers thick, in which the excited states are clearly not isolated from the surface, a very high QY can be achieved (for example at the conclusion of QD synthesis).[62] This demonstrates that molecular surface termination can be achieved in which almost no intergap states or resonant excitations are present. As-synthesized colloidal QD samples typically or inherently contain large concentrations of molecules that could coordinate the surface.[157] However, applications almost universally require purification and/or surface modification of as-synthesized QDs. Purification methods have frequently been seen to decrease QY[7,62,97,158] and also to decrease ligand populations.[124,158,159] It is essential to understand whether the changes in QY are reversible, how ensemble QY and decay profiles depend on ligand occupation, and the conditions under which surface structures that support high QY can be maintained or restored.[160]

Photophysical studies involving the effect of ligands on QDs have recently been reviewed.[155] Previous reports have largely focused on intraband relaxation,[161–163] on molecules that act as quenchers,[154,164–167] on core-only QDs,[153,168–172] or have not been accompanied by the analytical tools to assess the extent of binding as an independent variable controlling decay rates.[173] Mulvaney's group has studied the effects of Lewis bases and other ligands on radiative recombination in CdSe core-only QDs.[153] Ginger's

group has studied PL quenching in CdSe-based core and core/shell QDs upon introduction of ligands,[154,164] while PL enhancement in QDs has been observed with thiol-bearing ligands[174,175] and amine-bearing ligands[152,164,176–178] that are not present in the synthetic mixture. However, until now the effect of putative ligands present in as-synthesized core/shell QDs that display high QYs has not been studied.

We recently described[158] the use of size-exclusion chromatography with a polystyrene stationary phase (gel permeation chromatography, GPC) to separate natively capped colloidal QDs from small molecules in organic solvents. This has the effect of removing impurities and weakly bound ligands, including phosphines, phosphine oxides, and primary amines, enabling the preparation of QDs with surfaces bearing a low and consistent number of metal carboxylate equivalents.

In the present study, we take advantage of GPC purification of core/shell QDs to explore the role of neutral ligands in maintaining high QY. In particular, we measured the ensemble QY and PL decay profile of oleate-capped core/shell QDs before and after GPC and then upon reintroduction of putative ligands that were present in the growth solution. Historically, PL decays of QDs recorded at low excitation densities have frequently displayed multi-exponential behavior, which has been interpreted as a consequence of a distribution of trapping rates inhabited by different QDs in the ensemble.[179–181] Through lifetime analysis, it may be possible to distinguish between different modes of QY reduction and regeneration in QDs with different densities of unoccupied ligand binding sites. For example, a given reduction in the ensemble QY could be brought about by a reduction in QY among all QDs in the sample, leading to a reduction in lifetime among all decay components. Another possible mechanism would be selective quenching of a

portion of the QDs, leading to an increase in the relative amplitudes of short-lifetime decay components. The former case might be expected if nonradiative recombination in purified QDs occurs via a large number of traps associated with vacant surface sites, while the latter case might be expected if ligand occupation modulates stochastic quenching processes such as those responsible for fluorescence intermittency in single QDs.[144,154,182]

In analyzing the response of QDs to the introduction of neutral ligands, it is essential to know whether changes in ligand concentration lead to irreversible structural changes in the QDs. Therefore, we have also studied the reversibility of the QY regeneration process. Additionally, it is valuable to be able to evaluate the actual extent of ligand coverage on the QD surface: in other words, what fraction of the added ligand is interacting with the QD surface at one time. Changes in the NMR line shape between bound and free ligands may not be resolvable in the case of rapidly exchanging ligands, and changes in the effective diffusion constant as measured by diffusion-ordered NMR spectroscopy (DOSY)[158,183] may be difficult to detect for low bound-ligand mole fractions. Here, we used isothermal titration calorimetry (ITC)[172,184–188] to differentiate the extent of ligand binding in QD samples exposed to phosphine, primary amine, and phosphine oxide ligands in an organic solvent.

3.2. Quantum yield decrease upon purification.

We chose four types of CdSe-based core/shell QD materials that we synthesized by a selective ionic layer adhesion and reaction (SILAR) method.[62,189] The effect of ligand occupation on QY in QDs with either pure CdS or CdZnS alloy shells and with different shell thicknesses was studied. **CdSe/CdS_1** and **CdSe/CdZnS_1** are the thin shell samples (1.6 monolayer equivalent shell thickness), and **CdSe/CdS_2** and

CdSe/CdZnS_2 represent thicker shells (4 monolayer equivalent shell thickness). The formation of the shell was monitored by withdrawing a small aliquot and diluting into toluene; the aliquots were characterized by UV-vis absorption spectroscopy (**Figure 3.1A**, B) and fluorescence emission spectroscopy (**Figure 3.1C, D**).

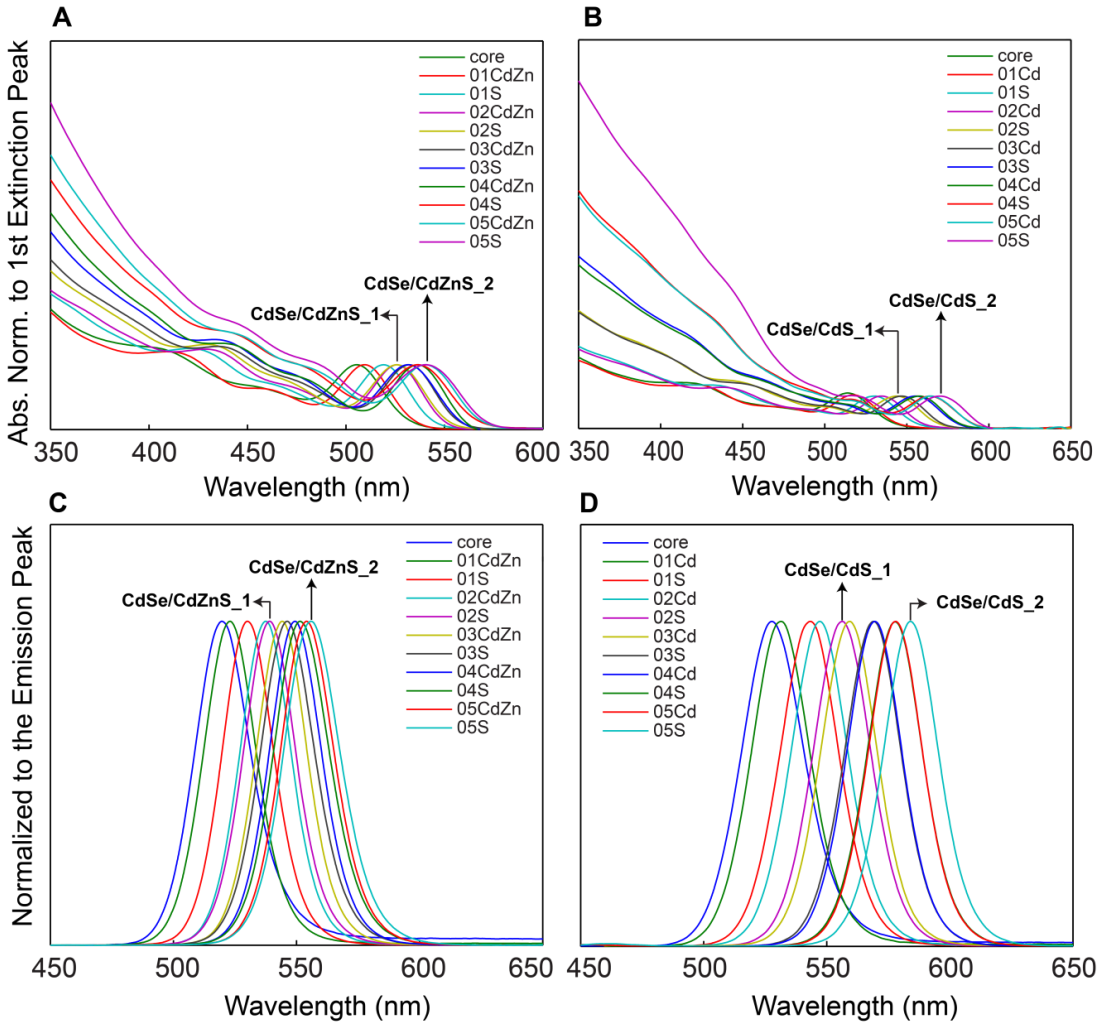

Figure 3.1 Absorption spectra and emission spectrum of aliquots taken during the CdZnS (left, A&C.) and CdS (right, B&D) overcoating processes. Aliquots were taken prior to the shell synthesis at reaction temperature and after each injection of the SILAR process (14 minutes after the start of the precursor addition). The spectra were normalized to the position of the lowest energy extinction peaks. The marks show the points where the desired thickness for thin shell (**CdSe/CdZnS_1** and **CdSe/CdS**_1) and thick shell (**CdSe/CdZnS_2** and **CdSe/CdS_2**) samples are achieved. Copyright 2015 American Chemical Society.

The QYs of these samples were recorded after isolation of the particles by one cycle of precipitation with acetone and redissolution in toluene. As shown in **Table 3.1** and **Figure 3.2**, the high QY indicates a complete formation of the shell onto the CdSe core materials.

Table 3.1 Characterizations of QD samples used before and after GPC purification.

QD samples	**CdSe/CdZnS_1**	**CdSe/CdZnS_2**	**CdSe/CdS_1**	**CdSe/CdS_2**
Core radius (nm) [a]	1.52	1.52	1.65	1.65
Shell thickness (ML) [b]	1.6	4	1.6	4
Absolute QY before GPC [c]	64%	88%	73%	81%
Relative QY drop after GPC	−84%	−23%	−70%	−28%
Olefin proton to QD ratio drop after GPC [d]	−93%	−94%	−93%	−95%
Removal of Phosphorus containing ligand after GPC?	Yes	Yes	Yes	Yes

[a] The core radius was estimated by a calibration curve describing the radius as a function of the position of the lowest-energy absorption peak.[119,120] [b] "ML" is the abbreviation of monolayer equivalents. [c] The QY of QD samples was measured relative to a rhodamine 590 standard (R590, QY= 99% in ethanol[190]). [d]The ratio was determined by quantitative ^{1}H NMR and UV-Vis as described previously.[158]

NMR has been demonstrated as a useful technique for the determination of the presence and interactions between ligands and nanocrystals, especially for ligands with a distinctive signal.[183] As a result, some of the best studied ligands on the QDs fall into two groups, namely, the phosphorus-containing group and the olefin-proton-containing group, which both can be distinguished easily in ^{31}P NMR or ^{1}H NMR spectra. The phosphorus-containing group includes trioctylphosphine (TOP) and trioctylphosphine oxide (TOPO),

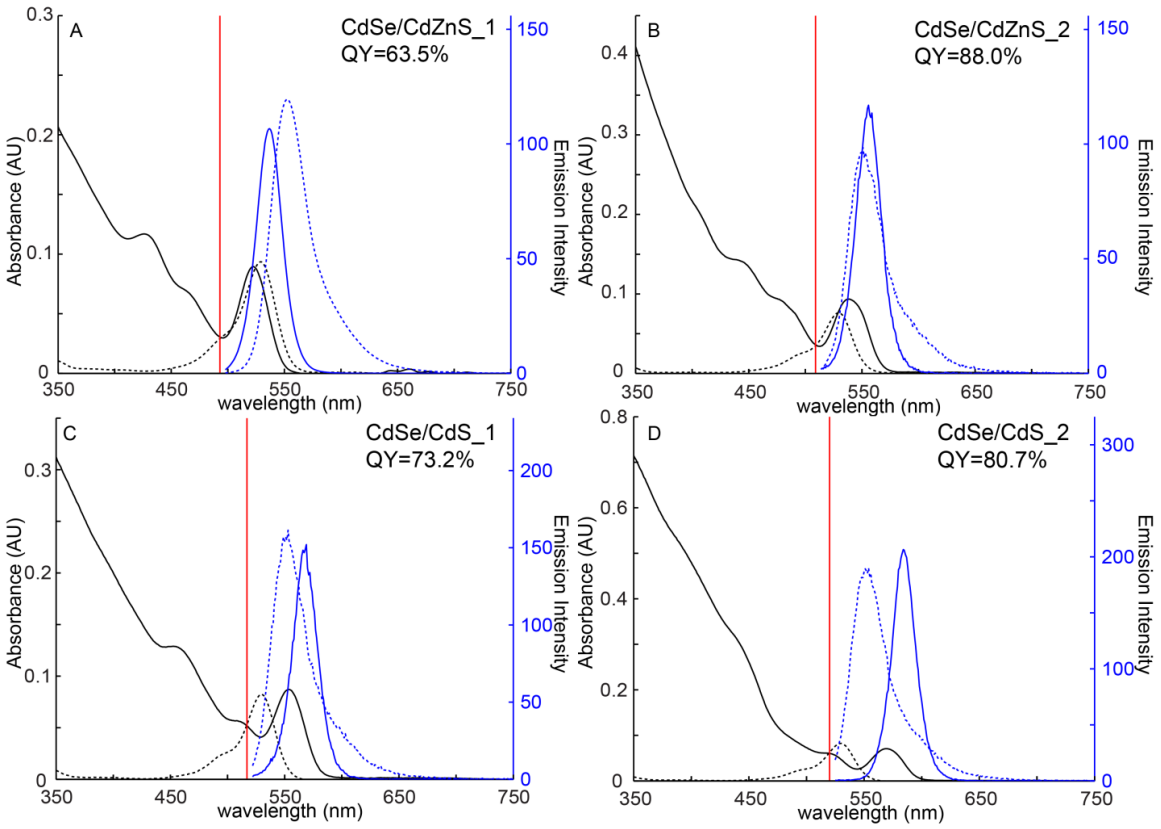

Figure 3.2 Quantum yield of **CdSe/CdZnS_1** (A), **CdSe/CdZnS_2** (B), **CdSe/CdS_1** (C) and **CdSe/CdS_2** (D) QD samples after 1 cycle of precipitation with acetone and redissolution in toluene. The excitation wavelengths used for each measurement are marked by the red line. Absorption spectra (black) and emission spectra (blue) of QDs are shown as solid lines, while dashed lines indicate rhodamine 590 in ethanol as the reference dye. Copyright 2015 American Chemical Society.

which are among the solvents used in core synthesis and shell growth, and tetradecylphosphonic acid (TDPA) and its cadmium salt (CdTDPA), which can be used as the Cd precursor during CdSe core preparation. The olefin-proton-containing species are frequently introduced in the shell growth process: for example, cadmium oleate (CdOA) and oleic acid (OA) as the Cd precursor, and oleylamine (OAm) and octadecene (ODE) as solvents.[64] Here, we used ^{31}P NMR and quantitative ^{1}H NMR to characterize

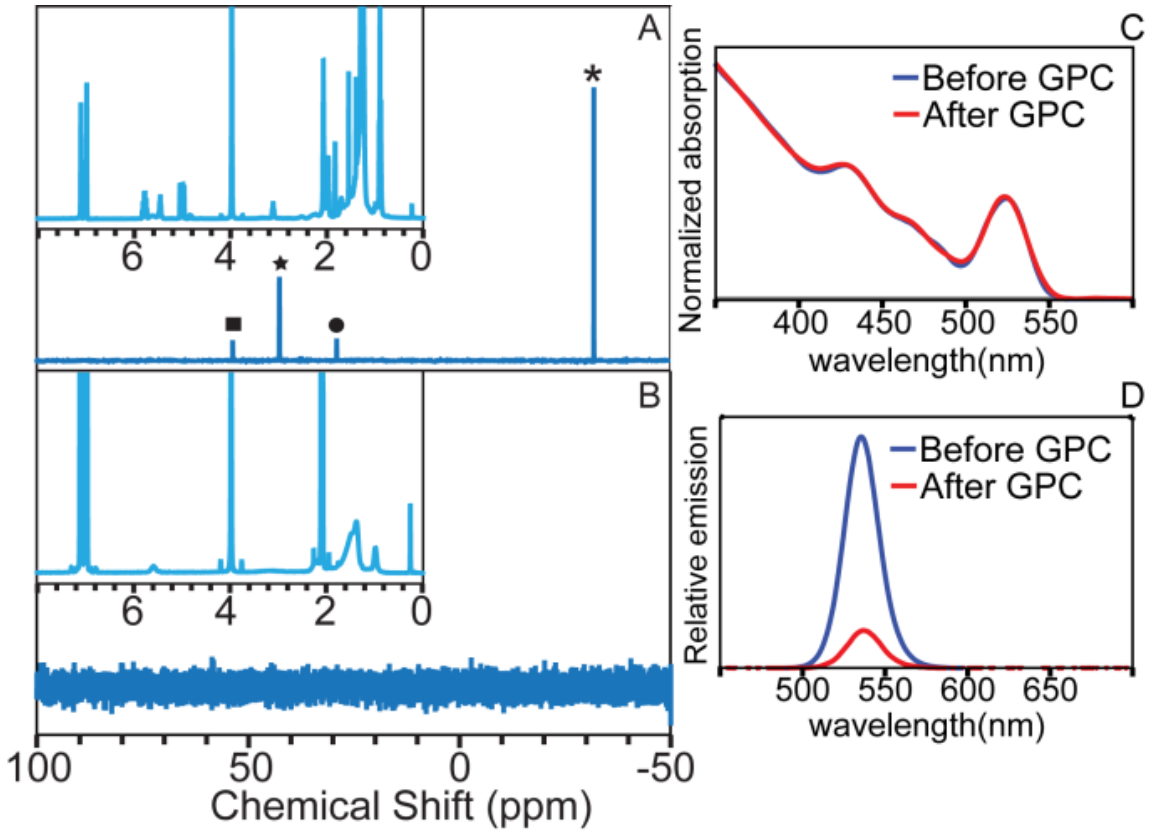

Figure 3.3 Characterization of **CdSe/CdZnS_1** sample before and after the GPC purification. The ^{31}P NMR spectra of the sample before the GPC purification (A) and after the GPC purification (B) with the ^{1}H NMR shown in the insets. The marks in (A) indicate the peaks associated with the phosphorus-containing molecules that are removed during the purification. (C) Absorption spectra of the sample (normalized to 365 nm) before and after the purification. (D) Relative emission spectra of the sample (normalized to the absorption of the excitation wavelength, 365 nm) before and after the purification. Copyright 2015 American Chemical Society.

the QD samples before and after the purification by GPC, which has been shown as a highly efficient and reproducible way to purify QDs[158] and oxide nanocrystals.[191] **Figure 3.3.** shows the NMR spectra of **CdSe/CdZnS_1** before (**Figure 3.3A**) and after (**Figure 3.3B**) the GPC purification in toluene. In **Figure 3.3A**, four sharp signals representing free TOPO (53.48 ppm), TDPA (42.34 ppm), dialkylpyrophosphonate (28.74 ppm), and TOP (–32.34 ppm) can be identified in the ^{31}P NMR spectra.[131,132,189] A

large amount of olefin-containing species (4.8-5.8 ppm, ~3950 olefin protons per QD) are represented in the ^{1}H NMR.[158] However, after the GPC purification, all the phosphorus-containing ligands have been removed completely and the total amount of olefin proton has significantly decreased (**Figure 3.3B**). The rounded shape peak in the olefin region indicates that the only remaining olefin ligands are strongly interacting with the QD surface; we attribute this to an ionic (X-type) binding mode of residual oleate.[131] **Figure 3.4** shows the other three QD samples show similar NMR responses to purification, and all the results have been summarized in **Table 3.1**.

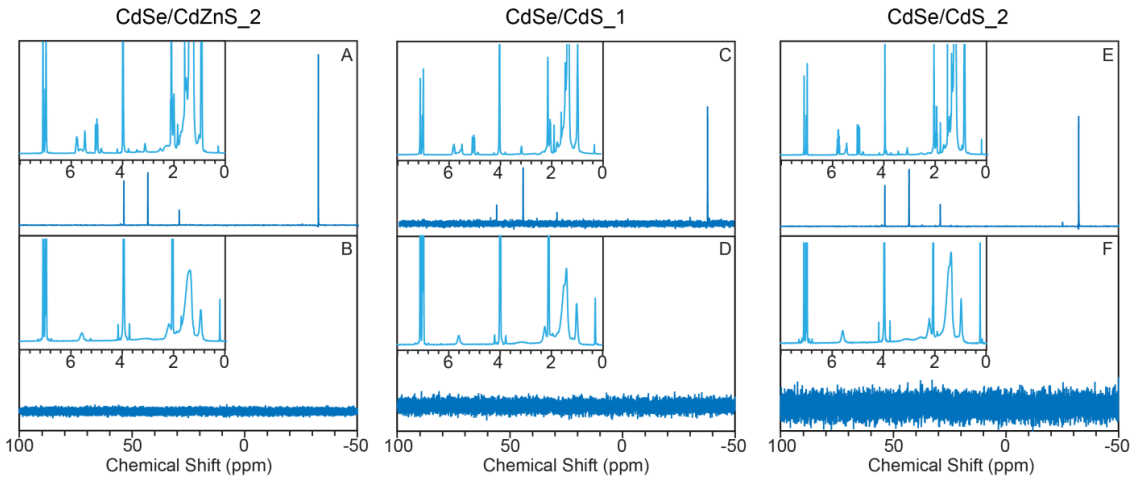

Figure 3.4 ^{31}P NMR spectra of samples before the GPC purification (A, C, E) and after the GPC purification (B, D, F) with the ^{1}H NMR shown in the insets for **CdSe/CdZn S_2** (A, B), **CdSe/CdS_1** (C, D) and **CdSe/CdS_2** (E, F). Copyright 2015 American Chemical Society.

Concurrent with the removal of the neutral ligands, the emission intensities of the particles all decrease upon GPC purification. The relative QY of **CdSe/CdZnS_1** decreased by 84% after GPC with no shift in the absorption and emission spectra, which implies that the decrease of brightness is not associated with etching/aggregation (**Figure 3.3C,D**).

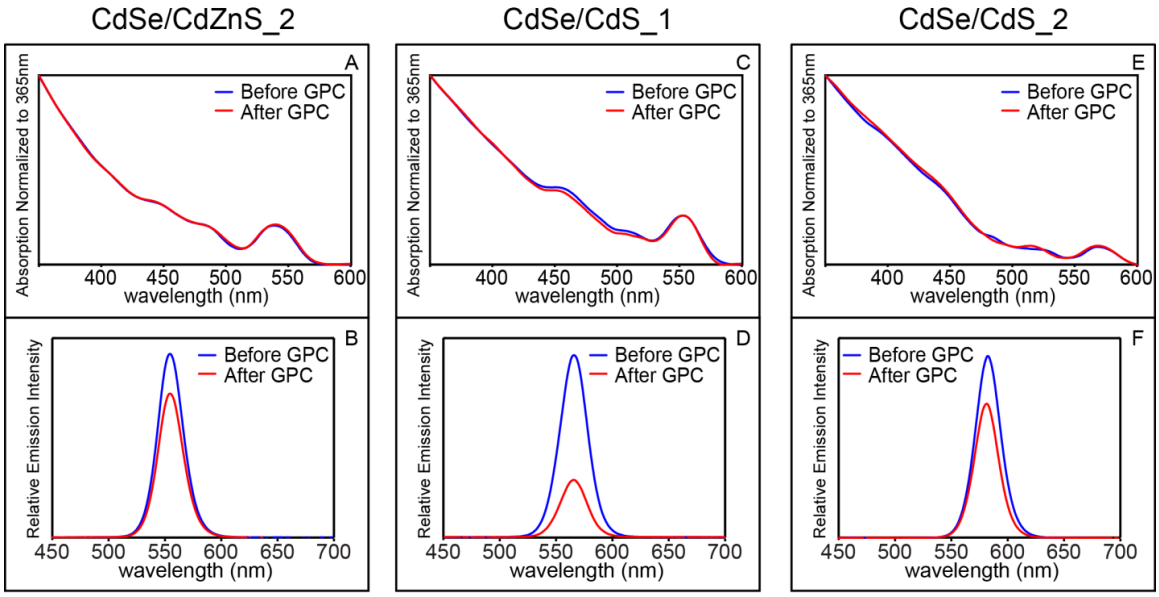

Figure 3.5 Absorption spectra of the samples (normalized to 365 nm) before and after the purification for **CdSe/CdZnS_2** (A), **CdSe/CdS_1** (C) and **CdSe/CdS_2** (E). Relative emission spectra of the samples (normalized to the absorption of the excitation wavelength, 365 nm) before and after the purification for **CdSe/CdZnS_2** (B), **CdSe/CdS_1** (D) and **CdSe/CdS_2** (F). Copyright 2015 American Chemical Society.

As discussed below, we attribute the QY decrease to an increase in nonradiative decay associated with the removal of weakly associating ligands. Similar results can also be observed in the other three samples (**Figure 3.5** and **Table 3.1**). Among the four samples, **CdSe/CdZnS_1** (84%) and **CdSe/CdS_1** (70%) samples show the higher emission intensity drop than **CdSe/CdZnS_2** (23%) and **CdSe/CdS_2** (28%) samples, which can be explained by better isolation of the excitons from the surface traps with a thicker shell. Importantly, these changes are brought about in the absence of any change in solvent or precipitation of the QDs or introduction of protic or nucleophilic species that are known to displace ligands from QD surfaces.[124,159,170] These well-characterized and isolated QDs therefore provide a good model system to study whether the above process is reversible and which ligands are responsible for the initial high QY.

3.3. QY regeneration by introduction of neutral ligands.

After the purification, the QDs were immediately transferred into a nitrogen-filled glovebox to suppress oxidation. According to the NMR spectra recorded before and after the GPC process, the ligands that were removed by GPC include OA, CdOA, OAm, and ODE from the olefin-proton-containing group and TOP, TOPO, TDPA, and CdTDPA from the phosphorus-containing group. We sought to determine whether reintroduction of these species to the system could restore the QY. In order to avoid possible ligand exchange reactions, we chose not to include TDPA and CdTDPA among the neutral binders studied in this work since phosphonic acid is known to displace oleate from the surface of CdSe QDs.[192] Therefore, we have introduced the first six ligands individually, as well as a mixture of TOP and CdOA, back to QD solution with two different ligand-to-QD ratios (300:1 and 3000:1). The lower number is intended to be roughly comparable to the total number of surface sites per QD, while the larger number represents an excess.[157,164,172]

After mixing the ligands and the purified QDs for a certain period of time (1 day and 7 days), the QY of each of the samples was measured and recorded. The relative QY among QDs with similar absorption spectra, emission spectra, and solvent can be measured with high precision, and therefore we reported this value. In particular, we measured the QY changes during the observation period by comparing to an as-synthesized QD solution reference. As shown in **Figure 3.6** (left column), the emission intensities of most of the GPC-purified QD solutions decreased upon storage in the glovebox for the longer period of time, though for sample **CdSe/CdZnS_2**, the QY increased slightly after 1 day of storage. The changes observed in purified samples during storage in dilute solution in the absence of ligand addition could be due to slow re-

equilibration of the surface-bound and/or free metal oleate, and these samples serve as a control for the response to ligand addition.

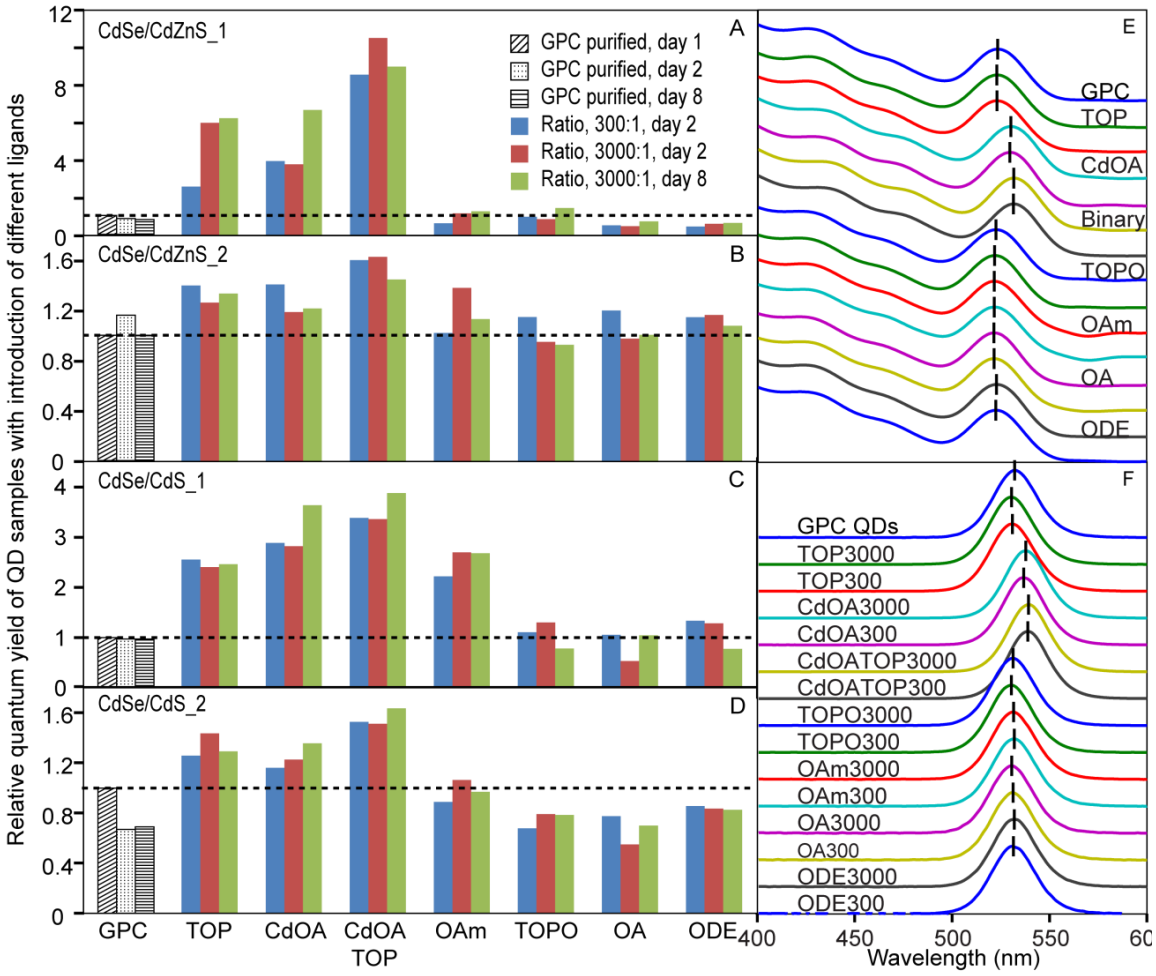

Figure 3.6 QY regeneration results with introduction of different ligands. (A-D) The relative QY of GPC-purified stock solution and ligand mixing solutions for **CdSe/CdZnS_1** (A), **CdSe/CdZnS_2** (B), **CdSe/CdS_1** (C), and **CdSe/CdS_2** (D). All of the results are normalized to the QY of the freshly GPC-purified samples shown with the dashed line. (E) Absorption spectra of the GPC purified **CdSe/CdZnS_1** QDs mixing with different ligands on day 2. Here, the CdOA and TOP mixture is described as binary in short. The labeled curves have a 3000:1 ligand-to-QD ratio, while the curves below have a ratio of 300:1. (F) Emission spectra during the regeneration process for **CdSe/CdZnS_1**. The label is a combination of the ligand type and ligand-to-QD ratio. The samples are the same as the absorption measurements in (E). Both absorption and emission spectra are normalized to the lowest energy extinction peaks. Copyright 2015 American Chemical Society.

We found that reintroduction of selected ligands resulted in a significant increase, or "regeneration", of QY in all samples tested. When we compare the response to introduction of the putative ligands, the QY is enhanced when TOP and CdOA are introduced in all four samples. The combination of TOP and CdOA always shows the greatest amount of QY regeneration, which indicates that these two ligands are increasing the QY in a complementary manner. OAm can regenerate the QY in CdSe/CdS samples (especially **CdSe/ CdS_1**), but the QY did not significantly increase with the presence of OA, ODE, or TOPO. For example, as shown in **Figure 3.6A**, compared to the freshly GPC purified **CdSe/CdZnS_1** sample, the QY increased 6-fold when the higher amount of TOP is introduced and remained at a level close to the initial QY before GPC purification for the 7-day measurement period. The binary ligand system shows the highest amount of QY regeneration, up to ~12 times the GPC-purified control at the same time point for **CdSe/CdZnS_1** (the QY of the GPC stock solution decreased 16% after 1 day of storage). The QY regeneration of the thin-shell QDs is much higher than that of the thick-shell samples, which mirrors the observation of a smaller decrease in QY after the GPC purification. We did not observe a large difference in response at the two different ligand to QD ratios, which indicates that the surface has been completely saturated at the lower concentration of neutral ligands.[153] All the ligands behave similarly for CdZnS and CdS shells except when OAm is introduced. When OAm is introduced to CdSe/CdZnS QDs, the QY does not increase; however, the QY does increase significantly when OAm is added to CdSe/CdS QDs. For **CdSe/CdS_1**, the response to OAm is close to that of TOP. One interpretation of the role of "L-type" ligands in maintaining QY is that ligand orbitals mix with interfacial localized states to move them

outside of the band gap.[155,193,194] In this interpretation, band-edge quantum-confined states are minimally affected. CdZnS has a larger bulk band gap than pure CdS, and so the interaction between OAm and the surface trap states is not strong enough to move the states outside of this larger shell band gap. The influence of relative binding strength on QY will be further addressed below.

Figure 3.6E and **F** show the absorption and emission spectra of GPC-purified **CdSe/CdZnS_1** QDs after mixing with different ligands as described above. An important goal of our study is to detect differences in structure and composition between initially prepared and purified QD samples that could be responsible for QY changes. Consequently it is important to check whether the initial absorption and emission spectra, which did not change significantly on purification, are maintained upon reintroduction of putative ligands. Both absorption and emission spectra remain constant with the introduction of the L-type ligands we investigated; however, in the case of CdOA, which behaves as an electrophilic "Z-type" ligand,[170] a significant red shift is observed. We observed similar results for pure CdS shell samples (**Figure 3.7A.B**). This indicates that the decreases in QY of the QDs after purification, which occurred without red or blue shift, are more directly related to the removal of the L-type ligands (TOP or OAm) than CdOA even though a higher coverage of Cd has also been shown to increase the brightness of CdSe and CdSe/CdS samples in published reports.[115,170] The red shift can also be observed when introducing CdOA to the QDs sample before the GPC purification, which confirms that the red-shift response is not a consequence of the GPC purification **(Figure 3.7C**).

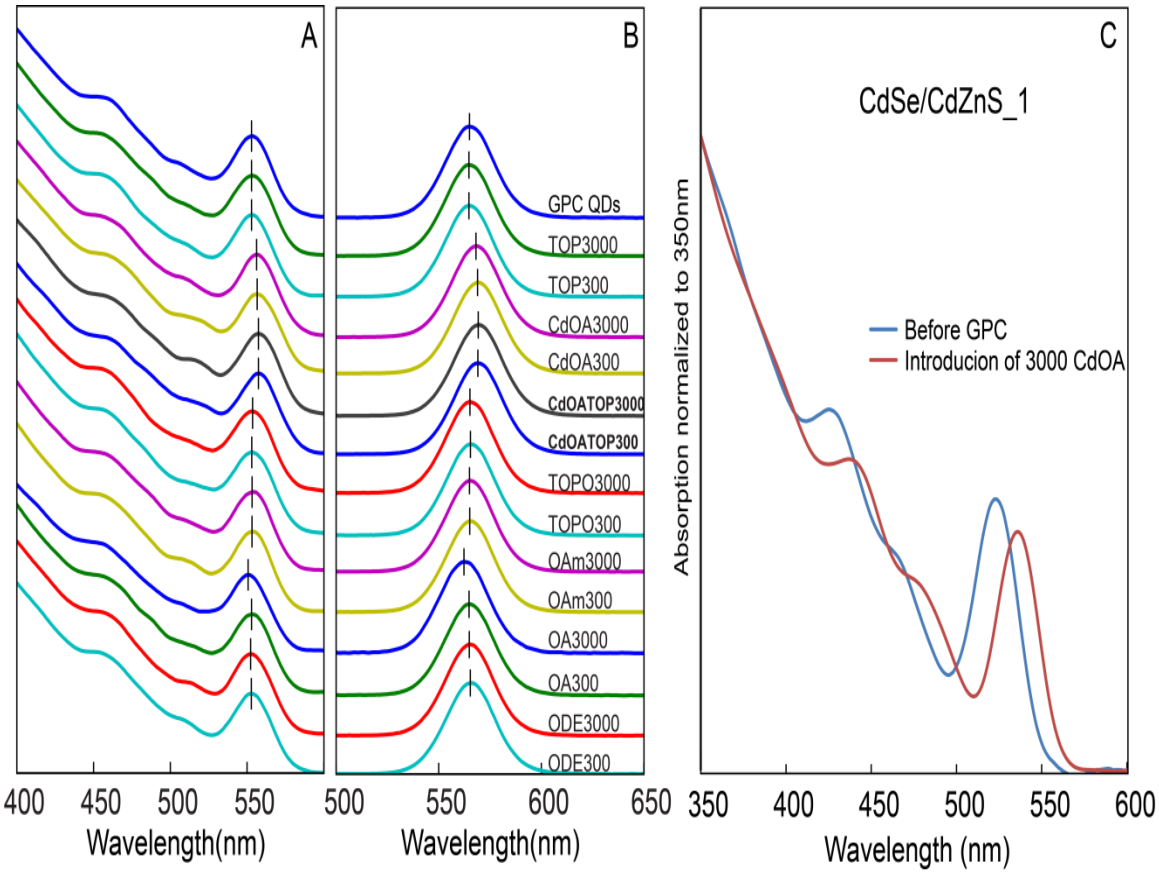

Figure 3.7 Absorption spectra (A) and emission spectra (B) of the GPC purified **CdSe/CdS_1** QDs after mixing with different ligands for 1 day. Both absorption and emission spectra are normalized at the position of the lowest energy peaks. (C) Absorption spectra of 1 × precipitated **CdSe/CdZnS_1** sample (no GPC purification) with and without the introduction of 3000 equivalents of CdOA in toluene. Copyright 2015 American Chemical Society.

3.4. Lifetime analysis by time-resolved fluorescence spectroscopy.

To gain additional insight on possible mechanisms for quenching and restoration of QY as a function of ligand concentration, we measured the PL decays of stirred QD samples in anhydrous toluene under 368 nm pulsed excitation, which is similar to the excitation wavelength we used for the relative QY measurements (365 nm). Since thin-shell QD samples display a larger response to the introduction of the ligands, we will

focus on **CdSe/CdZnS_1** and **CdSe/ CdS_1** samples in this discussion, results shown in **Figure 3.8**; the thick-shell QD samples **CdSe/CdZnS_2** and **CdSe/CdS_2** behaved similarly and shown in **Figure 3.9**. Data collected over 200 ns revealed multiple lifetime components (**Figure 3.8A,B** insets), including a long-lived tail with an apparent lifetime of > 50 ns. Previous reports of PL decays on QD samples with near-unity absolute QY[62,156,195] and reported decays of single QDs in the "on" state[147] support a radiative recombination lifetime $k_r^{-1} \approx$ 20-30 ns for CdSe-based QDs similar to those described here. Accordingly lifetime components are likely a result of trapping/detrapping processes.[148,181] In order to focus on the principal reasons for changes in ensemble QY, we chose to focus on the first 50 ns, which contain $> 90\%$ of the light emitted (**Figure 3.8A,B**). The lifetime curves of the samples mixed with TOPO, OAm, and TOP will be compared with the samples before and after the GPC purification. Since the introduction of CdOA results in a change in the band-edge electronic structure of the sample based on the absorption spectrum, the radiative recombination rate is not expected to be the same as in the other samples. Therefore, the lifetime result of CdOA cannot be directly compared to the above three ligands (see **Figure 3.10A,B**). Introduction of the ODE control resulted in only small changes in the decay traces (**Figure 3.10C**).

In general, the trend of the lifetime results is similar to the observation of the QY changes, where the samples with higher QYs have longer average lifetimes. The decays shown in **Figure 3.8A,B** show a relatively constant slope of the logarithm of intensity with respect to time in a window of ~20-50 ns, and this slope was similar among samples with different ensemble QYs. However, samples with lower QYs displayed significantly greater intensity loss within the first 10 ns. This trend is more clearly apparent when the

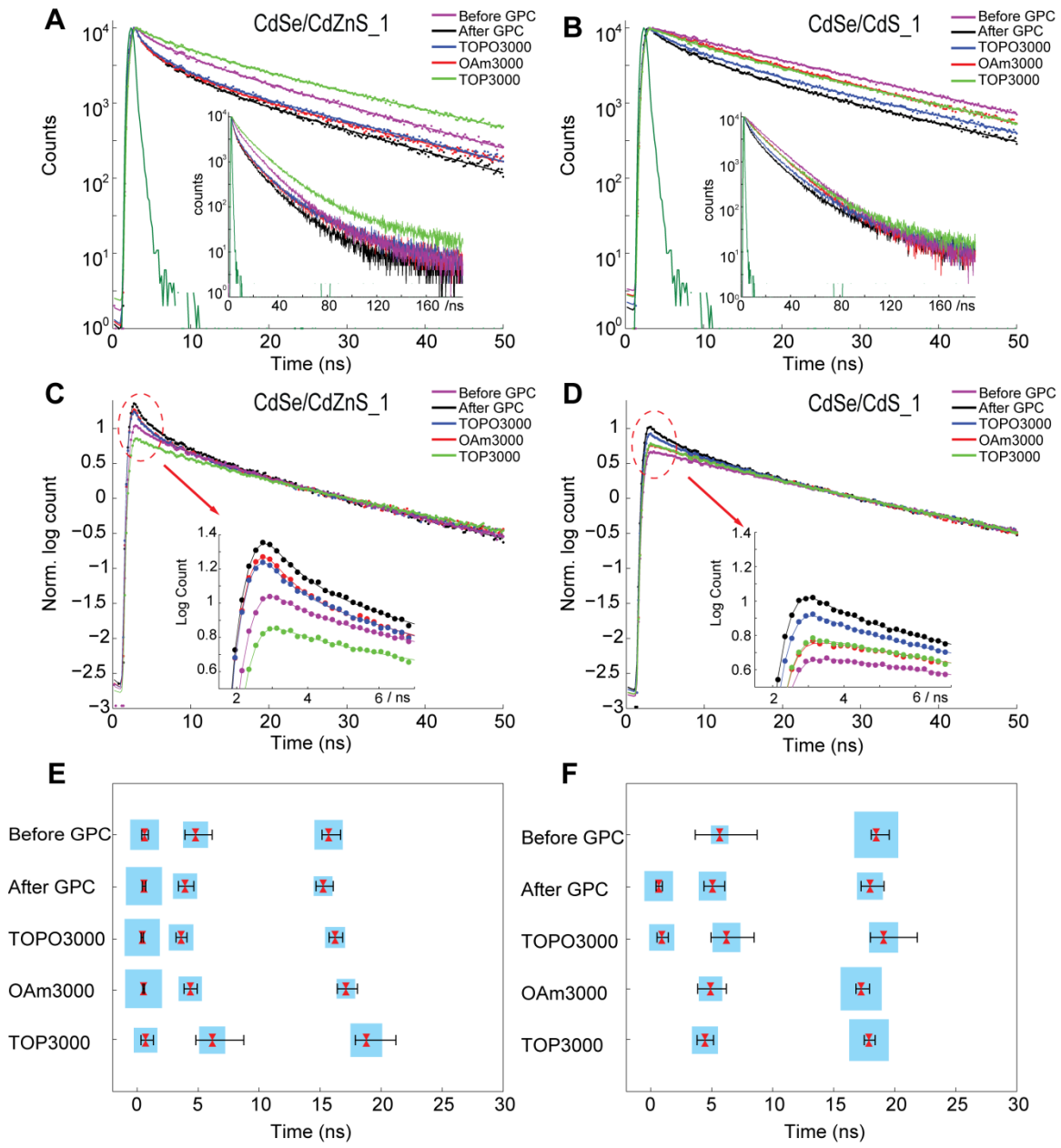

Figure 3.8 Comparison of fluorescence lifetime decays for **CdSe/CdZnS_1** (A) and **CdSe/CdS_1** (B) core/shell QDs before/after GPC purification and subsequently mixed with different ligands, focused on the first 50 ns. Data collected over 200 ns are shown in the insets. (C, D) Corresponding lifetime decays normalized at 30 ns; insets show detail. Lines are reconvolution fits. (E, F) Charts displaying lifetime values and corresponding amplitudes for reconvolution fits of PL decay traces for **CdSe/CdZnS_1** (E) and **CdSe/CdS_1** (F). The weighted amplitudes are represented by the areas of the blue squares, while the lifetime values are indicated by red marks at the center of each square. Error bars indicate the uncertainty of each lifetime component as obtained by support plane analysis with a confidence limit of 90%. (see **Table 3.2** for details) Copyright 2015 American Chemical Society.

decay traces are normalized at 30 ns to emphasize differences in decay rate at earlier times (**Figure 3.8C, D** and insets therein). After GPC purification, QY regeneration (as observed upon introduction of TOP in both samples and OAm in **CdSe/CdS_1**) is accompanied by reduction, but not complete elimination, of the accelerated decay at early times.

Analysis of rate dispersion in ensemble QD samples and time evolution of decay rates in single-QD photon counting experiments have supported an interpretation of rate dispersion as being primarily or entirely inhomogeneous in QD samples, the result of subpopulations with varying decay rates.[147,180] Subpopulations with lower QYs are expected to display shorter lifetimes because of elevated nonradiative decay rates. In this case, it may be possible to constrain models of nonradiative decay by decomposing the observed decays into several lifetime components. We employed a reconvolution fit with multiple decay lifetimes to analyze the decays within the first 50 ns. Uncertainty in the lifetime values was examined with support plane analysis[196] (a detailed description of the analysis is available in **the method and materials section**, Page 104). With this analysis, the longest lifetime approximates the decay seen in the ~15-25 ns window, while the shorter lifetimes describe the rapid decay seen at early times. By analyzing the rates and amplitudes of the lifetime components, we sought to distinguish whether quenching in GPC-purified samples and regeneration in ligand-introduced samples are associated chiefly with changes in lifetime among all lifetime components or with changes in the relative population fraction of QDs with different decay rates, as assessed from the amplitudes of the short and long lifetime components of the fit.

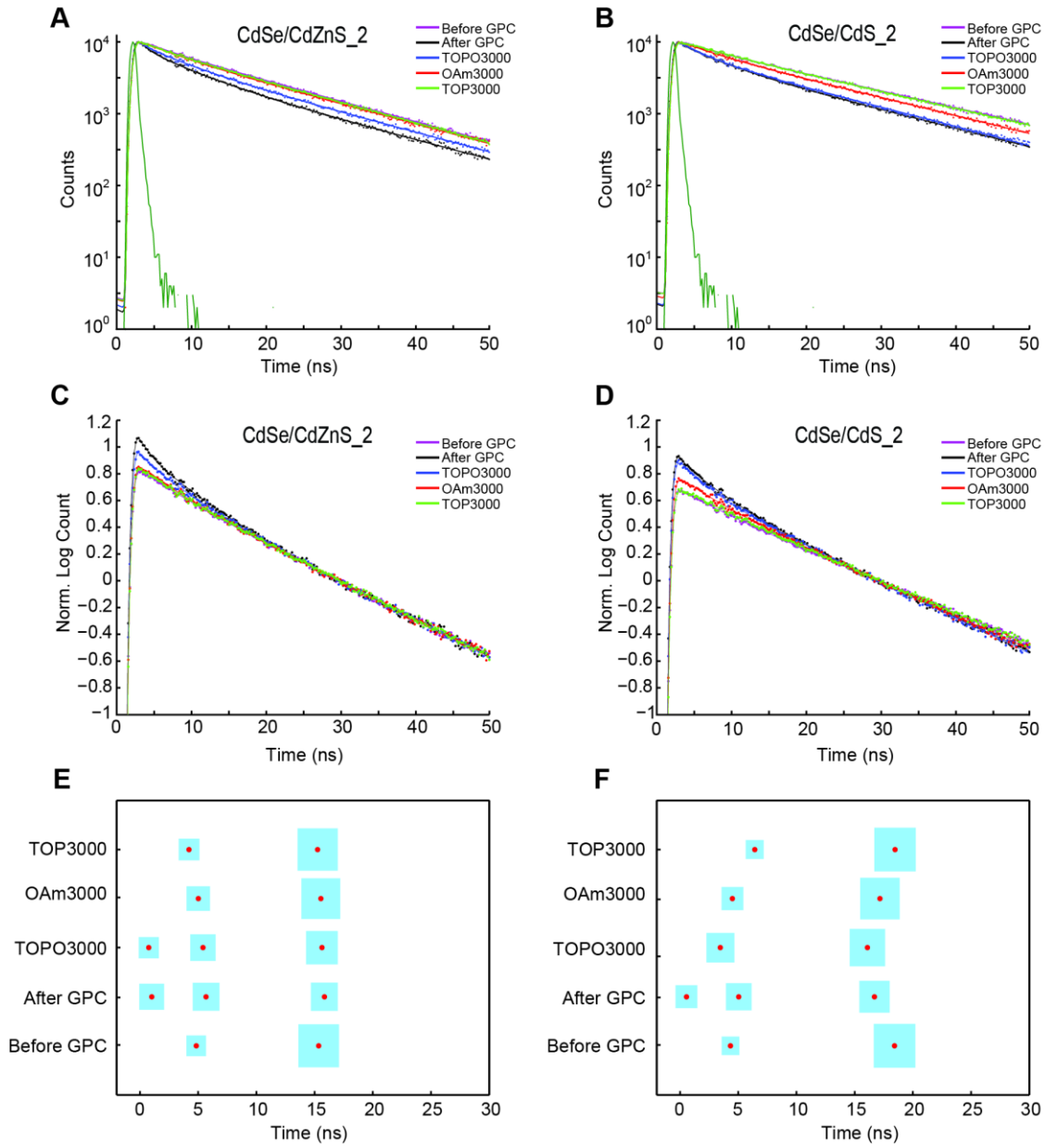

Figure 3.9 Comparison of fluorescence lifetime decays for **CdSe/CdZnS_2** (A) and **CdSe/CdS_2** (B) core/shell QDs before/after GPC and further mixed with different ligands (TOP, OAm and TOPO), focused on the first 50ns. (C, D) Corresponding lifetime decays normalized at 30 ns, emphasizing changes of the fast decay component with different ligands. (E,F) Re-convolution fits of the corresponding decays for **CdSe/CdZnS_2** (E) and **CdSe/CdS_2** (F) indicate the number of the exponential components as well as the weighted amplitude (area of blue squares) and lifetime value of each component (red dot at the center of each square). (see **Table 3.3** for detailed lifetime values and exponential amplitudes) Copyright 2015 American Chemical Society.

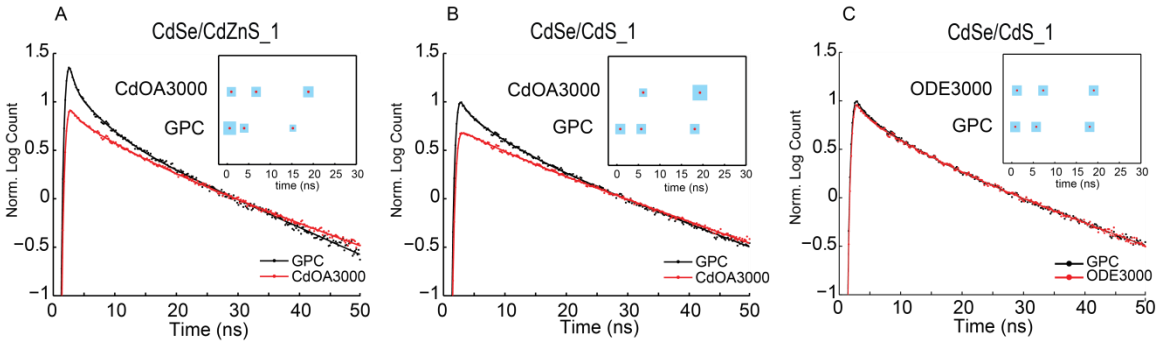

Figure 3.10 Fluorescence lifetime decays for **CdSe/CdZnS_1** (A) and **CdSe/CdS_1** (B) core/shell QDs after GPC and further mixed with CdOA. The lifetime decay curves are normalized at 30 ns. (C) Lifetime decays for **CdSe/CdS_1** after GPC and further mixed with ODE. The lifetime decay curves are normalized at 30 ns. Re-convolution fits of the corresponding decays are showed in the insets, where the weighted amplitude is proportional to the area of blue squares and lifetime value of each component is displayed as the red dot at the center of each square. Copyright 2015 American Chemical Society.

In the case of thin alloy shells (**Figure 3.8E**), we found that a three-component lifetime fit was statistically supported by the data, while the bright QD samples with pure CdS shell (**CdSe/CdS_1** before GPC, with TOP3000 and with OAm3000) required only two components (**Figure 3.8F**). We found that the change in QY between the samples before and after GPC, and between GPC and QY regenerated samples, is accompanied by a change in the amplitude of the lifetime components, with little change in the lifetime value. For example, the amplitude average lifetime of **CdSe/CdZnS_1** after the GPC purification is 3.77 ns; after mixing with TOP, the lifetime increases to 10.49 ns (we report amplitude average lifetimes because they are nominally proportional to the steady-state fluorescence intensity[197]). The values of the component lifetimes change no more than 30%, but the amplitude ratio between the shortest and longest lifetime components increases by a factor of 6.7. Similar results can be observed in comparing GPC-purified QDs to the initial samples prior to GPC (see **Table 3.2** and **Table 3.3** for detailed lifetime values and exponential amplitudes). Thus, the reduction in QY upon removal of L-type

ligands appears to be driven primarily by a large increase in decay rate among a subset of the QDs.

Table 3.2 Detailed lifetime values and relative population of the reconvolution fits on the PL decay curves shown in **Figure 3.8E** and **3.8F**.

QD sample	Ligands	Tau1[a]	wt.A1[b]	Tau2[a]	wt.A2[b]	Tau3[a]	wt.A3[b]	Tau_avg[a]
CdSe/CdZnS_1	1ppt	0.61	36.92%	4.79	27.63%	15.70	35.45%	7.11
	GPC	0.57	58.22%	3.93	25.94%	15.25	15.84%	3.77
	TOPO	0.43	55.12%	3.61	27.16%	16.22	17.72%	4.09
	OAm	0.54	60.49%	4.37	24.18%	17.11	15.33%	4.01
	TOP	0.70	24.90%	6.16	30.04%	18.78	45.07%	10.49
CdSe/CdS_1	1ppt	---	---	5.65	13.59%	18.48	86.41%	16.74
	GPC	0.66	36.34%	5.06	33.92%	17.97	29.75%	7.30
	TOPO	0.91	28.07%	6.21	34.53%	19.08	37.40%	9.54
	OAm	---	---	4.91	24.19%	17.24	75.81%	14.26
	TOP	---	---	4.45	30.32%	17.89	69.69%	13.81

[a] Tau is the lifetime component τ shown in the previous lifetime analysis method discussion. The unit for each lifetime component is ns.[b] wt.A is the weighted amplitude. $Wt.A_i=(A_i/\sum A)\times 100\%$

We can use the PL decay profiles to consider possible models for quenching in QDs with vacant L-type ligand sites. One model is to consider each vacant site to contribute a similar nonradiative decay rate, in an additive manner.[155,164] In this case, the distribution of decay rates in the purified samples will reflect the distribution in the number of vacant sites per QD. But because each QD presumably contains numerous binding sites for L-type ligands[164,172] and nearly all are vacant following GPC purification,

Table 3.3 Detailed lifetime values and relative population of the reconvolution fits on the PL decay curves shown in **Figure 3.9E** and **3.9F**.

QD sample	Ligands	Tau1[a]	wt.A1[b]	Tau2[a]	wt.A2[b]	Tau3[a]	wt.A3[b]	Tau_avg[a]
CdSe/CdZnS_2	1ppt	---	---	4.84	18.84%	15.36	81.16%	13.37
	GPC	1.01	30.08%	5.68	34.57%	15.84	35.34%	7.87
	TOPO	0.76	19.84%	5.41	31.40%	15.63	48.77%	9.47
	OAm	---	---	5.01	26.70%	15.54	73.30%	12.73
	TOP	---	---	4.22	20.64%	15.27	79.36%	12.99
CdSe/CdS_2	1ppt	---	---	4.34	15.17%	18.42	84.83%	16.28
	GPC	0.55	23.06%	5.04	32.20%	16.70	44.74%	9.22
	TOPO	---	---	3.46	38.43%	16.09	61.57%	11.24
	OAm	---	---	4.50	23.35%	17.17	76.65%	14.21
	TOP	---	---	6.42	15.60%	18.47	84.40%	16.59

[a] Tau is the lifetime component τ shown in the previous lifetime analysis method discussion. The unit for each lifetime component is ns.[b] wt.A is the weighted amplitude. $Wt.A_i=(A_i/\sum A)\times 100\%$

it would seem improbable that a significant fraction of the purified QDs would have zero vacant sites and thus remain unquenched. We therefore rule this model out. A second model considers a stochastic quenching process, such as the formation of charged QDs leading to Auger recombination,[144] whose probability is tuned by ligand coverage. In this model, ligand coverage does not significantly affect the component lifetimes, but rather tunes the population fraction that is in a bright or quenched configuration at a given time,

in a manner analogous to the fluorescence intermittency seen in single-particle studies.[100] A third possibility is that the most significant changes in QY arise from vacancies at a subset of L-type ligand binding sites that occur rarely enough that some QDs in the ensemble lack such sites and do not experience quenching at low ligand concentration. Measurements that link structure and QY among individual QDs[198] may be of value in distinguishing among these models. Spectroscopic techniques such as transient absorption, upconversion PL decay measurements that can more precisely resolve rapid decay processes, and multiple-pulse experiments have been applied to the analysis of QD radiative and nonradiative decay.[155,179,180,199,200] It is clear from the results presented here that the ensemble QY, average decay rate, and rate dispersion of QDs change in response to ligand concentration. Thus, spectroscopic analyses must ideally be performed on samples with well-specified ligand populations and concentrations if the results of such studies are to be compared or applied to new systems.

3.5. Time evolution of QY regenerated samples.

While the results in **Figure 3.6** show that QY regeneration upon introduction of excess ligands can be maintained over a period of at least a week, we sought to study the time evolution of QY and PL decay profiles in greater detail. We focused on the thin-shell QD samples with introduction of 3000 equiv. of TOP, a treatment that improved the ensemble QY in all cases. As shown in **Figure 3.11A** and **B**, the brightness of the QD samples can be fully regenerated to the level prior to GPC purification after mixing with TOP for 1 h, which suggests that the high QY of the sample before the purification is due to the presence of neutral ligands such as TOP. On the basis of the time evolution of the relative QY, the alloy shell sample requires a longer period of time to reach equilibrium; in this

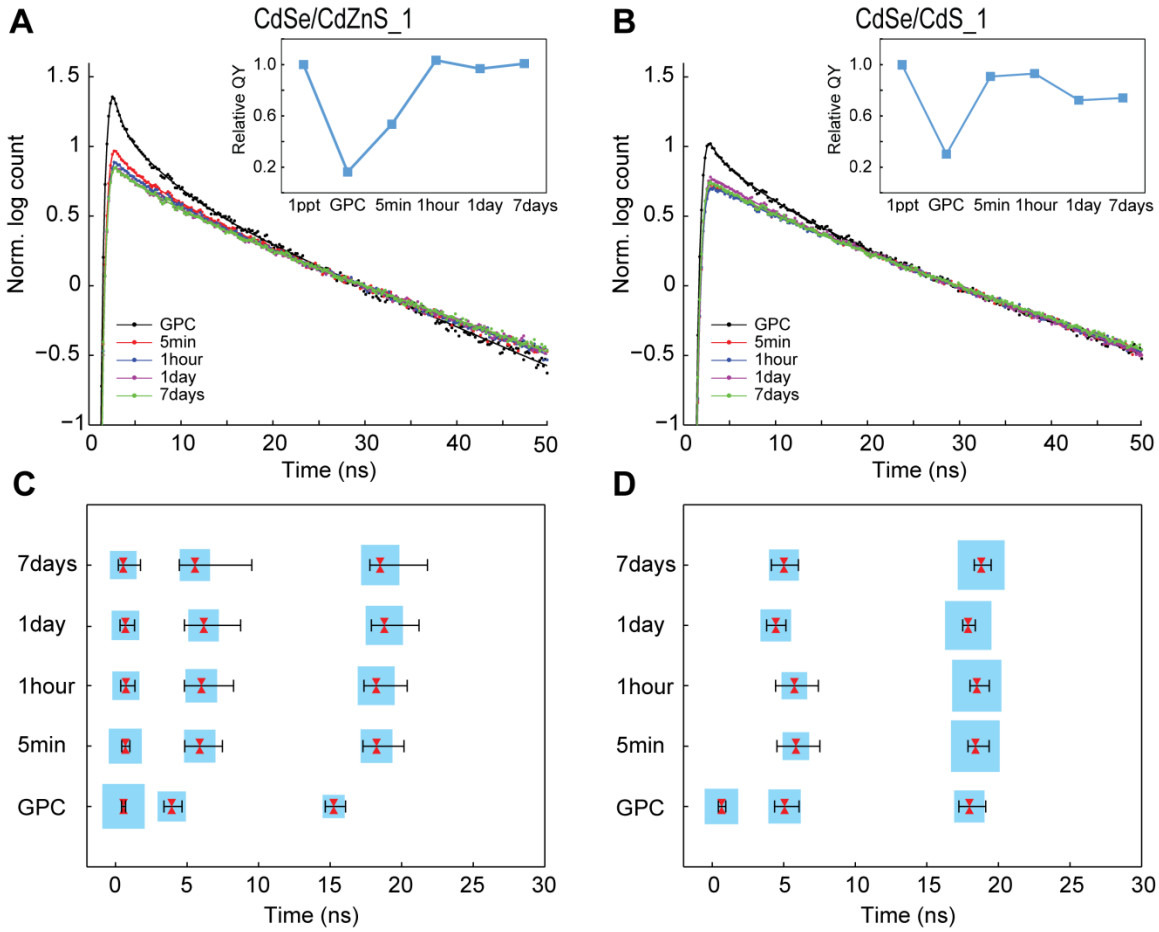

Figure 3.11. Fluorescence lifetime decays for **CdSe/CdZnS_1** (A) and **CdSe/CdS_1** (B) core/shell QDs after GPC purification, and then mixed with TOP at various time after introduction of TOP, normalized at 30 ns. Changes of relative QY are shown as insets. Here, the sample before GPC purification is described as "1ppt" in short. (C, D) A re-convolution fit of the corresponding decays gave the weighted amplitudes (area of blue squares) and lifetimes of each component (red marks at the center of each square) for **CdSe/CdZnS_1** (C) and **CdSe/CdS_1** (D) mixed with TOP over time. The uncertainties in each lifetime component was obtained by support plane analysis with confidence limit of 90%. Copyright 2015 American Chemical Society.

case the sample at 5 min is only halfway through its full regeneration, whereas at 5 min the pure CdS shell sample is close to its maximum brightness. The high QY in the TOP-introduced **CdSe/CdZnS_1** sample can be maintained for 7 days, but there is a decrease in QY with the TOP-introduced **CdSe/CdS_1** sample after 1 day. As shown in

Figure 3.11C and **D**, the lifetimes of each component for the TOP introduced samples are fairly similar at different waiting times (see **Table 3.4** for fit parameters). These results are consistent with changes in the relative population fraction of QDs with different decay rates driving QY regeneration in the GPC-purified samples.

Table 3.4 Detailed lifetime values and relative population of the reconvolution fits on the PL decay curves shown in **Figure 3.11C** and **3.11D**.

QD sample	Time	Tau1[a]	wt.A1[b]	Tau2[a]	wt.A2[b]	Tau3[a]	wt.A3[b]	Tau_avg[a]
CdSe/CdZnS_1	GPC	0.57	58.22%	3.93	25.94%	15.25	15.84%	3.77
	5min	0.69	35.48%	5.89	31.62%	18.24	32.90%	8.11
	1h	0.73	23.74%	6.00	32.51%	18.22	43.75%	10.10
	1day	0.70	24.90%	6.16	30.04%	18.78	45.07%	10.49
	7day	0.55	23.06%	5.55	29.61%	18.50	47.34%	10.53
CdSe/CdS_1	GPC	0.66	36.34%	5.06	33.92%	17.97	29.75%	7.30
	5min	---	---	5.85	22.84%	18.39	77.16%	15.53
	1h	---	---	5.74	21.35%	18.49	78.65%	15.77
	1day	---	---	4.45	30.32%	17.89	69.69%	13.81
	7day	---	---	5.02	28.76%	18.79	71.24%	14.83

[a] Tau is the lifetime component τ shown in the previous lifetime analysis method discussion. The unit for each lifetime component is ns.[b] wt.A is the weighted amplitude. $Wt.A_i=(A_i/\sum A)\times 100\%$

3.6. Reversibility of QY regeneration.

One concern is whether changes in ligand concentration lead to irreversible structural changes in the QDs. To investigate the reversibility of the regeneration process,

a second round of GPC was used to repurify the QY-regenerated thin-shell QD samples, subsequent to introduction of CdOA, TOP, or OAm. By comparing the absorption and emission spectra before and after the second purification, we can detect irreversible changes in size or shape associated with changes in ligand concentration.

QD samples are purified by GPC and mixed with 3000 equivalents of ligand. After stirring inside the glovebox for 1 day, the mixtures are purified again by GPC. Absorption and emission spectra are monitored during the process.

As shown in the initial QY regeneration results, when CdOA is introduced into both **CdSe/CdZnS_1** and **CdSe/CdS_1** samples, there is a red shift in the absorption spectra. As shown in **Figure 3.12A,B**, they did not shift back after the second GPC purification process, which indicates that the regeneration process with CdOA is not reversible. The small red shift in the **CdSe/CdS_1** sample on introduction of CdOA is analogous to that seen when CdOA is used as a Cd precursor in shell growth, but the irreversible nature could indicate some surface reconstruction.[189] When CdOA is added to the **CdSe/CdZnS_1** sample, a larger red shift is observed, and one possible reason is a cation exchange reaction between Zn from the shell and CdOA in the solution.[201–203] To confirm this, purified **CdSe/CdZnS_1** treated with CdOA solution or pure toluene was precipitated, and the supernatant portions of these two samples were digested and characterized by inductively coupled plasma-mass spectrometry (ICP-MS). As shown in **Figure 3.12C**, a much higher amount of Zn is observed in solution when CdOA is introduced. The total amount of excess Zn detected in the supernatant corresponds to 25.3 % of the Zn equivalents introduced during shell synthesis; this suggests that at least 25.3 % of the Zn in the shell has been replaced by Cd. One interesting observation is that

for GPC-purified **CdSe/CdS_1**, after treatment with a large excess of CdOA, a subsequent GPC purification found a significant portion of the sample to be retained on the GPC column. Interactions between polystyrene GPC media and metal-rich samples have been reported in other systems.[204] We have observed similar results previously when attempting to purify QDs synthesized under highly metal-rich conditions, which is consistent with CdOA adhesion to the CdSe/CdS QD surface in the present case.

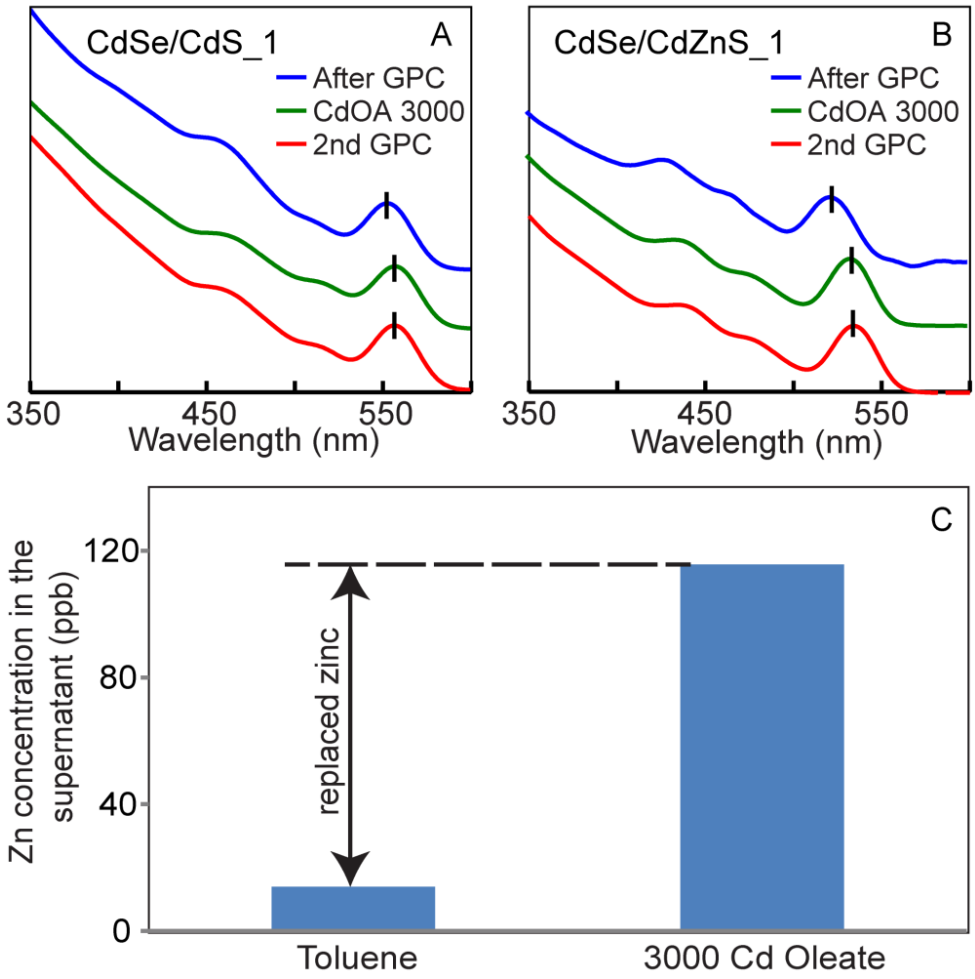

Figure 3.12. Reversibility test of CdOA. (A, B) The absorption spectra before and after the introduction of CdOA and after the second GPC purification for **CdSe/CdS_1** (A) and **CdSe/ CdZnS_1** (B). (C) ICP-MS analysis of the Zn content in digested supernatant of GPC-purified **CdSe/CdZnS_1** sample mixed with toluene or with 3000 equiv of CdOA solution. Copyright 2015 American Chemical Society.

On the other hand, **Figure 3.13D** and **E** show that, during introduction and removal of TOP, both CdSe/CdS and CdSe/CdZnS QD samples maintain their absorption features. This suggests that TOP does not change the effective size or size distribution of the quantum-confined band-edge states (there is an increase in relative absorption in the UV range, which may be associated with changes in higher energy excitations). After the second GPC purification, NMR confirms that TOP can once again be completely removed from the system and the absorption spectrum remains constant (**Figure 3.13A-C** and **Figure 3.14A-C**). On the basis of these results, we believe that the regeneration process with TOP is reversible. Similar results can also be observed with OAm, where the R-H disappeared after the second GPC purification (**Figure 3.14D-F**). According to the emission spectra, the QY decreased after removing TOP by the second GPC purification, but it remained higher than the first GPC-purified sample. This result suggests that the regeneration process with TOP might not be completely described as a simple adsorption reaction and the QD surface may reconstruct with the help of the introduced L-type ligands. Previous reports have identified a role of L-type ligands in displacing metal oleate from CdSe QD surfaces at high concentration.[170] Here, we also attempted to measure the oleate population after the second GPC purification, but due to the aggregation of the particles during the phase change process when switching to deuterated solvent (the absorption spectra changed and emission intensities significantly decreased after removal of the solvent and redissolution process, **Figure 3.14G, H**), we were unable to obtain consistent results based on NMR and absorption spectra.

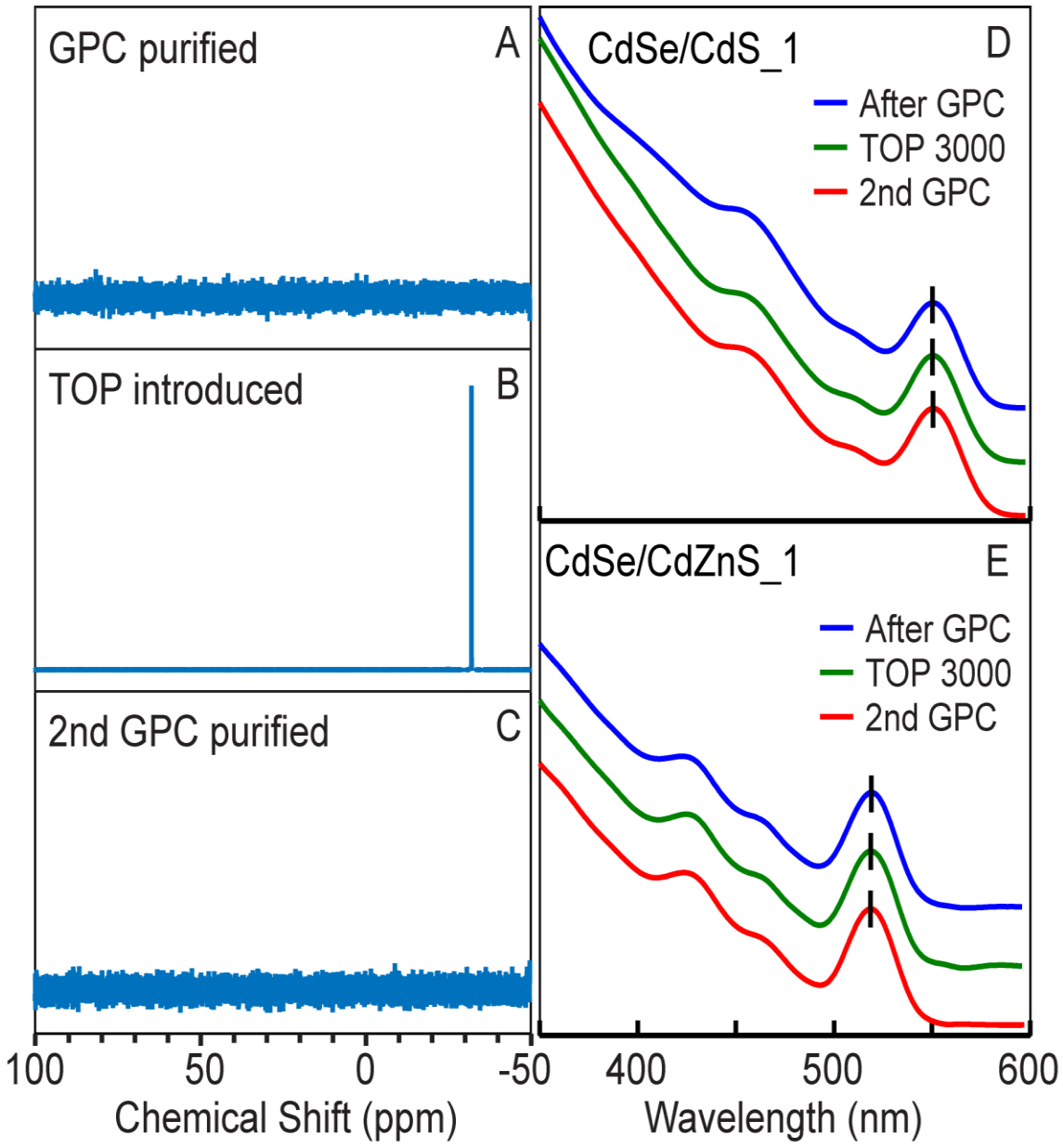

Figure 3.13. Reversibility test of TOP. ^{31}P NMR spectra before (A) and after (B) the introduction of TOP and followed by after the second GPC purification (C) of the GPC-purified **CdSe/ CdS_1** QDs. The absorption spectra during the process described above for **CdSe/CdS_1** (D) and **CdSe/CdZnS_1** (E).which showed no shifting of the bandgap absorption peaks. Copyright 2015 American Chemical Society.

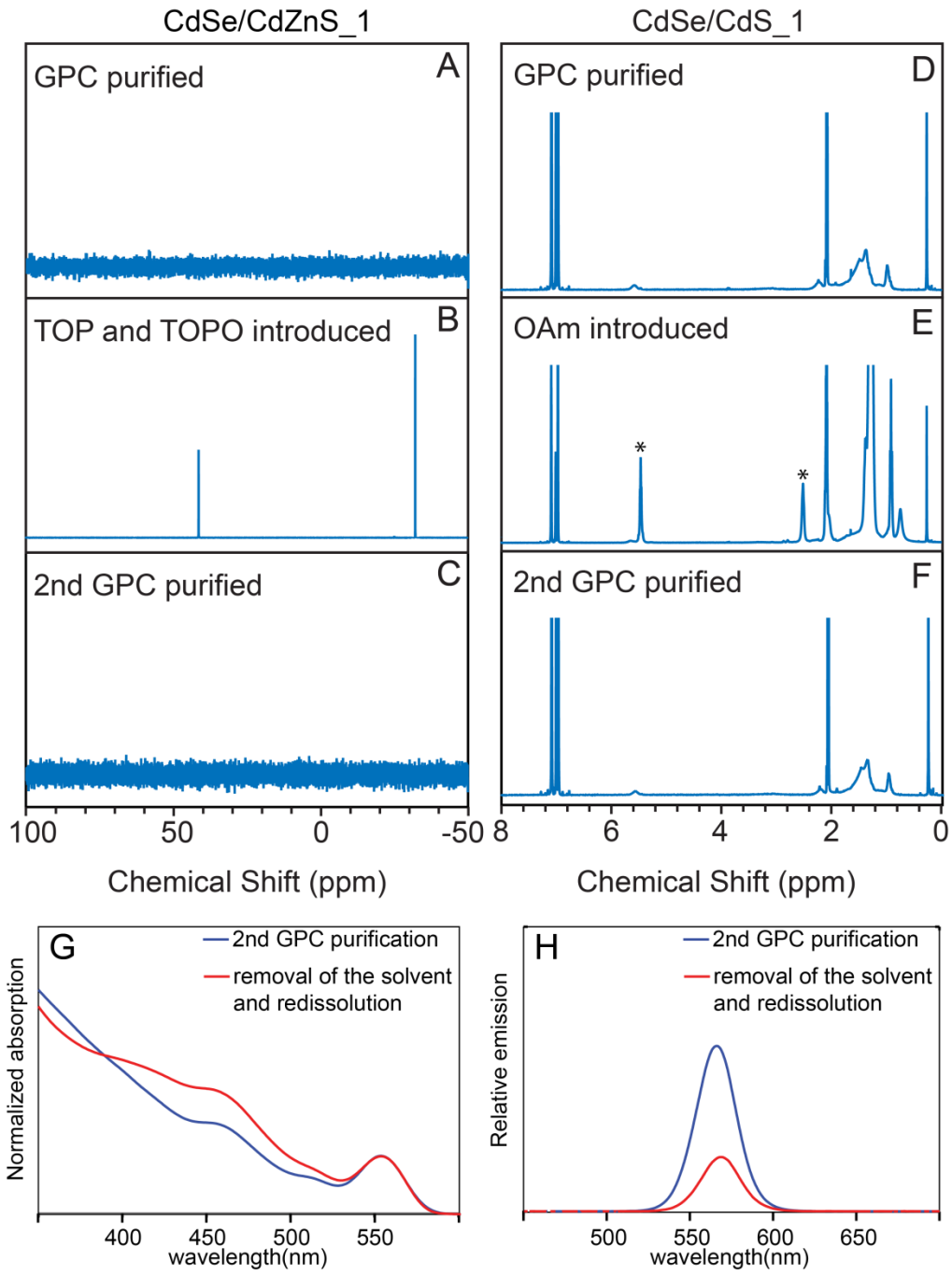

Figure 3.14 ^{31}P NMR spectra before (A) and after (B) the introduction of the mixture of TOP and TOPO, and after the 2nd GPC purification (C) for the GPC purified **CdSe/CdZnS_1** sample. ^{1}H NMR spectra before (D) and after (E) the introduction of OAm, and after the 2nd GPC purification (F) for the GPC purified **CdSe/CdS_1** sample. The marks in (E) indicate the free olefin proton and α-H in the OAm peaks that are removed during the 2nd GPC purification process. Absorption (G) and emission (H) spectra during the removal of the solvent and redissolution into deuterated solvent of the 2nd GPC purified **CdSe/CdS_1** sample. Copyright 2015 American Chemical Society.

3.7. Isothermal titration calorimetry of TOPO, TOP, and OAm ligand addition

On the basis of our results above as well as previous literature reports, L-type ligands (including TOP, TOPO, and OAm) can reversibly attach to and detach from the QD surface.[153,157,172] However, as shown in our regeneration and lifetime studies, not all of these ligands contribute equally to the photophysical property changes in QDs. Ligand/ QD interaction is known to influence the energy levels and occupation of interfacial states, affecting electron and hole trapping rates and intraband decay rates.[155] The effect of a certain total ligand concentration will depend on the adsorption isotherm and on the effect of such binding on the interfacial states. It is desirable to have an independent measurement of the extent of binding so that these factors can be distinguished. NMR has been proven to be a powerful technique for the determination of the interactions between ligands and the nanocrystal surface. Diffusion-ordered NMR analysis has been employed specifically to characterize the bound and free ligand population on QDs in previous work.[158,183] However, in this study, we did not observe any significant difference in diffusion constant measured by DOSY (**Figure 3.15**), T_1 measurement on ^{31}P, or NOE response on ^{1}H spectra with selective saturation on the ^{31}P resonance (data not shown) upon introduction of GPC-purified QDs to TOP or TOPO solutions. Both behaved similarly to free ligand controls in these NMR experiments. These results suggest a fast dynamic adsorption/desorption equilibrium, where the bound ligands are exchanging rapidly with the excess of unbound ligands in the solution.[205] Therefore, we employed isothermal titration calorimetry to detect and characterize the binding between the neutral ligands and QDs. Although widely used in biochemistry, ITC has only recently begun to be applied to nanoparticles to assign parameters for multiple binding problems.[172,186,188,206] In this study, we titrated the same amount of TOPO, OAm, and

TOP to the GPC purified **CdSe/CdZnS_1** sample to measure the heat response. Any response of the system as equilibrium is re-established that has nonzero enthalpy change, such as bond formation upon ligand binding, will generate a heat response. The shape of the heat response over the course of the titration can be used to characterize the equilibrium constant and stoichiometry of reactions, while the sign and magnitude of the signal characterize the associated enthalpy change. Due to the intolerance of the machine toward toluene, anhydrous tetrahydrofuran (THF) has been used as the solvent for this study.

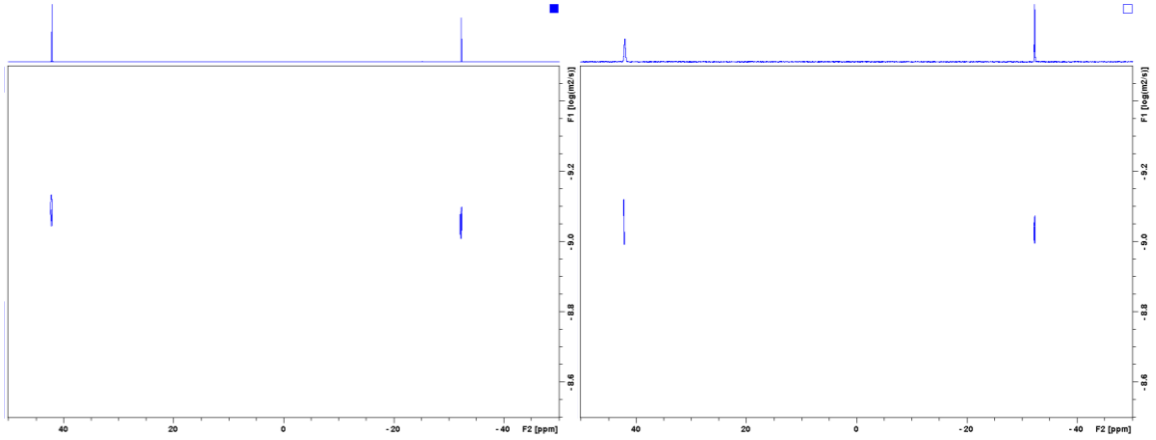

Figure 3.15 DOSY spectra on ^{31}P of free TOP/TOPO (left) and TOP/TOPO mixing with **CdSe/CdZnS_1** sample with a 300 ligand-to-QD ratio (right). Neither TOP nor TOPO can be distinguished from free ligands after mixing with QDs, where the diffusion constant of TOP is 9.3×10^{-10} m^2/s and TOPO is 8.6×10^{-10} m^2/s. The diffusion constant of QD is 1.9×10^{-10} m^2/s based on the DOSY measurement of the olefin proton. The diffusion constant of the solvent toluene is 2.4×10^{-9} m^2/s. Copyright 2015 American Chemical Society.

As shown in **Figure 3.16**, when TOPO is titrated, the overall heat response is small and no trend can be observed in the integrated curve, which indicates that there is no significant binding between TOPO and the QDs at these concentrations. The ITC trace for introduction of OAm shows a small exothermic response at low ligand concentration

that rapidly saturates. This rapid saturation indicates a high association equilibrium constant. The thermogram was fit with the simple independent identical sites model by varying the number of sites per QD *N*, equilibrium constant *K*, and molar enthalpy change ΔH. The best fit was obtained when the number of sites is close to 10, with $K = 2.3 \times 10^4$ M^{-1} and $\Delta H = -27$ kcal/mol. However, since the magnitude of the equilibrium constant *K* is small and the QD concentration is low, the molar enthalpy changes ΔH and the number of sites *N* are correlated in the fit. In particular, the shape of heat response curves within this model are parametrized by Brandt's c parameter (c = [QD]KN, [QD] is the concentration of the QDs).[184] For data that are characterized by c values smaller than 1 (indicating a small mole fraction of bound ligands out of the total added), the enthalpy change and the number of sites are correlated, but the equilibrium constant *K* is well constrained. When TOP is introduced, there is a much greater exothermic response than for the reaction with OAm (an overall exothermic heat approximately 14 times more than that of OAm). The greater heat indicates that TOP has a more negative molar enthalpy of binding and/or binds to a greater number of sites per QD than does OAm. As seen in the PL response during QY regeneration, slower kinetics are also observed in the raw heat signal, which does not rapidly return to baseline between injections when TOP is introduced to the **CdSe/CdZnS_1** QDs. The thermogram for TOP cannot be well-fit by a simple independent identical sites model. In order to compare the results for TOP and for OAm, one approach is to consider the difference in ΔH and *K* that would be required if the number of binding sites per QD is considered to be the same. In this case a fit with *N* fixed to 10 reveals $\Delta H_{TOP\_QD}/\Delta H_{OAm\_QD} = 37$ and $K = 4.3 \times 10^3$ M^{-1} for TOP.

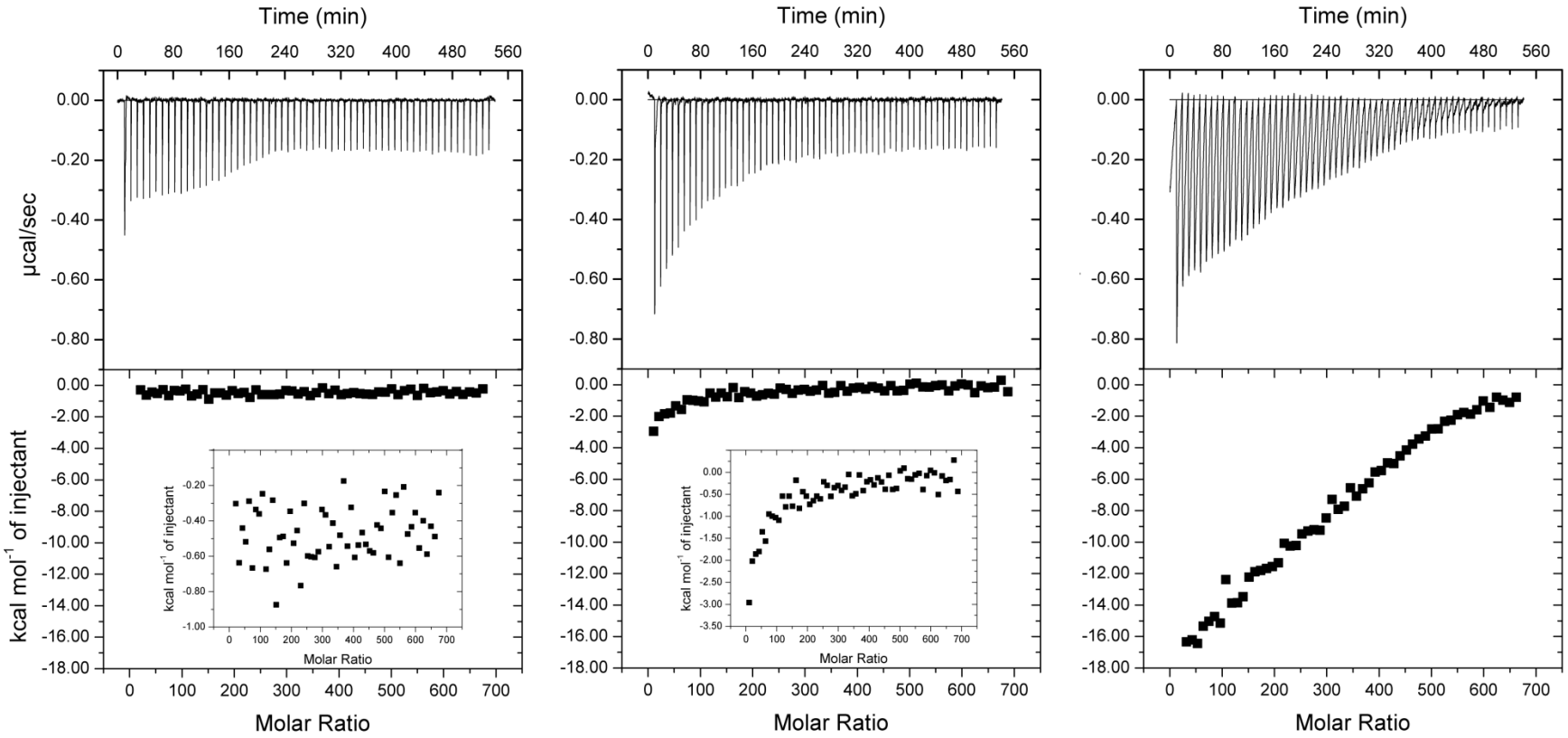

Figure 3.16 ITC traces for **CdSe/CdZnS_1** titrated with TOPO (A), OAm (B) and TOP (C) at the same concentrations. Top panel displays the raw heat per injection, while bottom panel shows the integrated curves adjusted to the scale for the TOP titration. Insets in bottom panels (A) and (B) show zoomed in integrated curves for TOPO and OAm titrations, respectively. Ligand-to-solvent reference titrations have been subtracted from the traces shown; solvent-to-solvent and solvent-to-QD runs gave negligible responses.

Despite an apparently larger equilibrium constant for OAm than for TOP, introduction of OAm leads to much less change in QY than TOP, particularly in alloy shell QDs. This could indicate that the ITC signal for OAm corresponds to binding to only a subset of active trapping/quenching sites or that binding of OAm does not sufficiently perturb the energy levels associated with trapping and recombination. However, due to the steric and electronic differences between these molecules, it is highly possible that OAm and TOP bind to different sites on the QD and the number of sites is not the same. The trends we observed in ligand binding strength are consistent with those predicted in Rempel's work for ligands binding to the Se-terminated (0001) surface of wurtzite CdSe.[86] The theoretical value of the binding energy between TOP to wurzite CdS S-terminated (0001) surface is 3.13 eV.[207] If we assume the binding behavior of TOP to the CdZnS alloy shell surface is similar to that for pure CdS, then the total heat response that we observe of about −200 eV/QD (obtained by integrating the response shown in **Figure 3.16C**) corresponds to about 60 available sites for TOP per QD. We believe that a more adequate model accounting for interactions among similar and dissimilar ligands is needed to describe such ligand association, dissociation, and exchange reactions more thoroughly, and this could be an important target for future studies. Nevertheless, it seems reasonable to argue,[155] particularly for ligands behaving as σ donors, that a strongly exothermic bond-forming step, leading to a large energy separation between bonding and antibonding orbitals, could assist in displacing electron traps from within the band gap. The trend of enthalpy change and QY regeneration that we observe supports this argument.

3.8. Conclusions

The maintenance of high PL QY is important to applications of QDs in lighting and displays, bio-imaging, and luminescent solar concentrators.[141,142] In optoelectronic devices such as solar cells it is likewise important to passivate interfaces in such a way as to limit non-radiative recombination.[140] Surface-adsorbed molecules (ligands) play at least two roles in the behavior of colloidal QDs: they maintain solubility and suppress aggregation, and except in QDs with very thick shells they are responsible for defining the electronic boundaries of the quantum well. In this study we used GPC purification to provide a well-defined initial state for association of neutral ligands to vacant sites. We have demonstrated that the decrease in QY observed on purification of QDs can be simply a result of ligand removal and is not necessarily due to irreversible changes or "damage" to the QD surface. Among the components of the CdSe-based core/shell samples tested here, the QY appears to be most critically affected by the loss of phosphine ligands on purification, because reintroduction of phosphine led to near-complete regeneration of QY with little change in absorption spectrum. In contrast, phosphine oxide and free carboxylic acid had a minimal effect on QY, and the primary amine showed significant QY regeneration only in the case of pure CdS shells. Introduction of Cd carboxylate equivalents led to a large increase in QY in a manner complementary to phosphine, but was also associated with irreversible structural changes.

Time-resolved PL allows us to conclude that the reduction and regeneration in QY are not experienced uniformly among the QDs in the ensemble, but are rather associated with the changes in the relative population between a subset with lifetime comparable to the radiative lifetime and a subset with significantly shorter lifetimes. A

simple model of quenching by a binomially distributed number of recombination centers appears to be insufficient to describe the role of vacant sites in limiting QY.

We also show that ITC, a technique that does not require specific nuclei as spectroscopic probes or deuterated solvents, can be used to measure ligand interactions with QDs with nonzero molar enthalpy of binding. We expect ITC to become a versatile tool for studying ligand binding and interactions on nanoparticle surfaces. Due to its sensitivity, ITC does require a well-controlled reaction system, and it is important to identify purification methods and sample metrics that can ensure repeatable results for compound semiconductor nanocrystals.

3.9. Methods and materials

Materials. The following chemicals were used as received. Cadmium oxide (CdO; 99.999%), Zinc oxide (ZnO; 99.999%), Trioctylphosphine (TOP; 97%) and Trioctylphosphine oxide (TOPO; 99%) were purchased from STREM Chemicals. Oleic Acid (OA; 99%), 1-Octadecene (ODE; 90% technical grade), and Selenium (Se; 99.999%) were purchased from Alfa Aesar. 1-Tetradecylphosphonic Acid (TDPA; >99%) was purchased from PCI synthesis. Bio-Beads S-X1 GPC medium was obtained from Bio-Rad Laboratories. Toluene-d_8 (D, 99.5%) was obtained from Cambridge Isotope Laboratories. Decylamine (95%) was purchased from Sigma Aldrich. Oleylamine (80-90%) and Bis(trimethylsilyl)sulfide ($(TMS)_2S$; 95%) were purchased from Acros Organics. Rhodamine 590 chloride (R590, MW 464.98) was obtained from Exciton. Toluene (99.5%) and Tetrahydrofuran (THF, 99%) were purchased from Mallinckrodt Chemicals. 200 Proof Ethyl Alcohol (Ethanol) was obtained from Decon Laboratories. Acetone (99.9%) was purchased from VWR. Methanol (99.9%) was purchased from

Fisher Scientific. Toluene was dried with activated 4A molecular sieves. THF was dried using the Puresolv system from Innovative Technologies. Synthetic or analytical procedures under inert conditions were carried out using Schlenk line techniques, in a glovebox, under N_2 atmosphere.

Optical spectroscopy. The optical absorption spectrum was recorded using a Thermo Scientific Evolution Array UV-Visible Spectrophotometer with toluene as the solvent as well as the blank in a 1cm path quartz cuvette. Routine emission spectra were recorded by an Ocean Optics USB 4000 spectrometer under ~365 nm excitation.

NMR analysis of QDs. Routine NMR samples of the QDs were prepared in toluene-d_8. The QDs' concentration is set at approximately 20 μM; the exact value in each case was measured by UV-Vis using the calculated molar extinction coefficient. The spectra were recorded on Bruker Avance III 400. The quantitative ^{1}H NMR spectra were measured with ferrocene as the internal standard and 30 s relaxation delay, allowing the system to reach a reliable equilibrium. The ^{31}P NMR spectra of QD samples were measured with 512 scans to increase the signal-to-noise ratio. T_1 is measured by the vendor-supplied inversion recovery pulse sequence experiment. Diffusion measurements and NOE difference measurements on ^{1}H spectra with selective saturation on the ^{31}P resonance were performed Bruker Avance III HD 400 and analyzed by the Topspin version 3.2 software.

Synthesis of CdSe QDs. The CdSe cores were prepared by a hot-injection method[189] using cadmium tetradecylphosphonate as the Cd precursor, trioctylphosphine selenide as the Se precursor and a mixture of TOP and TOPO as the solvent. The two precursors were mixed at high temperature (350 to 365 ℃) and cooled down with an air

blower immediately after the injection. The lowest energy absorption peak for the CdSe cores used to prepare the CdSe/CdZnS samples was at 509 nm, while that of the CdSe cores used for the CdSe/CdS sample was at 522 nm.

CdZnS and CdS overcoating. Shells were grown using a selective ionic layer adhesion reaction (SILAR) method described previously.[62,189] Briefly, a portion of as-synthesized CdSe cores was flocculated by methanol and acetone. After decanting the supernatant, the QDs were redissolved into hexane and stored in the freezer (4 ℃) for more than 12 hours. All the undissolved materials were removed by centrifugation and the sample was precipitated again by an addition of methanol and acetone. Afterward, the QDs were brought into a measured volume of hexane. The UV-Vis absorption spectrum was recorded at a known dilution of the sample to determine the size and quantity of QDs. The solution of QDs in hexane was transferred to a solvent of 1:2 oleylamine:ODE (v/v, 9 mL total) and degassed at 100 ℃ to remove hexane. Before the addition of the reagent *via* syringe pump, the system was heated to 200 ℃ under nitrogen. For the pure CdS shell growth, the Cd precursor is prepared by diluting 0.2 M $Cd(oleate)_2$ in ODE with 2 equivalents of decylamine and a volume of TOP to yield a concentration of 0.1 M. For the CdZnS alloy shell growth, the metal precursor is prepared similarly to the pure Cd precursor but using a mixture of $Cd(oleate)_2$ and $Zn(oleate)_2$ (the ratio of Cd:Zn is 3:7) to yield a metal concentration of 0.1 M. The S precursor was always a 0.1 M solution of $(TMS)_2S$ in TOP. The volume increase associated with 1 monolayer coverage in both cases is calculated based on the radius increase of 3.37 Å, which is the half of the wurtzite *c*-axis unit cell dimensions for CdS. Alternating injections of metal precursor and sulfur precursor were performed, adding the metal precursor solution first, with

injections starting every 15 minutes for CdS shell and 20 minutes for CdZnS shell. The flow rate was adjusted to complete each injection over the course of 3 minutes. The volume of each injection was calculated to apply 0.8 monolayers coverage each cycle (a cycle is defined as one metal precursor injection and one sulfur precursor injection). For the thin shell samples (**CdSe/CdS_1** and **CdSe/CdZnS_1**), two cycles were performed while five cycles were added to the thick shell samples (**CdSe/CdS_2** and **CdSe/CdZnS_2**). The growth processes were monitored by both UV-Vis absorption and fluorescence spectrometers. After the reaction, the mixture was cooled down to the room temperature and the molar extinction coefficient was estimated based on the amount of the core introduced at the beginning and the total volume of the solution after the synthesis.

Absolute quantum yield measurement. The absolute QY of QD samples was assigned by comparison to a rhodamine 590 standard (R590, QY= 99% in ethanol).[190,208] Fluorescence spectra of QD and R590 dye were taken under identical spectrometer conditions on a Varian fluorescence spectrometer in triplicate and averaged. The optical density was kept below 0.1 from the excitation wavelength to 800 nm to avoid internal filtering effects. The QY was calculated based on the integrated intensities of the emission spectra, the absorption at the excitation wavelength and the refraction index of the solvent using the equation:

$$\mathrm{QY_{QDs}} = \mathrm{QY_{dye}} * \frac{\mathrm{Absorbance_{dye}}}{\mathrm{Absorbance_{QDs}}} * \frac{\mathrm{Emission\ integral_{QDs}}}{\mathrm{Emission\ integral_{dye}}} * \frac{\mathrm{Refraction\ index^2_{toluene}}}{\mathrm{Refraction\ index^2_{ethanol}}} \quad \text{..... eq. 7}$$

The precision of this measurement in our case is limited by the precision of the absorbance measurement (~1%) while the accuracy among samples in different solvents will be limited by the accuracy of the refractive index correction term.

GPC purification of the QDs. The GPC column was packed by as previously described[158] with toluene as the eluent. The as-synthesized core/shell QDs were purified by 1 cycle of precipitation with acetone only and redissolution in toluene. Then the QD solution was added to the column and the sample was collected when the elution volume equaled ~1/3 of the total volume of the column (the expected void volume for irregularly spaced spherical beads); this volume corresponds to the fraction at which the purified QDs eluted. The GPC column was rinsed thoroughly (3 times the total volume of the column) between runs.

Preparation of pure Cd oleate. The cadmium oleate used as a ligand in the regeneration study was prepared as follows. CdO and oleic acid were introduced to a three neck flask (the ratio of CdO: OA is 1:5), where OA was used as both acid and solvent. The mixture was degassed and then heated to 270 ℃ under N_2 to form a colorless and clear solution. Then the sample was cooled and transferred to a refrigerator (4 ℃) to allow the product to precipitate. Excess oleic acid was separated by filtration and the insoluble $Cd(oleate)_2$ was washed with ethanol 5× to remove the remaining oleic acid. FTIR and ^1H NMR has been used to confirm the removal of oleic acid.

Quantum yield regeneration and relative quantum yield measurement. After GPC purification, the QD samples were transferred into sealed N_2 environment and pumped into glove box immediately to avoid any possible oxidation. The ligand solutions are also prepared in the glove box. For the regeneration process, the concentration of the QD samples are fixed to be 0.5 μM and the ligand concentration is controlled to be 1.5 mM or 0.15 mM to provide two different ligand-to-QD ratios (1:3000 and 1:300). The total volume of the mixing solutions is 1 mL and the solutions were kept gently

stirring for the 7 day measurement period. The relative QY is characterized by diluting a portion of the above solutions into dry toluene and measuring the absorption and emission spectra. The optical densities of the sample solutions were kept below 0.1 at wavelengths above the 365 nm excitation wavelength to avoid internal filtering effects. The relative QY is calculated by comparing the integration the emission spectrum divided by the absorption at 365 nm.

Time-resolved photoluminescence measurement. The PL decays of QDs in toluene were collected in front-face mode with 1 cm quartz cuvette in a lifetime spectrometer (Edinburgh Mini-τ) equipped with a 368 nm picosecond-pulsed-light-emitting diode. A stirring stage was set under the Mini-τ and a mini stirring bar was placed in the cuvette to stir the QD solution to avoid accumulation of photo-products during the measurement. The instrument response function (IRF) is recorded using Rayleigh scattering of pure water.

Analysis of photoluminescence decay lifetimes. Analysis follows the methods described in *Principles of Fluorescence Spectroscopy* by Lakowicz,J.R.[196] The PL decays were fit with a multi-exponential function re-convoluted with the recorded instrument response function (IRF). For example, if the decay was fit with a tri-exponential function, then:

$$I(t) = \int_0^t IRF(t') \cdot \left(C + \sum_{i=1}^{3} A_i \exp\left(-\frac{t - t'}{\tau_i} \right) \right) dt' \quad \text{..... eq. 8}$$

where $I(t)$ represents the intensity at time t, and τ_i and A_i are the exponential lifetime and amplitude, respectively, of decay component i.

The amplitude average PL lifetimes were calculated based on Equation 9.

$$\tau_{avg} = \frac{\left(A_1\tau_1 + A_2\tau_2 + A_3\tau_3\right)}{\left(A_1 + A_2 + A_3\right)} \quad \text{.....eq. 9}$$

The goodness of the fit is determined by nonlinear least-squares analysis (NLLS) which tests whether the fit is consistent with the raw data and to obtain the lifetimes and amplitudes for the fit that provide the best match between the measured raw data, $N(t_k)$, and the calculated decay, $N_c(t_k)$, where *N* represents the discrete sequence of intensities measured at times t_k and *k* is an index. A reduced χ_R^2 is then minimized to find the best-matched fit:

$$\chi_R^2 = \frac{1}{\nu} \cdot \sum_{k=1}^{n} \frac{\left[N(t_k) - N_c(t_k)\right]^2}{N(t_k)} \; ; \; \nu = n - p \quad \text{.....eq. 10}$$

where $\boldsymbol{\nu = n - p}$, is the number of degrees of freedom, *n* is the number of data-points, and *p* is the number of floating parameters. The reduced χ_R^2 is minimized for all the lifetime decay fits.

Support plane analysis was applied to obtain the uncertainty in the lifetime for each exponential component. The procedure is to change one lifetime τ_i (*i*=1~3) from its value where χ_R^2 is at a minimum, $\chi_{R,\min}^2$, to one of a series of possible lifetimes with offsets $\Delta\tau_k$ ($\tau_i \pm \Delta\tau_k$). Then, we re-run the least-squares fit, keeping $\tau_i \pm \Delta\tau_k$ constant, to minimize χ_R^2 again to $\chi_{R,par}^2$. The confidence probability was judged by the F_χ statistic:

$$F_\chi = \frac{\chi_{R,par}^2}{\chi_{R,\min}^2} \; ; \; F_{\chi,P} = 1 + \frac{p}{\nu} F(p,\nu,P) \quad \text{.....eq. 11}$$

where $F(p,\nu,P)$ is the F statistic with p parameters and ν degrees of freedom with a probability P that F_χ is due to random errors in the data. In this work, the uncertainty in the lifetime is obtained using P= 10%, suggesting there is less than 10% probability that F_χ is due to random error, in other words a 90% confidence limit. Confidence limits were calculated for decays illustrated in the preceding narrative

Reversibility test. CdSe/CdZnS_1 and CdSe/CdS_1. QD samples are purified by GPC and mixed with 3000 equivalents of ligand. After stirring inside the glovebox for 1 day, the mixtures are purified again by GPC. Absorption and emission spectra are monitored during the process.

Inductively coupled plasma-mass spectrometry analysis. Two samples were prepared. One is made by diluting 1 nmol of GPC purified **CdSe/CdZnS_1** QDs in 0.5 mL toluene; the other by mixing 1 nmol of the same QD sample with 3 μmol CdOA (3000:1 ratio) in 0.5 mL toluene. After stirring under N_2 overnight, these two samples were precipitated by acetone and the supernatants were transferred evacuated to dryness. 1 mL aqua regia was introduced and was allowed to digest the sample for 2 h. Then the solutions were brought to 50 mL in a volumetric flask with 2% HNO_3 in water. The concentrations of Zn were detected by a Thermo-Finnigan Element XR ICP-MS.

Isothermal titration calorimetry. Isothermal titration calorimetry (ITC) experiments were performed on a VP-ITC calorimeter (Microcal Inc., Northampton, MA). Ligand solutions were titrated from the 300 μL injection syringe to the sample cell loaded to its 1.8 mL filling capacity, and the heat response to maintain a constant temperature between the sample cell and reference was monitored. The sample cell was purged with nitrogen before loading the GPC purified QD solution to minimize the influence of the

oxidation reactions. Each experiment was conducted at 22 ℃ and midrange reference power; allowed to equilibrate prior to an initial 600 seconds delay; and in order to allow adequate equilibration between each injection, 8-9 min intervals were set between each injection for a total 60 injections in 5 μL increments. Dry THF was chosen as the solvent for both the ligands and QDs, as well as the blank solvent in the reference cell. Reference titrations were conducted to determine any significant heat of dilution between the solvent, ligand solution and QD solutions that may have accounted for signal in the final ligand-QD titrations. Only ligand-solvent reference titrations were subtracted from ligand-QD titrations, as other reference titrations were determined negligible. The QD solutions loaded in the sample cell were 0.5 μM (same as for QY regeneration) and ligand solutions loaded in the syringe were 1.5 mM.

CHAPTER 4

EFFECT OF AMINE ON ENHANCING GROWTH OF CDSE/CDS CORE/SHELL QUANTUM DOTS VIA SELECTIVE IONIC LAYER ADHESION REACTION

4.1. Introduction

Colloidal semiconductor nanoparticles are of interest because their high photoluminescence quantum yields (QY), size-tunable emission and high photo-stability. Forming an isotropic shell is desirable because it isolates the core from surface associated trap states and leads to enhanced QY. Lowering the density of defects at the core-shell interface using materials with low lattice mismatch[61] or forming a gradient shell with a transitional layer[65] have been demonstrated as effective strategies to increase the radiative decay rate and maintain high QY. Growing high quality shells requires shell precursors with high solubility in the reaction solvent and high conversion rate to the core surfaces. We have previously demonstrated that the commonly used cadmium precursor $Cd(oleate)_2$ has low conversion yield when added in monolayer-equivalent quantities during the growth of CdSe/CdS core/shell QDs via the SILAR technique. The growth solvent could potentially play an important role in governing precursor conversion, in particular by controlling precursor solubility and through competition for nanocrystal surface sites. Primary amines such as oleylamine and hexadecylamine have long been used as coordinating solvents for nanocrystal growth, with oleylamine a common choice for shell growth on CdSe QDs by SILAR. It has been reported that switching to a secondary amine (dioctylamine) improved the synthetic yield when growing CdS shell on

CdSe QDs, especially for larger shell thicknesses, but it was unclear what effect was achieved on precursor conversion or whether further optimization is possible.

In this work, we grew CdSe/CdS core/shell quantum dots in solvent mixtures with three different representative amines - primary, secondary and tertiary - via a SILAR technique. The course of the growth was monitored by UV-visible absorption and photoluminescence (PL) emission spectroscopy. Emission peaks at wavelengths shorter than the effective band-gap "blue peaks" appeared in the PL spectrum when QDs were grown in primary amine, suggesting nucleation of small CdS particles as a result of cross-reaction of the shell precursors as seen previously. Further evidence of such small particles was obtained from photoluminescence excitation (PLE) measurements. Time-correlated single photon counting (TCSPC) measurements also indicated the variations/ changes of PL lifetime are different when core/shell particles are grown under different amines. A possible mechanism for the influence of amine solvents on precursor conversion is occlusion of precursor binding sites by amines coordinating the QD surface. Proton NMR was applied to understand the interaction of different amines with the CdSe surface. Scanning transmission electron microscopy (STEM) proved the yield of the shell was higher when using trihexylamine as the growth solvent. Titration experiments in which metal precursors are titrated to QD cores under shell growth condition and the unreacted free metal precursors are monitored/measured by inductively coupled plasma mass spectrometry (ICP-MS), were designed to study the precursor conversion efficiency and completion of shell formation during the growth under different amines.

We demonstrated that the interaction between the solvent molecules and the nanoparticle surface is an issue influencing shell growth by SILAR, since the shell

precursor must compete with such interactions in order to saturate the surface prior to introduction of the complementary precursor for growth of the shell compound.

4.2. CdSe/CdS core/shell particles growth three types of amines

To investigate the impact of the amines on the growth of CdSe/CdS core/shell quantum dots, three parallel experiments were performed under the identical conditions but with different alkyl amines composing a portion of the shell growth solvent. The three amines were chosen to 1. represent primary/secondary/tertiary amines; and 2. have similar molecular weight and molar volume, so that similar amine:QD ratios (~50000:1) could be achieved at similar QD concentrations. A common batch of CdSe cores was used to minimize differences. The detailed experimental design and set up can be found in section 4.11. Briefly, the solvent mixture (2:1 ODE/amine (v/v, 9 mL total)) was prepared and degassed for 1 hr. After purification, CdSe cores in hexane were injected, and then hexane was removed under vacuum (2 hrs). Shell precursors ($Cd(oleate)_2$ and TMS_2S) were freshly prepared from stock solutions (the Cd precursor was prepared by diluting $Cd(oleate)_2$ stock solution in a solvent of 50:50 ODE and TOP with two equivalents of the same amine in the solvent mixture (vs. Cd) added to yield a Cd concentration of 0.1 M.; The sulfur precursor was 0.1 M solution of $(TMS)_2S$ dissolved in TOP.) and introduced into the reaction flask in an alternating fashion according to the SILAR technique, one monolayer equivalent (1 ML eq.) dose for each addition, with growth conducted up to 6 monolayer (ML) equivalent thickness of CdS shell in total. Each addition was slowly applied over 3 min, with 12 min waiting time before the next addition. Aliquots for monitoring of cores were drawn after degassing and before shell growth; aliquots for core/shell particles at series of shell thickness in terms of ML were

drawn at the end of each complete ML addition for both cadmium and sulfur precursors. The experimental results are listed in **Table 4.1**.

Table 4.1 Matched core/shell growth results with different amine solvents

Entry	core radius[a] (nm)	Shell (ML)	Amine solvent[b]	Abs. peak (nm)	Abs. width[c] (meV)	PL peak (nm)	PL width[d] (meV)
CdSe/CdS_OAM	1.69	6	**oleylamine**	586	106	600	93
CdSe/CdS_DOM	1.70	6	**dioctylamine**	586	86	597	84
CdSe/CdS_THM	1.69	6	**trihexylamine**	583	82	593	79

[a] From absorption based on calibration curve. [b] 1:2 v/v with ODE. [c] Twice HWHM from Gaussian fit to 1st exciton absorption peak. [d] FWHM from Gaussian fit to PL peak.

4.3. Absorption and photoluminescence measurements

During the course of the growth, aliquots with a consistent volume of 50 ± 5 μL was withdrawn and diluted in 2.0 ± 0.2 mL of hexane for monitoring by absorption and PL spectroscopy. The error in QD concentration among such aliquots was found to be < 25%. The nominal concentration of core/shell particles in aliquots decreased over the course of shell growth due to the increase in total volume as shell precursor solutions are introduced. The band-edge absorption all aliquots remained less than 0.1 AU such that little fluorescence light is re-absorbed when the samples are excited. Absorption and PL spectra of core/shell particles grown in the three amines are shown in **Figure 4.1**. To facilitate comparison, the absorption and PL spectra of successive aliquots have been scaled to compensate for the difference in nominal concentration of core/shell particles. (Dilution factor showed in **Table 4.2**) In particular, the absorbance and intensity values plotted should be representative of the signals seen at the same QD concentration (nominally 0.42 μM), with a scaling error of less than 25%. In all three shell growth experiments, the absorption spectra indicate a red shift in the lowest-energy (1S) exciton

resonance is observed with increasing shell thickness, accompanied by an increase in the height of the scaled 1S absorbance. An increase in the 1S molar extinction coefficient with increasing size of CdSe QDs has been described and modeled by Jasieniak *et al*.[120] The trend for the same model applied to the evolution of the 1S absorbance in the CdSe/CdS core/shell particles is indicated by the black curves in **Figure 4.1A-C**, with 25 %error indicated by dashed lines.

Table 4.2. Dilution factors for aliquots for three parallel core/shell growths.

	core	1 ML	2 ML	3 ML	4 ML	5 ML	6 ML
CdSe/CdS_OAM	1.00	0.90	0.80	0.69	0.59	0.50	0.42
CdSe/CdS_DOM	1.00	0.88	0.76	0.64	0.53	0.44	0.36
CdSe/CdS_THM	1.00	0.91	0.81	0.71	0.61	0.52	0.44

Table 4.3 Scaled emission peak intensity (counts) for **Figure 4.1D-F**

	PL	core[a]	1 ML	2 ML	3 ML	4 ML	5 ML	6 ML
CdSe/CdS_OAM	blue-peak	0	5.05995 E+02	1.03341 E+05	7.76619 E+05	1.09446 E+06	1.15821 E+06	1.15847 E+06
	main-peak	1.5396 8E+07	6.80266 E+07	9.33718 E+07	1.07703 E+08	1.22538 E+08	1.32306 E+08	1.46360 E+08
	ratio ($X10^{-3}$)	**0**	**0.0074**	**1.1068**	**7.2107**	**8.9316**	**8.7540**	**7.9152**
CdSe/CdS_DOM	blue-peak	0	6.27747 E+02	1.65251 E+04	1.27189 E+04	3.15963 E+04	1.64858 E+04	9.48596 E+03
	main-peak	2.7769 8E+06	4.57482 E+07	6.94194 E+07	8.48348 E+07	1.01604 E+08	1.22727 E+08	1.45911 E+08
	ratio ($X10^{-3}$)	**0**	**0.0137**	**0.2380**	**0.1499**	**0.3110**	**0.1343**	**0.0650**
CdSe/CdS_THM	blue-peak	0	6.55815 E+02	8.28643 E+02	1.28926 E+02	6.07081 E+03	1.00187 E+04	1.03908 E+04
	main-peak	1.1407 2E+06	3.52798 E+07	5.96057 E+07	8.18824 E+07	1.01119 E+08	1.20012 E+08	1.39634 E+08
	ratio ($X10^{-3}$)	**0**	**0.0186**	**0.0139**	**0.0016**	**0.0600**	**0.0835**	**0.0744**

[a]Prior to the addition of precursors, there are no emission at the range from 400 nm to 500 nm in the PL spectrum of core

.

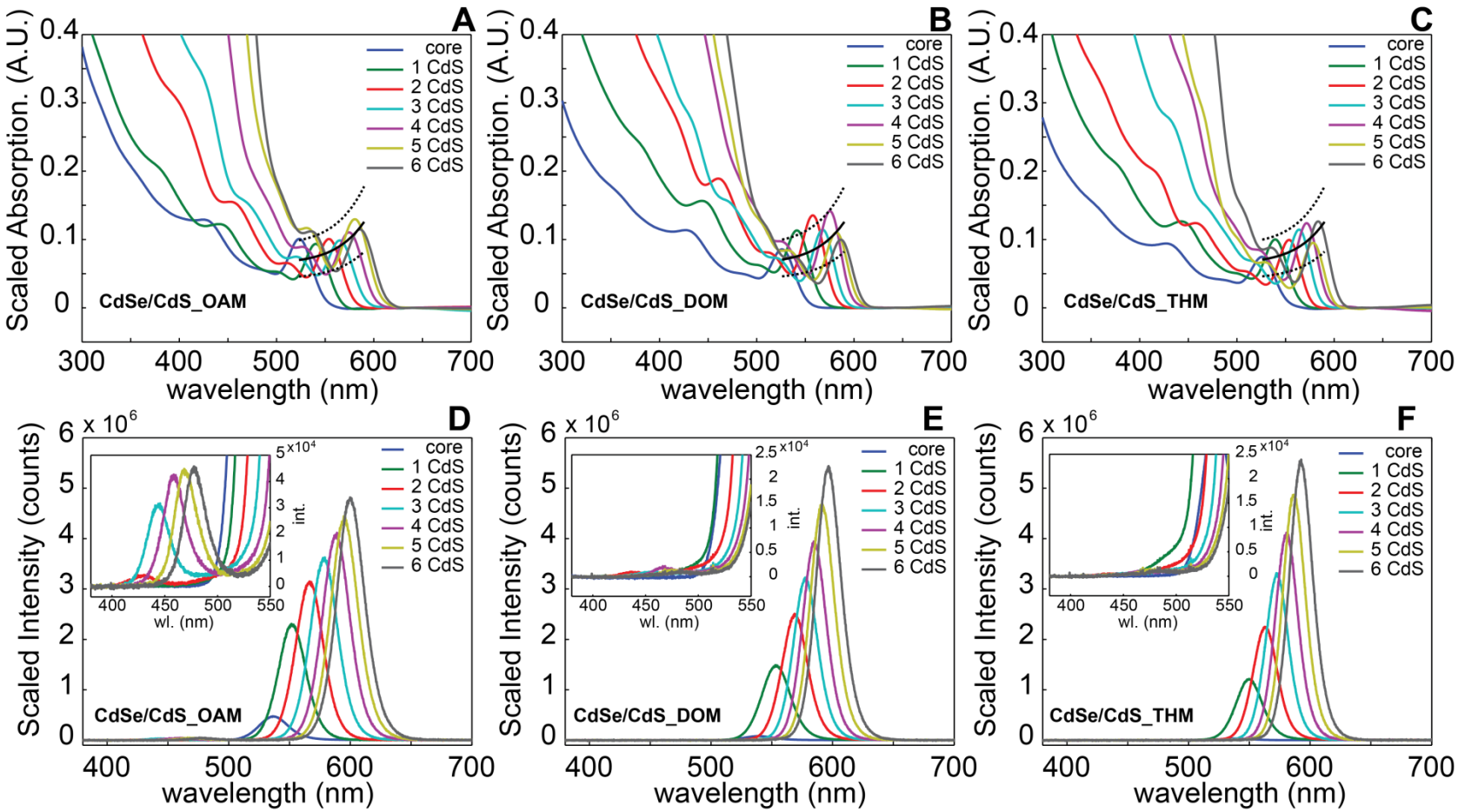

Figure 4.1 Scaled absorption and emission spectra over the curse of CdSe/CdS core/shell QDs growth in three amines. (A, D) **CdSe/CdS_OAM** grown in oleylamine; (B, E) **CdSe/CdS_DOM** grown in dioctylamine; (C, F) **CdSe/CdS_THM** grown in trihexylamine; Absorptions and emissions are normalized to the concentration of QDs in each aliquot, so that all the absorption and emission represent the absorption and intensity of the same amount of QDs, the dash lines represent the upper and lower band of 25% error for the QD concentration in each aliquot. The insets zoomed in the region of emission where "blue-peaks" appeared for **CdSe/CdS_OAM** and **CdSe/CdS_DOM,** and no "blue-peaks" in **CdSe/CdS_THM**.

In comparison of the scaled absorptions for QDs grown in different amines (**Figure 4.1A-C**), almost all the scaled bandgap absorptions are within 25% error bands suggesting the concentrations of aliquots could be treated the same within maximum of 25% error. So the scaled emission intensities (**Figure 4.1D-F**) represent the photoluminescence of the same numbers of core/shell particles, the differences in intensities origins from the photophysical properties of particles with difference structures (shell thickness, interface of the core and shell)

Figure 4.1D-F shows that in all three growths, the PL emission intensity of CdSe/CdS core/shell particles continuously increased with increasing CdS shell thickness (see **Table 4.3** for intensity values); this is a result of an increasing quantum yield as well as an increasing excitation rate at the same concentration due to enhanced absorption at short wavelengths due to the CdS shell.

Despite superficially similar absorption spectra and band-edge PL spectra among the three samples, a close examination of the emission spectra reveals a PL peak appearing between 400-500 nm ("blue peak") that is present in **CdSe/CdS_OAM** (the oleylamine case) **(Figure 4.1D)**, greatly diminished (~50× less intense) in **CdSe/CdS_DOM** (with dioctylamine), and nearly absent in **CdSe/CdS_THM** (with trihexylamine). The blue peaks are absent prior to introduction of shell precursors, are centered at wavelengths shorter than the emission of the CdSe cores used, and shift to longer wavelengths (from 430 nm to 478 nm) as additional shell precursors are introduced. These characteristics are all consistent with the appearance of a CdS nanoparticle side product. We have previously shown that nucleation of CdS nanoparticles can occur when growing CdSe/CdS core/shell QDs via SILAR technique

under 1 ML eq. dose per cycle.[189] The wavelengths of the blue peaks fall within the range of emissions for CdS nanoparticles with diameters 3.5-4.5 nm[209–214]. We offer additional evidence below, in the form of photoluminescence excitation (PLE) and STEM imaging, to support the conclusion that the blue peaks are PL from a CdS nanoparticle side product that is abundant in the case of oleylamine, but much reduced in the presence of the secondary and tertiary amines.

Generally, the enhancement of emission intensity could be a result of same amount of particles with enhanced photoluminescence (enhanced electron-hole recombination rate) because of less crystal defects[215] or better ligand passivation to the particle surface[216–218]; or a result of an increase of particle concentrations with the same and low photoluminescence. It is possible that the passivation by oleylamine in sample **CdSe/CdS_OAM** could enhance the intensity of "blue-peaks", however the fact that such passivation could lead to competition with shell precursors on the nanoparticle surface, and results in high free (unreacted) precursor concentration suggested larger number of nucleation in sample **CdSe/CdS_OAM** is the origin of the high intensity of "blue-peaks".

4.4. Changes in absorption and emission linewidth

Because the electronic transitions of QDs are size dependent, the absorption and PL spectrum linewidths can be used as a proxy for the size distribution in QD samples. We characterized the absorption linewidth (measured as half width at half maximum for a Gaussian fit: $HWHM_{UV}$, **Figure 4.2A**) and the PL linewidth (measured as full width at half maximum: $FWHM_{PL}$, **Figure 4.2B**) over the course of core/shell growth in three amines. After 6 ML of CdS shell growth, both **CdSe/CdS_DOM** and **CdSe/CdS_THM**

display narrower linewidths than **CdSe/CdS_OAM**. **CdSe/CdS_THM** has a slightly narrower $HWHM_{\_UV}$ and $FWHM_{\_PL}$ than **CdSe/CdS_DOM**. These results indicate larger size distributions among the core/shell QDs in **CdSe/CdS_OAM** versus the other two. Interestingly, the trend in linewidth for **CdSe/CdS_OAM** starts to depart from the trends of **CdSe/CdS_DOM** and **CdSe/CdS_THM** after 1 ML eq. of shell growth. This observation, taken together with the simultaneous arrival of the blue peak in the PL spectrum of **CdSe/CdS_OAM**, supports a scenario in which conversion of the shell precursors in oleylamine solvent is insufficient to suppress nucleation and inhomogeneous shell growth. By switching the growth solvent to trihexylamine, while keeping all other conditions the same, control of shell growth appears to be greatly enhanced.

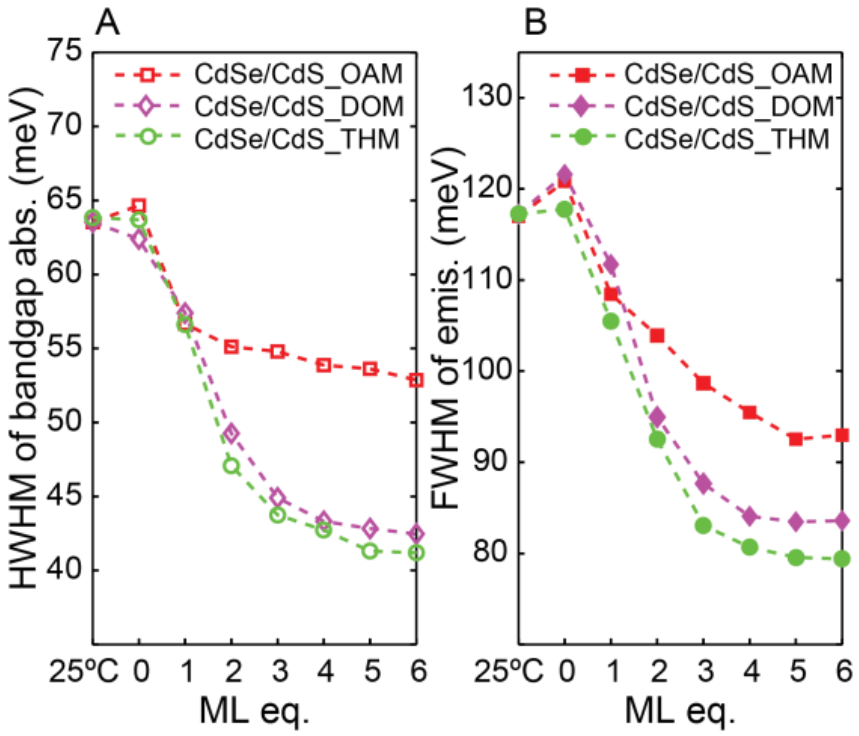

Figure 4.2 (A). Half width half maximum ($HWHM_{\_UV}$) of the band-gap absorption peak. (B). Full width half maximum ($FWHM_{\_PL}$) of the emission peak for CdSe/CdS core/shell particles grown in three amines.

4.5. Photoluminescence excitation spectroscopy

We conducted photoluminescence excitation (PLE) scans on all three core/shell samples to characterize the contribution of CdS nanoparticle nucleation to the observed ensemble absorption spectra. The PLE spectrum measures the emission intensity as a function of excitation wavelength. For a QD in which all excitations are presumed to rapidly thermalize to the band-edge exciton states, the PLE spectrum nominally contains the same information as the absorption spectrum. However, disconnected particles of the shell material as well as hot-carrier recombination processes will lead to a diminished PLE spectrum compared to the absorption spectrum. Technically, the PLE signal should be compared with the number of photons absorbed by the sample at each wavelength, which is proportional to $1-T$ where T is the optical transmittance.[219] The absorbance $A = -log(T)$ is described accurately by $1-T$ (within 10%) only when $A < 0.1$. In order to further minimize light attenuation considerations, the samples were diluted by hexane so that in all cases the absorbance was < 0.2 at wavelengths longer than 300 nm, as suggested by Rumbles et al.[220]

In **Figure 4.3A-C**, the excitation wavelength was scanned from 300 nm to 640 nm, which covers the absorption range for typical CdS and CdSe nanoparticles, while the emission wavelength was set at the band-edge PL emission maximum (PLE@600nm). At long wavelengths close to the band edge, the PLE lineshape closely matches $1-T$ as expected for the simple picture of a QD. Consequently, it is possible to scale the 1-T and PLE signals such that they are superimposed in this region (**Figure 4.3A-C**, insets, with the lowest-energy exciton peak set at 1 on the vertical scale), so that differences at higher energies (shorter wavelengths) can be examined. The raw absorbance signal A is plotted as well for comparison. Indeed, at shorter wavelengths, the

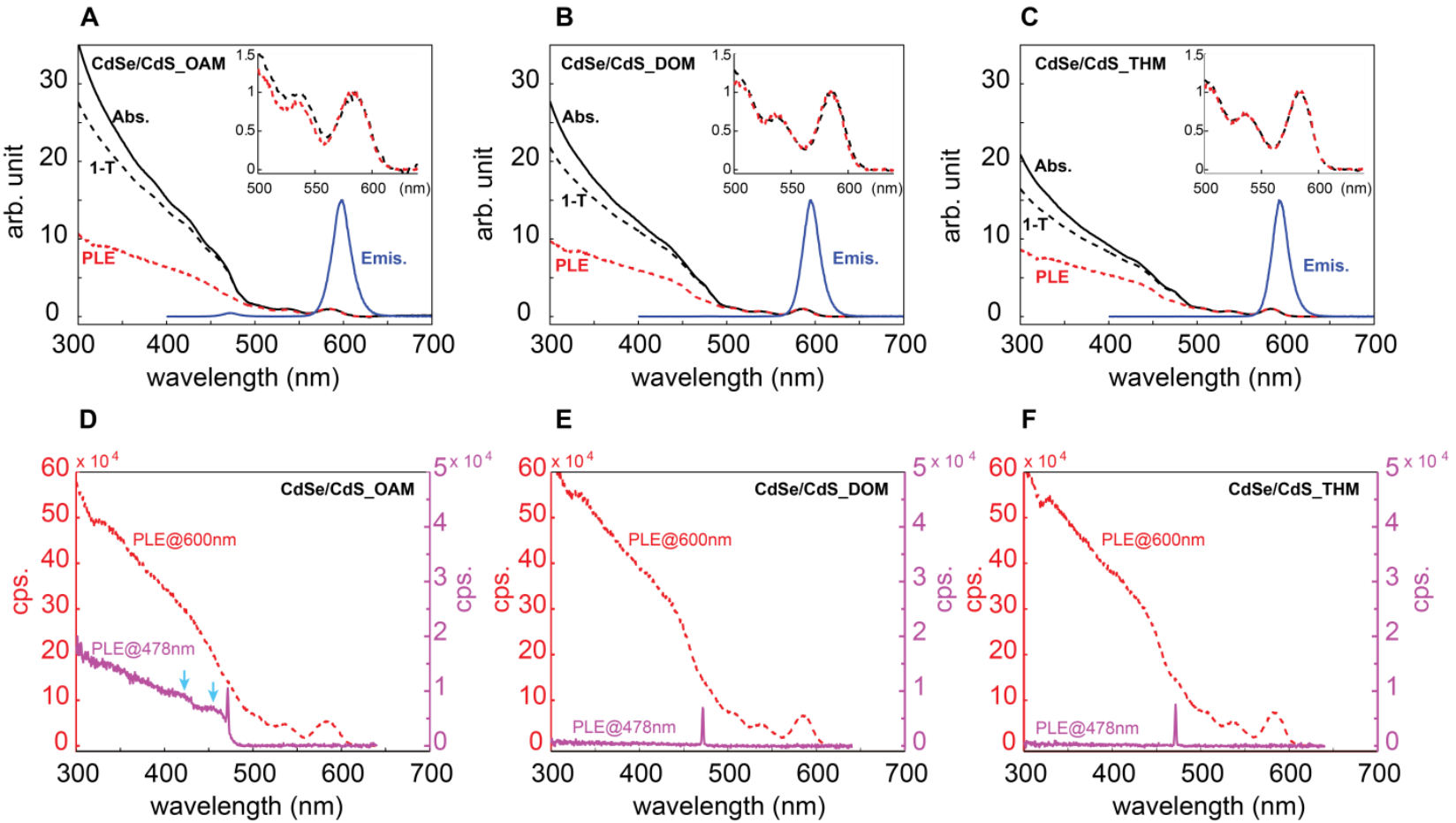

Figure 4.3 (A-C). Photoluminescence excitation (PLE) scan at emission maximum (@600nm) for CdSe/CdS core/shell particles grown in three amines are shown as red dash lines. PLE, Absorption (black solid lines) and 1-T (black dash lines) are shown and normalized to the bandgap absorption peak for comparison. Normalized emissions are shown as blue solid line. The insets shows PLE and 1-T at the bandgap (D-F) Comparison of PLE scans at emission maximum (@600nm, red dash lines) and PLE scans at "blue-peak" maximum (@478nm, purple solid lines) for three core/shell particle samples:

normalized 1−*T* signal greatly exceeds the PLE trace in all samples, indicating a lower ensemble QY for excitation at high energies. Comparing the three samples, it is clear that in the low wavelength region (300 nm to 500 nm), the absorbance and 1−*T* are the largest for **CdSe/CdS_OAM**, then **CdSe/CdS_DOM,** with **CdSe/CdS_THM** showing the lowest values, while PLEs@600nm showed negligible differences. These results suggest that the additional absorbance seen in **CdSe/CdS_OAM** at shorter wavelengths does not contribute to band-edge emission. We propose that the additional absorbance is contributed by the CdS nanoparticles that are responsible for blue emission peaks in the PL spectra. PLE scans with the emission wavelength set to 478 nm (PLE@478nm, **Figure 4.3D-E**) showed a substantial signal from 300 nm to 480 nm for **CdSe/CdS_OAM** (**Figure 4.3D**) that was absent for **CdSe/CdS_DOM** and **CdSe/CdS_THM**. All the above is consistent with the optical properties expected for CdS nanoparticles.

Additional insight on the behavior of the samples under excitation at low wavelengths can be gained by subtracting the normalized PLE@600nm spectrum from normalized 1−*T*. The difference represents photons being absorbed by the sample that do not lead to emission at 600nm. The difference signals are overlaid in **Figure 4.4A** on a scale relative to the PLE signal at the lowest energy exciton that allows the values for the three samples to be directly compared. In all cases a large difference signal grows in at wavelengths <500 nm. There two possible contributions to the difference signals shown: firstly, inefficient relaxation of delocalized, higher-energy excited states to the band-edge exciton localized at the QD core; and secondly, photon absorption by detached CdS nanoparticles. The latter of these contributions should mimic the absorption spectrum of

CdS QDs. **Figure 4.4B** shows that the profile of the 1−*T* difference spectrum for **CdSe/CdS_OAM** differs from that of the other two. If the spectra are normalized at a wavelength near the onset of the excess 1−*T* signal (**Figure 4.4C**), it is clear that the **CdSe/CdS_OAM** sample displays an additional contribution at shorter wavelengths with excitonic features that closely resemble what is expected for CdS QDs.[209] The remaining contribution that is common to all samples (though differing in amplitude) could be evidence of a direct non-radiative recombination pathway for hot carriers-in other words, a diminished QY of the core/shell QDs themselves when excited well above the band edge.

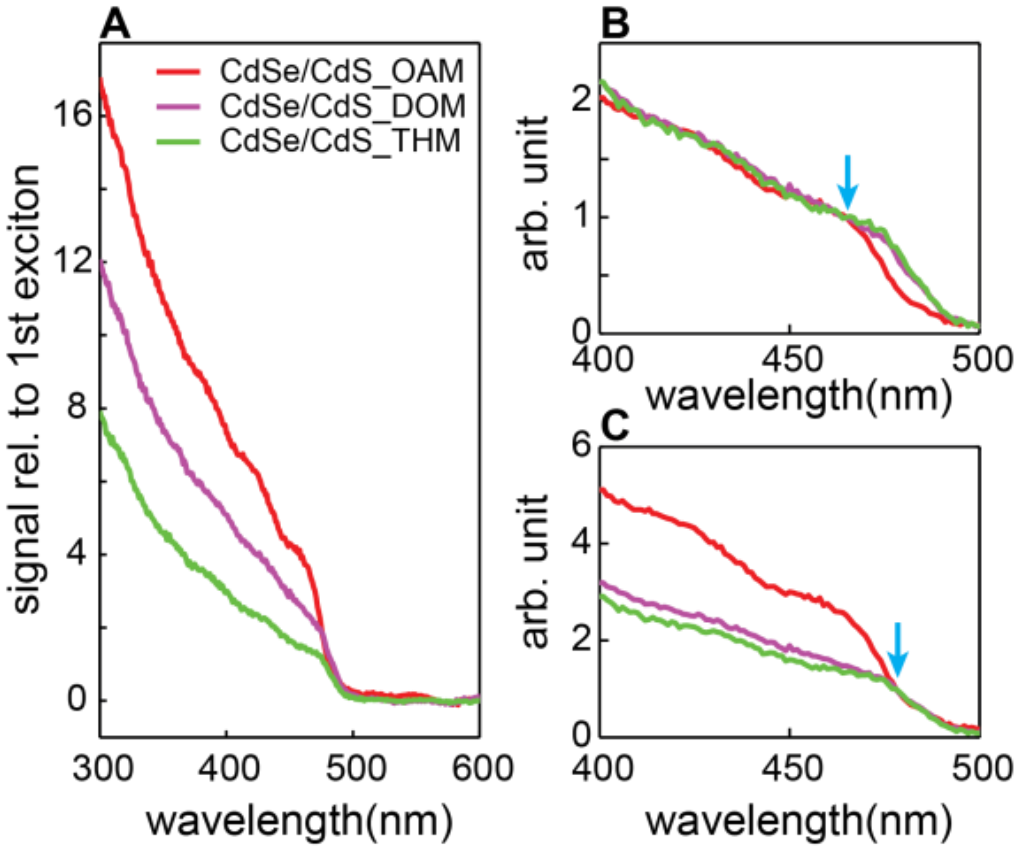

Figure 4.4 (A). Comparison of (1− *T)* − PLE@600nm for CdSe/CdS core/shell particles grew in three amines (B) (1− *T*) − PLE@600nm curves normalized to the first peak of sample **CdSe/CdS_OAM;** (C) (1− *T*) − PLE@600nm curves normalized to the signal onset.

4.6. Photoluminescence lifetime decays

We recorded time-resolved PL traces of aliquots drawn over the course of shell growth in the three amine solvents in order to characterize the average decay rate and decay rate dispersion in the samples. The amine solvent can act as a ligand for the QD surface and as such could inhibit the binding of shell growth precursors, in particular $Cd(oleate)_2$. We have shown previously that association of oleylamine to the surface of purified CdSe/CdS core/shell QDs increases the ensemble QY, increases the average PL lifetime, and decreases rate dispersion. Comparison of the PL decay traces of CdSe QDs and core/shell QDs in the presence of the three amine solvents could thus serve as a proxy measurement for ligand interactions with the QD surface that influence growth. Additionally, as shell growth proceeds, the solvent may modulate polydispersity and/or the formation of crystal defects during shell growth, which would affect radiative and non-radiative decay rates respectively.

Figure 4.5A-C shows the PL decays for each sample just prior to introduction of shell precursors and after each successive complete ML equivalent of growth. In order to isolate the influence of the amine solvents as ligands on the luminescence kinetics, we can focus on the traces for the cores (red traces). After heating in the shell growth solvent, but prior to introduction of shell precursors, the amplitude average lifetime was greatest for oleylamine: $\tau_{avg\_OAM} = 27.7$ ns $> \tau_{avg\_DOM} = 22.7$ ns $> \tau_{avg\_THM} = 12.6$ ns. All samples showed multi-exponential decays. Multi-exponential fits were re-convoluted with the recorded instrument response function (IRF) for quantitative analysis (**section 4.12**) and revealed the necessity for at least 3 exponential components for a reasonably good fit (χ^2<1.5). In each case, three-component fits returned an intermediate lifetime component (τ_2) on the order of the radiative lifetime, a short-lifetime component (τ_1), and

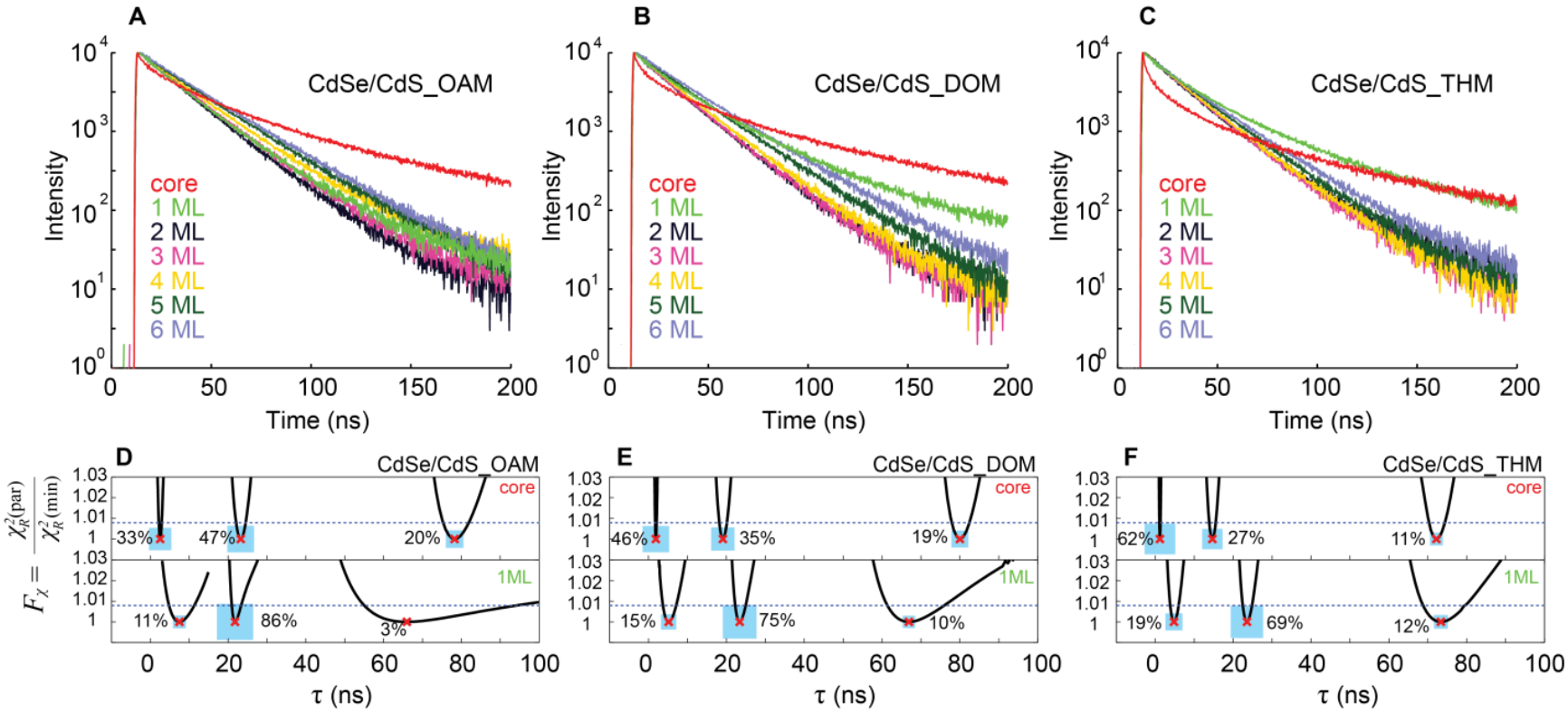

Figure 4.5 (A-C). Time-resolved PL monitored over the course of CdSe/CdS core/shell QDs growth in three amines. (D-F), Distribution of lifetimes for cores(top) and core/shell particles with 1ML eq. shell in three amines, as well as the relative amplitudes (blue squares, areai=wt. Ai for the ith component) for each exponential component. Support plane analysis is applied to determine the uncertainties of lifetimes of each component. Blue dashed line indicates 90% confidence limit for F statistic.

a long lifetime component (τ_3) that is likely associated with a trapping/de-trapping mechanism.[195] The shorter average lifetimes for dioctylamine and trihexylamine samples are driven both by a shift in τ_1 and τ_2 to smaller values (from τ_{1_OAM}=2.52 ns /τ_{2_OAM}=23.24 ns to τ_{1_DOM}=1.89 ns/τ_{2_OAM}=19.12 ns to τ_{1_THM}=1.19 ns/τ_{2_THM}=14.67 ns), and by a shift in relative amplitude towards the short-lifetime component (from wt.A_{1_OAM} =33% to wt.A_{1_DOM} =46% to wt.A_{1_THM} =62%) (**Figure 4.5D-F**, top), indicative of a larger fraction of the ensemble residing in a state with a large non-radiative decay rate. These observations are consistent with a stronger binding interaction of oleylamine with the QD surface, resulting in better electronic passivation of the QD surface, but also potentially interfering with precursor conversion during shell growth.

For the further core/shell growth in all three amines, the relative amplitude for short-lifetime (wt.A1) and long-life time (wt.A3) components continuously decreased, while the relative amplitude for the intermediate component (wt.A2) increased very greatly after only 1 ML (**Figure 4.5D-F**, bottom). In **Figure 4.6**, for **CdSe/CdS_OAM** the short lifetime component was completely eliminated after 2 ML shell: the amplitude average lifetimes kept increasing from 20.76 ns to 27.48 ns (and only require two exponential components to fit the decay); for **CdSe/CdS_DOM** the short lifetime component disappeared after 4ML shell, the amplitude average lifetimes increasing from 19.36 ns to 26.53 ns. However, for **CdSe/CdS_THM**, the short lifetime component existed even after 6 ML of shell growth, and the amplitude average lifetimes remained at 20~23 ns over the course of the growth. (**Figure 4.6**) This difference in average lifetime at the conclusion of 6 ML is primarily associated with the larger amplitude and smaller lifetime value of the τ_1 component; the value of τ_2 is nearly identical across the 3 samples.

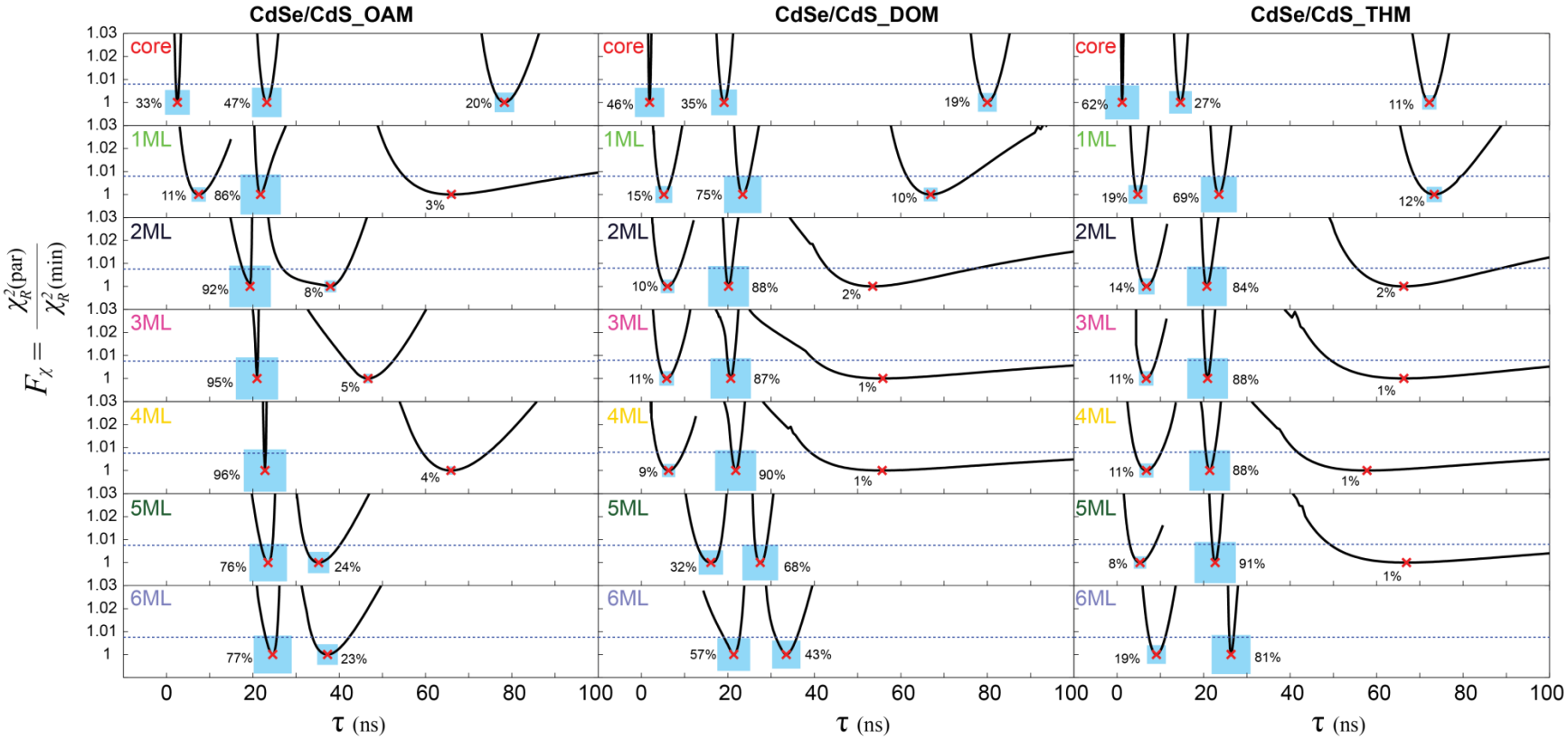

Figure 4.6 Support plane analysis for photoluminescence lifetime decays monitored over the curse of CdSe/CdS core/shell QDs growth in three amines. Distributions of lifetimes and relative amplitudes (blue squares, area$_i$=wt. A$_i$ for the *i*th component) for each exponential component are shown, the uncertainties of lifetimes of each component under 90% confident (indicated by the blue dash line)

Shell growth introduces an electronic barrier (at least for holes) between the core and surface. In our shell growth method, TOP is a component of the shell precursor solution; TOP binds exothermically to the QD surface and is known to strongly regenerate QY in purified samples.[221] Nonetheless, the difference in average lifetime and rate dispersion among the three amine solvents persists through 6 ML of shell growth, suggesting that effects of ligand occupation of the surface on precursor conversion may likewise persist through the course of shell growth in the presence of TOP.

The increase of the PL lifetime because the combination of two factors: (I). Surface trapping states of cores are strongly isolated by the CdS shell, (II). Surfaces of CdS shell are passivated by massive amines as ligands. The above results indicated that OAM is better passivation ligand than DOM, and DOM is better that THM, while THM shows limited/week passivation.

In terms of influence of three types of amines in growing core/shell particles, it is true that the passivation by oleylamine is beneficial to increase of PL lifetime and QY because of eliminating surface trap states, but during the course of the particle growth (shell growth) this is will lead to competition with the shell precursors and results in low surface occupation, hence limits the completion of shells, increase the probability of forming defects in the shell. In the contrast, trihexylamine only weekly passivates to nanoparticle surface, with no competition as oleylamine, the shell precursor conversion efficiency could be enhanced and thus forms more complete shells. Although, the average PL lifetime for **CdSe/CdS_THM** (τavg = 23.11 ns) is shorter than **CdSe/CdS_OAM** (τavg =27.48 ns), **CdSe/CdS_THM** has narrower size distribution and higher purity, later change with stronger passivating ligands will increase its PL lifetime and QY.

4.7. Langmuir-isotherm fit for Cd coverage

To further characterize the differences in precursor conversion efficiency among the three amines, we designed titration experiments to study the conversion of the Cd precursor, $Cd(oleate)_2$, to surface-adsorbed Cd equivalents during the addition cycle. In particular, we sought to characterize the change in the fractional surface coverage by Cd ($\Delta\theta$) as a function of the concentration of free Cd equivalents (e.g. unreacted $Cd(oleate)_2$, denoted here [Cd]) in the reaction mixture. We focused on titration of the metal precursor because we have previously shown that the sulfur precursor TMS_2S reacts quickly and quantitatively with added Cd equivalents, so the conversion of the metal precursor appears to be a key step in directing the course of shell growth. The experimental design and procedure for these experiments is similar to what we have described previously[189] and is detailed in the Section 4.12.

After preparing CdSe QDs in the solvent and at the temperature for shell growth, the metal precursor ($Cd(oleate)_2$) is introduced with a series of additions of 0.2 ML eq. dose each, up to 1 ML eq., followed by 5 additions of 0.48 ML eq. Aliquots of known volume (25 μL) were carefully taken and diluted in hexane, and precipitated with a consistent amount of acetone and methanol. The supernatant from each aliquot was evacuated to dryness, digested, and analyzed for Cd by ICP-MS. The Cd concentration detected was taken to characterize [Cd] in the reaction mixture during the course of titration. The error was determined to be less than 6% based on the control experiments with $Cd(oleate)_2$ solutions in our previous work.[189]

The concentrations of QDs in each aliquot are carefully determined by considering the change of the total volume by addition of precursors and withdrawing of aliquots, assuming QDs are evenly mixed in the reaction flask. Because the amount of

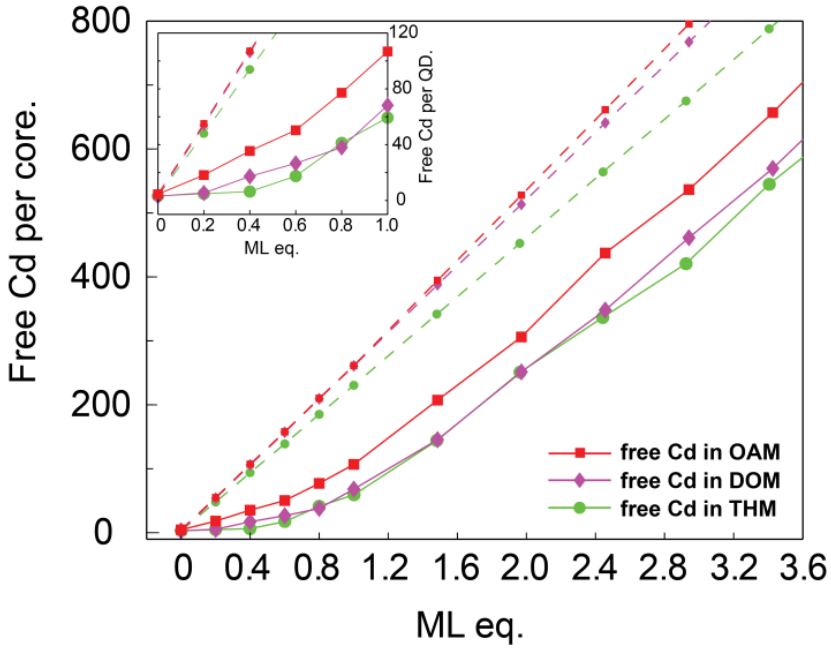

Figure 4.7 Titration of CdSe QDs with $Cd(oleate)_2$. Monitored free Cd concentrations over the course of titration with $Cd(oleate)_2$ under mixture of three amines. (A) Solid lines showed the free Cd per each CdSe core (mole ratio) over the course of titration in solvent mixture of oleylamine, dioctylamine and trihexylamine. Dashed lines: total Cd added per CdSe QD core, indicating amount of free Cd that would be expected in absence of precursor conversion. Inset: magnified view of free Cd per core within 1ML eq.

QDs in each aliquot equals to the total amount of QDs times the volume ratio of aliquot and total solution, assuming the solution in the reaction flask are well mixed and QD lost during the operation is negligible, the free Cd species per each QD can be determined by averaging free Cd amount by amount of QDs in each aliquot. (see experimental data in **Table 4.4**.) **Figure 4.7** showed the free Cd per each CdSe core over the course of titration experiments in solvent mixture of oleylamine, dioctylamine and trihexylamine.

Then for a single QD, the bonded Cd per QD surface (reacted $Cd(oleate)_2$) can be determined by subtracting free Cd (measured by ICP-MS) from the added Cd.Because the total amount of Cd precursor that has been added at any point in the titration is known, any Cd that is not found in solution can be assigned to the QD surface (**Figure 4.7**). This

is divided by the amount of Cd that would be required to form a CdSe shell of 1 ML thickness to arrive at $\Delta\theta$: (see section 4.12 for calculation detail)

$$\Delta\theta = (\textbf{bonded Cd per QD}) \,/\, (\textbf{1 ML eq. of Cd per QD}) \quad \text{.....eq. 12}$$

Table 4.4 Results for titration experiments under three amines

OAM ; CdSe core (r=1.62 nm)

ML eq.	**0.0**	**0.20**	**0.40**	**0.60**	**0.80**	**1.00**	**1.48**	**1.97**	**2.46**	**2.94**	**3.42**
Max Cd/QD	4	55	107	158	210	261	394	528	661	795	930
Exp Cd/QD	4	18	35	50	77	107	207	306	437	537	657
Bonded_Cd/QD	0	37	72	108	133	155	187	221	224	259	273
Ideal_surf_Cd/QD	0	51	102	153	203	254	254	254	254	254	254
[Cd] ($\times 10^{-3}$ M)	0.073	0.294	0.567	0.799	1.215	1.668	3.173	4.593	6.432	-	-
y	0.07	0.20	0.32	0.44	0.53	0.60	0.71	0.83	0.84	-	-

DOM ; CdSe core (r=1.62 nm)

ML eq.	**0.0**	**0.20**	**0.40**	**0.60**	**0.80**	**1.00**	**1.48**	**1.97**	**2.46**	**2.94**	**3.42**
Max Cd/QD	3	54	106	157	210	261	388	513	641	767	895
Exp Cd/QD	3	5	17	27	38	68	146	251	348	461	570
Bonded_Cd/QD	0	49	89	130	172	193	242	262	293	306	326
Ideal_surf_Cd/QD	0	51	102	153	203	254	254	254	254	254	254
[Cd] ($\times 10^{-3}$ M)	0.056	0.096	0.305	0.465	0.658	1.17	2.446	4.137	-	-	-
y	0.06	0.22	0.35	0.48	0.61	0.68	0.83	0.90	-	-	-

THM ; CdSe core (r=1.54 nm)

ML eq.	**0.0**	**0.20**	**0.40**	**0.60**	**0.80**	**1.00**	**1.48**	**1.96**	**2.44**	**2.92**	**3.40**
Max Cd/QD	3	48	94	139	185	230	342	452	564	675	788
Exp Cd/QD	3	5	6	17	41	59	144	251	337	421	545
Bonded_Cd/QD	0	43	88	122	144	171	198	201	227	255	243
Ideal_surf_Cd/QD	0	46	92	138	185	231	231	231	231	231	231
[Cd] ($\times 10^{-3}$ M)	0.067	0.1	0.131	0.354	0.83	1.183	2.802	4.783	-	-	-
y	0.20	0.36	0.53	0.65	0.74	0.84	0.94	0.95	-	-	-

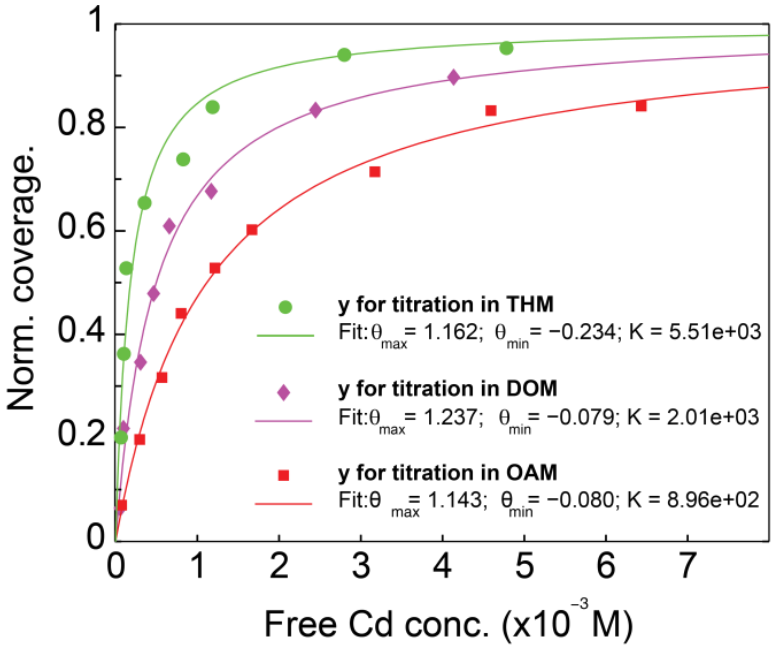

Figure 4.8 Langmuir-isotherm fit for QD surface coverage and free Cd concentration under mixture of three amines. It showed the CdSe core surface coverage changes over the free Cd concentration fitted with Langmuir-isotherm model.

To characterize Cd binding under the three different solvent conditions, we fit each data set with a Langmuir isotherm-based function. Because the CdSe core could potentially present a Cd-rich surface before shell growth, and because the amount of Cd required to saturate the surface is not precisely known, we can include the minimum coverage of Cd, θ_{min}, and maximum coverage of Cd, θ_{max}, as parameters to evaluate the relationship between surface coverage and [Cd]:

$$y = \frac{\Delta\theta - \theta_{min}}{\theta_{max}} = \frac{K \cdot [Cd]}{1 + K \cdot [Cd]} \quad \text{.....eq. 13}$$

in which, y is normalized surface coverage by Cd; K is the equilibrium constant. Solving for $\Delta\theta$ gives the curves shown in **Figure 4.8** and parameters are optimized with a least-square fit.

Figure 4.7 illustrates that under the typical synthetic condition for CdSe/CdS core/shell particle growth, the free Cd detected per QD is consistently increasing in the presence of each of the amine solvents, indicating incomplete conversion of the $Cd(oleate)_2$ precursor to the CdSe core surface. However, for titration in OAM, the free Cd per core was high even after the first addition (~20 Cd/core) compared to the titrations in DOM (~5 Cd/core) and THM (~4 Cd/core). By 1 ML eq. added, the free Cd per core in OAM has reached ~110 Cd/core; for the other two amines the free Cd per core at 1 ML is less but still represents a significant fraction of the Cd added: ~70 Cd/core for DOM and ~60 Cd/core for THM, indicating the CdSe core surfaces were not completely saturated by Cd at 1 ML in any of the solvent mixtures, though THM shows the greatest conversion. For subsequent addition of $Cd(oleate)_2$ to more than 2.4 ML eq., the trends become almost parallel to the dashed lines (which represent no binding), indicating saturating conditions under which addition of excess $Cd(oleate)_2$ no longer increases the number of bound Cd equivalents on the core surface.

Figure 4.8 shows the change in surface coverage $\Delta\theta$ as a function of free [Cd] for the three solvent mixtures. In all cases $\Delta\theta$ rises initially as Cd is introduced, and then saturates at close to +1 monolayer equivalent. The coverage rises more rapidly for the tertiary and secondary amine than for oleylamine. The data and Langmuir fits shown in **Figure 4.8** give association equilibrium constants $K_{THM} > K_{DOM} > K_{OAM}$, indicating that the different amines as the solvent strongly influence the equilibrium. The lower association constant in oleylamine could be brought about by stabilization of $Cd(oleate)_2$ in solution and/or by stronger interactions of oleylamine with the CdSe surface. Though the nucleophilic primary amine and electrophilic Cd presumably bind to different sites on

the NC surface, unfavorable steric and/or electronic effects could result in effective inhibition of Cd binding in the presence of the amine. The PL lifetime results support a stronger interaction of oleylamine with the CdSe/CdS surface compared to the more highly substituted amines as a contributing factor to the difference in *K*.

The results from our titration experiments indicate that growing core/shell particles in solvent mixture of OAM will lead to a large amount of free $Cd(oleate)_2$ at monolayer equivalency, which could promote cross reaction of shell precursors and CdS nucleation at the expense of surface reactions when TMS_2S is introduced.

4.8. STEM images of the core/shell QDs grown in three amines

Figure 4.9 shows the STEM images and radius distribution histograms for CdSe cores as well as the three core/shell products described in **Table 4.5**.- The radius histograms are determined by analysis of STEM images of the same magnification at 6~7 randomly selected regions; *N* is the number of particles analyzed. In comparing STEM images **Figure 4.9A-D** and the radius histograms **Figure 4.9E-H**, the differences in particle sizes and distributions are clearly displayed. We characterize the average radius and peak radius for particles; the average radius is obtained directly from the distribution (including small particles), while the peak radius is the center of a Gaussian fit (red curve, F**igure 4.9E-H**) to the distribution and represents a characteristic radius for core/shell particles in the sample.

The average radius and the peak radius of the CdSe cores are r_{avg} = 1.70 ± 0.16 nm and r_{peak}=1.70 ± 0.00(1) nm based on the analysis of *N* = 1997 different particles, in agreement with the core radius that was determined by the CdSe size calibration curve,[62,118,189] with narrow size distribution.

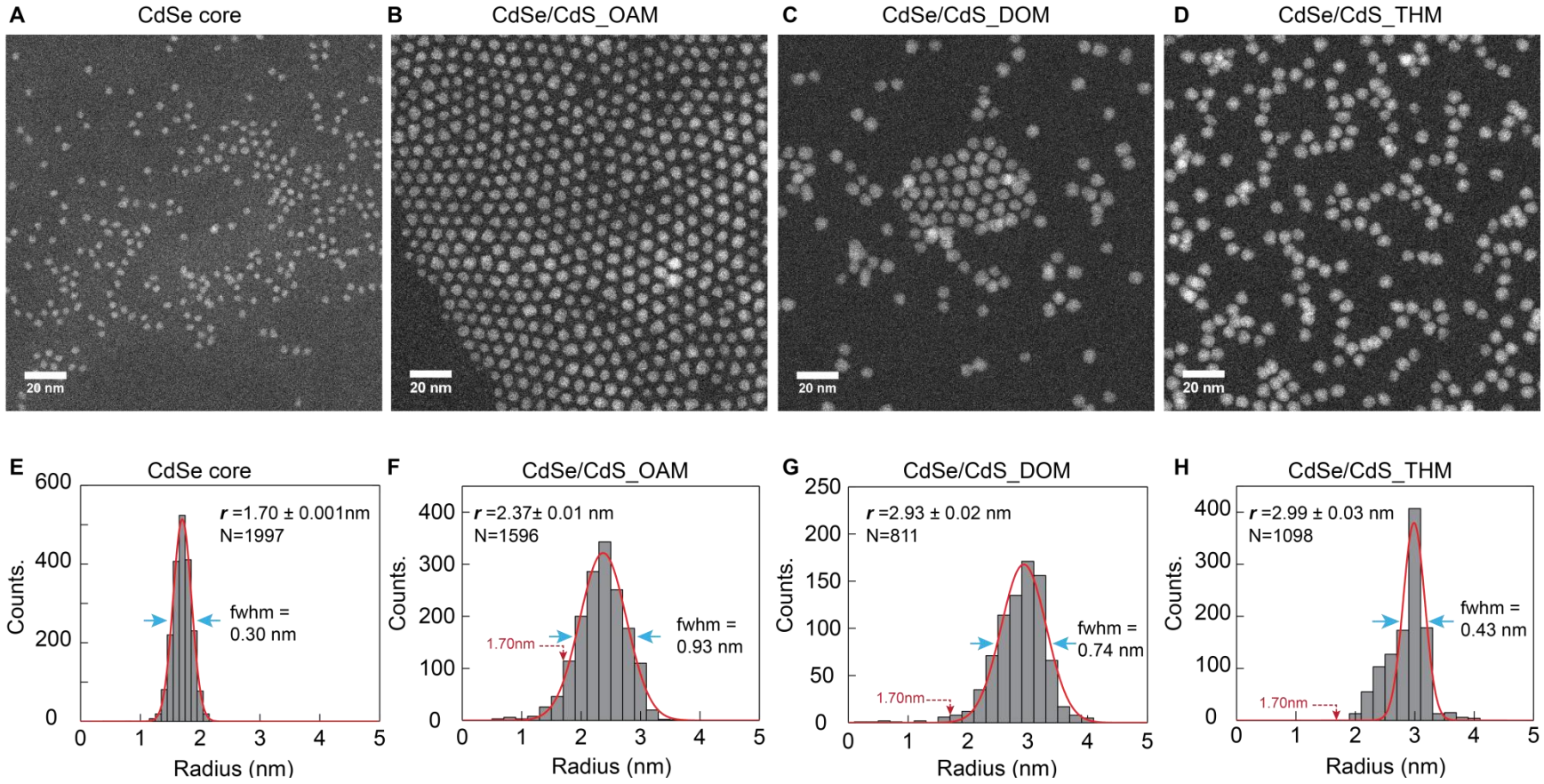

Figure 4.9 STEM images and radius histograms for CdSe cores (A, E) and samples **CdSe/CdS_OAM** (B, F), **CdSe/CdS_DOM** (C, G), and **CdSe/CdS_THM** (D, H). The histograms are fitted by Gaussian functions (red curves) to determine the peak radius (shown in **Figure 4.9E-F**) for core/shell particles; the fwhm is indicated by blue arrows.

Table 4.5 Particle size characteristics of core/shell samples

	CdSe	**CdSe/CdS_OAM**	**CdSe/CdS_DOM**	**CdSe/CdS_THM**
r_{avg} (nm)[a]	1.70 ± 0.16	2.34 ± 0.41	2.86 ± 0.44	2.86 ± 0.32
r_{peak} (nm)[b]	1.70 ± 0.00(1)	2.37 ± 0.01	2.93 ± 0.02	2.99 ± 0.03
N	1997	1596	811	1098
fwhm (nm)[c]	0.30	0.93	0.74	0.43

[a] Number average radius. Each particle is assigned the radius of a circle with equivalent cross-sectional area. Uncertainty reflects standard deviation of radius distribution. [b] Peak radius of a Gaussian fit to radius distribution. Uncertainty reflects confidence limit in r_{peak} fit parameter. [c] FWHM of Gaussian fit.

A majority of particles in the core/shell samples showed a radius larger than that of the cores and commensurate with shell growth; however, **CdSe/CdS_DOM** (**Figure 4.9C**) and **CdSe/CdS_THM** (**Figure 4.9D**) showed larger average and peak radius compared to **CdSe/CdS_OAM** (**Figure 4.9B**). Additionally, both **CdSe/CdS_DOM** and **CdSe/CdS_THM** showed narrower size distributions and showed particles with more uniform shapes. Inspection of the STEM images reveals the presence of a significant number of particles smaller than the CdSe cores in **CdSe/CdS_OAM**: these can easily be seen in STEM images with higher magnifications (**Figure 4.11**). Although the STEM images cannot clearly resolve CdS from CdSe, we can assign the smallest particles as a CdS nanoparticle side product. These small particles contribute to the smaller average radius (r_{avg} = 2.34 ±0.41 nm) in this sample. The peak radius rpeak primarily describes the core/shell product; it is smallest in **CdSe/CdS_OAM** as well, indicative of thinner CdS shells due to loss of material to the side product. At the same time, the distribution of radius for **CdSe/CdS_OAM** (fwhm=0.93 nm) is broader than **CdSe/CdS_DOM**

(fwhm=0.74 nm) and **CdSe/CdS_THM** (fwhm=0.43 nm). Core/shell particles growing in trihexlylamine maintained a very narrow size distribution, nearlyas good as the cores (fwhm=0.30 nm), although a small fraction of particles with radius down to 2.5 nm (**Figure 4.9H**) remained present.

The STEM results confirm that the more highly substituted amines dioctylamine and especially trihexylamine were effective in suppressing the nucleation of small particles during shell growth, and the observation of small particles in the **CdSe/CdS_OAM** and **CdSe/CdS_DOM** samples corroborates the assignment of the blue PL peaks as radiative recombination from CdS nanoparticles. Examination of the shapes of nanocrystals in the three core/shell samples appears to show greater roundness in **CdSe/CdS_DOM** and **CdSe/CdS_THM**, suggesting that conditions that suppress nucleation also help to enforce isotropic shell growth. A similar trend was observed for shell growth in oleylamine at low dose per cycle in our previous work.[189]

Comparing with the radius histograms, it is shown that the radius of the CdSe core r=1.70 nm, however in **Figure 4.9F**,**G** for **CdSe/CdS_OAM** and **CdSe/CdS_DOM**, that showed the existence of a fraction of particles with r <1.70 nm and with significant counts. Even though CdSe cores might contribute to these counts because of its size distribution (fwhm=0.30 nm), there are some particles even with r lower than 1.40 nm, which can also be seen in STEM images with Higher magnifications.(**Figure 4.11**) As in **CdSe/CdS_THM** there are no particles with radius lower than 2 nm. We believed these particles are the CdS nucleation that generated while using oleylamine and dioctylamine with stronger nanoparticle surface interactions as solvents for particle growth, in accordance to our conclusion from previous sections.

Finally, we noted that although the STEM grids were prepared with same method and same concentration of QDs for all samples, **CdSe/CdS_OAM** formed a close-packed pattern while **CdSe/CdS_DOM** and **CdSe/CdS_THM** were more randomly dispersed, which could imply a difference in solubility or intermolecular forces brought about by the different coordinating amine solvents. It is interesting that **CdSe/CdS_OAM** formed/self-assembled a closer hexagonal pattern on the STEM grid than **CdSe/CdS_DOM** and **CdSe/CdS_THM** which were more randomly and widely dispersed. Although the assembly of nanoparticle into macroscopic structure is driven by particle concentrations, solvent, evaporation method, temperature, substrate and interactions between particles; and such arrays typically show hexagonal packing corresponding to maximal packing density of nanoparticles in 2D and the strongest van der Waals interactions,[222] the fact that the same STEM grids were prepared with same method (same dilution solvent and same evaporation method) and same concentration of QD samples (See section 4.11 for experimental details) suggesting the reasons for differences in patterns should associated with the nature of the surface passivating ligands. Our previous experiments lead to the conclusions that the interaction affinities of amines to the nanoparticle surface are in the order of oleylamine > dioctylamine > trihexylamine from strong to weak. (Also can be proved by the ^{1}H NMR in section 4.9) For **CdSe/CdS_OAM**, large amount of oleylamine still bonded to the particle surface even after purification because of its strong affinity. We argue the strong bonded oleylamine ligand and such high ligand density on the nanoparticles surface enhanced the hexagonal order by increasing interactions between particles, with less particle mobility the hexagonal pattern can be stable when formed upon evaporation; for **CdSe/CdS_THM**, trihexylamine ligands has nearly no

interaction with nanoparticles surface, with less particle to particle (or inter-particle) interactions the nanoparticles almost moved freely to all directions in 2D when evaporated and cannot form a stable hexagonal pattern.(**Figure 4.9D**) The larger particle spacing in **Figure 4.9B** than in **Figure 4.9D** also indicating the presence of oleylamine with longer length as capping ligand in **CdSe/CdS_OAM** than trihexylamine in **CdSe/CdS_THM**. Even though, structure of trihexylamine is beneficial to prevent aggregation. (**Figure 4.10** showed precipitation/aggregation of particles at the bottom) For **CdSe/CdS_DOM**, with the bonding affinity of dioctylamine is between the other two amines, partially hexagonal pattern can be formed with majority of particles are dispersed randomly. (**Figure 4.9C**)

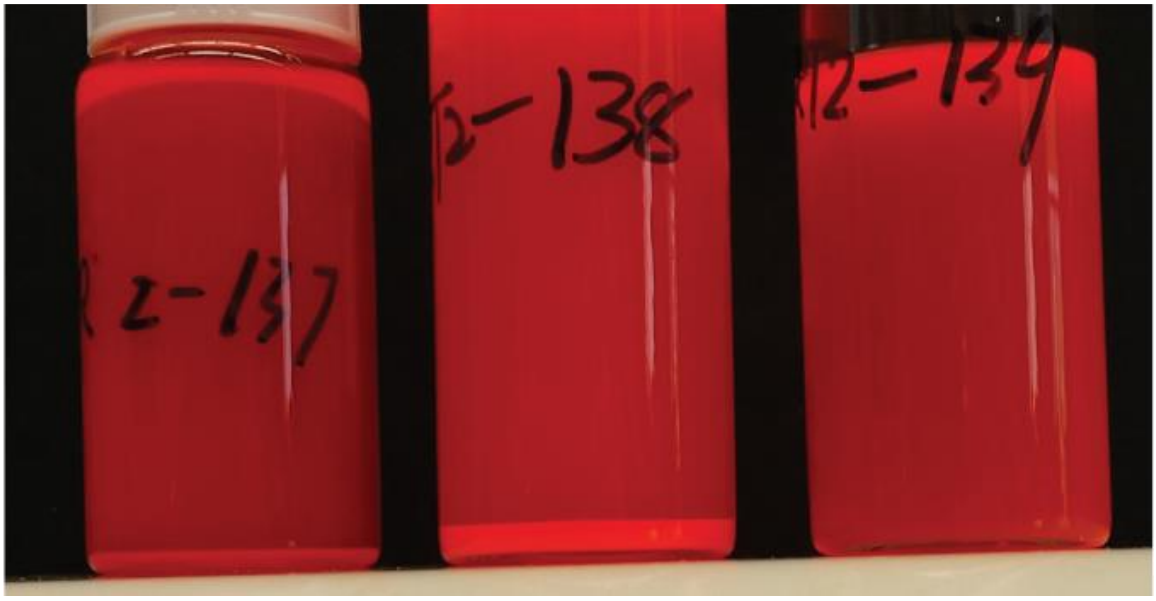

Figure 4.10 As synthesized **CdSe/CdS_OAM** (left), **CdSe/CdS_DOM** (center) and **CdSe/CdS_THM** (right) in solvent mixture of different amines, showed different solubility.

Figure 4.11 displayed the STEM images with high magnifications; all scale bars are 5 nm in length. The images for CdSe cores (**Figure 4.11A-D**) showed that they are more uniform in size and shape as well as with narrow size distributions. It is also clear in the images for **CdSe/CdS_OAM**, the particle sizes varied in a very broad range (**Figure 4.11E-F**); ultra-small particles can be seen especially along the edges of the closely packed pattern of larger particles (**Figure 4.11E-F**); particles with completely different morphologies can also be found including sphere, ellipse and even trapezoid in shapes (**Figure 4.11G-H**).

In comparison of **Figure 4.11I-J** and **Figure 4.11M-N** for **CdSe/CdS_DOM** and **CdSe/CdS_THM**, it is shown that the difference in sizes are small, and the particles are nearly spherical and with uniform morphology. Even though couple of small particles can be found in **Figure 4.11J-L** for **CdSe/CdS_DOM**, the sizes are still close to the majority of particles and larger than the CdSe core sizes, the distribution of sizes is narrower than **CdSe/CdS_DOM.** For **CdSe/CdS_THM** (**Figure 4.11M-P**) there are almost no difference in terms of size for all the particles, at the same time, and all particles are with consistent and uniform morphology. The HR-STEM images directly illustrated the major difference among the CdSe core and the typical samples for the core/shell particles grew in different amines, which in good agreement to our conclusions that trihexylamine is better in terms of resulting high quality core/shell particles with higher synthetic yield, better size distribution and morphology via the SILAR method.

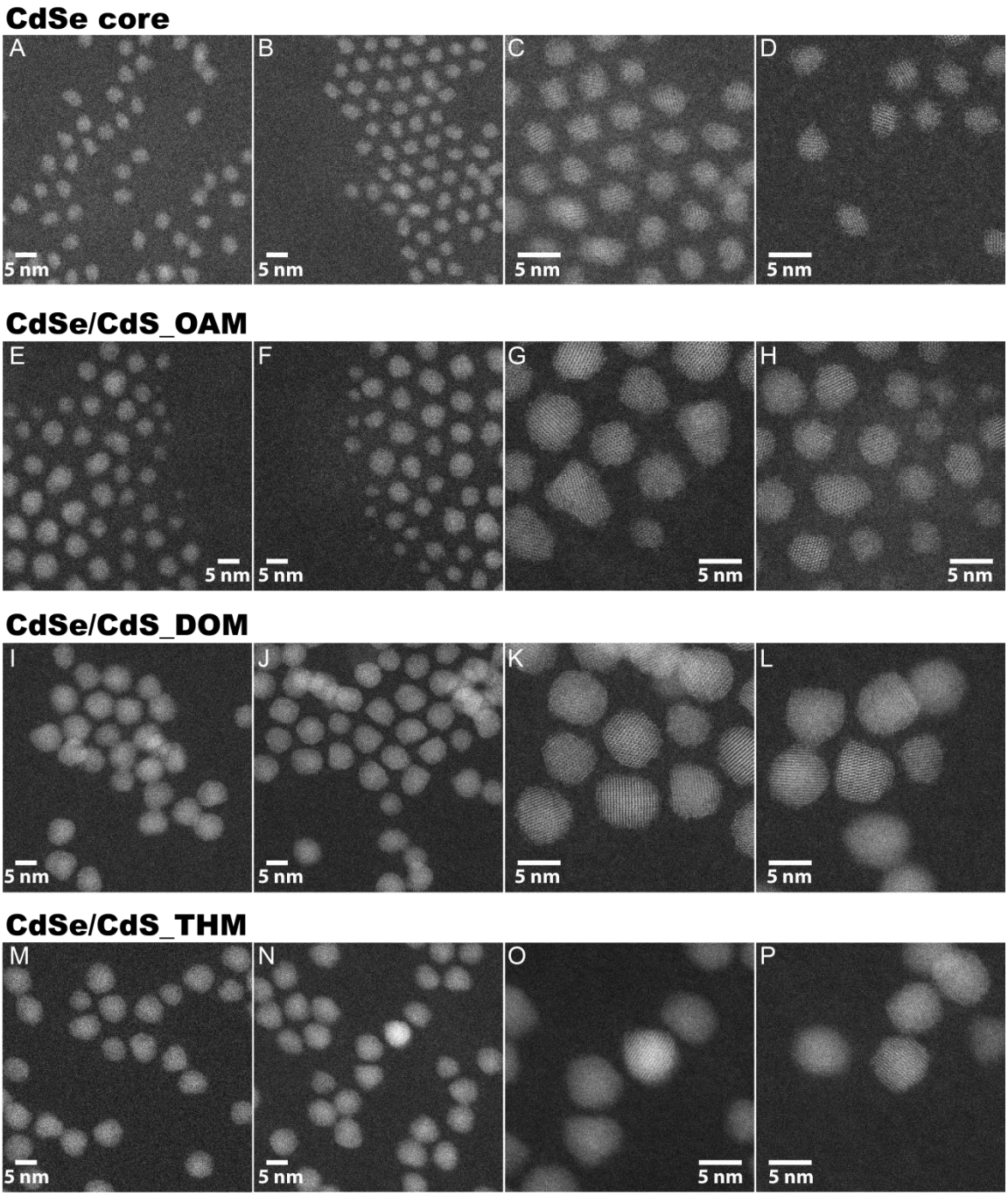

Figure 4.11 High magnification Scanning Transmission Electron Microscopy images for CdSe cores and sample **CdSe/CdS_OAM CdSe/CdS_DOM, CdSe/CdS_THM.** The scale bar is 5nm.

4.9. ^{1}H NMR

We investigated amine interactions with the CdSe QD surface under mild and controlled conditions using ^{1}H NMR of mixtures of CdSe cores and each of the amine solvents diluted in d_8-toluene. The distinguishable chemical shift of α-proton at around 2.5 ppm for all three amines has enable us to monitor and understand the behavior of amines mixed with nanoparticles.

Figure 4.13A shows the α-proton and olefin peaks of oleylamine in the presence of CdSe cores, as well as a reference spectrum of oleylamine in toluene. In the presence of the QDs, the peaks are significantly broadened, which is evidence of a strong interaction between oleylamine and the nanoparticle surface.[183] In contrast, in **Figure 4.13B,C** ,a mixture of dioctylamine with the CdSe cores shows only a small degree of broadening and a small downfield shift, and a mixture of trihexylamine with the CdSe cores shows almost no change versus the free molecule. These results indicate weaker interactions between dioctylamine and trihexylamine molecules and the nanoparticle surface compared to oleylamine.

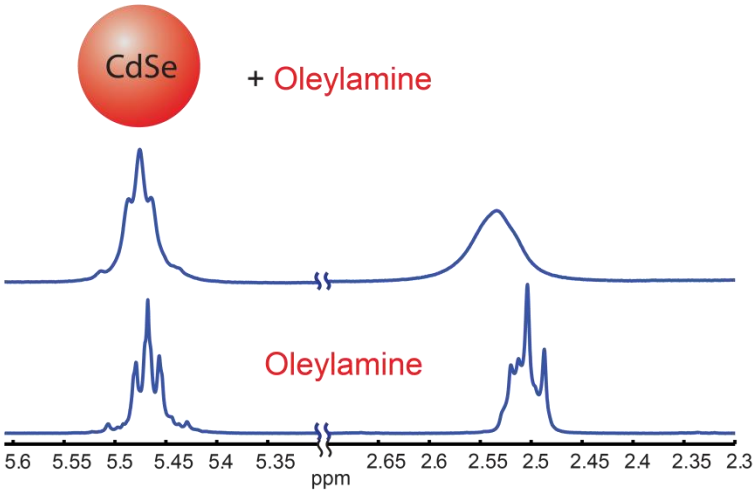

Figure 4.12 ^{1}H NMR for olefin peaks and α-proton for CdSe core + oleylamine, and pure oleylamine

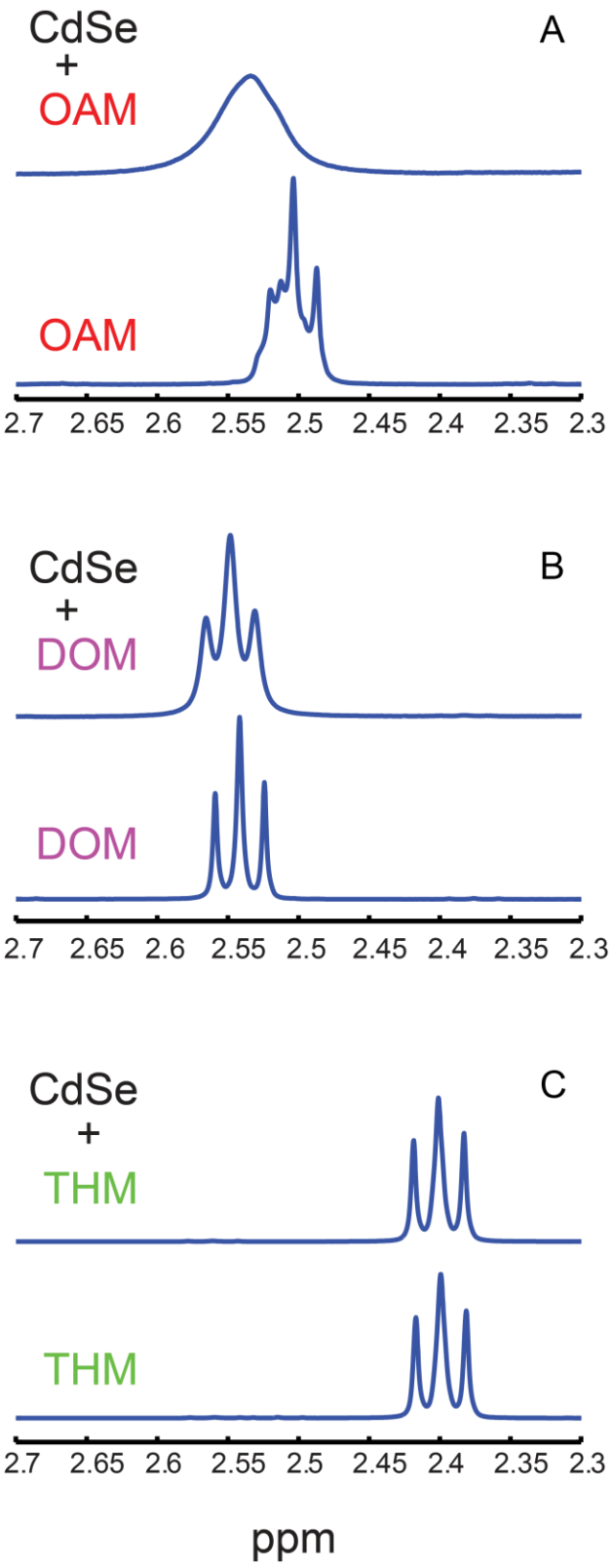

Figure 4.13 ^{1}H NMR for α-proton for three amines in CdSe core and comparison with pure amines.

4.10. Conclusion

High photoluminescent quantum yield, narrow emission and photostability of colloidal semiconductor core/shell nanoparticles are the most striking properties for applications as light emitting diodes, bio-imaging/labelling and low threshold lasers. In order to maintain these photophysical properties, it is very fundamental and important to achieve high quality particles with defect free and robust structure to begin with, before any other studies, treatments and applications. We have studied the influence of solvent mixture with three types of amines on the growth of colloidal CdSe/CdS core/shell nanoparticles via SILAR technique. We found that during the growth, the conventional solvent mixture with oleylamine will lead to incomplete metal precursor conversion, as a result cannot limit the cross-reaction of shell precursors and cause nucleation of CdS nanoparticles. We have utilized PL emission, PLE scan and STEM to prove the existence of the CdS nanoparticles. And so the final as-synthesized core/shell particles suffer with low synthetic yield, impurity of other particles, broad size distribution and morphology. Switching solvent mixtures to tertiary amine which has less interaction with nanoparticle surfaces will result in enhancement of precursor conversion, and increased synthetic yield, larger particles, elimination of nucleation, and narrow size distribution and uniform morphology. We have design titration experiments and proved with Langmuir-isotherm model that tertiary amine has greatly enhanced the fractional occupation of shell precursor equivalents on the QD surface.

Even though the photoluminescent life time of core/shell particles is longer in the environment of primary amine than tertiary amine, it is because the nanoparticle surface is better passivated/interacted by primary amine than tertiary amine. And we have proved such interaction difference by ^{1}H NMR. In fact, during shell growth, primary amines

occupies the nanoparticle surfaces because of such passivation/interaction, the introduced shell precursors have to compete with primary amines to react with nanoparticle surface, and lower the probabilities of precursor conversions. Tertiary amine doesn't have such interaction and leave a bare, more active nanoparticle surface for further growth of shells. Without surface passivation for the final core/shell particles in tertiary amine, particles have slightly lower brightness and shorter PL lifetime. However, after the high quality core/shell particles are formed, applying further ligand exchange with primary amine or other ligands with even better passivation will result in regeneration of quantum yield. And it could perform even better photophysical properties and robust to further applications.

Based on the above systematic study of the effect of amines in growing CdSe/CdS core/shell nanoparticles, we can conclude that oleylamine effectively competes with the precursor $Cd(oleate)_2$ for occupation of nanocrystal surface sites, leading to a significant amount of cross-reaction and nucleation of CdS particles during CdS shell growth by SILAR (**Figure 4.14**). We have confirmed that replacing oleylamine with a secondary amine, dioctylamine, suppresses nucleation and improves core/shell growth, and we have shown that moving to a tertiary amine, trihexylamine, is even more effective. We have also shown through measurement of Cd fractionation in collected aliquots, time-resolved PL, and NMR spectroscopy that the more highly substituted amines bind less strongly to the CdSe QD surface and permit greater precursor conversion under experimental conditions. While highlighting the limitations of oleylamine as a solvent for SILAR shell growth on CdSe, our result suggests that solvents that promote greater precursor conversion can indeed steer the course of the reaction toward layer by layer growth

without solution-phase cross reactions. This is an important prerequisite for the development of SILAR techniques for more sophisticated epilayer structures and colloidal substrates.

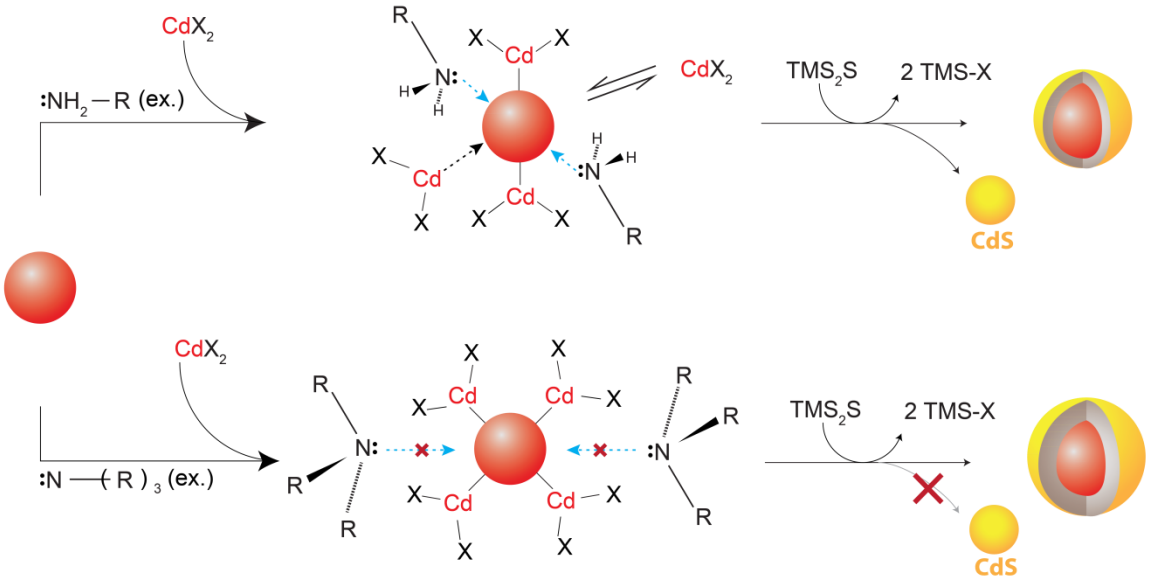

Figure 4.14 Scheme of influences of types of amines on core/shell quantum dots growth

To sum up, it is proved by our study that high quality core/shell nanoparticles could be achieved when growing in a solvent mixture with tertiary amine which has less interaction with particle surface and good solubility for particles. A further purification by GPC followed with ligand exchange could provide more surface protection and passivation and lead to enhanced photostability. Potentially, the combination of the optimized solvent condition and the modified SILAR procedure could lead to even better control and higher synthetic yield.

The next section presents the preliminary results when we tried growing CdSe/CdS core/shell particles in a sub-monolayer dose SILAR procedure in different amine mixture.

4.11. Preliminary results: grow with sub-ML dose SILAR in optimized solvent

Based on the research about the core/shell nanoparticles growth, we proved that modifying the growth procedure to sub-monolayer equivalent dose via SILAR and optimization of the solvent condition can increase the synthetic yield as well as producing high quality core/shell particles with narrow size distribution and uniform morphology respectively. From the results of the titration experiment of Cd precursor and the Langmuir-isotherm fits in section 4.7, significant amount free Cd still existent after the addition of one ML eq. even under solvent mixture with trihexylamine, which leaving some space for growth improvements. Potentially, combination of the sub-monolayer dose method and optimized solvent should be able to achieve a better result and core/shell particles with better qualities. In this section, we reported preliminary experimental results for the core/shell particles grown by the modified SILAR procedures with sub-monolayer dose method in optimized solvent conditions. Parallel experiments with different amines were tried for comparison.

Methods and experimental design for CdSe cores preparation as well as the core/shell growth are the same as described in the experimental section 4.12. Sample entry is listed in **Table 4.6** below and in **Figure 4.15**-**Figure 4.17**:

Table 4.6 Matched core/shell growth results with sub-monolayer dose of 0.6 ML eq. with different amine solvents

Entry	core radius[a] (nm)	Shell (ML)	Amine solvent[b]	Abs. peak (nm)	Abs. width[c] (meV)	PL peak (nm)	PL width[d] (meV)
CdSe/CdS_1	1.61	6	**oleylamine**	586	113	600	89
CdSe/CdS_2	1.62	6	**dioctylamine**	585	99	597	92
CdSe/CdS_3	1.62	6	**trihexylamine**	581	93	591	84

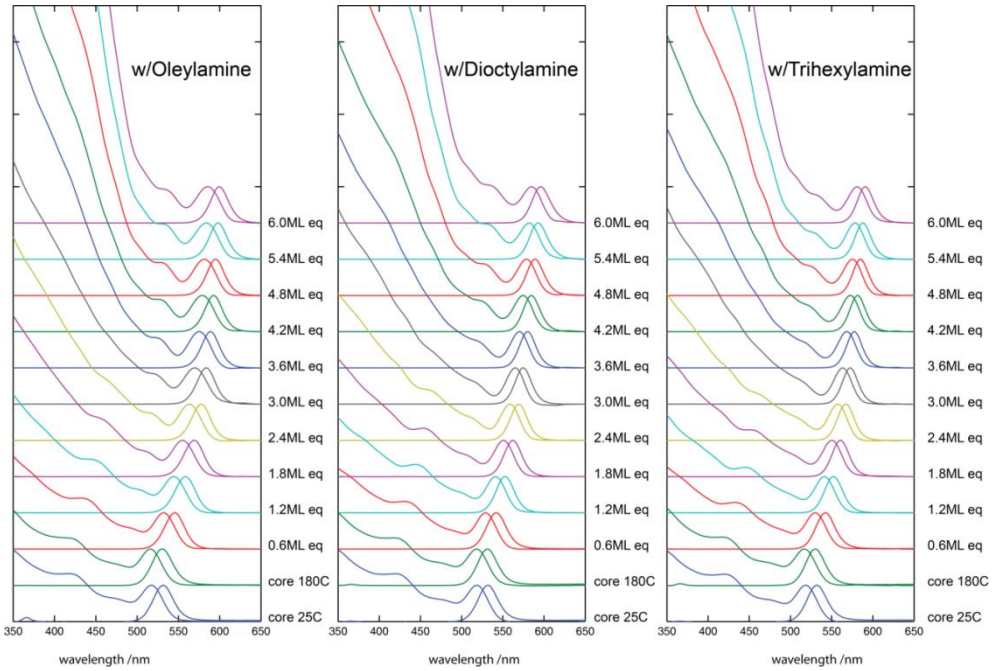

Figure 4.15 1st absorption peak and emission are normalized to 1.

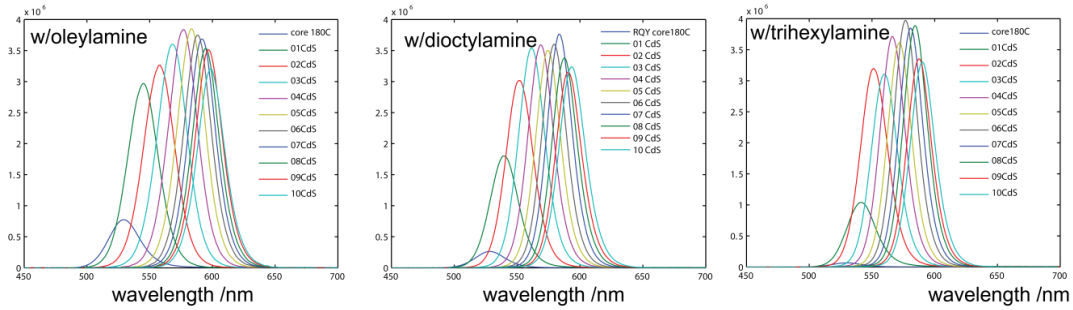

Figure 4.16 Raw emission over the particle growth.

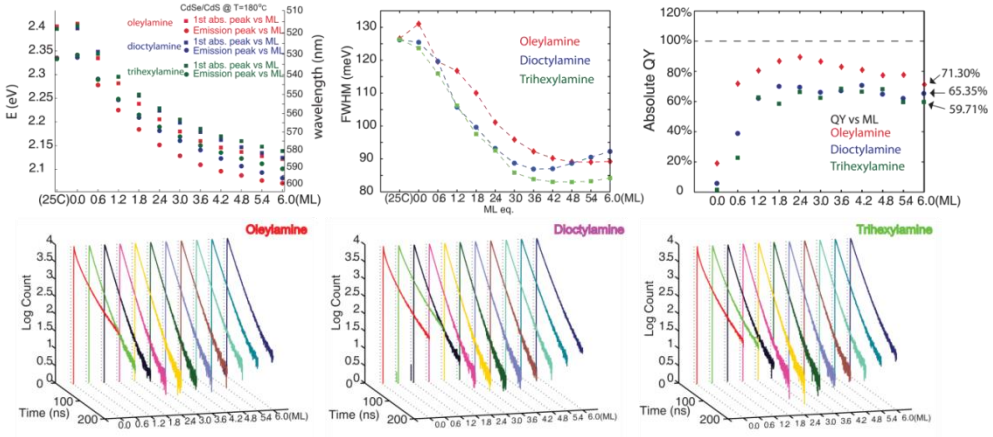

Figure 4.17 Energy vs. ML eq.; FWHM of emission; Relative QY and PL lifetime

In **Figure 4.15-Figure 4.17, p**reliminary results indicated similar conclusions as we discussed previously in this chapter. Trihexylamine leads to core/shell particles with narrow size distribution based on FWHM of emission in **Figure 4.17**, more measurement such as HR-TEM or HR-STEM could provide more information to support our conclusion.

4.12. Supporting information

Raw HNMR spectrum

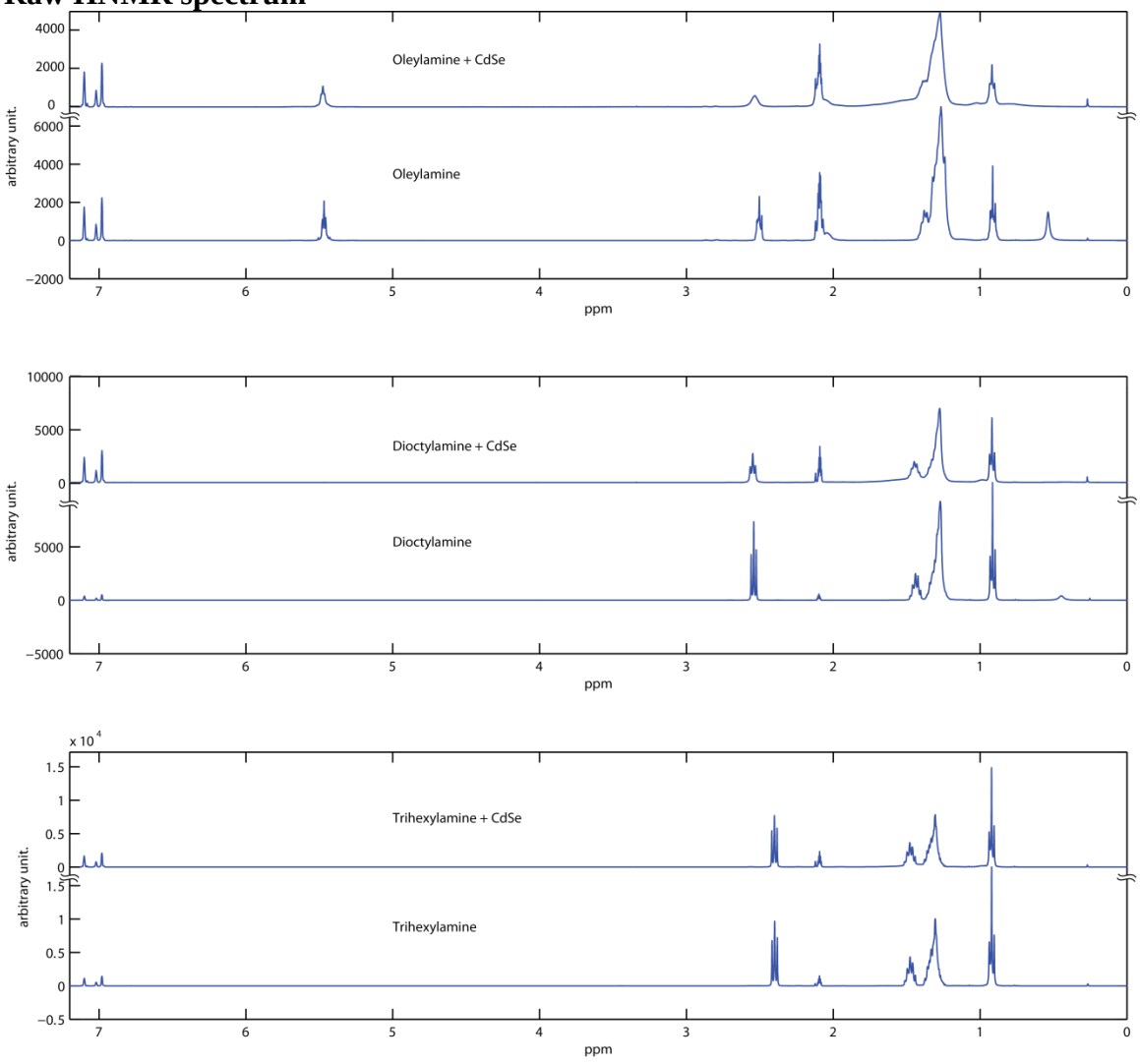

Figure 4.18 Full ^{1}HNMR Spectrum for CdSe/CdS_OAM (B, F), CdSe/CdS_DOM (C, G), and CdSe/CdS_THM

Time-resolved photoluminescence measurement and methods of analysis can be found in section 3.9 in Chapter 3.

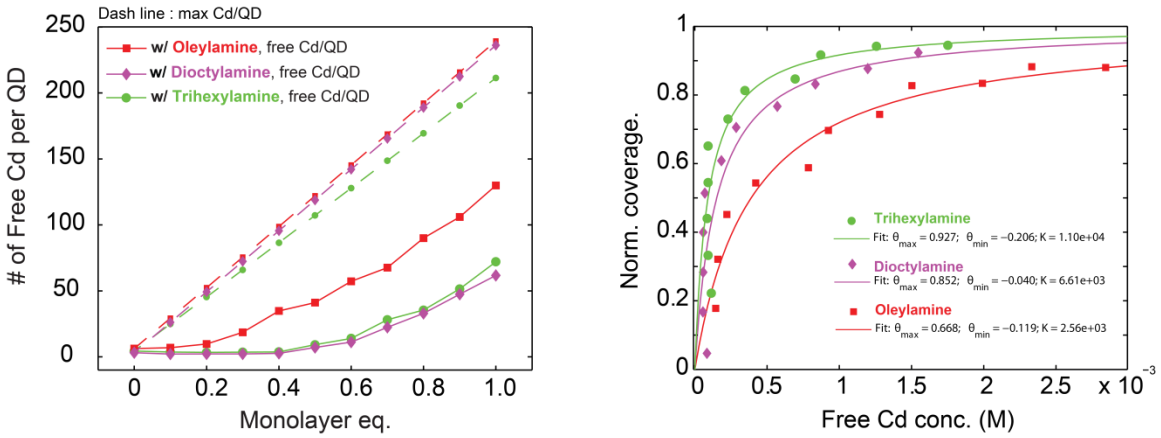

Figure 4.19 Experimental data for titration of $Cd(oleate)_2$ into CdSe cores, under condition of solvent mixture of oleylamine, dioctylamine and trihexylamine. Each titration with dose of 0.1 ML eq. of $Cd(oleate)_2$. Left: Free Cd concentration changes over ML eq. up to 1 ML; right: normalized surface coverage vs. free [Cd].

Methods for measurements and calculations in **Figure 4.19** are the same as section 4.7, except experiments here with titration dose of 0.1 ML eq. Equilibrium constant follows the same trend $K_{THM} > K_{DOM} > K_{OAM}$ as the titration experiment in section 4.7. The absolute values of corresponded equilibrium constants here based on 0.1 ML eq. titration manner are different compare to the titration in 0.2 ML eq. manner, might because that the concentrations of QDs of each aliquot in 0.1 ML eq. titration manner are actually half of the QD concentrations of each aliquot in 0.2 ML eq. titration manner, however the ratio of equilibrium constants between two titration experiments are consistent, indicating the good agreement to the conclusion that larger equilibrium constant of $Cd(oleate)_2$ to the CdSe core surface and higher surface coverage under the solvent mixture of tertiary amines. And the precursor conversion efficiency is enhanced as well as high surface saturation which is optimized for isotropic shell growth.

4.13. Experimental section

Materials. The following chemicals were used as received. Cadmium oxide (CdO; 99.999%), trioctylphosphine (TOP; 97%), and trioctylphosphine oxide (TOPO; 99%) were purchased from Strem Chemicals. Oleic acid (OA; 99%), 1-octadecene (ODE; 90% technical grade), 1-tetradecylphosphonic acid (TDPA; 98%), and Se (99.999%) were purchased from Alfa Aesar. Dio-n-ctylamine, 98% (LOT:10178704) and Tri-n-hexylamine, 97% (LOT:G18S028) are purchased from Alfa Aesar. Decylamine (95%) was purchased from Sigma Aldrich. Oleylamine (80-90%) and bis(trimethylsilyl) sulfide ($(TMS)_2S$; 95%) were purchased from Acros Organics. Toluene-d_8 (D, 99.5%) was purchased from Cambridge Isotope Laboratories, Inc. 200 proof ethyl alcohol (ethanol) was obtained from Decon Laboratories, Inc. Acetone (99.9%) was purchased from VWR. Ethanol (99.9%) was purchased from Fisher Scientific. TOPSe (2.2 M) was prepared by dissolving Se in TOP. A stock solution of $Cd(oleate)_2$ (0.2 M) in ODE was prepared by heating CdO in ODE with 2.2 equiv. of oleic acid at 260 ℃ under nitrogen, followed by degassing under vacuum at 100 ℃ for 20 min. The sulfur precursor was 0.1 M solution of $(TMS)_2S$ dissolved in TOP. Nanocrystal core and shell growth was carried out under nitrogen (N_2) using Schlenk line techniques; air-sensitive reagents were prepared in a nitrogen filled glovebox.

Synthesis of CdSe cores: A hot-injection technique was applied for synthesis of CdSe nanocrystals (NCs) cores.[62] For a representative synthetic route, CdO (0.12 g) was heated with TDPA (0.5500 g) at 330 ℃ in a solvent TOP (6 ml) and TOPO (6 g) under nitrogen flow until the solution became colorless. Following removal of evolved H2O under vacuum at 130 ℃, the solution was heated again to 360 ℃ under nitrogen. As-prepared TOPSe (1.3 mL) was injected rapidly into the reaction pot, which was

immediately allowed to cool down to room temperature and stored as a yellow waxy solid. The Cd:TDPA:Se molar ratio is 1:2:3. The core radius was estimated by a calibration curve[62,118] describing the radius as a function of the position of the lowest-energy absorption peak. One batch of cores provided sufficient material for several core/shell growth experiments; all core/shell particles were made based on the CdSe QD cores taken from the same batch.

Synthesis of core/shell nanoparticles in different amines: The method for CdSe/CdS core/shell particle growth was modified from our previous work.[62,189] (see Chapter 1) The difference was switching different types of amines (oleylamine, dioctylamine, trihexylamine) in the solvent mixture. And the Cd precursor was prepared by diluting $Cd(oleate)_2$ stock solution in a solvent of 50:50 ODE and TOP with two equivalents of the same amine in the solvent mixture (vs. Cd) added to yield a Cd concentration of 0.1 M.; The sulfur precursor was 0.1 M solution of $(TMS)_2S$ dissolved in TOP. The CdS shell was grown by alternatively introducing Cd & sulfur precursors into the reaction flask, 1 ML eq. (or 0.6 ML eq.) of precursors added per cycle, and forming 6 ML of CdS shell in total after six (or ten) cycles. Reaction progress was monitored by periodically withdrawing a small aliquot of a measured volume (typically 50 μL) from the reaction flask and diluting it in hexanes at room temperature; these aliquots were analyzed for UV-vis absorption and fluorescence emission in hexanes solution. The absorption spectra were recorded by a Thermo Scientific Evolution Array UV-visible spectrophotometer with hexane as the solvent as well as the blank in a 1 cm path quartz cuvette. The emission spectra were recorded by an Ocean Optics USB 4000 spectrometer under 365 nm LED excitation.

Titration of Cd(oleate)2 to CdSe cores in different amines. CdSe cores were washed via two cycles of precipitation/redissolution as described previously, and then brought into a known volume of hexane for absorption measurements to determine the size and quantity. Then injected into the overcoating solvent and degassed at 80 ℃ for 2 h to remove hexane. The solvent was a mixture of amines and ODE with a volume ratio of 1:2, 9 mL in total. Different amines (Oleylamine/Dioctylamine/Trihexylmaine) were used for the solvent mixture. After degasing the system was placed under nitrogen and brought to growth temperature (180 ℃) before titrating with Cd precursor. The Cd precursor was prepared by introducing $Cd(oleate)_2$ stock solution with 2 equiv (vs Cd) of the same amine as in the solvent mixture, balanced by TOP to yield a Cd concentration of 0.1 M. A computer-controlled syringe pump (J-KEM Scientific Dual Syringe Pump, model 2250) was used to introduce reagents according to the dose and timing. Briefly, a series of additions of 0.2 ML eq. dose each, up to 1 ML eq., followed by 5 additions of 0.48 ML eq. of Cd precursor (0.1 M) was added periodically at a constant rate over a 3 min injection time, a total of 15 min was allowed to elapse for each addition. A small aliquot of 25.0 μL ($V_{aliquot}$) was withdrawn by Hamilton®Microliter syringe from the reaction flask and injected into minimum amount hexane (2 mL) at room temperature. Then, the aliquots were treated by adding 1 mL of acetone and 3 mL of methanol to precipitate QDs; followed centrifuging at 5000 rpm (~3000 × g) for 5 min. The supernatant was transferred into 20 mL sealed vials, and checked with UV light to make sure that it showed no absorption or fluorescence indicative of QDs left in solution. The samples were dried by removing the solvent by vacuum pump. A 1 mL portion of aqua regia (3:1 hydrochloric acid/nitric acid. Caution! Highly corrosive; oxidizer) was introduced and

was allowed to digest the sample for 2 hrs. Each of the samples was then quantitatively transferred into a volumetric flask and brought to 50.0 mL with 2% HNO_3, and the concentration of Cd^{2+} was measured by a Themo-Finnigan Element XR ICP-MS. A control experiment using $Cd(oleate)_2$ in ODE was designed to investigate the accuracy of this method in quantifying the amount of Cd^{2+}. The error was determined to be less than 6%.

The concentration of free Cd^{2+} measured by ICP-MS is $[Cd]_{ICP\text{-}MS}$ (ppb.) can be converted to [Cd]:

$$[Cd] = [Cd]_{flask} = [Cd]_{aliquot} = \frac{[Cd]_{ICP-MS}(ppb.) \times 1\mu g / L \times 50mL}{1ppb. \times MW_{Cd}(g / mol) \times V_{aliquot}} \quad \text{.....eq. 14}$$

$$[Cd]_i = [Cd]_{i,\,flask} = [Cd]_{i,aliquot} = \frac{[Cd]_{i,ICP-MS}(ppb.) \times 1\mu g / L \times 50mL}{1ppb. \times MW_{Cd}(g / mol) \times V_{aliquot}} \quad \text{.....eq. 15}$$

i indicate the concentration after the *i*th titration/addition; *QD* concentration [*QD*] can be determined by:

$$QD_i = \left(QD_{flask} - QD_{i-1}\right) \times \left(\frac{V_{aliquot}}{V_{tot} + \sum_i V_i - (i-1) \cdot V_{aliquot}} \right) \quad \text{.....eq.16}$$

$$[QD_i] = \frac{QD_i}{V_{alilquot}} \quad \text{.....eq.17}$$

where QD_i is the amount of *QD*s in the *i*th aliquot; QD_{flask} is initial total amount of *QD*s; V_i (mL) is the volume of the *i*th titration/addition point; V_{tot} = 9 mL is the initial total volume.

The added amount of Cd after the *i*th titration point is:

$$added\_Cd_i = \left(\sum_i V_i \times (0.1M) - \sum_i added\_Cd_{i-1} \right) \times \left(\frac{V_{aliquot}}{V_{tot} + \sum_i V_i - (i-1) \cdot V_{aliquot}} \right)$$

……eq. 18

$$[added\_Cd_i] = \frac{added\_Cd_i}{V_{aliquot}}$$ ……eq. 19

$$\max\_Cd_i = added\_Cd_i + initial\_free\_Cd \cdot V_{aliquot}$$ ……eq. 20

$$[\max\_Cd_i] = \frac{\max\_Cd_i}{V_{aliquot}}$$ ……eq. 21

Initial_free_Cd=$[Cd]_0$ is the free Cd prior to addition of Cd(oleate)$_2$, determined by ICP-MS. So, the bonded Cd per QD can be determined by:

bonded Cd per QD = ($[\max\_Cd_i] - [Cd]_i$) / $[QD]$ .....eq. 22

(or **bonded Cd per QD** = ($\max\_Cd_i - Cd_i$) / QD) .....eq. 23

The **1 ML eq. of Cd per QD** can be determined by:

1 ML eq. of Cd per QD= $\frac{\frac{4\pi}{3}\left[\left(r+\frac{c}{2}\right)^3 - r^3\right]}{V_{m,CdSe}}$ .....eq. 24

Where c is the wurtzite *c*-axis unit cell dimension for CdSe; r is the radius of the QD; $V_{m,CdSe}$ is molar volume of CdSe.

Scanning Transmission Electron Microscopy imaging: After purification, the CdSe or CdSe/CdS core/shell QDs were brought into hexane to form a dilute solution (1.1 μM), one drop of the solution was drop-casted on a clean TEM grid (400 mesh Cu grid with ultrathin carbon support film, Type-A, Ted Pella, Inc.) and pumped dry under vacuum for 2 hours. The STEM samples were imaged by JEOL 2100F 200 kV FEG-

STEM/TEM equipped with a CEOS CS corrector on the illumination system. Prior to high magnification observation, a large specimen area was pre-irradiated with electrons for 10 minutes to polymerize surface hydrocarbons and therefore prevent their diffusion to the focused probe. The geometrical aberrations were measured and controlled to provide less than a $\pi/4$ phase shift of the incoming electron wave over the probe-defining aperture of 17.5 mrad. High angle annular dark-field (HAADF) STEM images were acquired on a Fischione Model 3000 HAADF detector with a camera length such that the inner cut-off angle of the detector was 75 mrad. A pixel dwell time of 16 μs was chosen.

REFERENCES

(1) Smith, A. M.; Nie, S. *Analyst* **2004**, *129* (8), 672–677.

(2) Kuno, M.; Lee, J. K.; Dabbousi, B. O.; Mikulec, F. V.; Bawendi, M. G. *J. Chem. Phys.* **1997**, *106* (23), 9869–9882.

(3) Adam, S.; Talapin, D. V.; Borchert, H.; Lobo, A.; McGinley, C.; Castro, A. R. B. de; Haase, M.; Weller, H.; Möller, T. *J. Chem. Phys.* **2005**, *123* (8), 084706.

(4) Haug, H.; Koch, S. *Quantum Theory of the Optical and Electronic Properties of Semiconductors*, 3rd edition.; World Scientific Pub Co Inc, 1994.

(5) Efros, A. L.; Rosen, M. *Annu. Rev. Mater. Sci.* **2000**, *30* (1), 475–521.

(6) Murray, C.; Norris, D.; Bawendi, M. *J. Am. Chem. Soc.* **1993**, *115* (19), 8706–8715.

(7) Liu, W.; Howarth, M.; Greytak, A. B.; Zheng, Y.; Nocera, D. G.; Ting, A. Y.; Bawendi, M. G. *J. Am. Chem. Soc.* **2008**, *130* (4), 1274–1284.

(8) Liu, W.; Greytak, A. B.; Lee, J.; Wong, C. R.; Park, J.; Marshall, L. F.; Jiang, W.; Curtin, P. N.; Ting, A. Y.; Nocera, D. G.; Fukumura, D.; Jain, R. K.; Bawendi, M. G. *J. Am. Chem. Soc.* **2010**, *132* (2), 472–483.

(9) Larson, D. R.; Zipfel, W. R.; Williams, R. M.; Clark, S. W.; Bruchez, M. P.; Wise, F. W.; Webb, W. W. *Science* **2003**, *300* (5624), 1434–1436.

(10) Wu, X.; Liu, H.; Liu, J.; Haley, K. N.; Treadway, J. A.; Larson, J. P.; Ge, N.; Peale, F.; Bruchez, M. P. *Nat. Biotechnol.* **2003**, *21* (1), 41–46.

(11) Medintz, I. L.; Uyeda, H. T.; Goldman, E. R.; Mattoussi, H. *Nat Mater* **2005**, *4* (6), 435–446.

(12) Erathodiyil, N.; Ying, J. Y. *Acc Chem Res* **2011**, *44* (10), 925–935.

(13) Lemon, C. M.; Curtin, P. N.; Somers, R. C.; Greytak, A. B.; Lanning, R. M.; Jain, R. K.; Bawendi, M. G.; Nocera, D. G. *Inorg. Chem.* **2014**, *53* (4), 1900–1915.

(14) Zhang, B.; Hu, R.; Wang, Y.; Yang, C.; Liu, X.; Yong, K.-T. *Rsc Adv.* **2014**, *4* (27), 13805–13816.

(15) Anikeeva, P. O.; Halpert, J. E.; Bawendi, M. G.; Bulović, V. *Nano Lett.* **2009**, *9* (7), 2532–2536.

(16) Dabbousi, B. O.; Bawendi, M. G.; Onitsuka, O.; Rubner, M. F. *Appl. Phys. Lett.* **1995**, *66* (11), 1316.

(17) Lim, J.; Jeong, B. G.; Park, M.; Kim, J. K.; Pietryga, J. M.; Park, Y.-S.; Klimov, V. I.; Lee, C.; Lee, D. C.; Bae, W. K. *Adv. Mater.* **2014**, *26* (47), 8034–8040.

(18) Bae, W. K.; Park, Y.-S.; Lim, J.; Lee, D.; Padilha, L. A.; McDaniel, H.; Robel, I.; Lee, C.; Pietryga, J. M.; Klimov, V. I. *Nat. Commun.* **2013**, *4*.

(19) Qian, L.; Zheng, Y.; Xue, J.; Holloway, P. H. *Nat Photon* **2011**, *advance online publication*.

(20) Choi, M. K.; Yang, J.; Kang, K.; Kim, D. C.; Choi, C.; Park, C.; Kim, S. J.; Chae, S. I.; Kim, T.-H.; Kim, J. H.; Hyeon, T.; Kim, D.-H. *Nat. Commun.* **2015**, *6*.

(21) Yang, Y.; Zheng, Y.; Cao, W.; Titov, A.; Hyvonen, J.; Manders, J. R.; Xue, J.; Holloway, P. H.; Qian, L. *Nat. Photonics* **2015**, *9* (4), 259–266.

(22) Dai, X.; Zhang, Z.; Jin, Y.; Niu, Y.; Cao, H.; Liang, X.; Chen, L.; Wang, J.; Peng, X. *Nature* **2014**, *515* (7525), 96 – +.

(23) Zhao, J.; Bardecker, J. A.; Munro, A. M.; Liu, M. S.; Niu, Y.; Ding, I.-K.; Luo, J.; Chen, B.; Jen, A. K.-Y.; Ginger, D. S. *Nano Lett.* **2006**, *6* (3), 463–467.

(24) Pal, B. N.; Ghosh, Y.; Brovelli, S.; Laocharoensuk, R.; Klimov, V. I.; Hollingsworth, J. A.; Htoon, H. *Nano Lett.* **2012**, *12* (1), 331–336.

(25) Kim, H. H.; Park, S.; Yi, Y.; Son, D. I.; Park, C.; Hwang, D. K.; Choi, W. K. *Sci. Rep.* **2015**, *5*.

(26) Somers, R. C.; Lanning, R. M.; Snee, P. T.; Greytak, A. B.; Jain, R. K.; Bawendi, M. G.; Nocera, D. G. *Chem. Sci.* **2012**, *3* (10), 2980–2985.

(27) Jin, T.; Sasaki, A.; Kinjo, M.; Miyazaki, J. *Chem. Commun.* **2010**, *46* (14), 2408–2410.

(28) Liang, R.; Tian, R.; Shi, W.; Liu, Z.; Yan, D.; Wei, M.; Evans, D. G.; Duan, X. *Chem. Commun.* **2013**, *49* (10), 969–971.

(29) Li, Y.; Li, B. Q. *RSC Adv.* **2014**, *4* (47), 24612–24618.

(30) Geyer, S. M.; Scherer, J. M.; Moloto, N.; Jaworski, F. B.; Bawendi, M. G. *Acs Nano* **2011**, *5* (7), 5566–5571.

(31) LaMer, V. K.; Dinegar, R. H. *J. Am. Chem. Soc.* **1950**, *72* (11), 4847–4854.

(32) Owen, J. S.; Chan, E. M.; Liu, H.; Alivisatos, A. P. *J. Am. Chem. Soc.* **2010**, *132* (51), 18206–18213.

(33) Clark, M. D.; Kumar, S. K.; Owen, J. S.; Chan, E. M. *Nano Lett.* **2011**, *11* (5), 1976–1980.

(34) Steigerwald, M. L.; Alivisatos, A. P.; Gibson, J. M.; Harris, T. D.; Kortan, R.; Muller, A. J.; Thayer, A. M.; Duncan, T. M.; Douglass, D. C.; Brus, L. E. *J. Am. Chem. Soc.* **1988**, *110* (10), 3046–3050.

(35) Bawendi, M. G.; Kortan, A. R.; Steigerwald, M. L.; Brus, L. E. *J. Chem. Phys.* **1989**, *91* (11), 7282–7290.

(36) Williams, J. V.; Kotov, N. A.; Savage, P. E. *Ind. Eng. Chem. Res.* **2009**, *48* (9), 4316–4321.

(37) Zhang, L.-J.; Shen, X.-C.; Liang, H.; Guo, S.; Liang, Z.-H. *J. Colloid Interface Sci.* **2010**, *342* (2), 236–242.

(38) Joo, J.; Pietryga, J. M.; McGuire, J. A.; Jeon, S.-H.; Williams, D. J.; Wang, H.-L.; Klimov, V. I. *J. Am. Chem. Soc.* **2009**, *131* (30), 10620–10628.

(39) Houtepen, A. J.; Koole, R.; Vanmaekelbergh, D.; Meeldijk, J.; Hickey, S. G. *J. Am. Chem. Soc.* **2006**, *128* (21), 6792–6793.

(40) de Mello Donegá, C.; Liljeroth, P.; Vanmaekelbergh, D. *Small* **2005**, *1* (12), 1152–1162.

(41) Steckel, J. S.; Zimmer, J. P.; Coe-Sullivan, S.; Stott, N. E.; Bulović, V.; Bawendi, M. G. *Angew. Chem.* **2004**, *116* (16), 2206–2210.

(42) Zhong, X.; Han, M.; Dong, Z.; White, T. J.; Knoll, W. *J. Am. Chem. Soc.* **2003**, *125* (28), 8589–8594.

(43) Bailey, R. E.; Nie, S. *J. Am. Chem. Soc.* **2003**, *125* (23), 7100–7106.

(44) Cao; Banin, U. *J. Am. Chem. Soc.* **2000**, *122* (40), 9692–9702.

(45) Ou, K.-L.; Fan, J.-C.; Chen, J.-K.; Huang, C.-C.; Chen, L.-Y.; Ho, J.-H.; Chang, J.-Y. *J. Mater. Chem.* **2012**, *22* (29), 14667–14673.

(46) Wei, H.; Guo, W.; Sun, Y.; Yang, Z.; Zhang, Y. *Mater. Lett.* **2010**, *64* (13), 1424–1426.

(47) Herman, D. A. J.; Ferguson, P.; Cheong, S.; Hermans, I. F.; Ruck, B. J.; Allan, K. M.; Prabakar, S.; Spencer, J. L.; Lendrum, C. D.; Tilley, R. D. *Chem. Commun.* **2011**, *47* (32), 9221–9223.

(48) Kamble, A.; Mokurala, K.; Gupta, A.; Mallick, S.; Bhargava, P. *Mater. Lett.* **2014**, *137*, 440–443.

(49) Chen, O.; Chen, X.; Yang, Y.; Lynch, J.; Wu, H.; Zhuang, J.; Cao, Y. C. *Angew. Chem. Int. Ed.* **2008**, *47* (45), 8638–8641.

(50) Hendricks, M. P.; Campos, M. P.; Cleveland, G. T.; Plante, I. J.-L.; Owen, J. S. *Science* **2015**, *348* (6240), 1226–1230.

(51) Peng, X.; Schlamp, M. C.; Kadavanich, A. V.; Alivisatos, A. P. *J. Am. Chem. Soc.* **1997**, *119* (30), 7019–7029.

(52) Dabbousi, B. O.; Rodriguez-Viejo, J.; Mikulec, F. V.; Heine, J. R.; Mattoussi, H.; Ober, R.; Jensen, K. F.; Bawendi, M. G. *J. Phys. Chem. B* **1997**, *101* (46), 9463–9475.

(53) Talapin, D. V.; Rogach, A. L.; Kornowski, A.; Haase, M.; Weller, H. *Nano Lett.* **2001**, *1* (4), 207–211.

(54) Talapin, D. V.; Koeppe, R.; Götzinger, S.; Kornowski, A.; Lupton, J. M.; Rogach, A. L.; Benson, O.; Feldmann, J.; Weller, H. *Nano Lett.* **2003**, *3* (12), 1677–1681.

(55) Talapin, D. V.; Nelson, J. H.; Shevchenko, E. V.; Aloni, S.; Sadtler, B.; Alivisatos, A. P. *Nano Lett.* **2007**, *7* (10), 2951–2959.

(56) Kim, S.; Fisher, B.; Eisler, H.-J.; Bawendi, M. *J. Am. Chem. Soc.* **2003**, *125* (38), 11466–11467.

(57) Park, Y.-S.; Malko, A. V.; Vela, J.; Chen, Y.; Ghosh, Y.; García-Santamaría, F.; Hollingsworth, J. A.; Klimov, V. I.; Htoon, H. *Phys. Rev. Lett.* **2011**, *106* (18), 187401.

(58) Bussian, D. A.; Crooker, S. A.; Yin, M.; Brynda, M.; Efros, A. L.; Klimov, V. I. *Nat. Mater.* **2009**, *8* (1), 35–40.

(59) Vlaskin, V. A.; Beaulac, R.; Gamelin, D. R. *Nano Lett.* **2009**, *9* (12), 4376–4382.

(60) Ethayaraja, M.; Ravikumar, C.; Muthukumaran, D.; Dutta, K.; Bandyopadhyaya, R. *J. Phys. Chem. C* **2007**, *111* (8), 3246–3252.

(61) McBride, J.; Treadway, J.; Feldman, L. C.; Pennycook, S. J.; Rosenthal, S. J. *Nano Lett.* **2006**, *6* (7), 1496–1501.

(62) Greytak, A. B.; Allen, P. M.; Liu, W.; Zhao, J.; Young, E. R.; Popović, Z.; Walker, B. J.; Nocera, D. G.; Bawendi, M. G. *Chem. Sci.* **2012**, *3* (6), 2028–2034.

(63) Chen, O.; Zhao, J.; Chauhan, V. P.; Cui, J.; Wong, C.; Harris, D. K.; Wei, H.; Han, H.-S.; Fukumura, D.; Jain, R. K.; Bawendi, M. G. *Nat. Mater.* **2013**, *12* (5), 445–451.

(64) Li, J. J.; Wang, Y. A.; Guo, W. Z.; Keay, J. C.; Mishima, T. D.; Johnson, M. B.; Peng, X. G. *J Am Chem Soc* **2003**, *125* (41), 12567–12575.

(65) Xie, R.; Kolb, U.; Li, J.; Basche, T.; Mews, A. *J Am Chem Soc* **2005**, *127* (20), 7480–7488.

(66) van Embden, J.; Jasieniak, J.; Mulvaney, P. *J. Am. Chem. Soc.* **2009**, *131* (40), 14299–14309.

(67) Cao, Y.-W.; Banin, U. *Angew. Chem. Int. Ed.* **1999**, *38* (24), 3692–3694.

(68) Liu, W.; Choi, H. S.; Zimmer, J. P.; Tanaka, E.; Frangioni, J. V.; Bawendi, M. *J. Am. Chem. Soc.* **2007**, *129* (47), 14530–14531.

(69) Xie, R.; Peng, X. *Angew. Chem. Int. Ed.* **2008**, *47* (40), 7677–7680.

(70) Müller, J.; Lupton, J. M.; Rogach, A. L.; Feldmann, J.; Talapin, D. V.; Weller, H. *Phys. Rev. B* **2005**, *72* (20), 205339.

(71) Müller, J.; Lupton, J. M.; Lagoudakis, P. G.; Schindler, F.; Koeppe, R.; Rogach, A. L.; Feldmann, J.; Talapin, D. V.; Weller, H. *Nano Lett.* **2005**, *5* (10), 2044–2049.

(72) Hines, M. A.; Guyot-Sionnest, P. *J. Phys. Chem.* **1996**, *100* (2), 468–471.

(73) Yu, K.; Zaman, B.; Romanova, S.; Wang, D.; Ripmeester, J. A. *Small* **2005**, *1* (3), 332–338.

(74) Oron, D.; Kazes, M.; Banin, U. *Phys. Rev. B* **2007**, *75* (3), 035330.

(75) Balet, L. P.; Ivanov, S. A.; Piryatinski, A.; Achermann, M.; Klimov, V. I. *Nano Lett.* **2004**, *4* (8), 1485–1488.

(76) Ivanov, S. A.; Nanda, J.; Piryatinski, A.; Achermann, M.; Balet, L. P.; Bezel, I. V.; Anikeeva, P. O.; Tretiak, S.; Klimov, V. I. *J. Phys. Chem. B* **2004**, *108* (30), 10625–10630.

(77) Klimov, V. I.; Ivanov, S. A.; Nanda, J.; Achermann, M.; Bezel, I.; McGuire, J. A.; Piryatinski, A. *Nature* **2007**, *447* (7143), 441–446.

(78) Mauser, C.; Da Como, E.; Baldauf, J.; Rogach, A. L.; Huang, J.; Talapin, D. V.; Feldmann, J. *Phys. Rev. B* **2010**, *82* (8), 081306.

(79) Mauser, C.; Limmer, T.; Da Como, E.; Becker, K.; Rogach, A. L.; Feldmann, J.; Talapin, D. V. *Phys. Rev. B* **2008**, *77* (15), 153303.

(80) Lutich, A. A.; Mauser, C.; Da Como, E.; Huang, J.; Vaneski, A.; Talapin, D. V.; Rogach, A. L.; Feldmann, J. *Nano Lett.* **2010**, *10* (11), 4646–4650.

(81) Ruberu, T. P. A.; Vela, J. *ACS Nano* **2011**, *5* (7), 5775–5784.

(82) Tomaselli, M.; Yarger, J. L.; Bruchez, M.; Havlin, R. H.; deGraw, D.; Pines, A.; Alivisatos, A. P. *J. Chem. Phys.* **1999**, *110* (18), 8861–8864.

(83) Rosenthal, S. J.; McBride, J.; Pennycook, S. J.; Feldman, L. C. *Surf. Sci. Rep.* **2007**, *62* (4), 111–157.

(84) Smith, A. M.; Nie, S. *Acc. Chem. Res.* **2010**, *43* (2), 190–200.

(85) Rempel, J. Y.; Trout, B. L.; Bawendi, M. G.; Jensen, K. F. *J. Phys. Chem. B* **2005**, *109* (41), 19320–19328.

(86) Rempel, J. Y.; Trout, B. L.; Bawendi, M. G.; Jensen, K. F. *J. Phys. Chem. B* **2006**, *110* (36), 18007–18016.

(87) Guo, Y.; Alvarado, S. R.; Barclay, J. D.; Vela, J. *ACS Nano* **2013**, *7* (4), 3616–3626.

(88) Borys, N. J.; Walter, M. J.; Huang, J.; Talapin, D. V.; Lupton, J. M. *Science* **2010**, *330* (6009), 1371–1374.

(89) Choi, C. L.; Koski, K. J.; Sivasankar, S.; Alivisatos, A. P. *Nano Lett.* **2009**, *9* (10), 3544–3549.

(90) Ruberu, T. P. A.; Albright, H. R.; Callis, B.; Ward, B.; Cisneros, J.; Fan, H.-J.; Vela, J. *ACS Nano* **2012**, *6* (6), 5348–5359.

(91) Vela, J. *J. Phys. Chem. Lett.* **2013**, *4* (4), 653–668.

(92) Kirsanova, M.; Nemchinov, A.; Hewa-Kasakarage, N. N.; Schmall, N.; Zamkov, M. *Chem. Mater.* **2009**, *21* (18), 4305–4309.

(93) Mahler, B.; Nadal, B.; Bouet, C.; Patriarche, G.; Dubertret, B. *J. Am. Chem. Soc.* **2012**, *134* (45), 18591–18598.

(94) Saba, M.; Minniberger, S.; Quochi, F.; Roither, J.; Marceddu, M.; Gocalinska, A.; Kovalenko, M. V.; Talapin, D. V.; Heiss, W.; Mura, A.; Bongiovanni, G. *Adv. Mater.* **2009**, *21* (48), 4942–4946.

(95) Khon, E.; Lambright, K.; Khnayzer, R. S.; Moroz, P.; Perera, D.; Butaeva, E.; Lambright, S.; Castellano, F. N.; Zamkov, M. *Nano Lett.* **2013**, *13* (5), 2016–2023.

(96) Htoon, H.; Malko, A. V.; Bussian, D.; Vela, J.; Chen, Y.; Hollingsworth, J. A.; Klimov, V. I. *Nano Lett.* **2010**, *10* (7), 2401–2407.

(97) Chen, Y.; Vela, J.; Htoon, H.; Casson, J. L.; Werder, D. J.; Bussian, D. A.; Klimov, V. I.; Hollingsworth, J. A. *J Am Chem Soc* **2008**, *130* (15), 5026–5027.

(98) Pons, T.; Lequeux, N.; Mahler, B.; Sasnouski, S.; Fragola, A.; Dubertret, B. *Chem. Mater.* **2009**, *21* (8), 1418–1424.

(99) Kortan, A. R.; Hull, R.; Opila, R. L.; Bawendi, M. G.; Steigerwald, M. L.; Carroll, P. J.; Brus, L. E. *J. Am. Chem. Soc.* **1990**, *112* (4), 1327–1332.

(100) Galland, C.; Ghosh, Y.; Steinbrück, A.; Sykora, M.; Hollingsworth, J. A.; Klimov, V. I.; Htoon, H. *Nature* **2011**, *479* (7372), 203–207.

(101) Mahler, B.; Lequeux, N.; Dubertret, B. *J. Am. Chem. Soc.* **2010**, *132* (3), 953–959.

(102) Nan, W.; Niu, Y.; Qin, H.; Cui, F.; Yang, Y.; Lai, R.; Lin, W.; Peng, X. *J. Am. Chem. Soc.* **2012**, *134* (48), 19685–19693.

(103) George, S. M.; Ott, A. W.; Klaus, J. W. *J. Phys. Chem.* **1996**, *100* (31), 13121–13131.

(104) Hausmann, D.; Becker, J.; Wang, S. L.; Gordon, R. G. *Science* **2002**, *298* (5592), 402–406.

(105) George, S. M. *Chem. Rev.* **2010**, *110* (1), 111–131.

(106) Knez, M.; Nielsch, K.; Niinistö, L. *Adv. Mater.* **2007**, *19* (21), 3425–3438.

(107) Park, S.; Clark, B. L.; Keszler, D. A.; Bender, J. P.; Wager, J. F.; Reynolds, T. A.; Herman, G. S. *Science* **2002**, *297* (5578), 65–65.

(108) Lindroos, S.; Leskelä, M. In *Solution Processing of Inorganic Materials*; Mitzi, D. B., Ed.; John Wiley & Sons, Inc., 2008; pp 239–282.

(109) Park, S.; DiMasi, E.; Kim, Y.-I.; Han, W.; Woodward, P. M.; Vogt, T. *Thin Solid Films* **2006**, *515* (4), 1250–1254.

(110) Guo, Y.; Marchuk, K.; Sampat, S.; Abraham, R.; Fang, N.; Malko, A. V.; Vela, J. *J. Phys. Chem. C* **2012**, *116* (4), 2791–2800.

(111) Kaniyankandy, S.; Rawalekar, S.; Ghosh, H. N. *J. Mater. Chem. C* **2013**, *1* (15), 2755–2763.

(112) Ithurria, S.; Talapin, D. V. *J. Am. Chem. Soc.* **2012**, *134* (45), 18585–18590.

(113) Lee, H.; Wang, M.; Chen, P.; Gamelin, D. R.; Zakeeruddin, S. M.; Graetzel, M.; Nazeeruddin, M. K. *Nano Lett.* **2009**, *9* (12), 4221–4227.

(114) Khon, E.; Lambright, S.; Khon, D.; Smith, B.; O'Connor, T.; Moroz, P.; Imboden, M.; Diederich, G.; Perez-Bolivar, C.; Anzenbacher, P.; Zamkov, M. *Adv. Funct. Mater.* **2012**, *22* (17), 3714–3722.

(115) Jasieniak, J.; Mulvaney, P. *J. Am. Chem. Soc.* **2007**, *129* (10), 2841–2848.

(116) Wei, H. H.-Y.; Evans, C. M.; Swartz, B. D.; Neukirch, A. J.; Young, J.; Prezhdo, O. V.; Krauss, T. D. *Nano Lett.* **2012**, *12* (9), 4465–4471.

(117) van Embden, J.; Jasieniak, J.; Gomez, D. E.; Mulvaney, P.; Giersig, M. *Aust. J. Chem.* **2007**, *60* (7), 457–471.

(118) Kuno, M. Band Edge Spectroscopy of CdSe Quantum Dots. PhD Thesis, MIT, 1998.

(119) Leatherdale, C. A.; Woo, W.-K.; Mikulec, F. V.; Bawendi, M. G. *J. Phys. Chem. B* **2002**, *106* (31), 7619–7622.

(120) Jasieniak, J.; Smith, L.; van Embden, J.; Mulvaney, P.; Califano, M. *J. Phys. Chem. C* **2009**, *113* (45), 19468–19474.

(121) Yu, W. W.; Qu, L.; Guo, W.; Peng, X. *Chem. Mater.* **2003**, *15* (14), 2854–2860.

(122) Li, Z.; Ji, Y.; Xie, R.; Grisham, S. Y.; Peng, X. *J. Am. Chem. Soc.* **2011**, *133* (43), 17248–17256.

(123) Thomson, J. W.; Nagashima, K.; Macdonald, P. M.; Ozin, G. A. *J. Am. Chem. Soc.* **2011**, *133* (13), 5036–5041.

(124) Morris-Cohen, A. J.; Donakowski, M. D.; Knowles, K. E.; Weiss, E. A. *J. Phys. Chem. C* **2010**, *114* (2), 897–906.

(125) Cirillo, M.; Strubbe, F.; Neyts, K.; Hens, Z. *ACS Nano* **2011**, *5* (2), 1345–1352.

(126) Abe, S.; Čapek, R. K.; De Geyter, B.; Hens, Z. *ACS Nano* **2012**, *6* (1), 42–53.

(127) Frydman, A.; Castner, D. G.; Schmal, M.; Campbell, C. T. *J. Catal.* **1995**, *157* (1), 133–144.

(128) Katari, J. E. B.; Colvin, V. L.; Alivisatos, A. P. *J. Phys. Chem.* **1994**, *98* (15), 4109–4117.

(129) Zorn, G.; Dave, S. R.; Gao, X.; Castner, D. G. *Anal. Chem.* **2011**, *83* (3), 866–873.

(130) Tanuma, S.; Powell, C. J.; Penn, D. R. *Surf. Interface Anal.* **1994**, *21* (3), 165–176.

(131) Owen, J. S.; Park, J.; Trudeau, P.-E.; Alivisatos, A. P. *J. Am. Chem. Soc.* **2008**, *130* (37), 12279–12281.

(132) Kopping, J. T.; Patten, T. E. *J. Am. Chem. Soc.* **2008**, *130* (17), 5689–5698.

(133) Foos, E. E.; Wilkinson, J.; Mäkinen, A. J.; Watkins, N. J.; Kafafi, Z. H.; Long, J. P. *Chem. Mater.* **2006**, *18* (12), 2886–2894.

(134) Anderson, N. C.; Owen, J. S. *Chem. Mater.* **2013**, *25* (1), 69–76.

(135) Caldwell, M. A.; Albers, A. E.; Levy, S. C.; Pick, T. E.; Cohen, B. E.; Helms, B. A.; Milliron, D. J. *Chem Commun* **2011**, *47* (1), 556–558.

(136) Blanton, S. A.; Hines, M. A.; Schmidt, M. E.; Guyot-Sionnest, P. *J. Lumin.* **1996**, *70* (1-6), 253–268.

(137) Dmitri V Talapin, J.-S. L. *Chem. Rev.* **2009**, *110* (1), 389–458.

(138) Panthani, M. G.; Kurley, J. M.; Crisp, R. W.; Dietz, T. C.; Ezzyat, T.; Luther, J. M.; Talapin, D. V. *Nano Lett.* **2014**, *14* (2), 670–675.

(139) Zhang, J.; Gao, J.; Miller, E. M.; Luther, J. M.; Beard, M. C. *ACS Nano* **2014**, *8* (1), 614–622.

(140) Zhitomirsky, D.; Voznyy, O.; Levina, L.; Hoogland, S.; Kemp, K. W.; Ip, A. H.; Thon, S. M.; Sargent, E. H. *Nat. Commun.* **2014**, *5*, 3803.

(141) Meinardi, F.; Colombo, A.; Velizhanin, K. A.; Simonutti, R.; Lorenzon, M.; Beverina, L.; Viswanatha, R.; Klimov, V. I.; Brovelli, S. *Nat. Photonics* **2014**, *8* (5),

392–399.

(142) Erickson, C. S.; Bradshaw, L. R.; McDowall, S.; Gilbertson, J. D.; Gamelin, D. R.; Patrick, D. L. *ACS Nano* **2014**, *8* (4), 3461–3467.

(143) Zhu, H.; Yang, Y.; Lian, T. *Acc. Chem. Res.* **2013**, *46* (6), 1270–1279.

(144) Efros, A. L.; Rosen, M. *Phys. Rev. Lett.* **1997**, *78* (6), 1110.

(145) Frantsuzov, P. A.; Volkán-Kacsó, S.; Jankó, B. *Phys. Rev. Lett.* **2009**, *103* (20), 207402.

(146) Mahler, B.; Spinicelli, P.; Buil, S.; Quelin, X.; Hermier, J.-P.; Dubertret, B. *Nat Mater* **2008**, *7* (8), 659–664.

(147) Spinicelli, P.; Buil, S.; Quelin, X.; Mahler, B.; Dubertret, B.; Hermier, J.-P. *Phys. Rev. Lett.* **2009**, *102* (13), 136801.

(148) Efros, A. L.; Rosen, M.; Kuno, M.; Nirmal, M.; Norris, D. J.; Bawendi, M. *Phys Rev B* **1996**, *54* (7), 4843–4856.

(149) Schlegel, G.; Bohnenberger, J.; Potapova, I.; Mews, A. *Phys. Rev. Lett.* **2002**, *88* (13), 137401.

(150) Fisher, B. R.; Eisler, H. J.; Stott, N. E.; Bawendi, M. G. *J. Phys. Chem. B* **2004**, *108* (1), 143–148.

(151) Mooney, J.; Krause, M. M.; Saari, J. I.; Kambhampati, P. *J. Chem. Phys.* **2013**, *138* (20), 204705.

(152) Kalyuzhny, G.; Murray, R. W. *J. Phys. Chem. B* **2005**, *109* (15), 7012–7021.

(153) Bullen, C.; Mulvaney, P. *Langmuir* **2006**, *22* (7), 3007–3013.

(154) Munro, A. M.; Ginger, D. S. *Nano Lett.* **2008**, *8* (8), 2585–2590.

(155) Peterson, M. D.; Cass, L. C.; Harris, R. D.; Edme, K.; Sung, K.; Weiss, E. A. *Annu. Rev. Phys. Chem.* **2014**, *65* (1), 317–339.

(156) Qin, H.; Niu, Y.; Meng, R.; Lin, X.; Lai, R.; Fang, W.; Peng, X. *J. Am. Chem. Soc.* **2013**, *136* (1), 179–187.

(157) Morris-Cohen, A. J.; Malicki, M.; Peterson, M. D.; Slavin, J. W. J.; Weiss, E. A. *Chem. Mater.* **2013**, *25* (8), 1155–1165.

(158) Shen, Y.; Gee, M. Y.; Tan, R.; Pellechia, P. J.; Greytak, A. B. *Chem. Mater.* **2013**, *25* (14), 2838–2848.

(159) Hassinen, A.; Moreels, I.; De Nolf, K.; Smet, P. F.; Martins, J. C.; Hens, Z. *J. Am. Chem. Soc.* **2012**, *134* (51), 20705–20712.

(160) Owen, J. *Science* **2015**, *347* (6222), 615–616.

(161) Guyot-Sionnest, P.; Wehrenberg, B.; Yu, D. *J. Chem. Phys.* **2005**, *123* (7), 074709.

(162) McArthur, E. A.; Morris-Cohen, A. J.; Knowles, K. E.; Weiss, E. A. *J. Phys. Chem. B* **2009**, *114* (45), 14514–14520.

(163) Kilina, S.; Velizhanin, K. A.; Ivanov, S.; Prezhdo, O. V.; Tretiak, S. *ACS Nano* **2012**, *6* (7), 6515–6524.

(164) Munro, A. M.; Jen-La Plante, I.; Ng, M. S.; Ginger, D. S. *J. Phys. Chem. C* **2007**, *111* (17), 6220–6227.

(165) Knowles, K. E.; Tice, D. B.; McArthur, E. A.; Solomon, G. C.; Weiss, E. A. *J. Am. Chem. Soc.* **2009**, *132* (3), 1041–1050.

(166) Morris-Cohen, A. J.; Vasilenko, V.; Amin, V. A.; Reuter, M. G.; Weiss, E. A. *ACS Nano* **2011**, *6* (1), 557–565.

(167) Zhu, H.; Song, N.; Lian, T. *J. Am. Chem. Soc.* **2011**, *133* (22), 8762–8771.

(168) Zhao, H.; Chaker, M.; Ma, D. *Phys. Chem. Chem. Phys.* **2010**, *12* (44), 14754–14761.

(169) Lee, J. R. I.; Whitley, H. D.; Meulenberg, R. W.; Wolcott, A.; Zhang, J. Z.; Prendergast, D.; Lovingood, D. D.; Strouse, G. F.; Ogitsu, T.; Schwegler, E.; Terminello, L. J.; van Buuren, T. *Nano Lett.* **2012**, *12* (6), 2763–2767.

(170) Anderson, N. C.; Hendricks, M. P.; Choi, J. J.; Owen, J. S. *J. Am. Chem. Soc.* **2013**, *135* (49), 18536–18548.

(171) Ji, X.; Copenhaver, D.; Sichmeller, C.; Peng, X. *J. Am. Chem. Soc.* **2008**, *130* (17), 5726–5735.

(172) Williams, E. S.; Major, K. J.; Tobias, A.; Woodall, D.; Morales, V.; Lippincott, C.; Moyer, P. J.; Jones, M. *J. Phys. Chem. C* **2013**, *117* (8), 4227–4237.

(173) Yang, J.; Yang, P. *J. Nanosci. Nanotechnol.* **2012**, *12* (9), 7322–7328.

(174) Park, C.; Yoon, T. H. *Colloids Surf. B Biointerfaces* **2010**, *75* (2), 472–477.

(175) Chen, C.-J.; Chiang, R.-K.; Huang, C.-Y.; Lien, J.-Y.; Wang, S.-L. *RSC Adv.* **2015**, *5* (13), 9819–9827.

(176) Wang, M.; Zhang, M.; Qian, J.; Zhao, F.; Shen, L.; Scholes, G. D.; Winnik, M. A. *Langmuir* **2009**, *25* (19), 11732–11740.

(177) Oszajca, M.; Lincheneau, C.; Amelia, M.; Schäfer, C.; Szaciłowski, K.; Credi, A. *Eur. J. Inorg. Chem.* **2013**, *2013* (20), 3550–3556.

(178) Sharma, S. N.; Pillai, Z. S.; Kamat, P. V. *J. Phys. Chem. B* **2003**, *107* (37), 10088–10093.

(179) Burda, C.; Link, S.; Mohamed, M.; El-Sayed, M. *J. Phys. Chem. B* **2001**, *105* (49), 12286–12292.

(180) Kern, S. J.; Sahu, K.; Berg, M. A. *Nano Lett.* **2011**, *11* (8), 3493–3498.

(181) Jones, M.; Lo, S. S.; Scholes, G. D. *Proc. Natl. Acad. Sci.* **2009**, *106* (9), 3011–3016.

(182) Zhao, J.; Nair, G.; Fisher, B. R.; Bawendi, M. G. *Phys. Rev. Lett.* **2010**, *104* (15), 157403.

(183) Hens, Z.; Martins, J. C. *Chem. Mater.* **2013**, *25* (8), 1211–1221.

(184) Freyer, M. W.; Lewis, E. A. *Methods Cell Biol.* **2008**, *84*, 79–113.

(185) Grossoehme, N.; Spuches, A.; Wilcox, D. *J. Biol. Inorg. Chem.* **2010**, *15* (8), 1183–1191.

(186) Ravi, V.; Binz, J. M.; Rioux, R. M. *Nano Lett.* **2013**, *13* (9), 4442–4448.

(187) Lindman, S.; Lynch, I.; Thulin, E.; Nilsson, H.; Dawson, K. A.; Linse, S. *Nano Lett.* **2007**, *7* (4), 914–920.

(188) Mondal, S.; Ghosh, S.; Ghosh, D.; Saha, A. *J. Phys. Chem. C* **2012**, *116* (17), 9774–9782.

(189) Tan, R.; Blom, D. A.; Ma, S.; Greytak, A. B. *Chem. Mater.* **2013**, *25* (18), 3724–3736.

(190) Beaumont, P. C.; Johnson, D. G.; Parsons, B. J. *J. Chem. Soc. Faraday Trans.* **1993**, *89* (23), 4185.

(191) Davis, K.; Qi, B.; Witmer, M.; Kitchens, C. L.; Powell, B. A.; Mefford, O. T. *Langmuir* **2014**, *30* (36), 10918–10925.

(192) Gomes, R.; Hassinen, A.; Szczygiel, A.; Zhao, Q.; Vantomme, A.; Martins, J. C.; Hens, Z. *J. Phys. Chem. Lett.* **2011**, *2* (3), 145–152.

(193) Knowles, K. E.; Frederick, M. T.; Tice, D. B.; Morris-Cohen, A. J.; Weiss, E. A. *J. Phys. Chem. Lett.* **2012**, *3* (1), 18–26.

(194) Ning, Z.; Molnar, M.; Chen, Y.; Friberg, P.; Gan, L.; Agren, H.; Fu, Y. *Phys. Chem. Chem. Phys.* **2011**, *13* (13), 5848–5854.

(195) Minotto, A.; Todescato, F.; Fortunati, I.; Signorini, R.; Jasieniak, J. J.; Bozio, R. *J. Phys. Chem. C* **2014**, *118* (41), 24117–24126.

(196) Lakowicz, J. R. *Principles of Fluorescence Spectroscopy*, 3rd ed.; Springer: New York, 2006.

(197) Sillen, A.; Engelborghs, Y. *Photochem. Photobiol.* **1998**, *67*, 475–486.

(198) Orfield, N. J.; McBride, J. R.; Keene, J. D.; Davis, L. M.; Rosenthal, S. J. *ACS Nano* **2014**, *9* (1), 831–839.

(199) Tyagi, P.; Kambhampati, P. *J. Chem. Phys.* **2011**, *134* (9), 094706.

(200) Singh, G.; Guericke, M. A.; Song, Q.; Jones, M. *J. Phys. Chem. C* **2014**, *118* (26), 14692–14702.

(201) Son, D. H.; Hughes, S. M.; Yin, Y.; Paul Alivisatos, A. *Science* **2004**, *306* (5698), 1009–1012.

(202) Lambert, K.; Geyter, B. D.; Moreels, I.; Hens, Z. *Chem. Mater.* **2009**, *21* (5), 778–780.

(203) Li, H.; Zanella, M.; Genovese, A.; Povia, M.; Falqui, A.; Giannini, C.; Manna, L. *Nano Lett.* **2011**, *11* (11), 4964–4970.

(204) Ren, L.; Hardy, C. G.; Tang, S.; Doxie, D. B.; Hamidi, N.; Tang, C. *Macromolecules* **2010**, *43* (22), 9304–9310.

(205) Hassinen, A.; Moreels, I.; de Mello Donegá, C.; Martins, J. C.; Hens, Z. *J. Phys. Chem. Lett.* **2010**, *1* (17), 2577–2581.

(206) Fleischer, C. C.; Payne, C. K. *J. Phys. Chem. B* **2014**, *118* (49), 14017–14026.

(207) Shanavas, K. V.; Sharma, S. M.; Dasgupta, I.; Nag, A.; Hazarika, A.; Sarma, D. D. *J. Phys. Chem. C* **2012**, *116* (11), 6507–6511.

(208) Grabolle, M.; Spieles, M.; Lesnyak, V.; Gaponik, N.; Eychmüller, A.; Resch-Genger, U. *Anal. Chem.* **2009**, *81* (15), 6285–6294.

(209) Thessing, J.; Qian, J.; Chen, H.; Pradhan, N.; Peng, X. *J. Am. Chem. Soc.* **2007**, *129* (10), 2736–2737.

(210) Yong-Ill, L. *J. Korean Phys. Soc.* **2011**, *59* (51), 3293.

(211) Kim, J. I.; Kim, J.; Lee, J.; Jung, D.-R.; Kim, H.; Choi, H.; Lee, S.; Byun, S.; Kang, S.; Park, B. *Nanoscale Res. Lett.* **2012**, *7* (1), 482.

(212) la Rosa-Fox, N. de; Piñero, M.; Litrán, R.; Esquivias, L. *J. Sol-Gel Sci. Technol.* **2003**, *26* (1-3), 947–951.

(213) Beato-Lpez, J. J.; Fernndez-Ponce, C.; Blanco, E.; Barrera-Solano, C.; Ramrez-del-Solar, M.; Domnguez, M.; Garca-Cozar, F.; Litr, R. *Nanomater. Nanotechnol.* **2012**, 1.

(214) Li, Q.; Guo, S.; Xu, P.; Wu, L. *Cryst. Res. Technol.* **2013**, *48* (11), 977–982.

(215) Chen, H.-S.; Chung, S.-R.; Chen, Y.-C.; Chen, T.-Y.; Liu, C.-Y.; Wang, K.-W. *CrystEngComm* **2015**, *17* (27), 5032–5037.

(216) Tang, J.; Kemp, K. W.; Hoogland, S.; Jeong, K. S.; Liu, H.; Levina, L.; Furukawa, M.; Wang, X.; Debnath, R.; Cha, D.; Chou, K. W.; Fischer, A.; Amassian, A.; Asbury, J. B.; Sargent, E. H. *Nat. Mater.* **2011**, *10* (10), 765–771.

(217) Park, H. W.; Kim, D.-H. *J. Nanomater.* **2012**, *2012*, e892506.

(218) Zhang, Y.; Clapp, A. *Sensors* **2011**, *11* (12), 11036–11055.

(219) Tonti, D.; van Mourik, F.; Chergui, M. *Nano Lett.* **2004**, *4* (12), 2483–2487.

(220) Rumbles, G.; Selmarten, D. C.; Ellingson, R. J.; Blackburn, J. L.; Yu, P.; Smith, B. B.; Mićić, O. I.; Nozik, A. J. *J. Photochem. Photobiol. Chem.* **2001**, *142* (2–3), 187–195.

(221) Shen, Y.; Tan, R.; Gee, M. Y.; Greytak, A. B. *ACS Nano* **2015**, *9* (3), 3345–3359.

(222) Rogach, A. *Semiconductor Nanocrystal Quantum Dots*; Rogach, A. L., Ed.; p126-p133; Springer Wien New York: Austria, 2008.

APPENDIX-COPYRIGHT PERMISSION

Home | Account Info | Help

ACS Publications
Most Trusted. Most Cited. Most Read.

Title: Probing Surface Saturation Conditions in Alternating Layer Growth of CdSe/CdS Core/Shell Quantum Dots

Author: Rui Tan, Douglas A. Blom, Shuguo Ma, et al

Publication: Chemistry of Materials

Publisher: American Chemical Society

Date: Sep 1, 2013

Copyright © 2013, American Chemical Society

Logged in as:
Rui Tan
Account #:
3000933740

LOGOUT

PERMISSION/LICENSE IS GRANTED FOR YOUR ORDER AT NO CHARGE

This type of permission/license, instead of the standard Terms & Conditions, is sent to you because no fee is being charged for your order. Please note the following:

- Permission is granted for your request in both print and electronic formats, and translations.
- If figures and/or tables were requested, they may be adapted or used in part.
- Please print this page for your records and send a copy of it to your publisher/graduate school.
- Appropriate credit for the requested material should be given as follows: "Reprinted (adapted) with permission from (COMPLETE REFERENCE CITATION). Copyright (YEAR) American Chemical Society." Insert appropriate information in place of the capitalized words.
- One-time permission is granted only for the use specified in your request. No additional uses are granted (such as derivative works or other editions). For any other uses, please submit a new request.

BACK | CLOSE WINDOW